



**HAL**  
open science

# Physical modeling of electromagnetic effects in IC interconnects

Salvador Ortiz

► **To cite this version:**

Salvador Ortiz. Physical modeling of electromagnetic effects in IC interconnects. Physics [physics]. Université Joseph-Fourier - Grenoble I, 2007. English. NNT : . tel-00165969v2

**HAL Id: tel-00165969**

**<https://theses.hal.science/tel-00165969v2>**

Submitted on 19 Feb 2008

**HAL** is a multi-disciplinary open access archive for the deposit and dissemination of scientific research documents, whether they are published or not. The documents may come from teaching and research institutions in France or abroad, or from public or private research centers.

L'archive ouverte pluridisciplinaire **HAL**, est destinée au dépôt et à la diffusion de documents scientifiques de niveau recherche, publiés ou non, émanant des établissements d'enseignement et de recherche français ou étrangers, des laboratoires publics ou privés.

Université Joseph Fourier (Grenoble 1)  
École doctorale Mathématiques, Sciences et  
Technologies de l'Information, Informatique  
(ED 0217)

Thèse de Doctorat  
spécialité: Mathématiques Appliquées

Salvador ORTIZ

**Modélisation physique des effets électromagnétiques pour les  
interconnexions dans les circuits intégrés**  
**(Physical modelling of electromagnetic effects in IC interconnects)**

thèse dirigée par Roberto SUAYA et Gerd FINKE  
et soutenu le 11 juillet, 2007 à Grenoble

Jury composé de:

M. Lionel PICHON	Examineur
M. Sachin SAPATNEKAR	Rapporteur
M. Luca DANIEL	Rapporteur
M. Gerd FINKE	Co-Directeur de thèse
M. Roberto SUAYA	Co-Directeur de thèse



# Abstract

In this Thesis, we study three problems related to the modeling of interconnects in Integrated Circuits. The common denominator among them is the use of physical arguments in order to produce efficient models that simplify the mathematical complexity of each problem.

The first problem deals with a fast and accurate calculation of mutual inductance. We adopt a loop inductance formalism, wherein the circuit elements represent current loops. Within this formalism, we develop the dipole approximation, which keeps the leading-order terms for the inverse separations, and leads to significant reductions in the cost of computing mutual inductance. We show representative examples for parasitics extraction, as well as for the estimation of noise figures between intentional inductors. Ranges of validity are for separations larger than a threshold comparable the typical sizes of loops.

The second problem is related to the modeling of non-uniform currents, along the conductors' cross-sectional dimensions, due to skin and proximity effects. We represent this non-uniformity by expanding the current distribution with a reduced set of basis functions, called conduction modes, which are eigenfunctions to the differential equation satisfied by the current density inside the conductors. Our contributions fall in two main categories: on one side, we have expanded the existing one-dimensional current formulation into a three dimensional one, including currents and charges; on the other, we have systematically optimized the computation of non-trivial integrals appearing in the conduction modes formulation, translating the previously reported gains in size into savings in runtimes, of two orders of magnitude compared to the standard references.

The third problem concerns the representation of the frequency behavior of loop impedance using simple circuits. In order to capture the expected transitions, we use Foster pairs. These circuits are particularly useful in conjunction with realizable circuit approaches to model order reduction. We reproduce the salient features related to proximity effects and skin effects in IC's, and suggest enhancements to represent the frequency variation of mutual inductance between circuit elements.



# Résumé

Dans cette thèse, nous étudions trois problèmes liés à la modélisation des interconnexions de circuits intégrés. Leur dénominateur commun est l'utilisation d'arguments physiques afin de produire des modèles efficaces qui simplifient la complexité mathématique de chaque problème.

Le premier problème abordé est le calcul rapide et précis de l'inductance mutuelle. Nous adoptons un formalisme d'inductance de boucle, où nous développons l'approximation dipolaire, qui garde les contributions principales pour les inverses des séparations, et réduit significativement le coût du calcul de l'inductance mutuelle. Nous montrons des exemples représentatifs pour l'extraction des parasites, aussi bien que pour l'évaluation des chiffres de bruit entre inducteurs intentionnels. Les domaines de validité de l'approximation sont établis pour des séparations plus grandes qu'un seuil comparable aux tailles typiques des boucles.

Le deuxième problème est lié à la modélisation des courants non-uniformes, le long des dimensions transversales des conducteurs, dus aux effets de peau et proximité. Nous développons la distribution de courant avec un ensemble réduit de fonctions de base, appelées les "modes de conduction", qui sont des fonctions propres à l'équation satisfaite par la densité de courant à l'intérieur des conducteurs. Nos contributions dans ce domaine sont: d'un côté, nous avons étendu la formulation existante, e valide pour des courants unidimensionnels, à une formulation tridimensionnelle, comprenant des courants et des charges; de l'autre, nous avons systématiquement optimisé le calcul des intégrales non triviales apparaissant dans la formulation des modes de conduction, traduisant les gains rapportés dans la littérature pour la taille en gains pour les temps d'exécution, de deux ordres de magnitude comparés aux références standard.

Le troisième problème concerne la représentation du comportement de l'impédance de boucle en fonction de la fréquence avec des circuits simples. Afin de capturer les transitions attendues, nous employons des pairs Foster. Ces circuits sont particulièrement utiles en conjonction avec des approches à la réduction d'ordre basés sur des circuits réalisables. Nous reproduisons les caractéristiques saillantes, liées aux effets de proximité et aux effets de peau en IC, et suggérons le perfectionnement pour représenter la variation de fréquence de l'inductance mutuelle.



# Acknowledgments

First of all, my gratitude to Roberto for being always there to help, propose and discuss. I also thank him for not having any deadly weapon in his office, allowing us both to survive this process without any serious injury! I truly believe that, when we were not looking for those weapons, we had some very rewarding interactions, mainly concerning work, but also on whatnots, which have led to this wonderful moment in my career.

Special thanks go also to Gerd, for his very kind and patient disposition toward me.

The two rapporteurs of my thesis, Sachin and Luca, have generously devoted a very important part of their time and effort to my manuscript. Their written comments and presence at the defense made an enormous difference, from my perspective, in the quality of the discussions. I also wish to acknowledge the contribution of Lionel, the president of the jury.

One special person that I wish to thank at this time is Roberto Perazzo, who has been always counseled me like a father, and whose wise words at critical moments were extremely helpful.

Although not a person, Mentor Graphics deserves my personal thanks, since it has offered me ideal conditions in which to do my research, supporting me in tough moments and rewarding me in the good ones. It is difficult to ask for a better ambiance.

Of all my colleagues at Mentor, I would like to underline those who have had a positive influence on my Phd work. Rafael Escovar is first among them, as he has spent more time with me than anyone else over these last years, meaning that he knows all my secrets, so it is convenient to distinguish him specifically. It has been a pleasure to work and share discussions, professional as well as others, with Navin Srivastava, Bernie Sheehan, Xavier Ren, Dusan Petranovic, and Shrinath Telepaurath. Also important were the permanent encouragement and friendship from Jean-Cristophe Tempesta, Olivier Toublan, Jorge Entradas, Fahd Chaoui, Clement Moyroud and Samuel Benhamous, among others at the Grenoble office.

In order to avoid forgetting somebody important, a cheap trick that comes in handy: I thank anybody who feels happy for me at this special moment.

And of course, a special word for my lovely Dr. Sladkaya, who kept me company and understood me like no-one else could, even though she cheated by going through the same process at the same time, and beating me by two weeks!



# Table of Contents

<b>Introduction Générale (version française)</b>	<b>1</b>
<b>1 General Introduction</b>	<b>13</b>
1.1 Electromagnetic modeling . . . . .	14
1.2 Overview of approaches . . . . .	15
1.2.1 Time / Frequency domain . . . . .	16
1.2.2 Quasistatic / Fullwave regimes . . . . .	16
1.2.3 Integral / Differential methods . . . . .	17
1.2.4 Loop / Partial inductance . . . . .	18
1.3 Mentor Graphics . . . . .	18
1.4 Outline of this Thesis . . . . .	19
1.4.1 Efficient mutual inductance calculation . . . . .	19
1.4.2 High frequency modeling of sources . . . . .	20
1.4.3 Broadband representation with simple circuits . . . . .	21
<b>A Efficient evaluation of mutual inductance</b>	<b>23</b>
<b>2 An Improved Long Distance Treatment for Mutual Inductance</b>	<b>27</b>
2.1 Partial vs Loop Inductance treatments . . . . .	29
2.1.1 Long distance behavior . . . . .	30
2.1.2 Sparsification of the partial inductance matrix . . . . .	32
2.1.3 On positive definiteness of the loop inductance matrix . . . . .	33
2.1.4 Size of loop and partial inductance matrices . . . . .	35
2.2 Return path in the loop inductance formulation . . . . .	36
2.3 Mutual inductance and the Dipole Approximation . . . . .	39
2.4 Results . . . . .	44
2.4.1 Dipole selection rules . . . . .	45
2.4.2 Validation . . . . .	47

2.4.3	Performance analysis . . . . .	48
2.5	Discussion . . . . .	50
<b>3</b>	<b>Mutual Inductance between Intentional Inductors</b>	<b>55</b>
3.1	Classical Approach . . . . .	57
3.2	Dipole Approximation for inductors . . . . .	57
3.3	High frequency extensions . . . . .	61
3.4	Validation . . . . .	63
3.5	Performance analysis . . . . .	65
3.6	Conclusions . . . . .	66
<b>B</b>	<b>High-frequency modeling of currents and charges using conduction modes</b>	<b>69</b>
<b>4</b>	<b><i>RLC</i> conduction modes formalism and examples</b>	<b>73</b>
4.1	From Maxwell's equations to a MPIE . . . . .	76
4.2	From the MPIE to a linear system . . . . .	78
4.2.1	Quasi-static approximation . . . . .	81
4.2.2	<i>RLC</i> mixed representation . . . . .	82
4.3	Definition of conduction mode functions . . . . .	83
4.3.1	<i>RL</i> functions . . . . .	84
4.3.2	<i>RLC</i> functions . . . . .	85
4.4	<i>RLC</i> conduction modes and TEM waves . . . . .	87
4.4.1	TEM fields and transmission line behavior . . . . .	87
4.4.2	Boundary conditions for conduction modes . . . . .	88
4.4.3	Conduction mode parameters and quasi-TEM fields . . . . .	89
4.5	Solvers . . . . .	91
4.5.1	Admittance matrix . . . . .	92
4.5.2	Shorted transmission line . . . . .	93
4.5.3	Serial circuit / inductors . . . . .	94
4.6	Code organization: global structure . . . . .	95
4.7	Examples . . . . .	97
4.7.1	Shorted transmission line . . . . .	98
4.7.2	<i>RLC</i> inductor . . . . .	100
4.8	Conclusions . . . . .	102
<b>5</b>	<b>Conduction Modes Matrix Elements: <i>RL</i> case</b>	<b>107</b>
5.1	Statement of the problem . . . . .	109
5.2	General considerations . . . . .	110

5.3	Same-conductor integrals . . . . .	115
5.3.1	Exponential decays: $E$ -type contributions . . . . .	115
5.3.2	Linear decays: $L$ -type contributions . . . . .	116
5.3.3	Flat terms: $L - L$ integral types . . . . .	117
5.4	Different-conductor integrals . . . . .	120
5.4.1	Exponential contributions . . . . .	121
5.4.2	Linear or Flat contributions . . . . .	123
5.4.3	Mixed Flat/Exponential . . . . .	123
5.5	Code organization: Integral calculation blocks . . . . .	124
5.6	Performance/accuracy analysis . . . . .	127
5.6.1	$T_d$ and $G_d$ sensitivity . . . . .	128
5.6.2	$G_{lag}$ sensitivity . . . . .	132
5.6.3	$\rho_c$ sensitivity . . . . .	133
5.7	Examples . . . . .	134
5.7.1	Configuration space exploration . . . . .	135
5.7.2	Bundle example . . . . .	138
5.7.3	Power and ground grid . . . . .	139
5.8	Discussion . . . . .	142
<b>6</b>	<b>Generalization of conduction modes</b>	<b>147</b>
6.1	$L$ - and $P$ -matrix elements for $RLC$ extraction . . . . .	148
6.1.1	$P$ integrals for different conductors using Stokes' Theorem . . . . .	150
6.1.2	$P$ integrals for same conductors . . . . .	153
6.2	Accelerated $RLC$ integral calculations . . . . .	155
6.2.1	Same-conductor integrals . . . . .	156
6.2.2	Different-conductor integrals . . . . .	157
6.2.3	Preliminary examples . . . . .	158
6.3	Interpolation/Parametrization of self matrix elements . . . . .	160
6.4	Enlarging the conduction modes basis . . . . .	162
6.4.1	Dissipative modes . . . . .	163
6.4.2	Charge reaccomodation modes . . . . .	165
6.5	Arbitrary 3-d geometries . . . . .	166
6.5.1	Non-Manhattan configurations . . . . .	166
6.5.2	"Fat" wires . . . . .	166

<b>C</b>	<b>Broadband representation of <i>RL</i> behavior</b>	<b>169</b>
<b>7</b>	<b>Single-transition Foster pairs</b>	<b>173</b>
7.1	Characterization of Foster pairs . . . . .	175
7.2	One-pair Foster circuit parameters . . . . .	176
7.3	Equivalence between ladder and Foster pairs . . . . .	178
7.4	Implementation . . . . .	180
7.5	Examples . . . . .	182
7.5.1	Example with return-path selection . . . . .	182
7.5.2	Example with skin-effect current crowding . . . . .	184
<b>8</b>	<b>Multiple-transition Foster pairs</b>	<b>189</b>
8.1	Two-pair system . . . . .	189
8.2	Solving the equations . . . . .	191
8.2.1	Fixed-point iteration . . . . .	192
8.2.2	Convergence conditions . . . . .	195
8.3	Examples . . . . .	196
8.4	Discussion and further work . . . . .	199
8.4.1	Generalization to $n$ -pairs . . . . .	200
8.4.2	Higher-order ladder networks . . . . .	201
8.4.3	Broadband mutual impedance . . . . .	203
8.5	Conclusions . . . . .	206
	<b>General Conclusions</b>	<b>207</b>
	<b>Conclusions Générales (version française)</b>	<b>211</b>
	<b>Bibliography</b>	<b>214</b>

# List of Figures

1	Composants principaux impliqués dans la modélisation des effets électromagnétiques des interconnexions dans les IC. . . . .	3
1.1	Main components involved in the modeling of electromagnetic effects in IC interconnects. . . . .	15
2.1	Representative worst case scenarios for diagonal-dominance of the loop inductance matrix. . . . .	34
2.2	Example used in comparison of size in loop and partial inductance treatments. . . . .	36
2.3	Circuit equivalence of a bundle . . . . .	37
2.4	Schematic view of the dipole approximation for calculating the interaction between two bundles. . . . .	40
2.5	Calculation of dipole moment for a bundle . . . . .	41
2.6	Simple configuration for the sake of comparison of (2.24) with Grover's expressions: (a) transverse coupling; (b) forward coupling. . . . .	43
2.7	Dipole Selection Rule 1: Completely symmetric configuration, in which the return currents are balanced with respect to the signal line, having a zero net dipole moment. . . . .	46
2.8	Dipole Selection Rule 2, showing the angular dependence of mutual inductance for different separation between bundles . . . . .	47
2.9	Comparison of between the dipole approximation and FastHenry for perpendicular bundles . . . . .	48
2.10	Comparison between the dipole approximation and FastHenry for parallel bundles . . . . .	49
2.11	Comparison between the dipole approximation and FastHenry for a configuration with several return wires in each bundle. . . . .	49
3.1	Symmetric and spiral polygonal inductors . . . . .	59
3.2	Circuit equivalent of a filament discretization of an inductor . . . . .	62
3.3	Frequency variation of resistance, self inductance, and mutual inductance for a configuration consisting of two spiral inductors . . . . .	63

3.4	Mutual inductance coupling for Dipole approximation, Classical Grover expressions and FastHenry . . . . .	64
3.5	Comparative runtimes for the three methods described in the text, as a function of the number of turns for two identical octagonal symmetric inductors. . . . .	66
4.1	Conductors' surface $S(V)$ , decomposed into two contact surfaces $S_{top}$ and $S_{bot}$ , and one non-contact surface $S_{side}$ . . . . .	79
4.2	Distribution of currents for a corner $RL$ conduction mode at different frequencies	85
4.3	Geometry for the analysis of fields at the boundary between conducting and non-conducting media (non-contact surfaces). . . . .	88
4.4	Distribution of currents for a corner $RLC$ conduction mode for different frequencies . . . . .	89
4.5	Configurations for the three types of matrix solve analysed . . . . .	92
4.6	Conduction modes flow. . . . .	96
4.7	Shorted Transmission Lines example configuration. . . . .	98
4.8	Modulus and argument of admittance for the shorted transmission line example	99
4.9	Modulus and argument of shorted current for the shorted transmission line example . . . . .	99
4.10	Configuration and circuit equivalence for the 3-turn square inductor, for $RL + C$ and $RLC$ extraction . . . . .	101
4.11	Comparison between $RLC$ conduction modes and mixed $RL + C$ results for the square inductor example in the vicinity of its first resonant frequency. . . . .	102
5.1	Examples of Mode equivalence for same-conductor integrals. . . . .	111
5.2	Change of variables in eq.(5.3), exemplified for the x-integration. . . . .	111
5.3	Weight functions $\xi_x(x)$ and $\xi_y(y)$ . . . . .	114
5.4	Integration domains for $L - L$ same-conductor terms in cartesian and polar variables. . . . .	118
5.5	Taylor approximations for the polar-variable integration of same-conductor $L-L$ terms . . . . .	119
5.6	Taylor approximations for exponential terms in different-conductor integrals. . . . .	121
5.7	Flow for the computation of a matrix block for the same conductor. . . . .	125
5.8	Flow for the computation of a matrix block for the different conductors. . . . .	126
5.9	Accuracy/cost trade-off of Taylor-Jacobi integration for different-conductor integrals, as a function of parameters $G_d$ and $T_d$ . . . . .	129
5.10	Convergence of Taylor-Jacobi as a function of the number of points for the Gauss-Jacobi rules ( $G_d$ ), and the order of the Taylor polynomial ( $T_d$ ) . . . . .	130
5.11	Detail of Taylor approximations for $F(\rho)$ and errors involved . . . . .	130

5.12	Accuracy/cost trade-off of Gauss-Laguerre integration for same-conductor integrals, varying the parameter $G_{lag}$ . . . . .	132
5.13	Errors for polar variables method applied to the same-conductor flat integrals, as a function of $\rho_c$ and aspect ratio $w/h$ . . . . .	133
5.14	Curves $\rho_c(w/h)$ for different $L$ , result of minimizing errors in graphs 5.13. . . . .	134
5.15	Histograms and error distributions for the configuration space exploration using 4 side conduction modes. . . . .	136
5.16	Bundle example configuration . . . . .	138
5.17	Loop inductance and resistance behavior for the example 5.16, comparing 4 conduction modes against FastHenry at high precision. . . . .	138
5.18	Relative errors against reference, for different levels of FastHenry precision and 4 conduction modes per conductor. . . . .	139
5.19	Configuration for the power and ground grid example of $RL$ extraction. . . . .	140
5.20	Input impedance for the example in Fig. 5.19, showing the first resonant peaks, comparing for 4 conduction modes against different levels of FastHenry accuracy . . . . .	140
6.1	Checker-board structure of the $RLC$ conduction mode matrix . . . . .	149
6.2	Schematic of geometry for calculation of $P$ elements using Stokes' theorem. . . . .	150
6.3	Diagram for same-conductor $P$ integrals; the table at right shows the decomposition of the 16 surface terms for the two surface charge distributions. . . . .	153
6.4	Example of Taylor approximation for $RLC$ conduction mode integrals . . . . .	159
6.5	Same-conductor $RLC$ integrals, analyzed for variations in width, length, and frequency . . . . .	161
7.1	Basic circuit: a resistance and inductance in series with one Foster pair, as a representation of a frequency-dependent $RL$ circuit. . . . .	174
7.2	Characteristic function $\psi(\omega)$ and its derivative $d\psi/d\omega$ for a Foster pair . . . . .	176
7.3	Equivalence between a ladder circuit and a corresponding Foster pair circuit. . . . .	178
7.4	Foster pair flow diagram inserted into the Calibre xL extraction tool. . . . .	181
7.5	Configuration for capturing return-path selection effects; one signal with 17 return paths . . . . .	182
7.6	Result of fitting with one Foster pair for test case in Fig.7.5. . . . .	183
7.7	Errors for Figs.7.6 and 7.8. . . . .	183
7.8	Same results as Fig. 7.6, plotting modulus and argument of impedance. . . . .	183
7.9	Balanced sandwich configuration for the study of skin-effect current crowding. . . . .	184
7.10	Resistance and inductance figures for the configuration on Fig.7.9, comparing Foster pair fit to original data produced with FastHenry at high precision $9 \times 9$ discretization. . . . .	185

7.11	Same results as Fig. 7.10, plotting modulus and argument of total impedance. . .	185
8.1	Circuit for representing frequency dependence in the presence of two transi- tions: a resistance and inductance in series with two Foster pair. . . . .	190
8.2	Graphical view of the solution of the 2-pair Foster system (8.6) . . . . .	192
8.3	Convergence of the fixed point for a typical-case two Foster pair circuits . . . .	193
8.4	Configuration of wires for 2-pair <i>RL</i> extraction (signal wire shaded). . . . .	196
8.5	Two-pair Foster fit for the configuration of Fig. 8.4, and original data produced with FastHenry at $9 \times 9$ discretization. . . . .	197
8.6	Same data as Fig. 8.5, plotting modulus and argument of impedance. . . . .	197
8.7	Verification of conditions in (8.10) for the 2-pair Foster solution of Fig. 8.4, as a function of the intermediate frequency . . . . .	198
8.8	Average errors for the 2-pair Foster fits as function of the intermediate frequency	199
8.9	Two-ladder circuit and its reduction to a 1-ladder circuit. . . . .	201
8.10	Two-bundle example configuration for study of mutual broadband <i>RL</i> . . . . .	203
8.11	Model and circuit representation containing the notation for frequency-dependent mutual impedance. . . . .	204

# List of Tables

1	Outils de Mentor Graphics pour la modélisation électromagnétique . . . . .	7
1.1	Mentor Graphics' tools for EM modeling . . . . .	19
2.1	Summary of comparative advantages and disadvantages of Loop inductance methods with respect to Partial inductance ones. . . . .	28
2.2	Number of RLC elements in the PEEC and loop netlists . . . . .	36
2.3	Classification of frequency regimes and related physical phenomena . . . . .	38
2.4	Comparative runtimes for Dipole approximation (DA) and Grover's expressions (GE) as a function of the number of return paths $N$ ; times expressed in microseconds per evaluation . . . . .	50
3.1	Comparative runtimes for Loop Dipole approximation (DA), Classical Grover expressions (CG), and FastHenry (FH) as a function of the number of turns $N_{turns}$ for two identical octagonal symmetric inductors; times expressed in microseconds per calculation . . . . .	67
4.1	List of well-known electromagnetic solvers and their characteristics . . . . .	74
4.2	Electroquasistatic (EQS) and Magneto-quasi-static (MQS) approximations and relationship to linear system in (4.13) . . . . .	81
4.3	Comparative sizes for the different methods . . . . .	101
5.1	Classification of integral types according to the behaviors of the participating conduction modes. . . . .	113
5.2	Sizes and Runtimes for the different methods considered: "CM Taylor" refers to the savings obtained with the different-conductor approximations (Section 5.4); "CM Taylor/Gauss" refers to the complete approximations in this chapter; "CM - AQ" is using AQ algorithm for all integrals. . . . .	141



# Introduction Générale

## (version française)

Les circuits intégrés (IC) se composent de transistors et de fils; les premiers réalisent la fonctionnalité du circuit; les seconds fournissent les interconnexions nécessaires parmi les transistors. Dès le début de l'industrie d'IC, une croissance exponentielle dans le nombre maximum des transistors par pouce a été vérifiée. Elle a été accomplie grâce à une réduction des tailles typiques des surfaces des dispositifs à imprimer, d'un facteur 2 tous les deux ans. Connue comme la loi de Moore [1], elle s'applique également à la vitesse maximale d'échange dans les transistors, qui décroît comme l'inverse du facteur d'échelle; autrement dit, les vitesses maximales dans les IC sont doublées tous les deux ans. Des transistors plus rapides se traduisent en régimes plus larges de fréquence pour la propagation sur les fils. Pendant les premiers temps des IC, avec des fréquences maximales de  $10\text{MHz}$ , la longueur d'onde  $\lambda$  correspondante sur  $\text{SiO}_2$  était de  $15\text{m}$ , beaucoup plus grande que les dimensions d'un pouce, qui sont demeurées fixes autour de  $1\text{cm}$ . Après l'augmentation graduelle de la vitesse (par exemple: pour la génération de  $250\text{nm}$ , des fréquences maximales de  $1\text{GHz}$  sont associées à la longueur d'onde de  $15\text{cm}$ ), nous arrivons à la génération actuelle de  $65\text{nm}$  avec des fréquences de dizaines de  $\text{GHz}$ , qui correspondent à des longueurs d'onde de l'ordre du  $\text{mm}$ , sensiblement inférieures aux longueurs de fil de certaines interconnexions.

Les fils sont le sujet de cette dissertation; ils mènent aux systèmes linéaires qui représentent la loi d'Ohm et les équations de Maxwell. Historiquement, le traitement des interconnexions a subi plusieurs étapes différentes. Au début, leurs effets pouvaient être négligés sans risque par rapport à ceux dus aux transistors. Le premier vrai traitement des fils les représentait simplement comme une résistance ( $R$ ) et une capacitance ( $C$ ) par interconnexion [2]. De meilleures approximations de  $R$  sont obtenues en incluant une version distribuée des morceaux de  $RC$ ; dans la limite d'un nombre infini de morceaux, un circuit distribué de  $RC$  est équivalent à l'équation de diffusion [3].

Plus récemment, lorsque les fréquences atteignent la gamme des  $\text{GHz}$ , l'effet de l'inductance ( $L$ ) est devenu important; c'est une conséquence directe de la forme dans laquelle  $L$  apparaît

dans les équations du système, à savoir comme produit  $\omega L$ , où  $\omega$  est la fréquence angulaire. Des circuits comprenant l'inductance peuvent être modélisés avec des morceaux distribués *RLC*, qui, dans le cas limite, mènent à un modèle de ligne de transmission représenté par l'équation du télégraphiste [4]. La gamme des dimensions dans lesquelles les effets d'inductance sont importants ont été discutées en détail dans [2, 5].

Dans cette thèse, nous considérons différents problèmes liés à la manière dont les paramètres de circuit pour les fils sont calculés, partant d'une description de leur géométrie, de leurs propriétés électriques et de leurs interconnexions. Les domaines d'application sont la vérification des circuits numériques à grande vitesse, la radiofréquence (RF) et les circuits analogues d'ondes millimétriques, ainsi que certains circuits de signaux mixtes qui incorporent les dispositifs passifs, comme par exemple les circuits à phase-verrouillés pour la génération de l'horloge (PLL). Afin de situer les contributions de notre travail, il convient de décrire brièvement les procédés principaux impliqués dans la modélisation des effets électromagnétiques des fils pour ces applications.

## Modélisation électromagnétique

Modéliser les interconnexions exige le calcul des courants et des charges, ou des champs électromagnétiques, pour le très grand nombre de fils dans un dessin IC. Pour ceci, il est nécessaire de résoudre, d'une façon approximative, l'ensemble de quatre équations partielles (PDE) de Maxwell. Cette tâche est évidemment très difficile.

Dans l'industrie du dessin assisté par ordinateur (CAD, selon les sigles en anglais), des outils associés à cette tâche sont connus comme ceux d'extraction et de simulation. En un mot, les premiers calculent des paramètres de circuit, qui sont transmis aux deuxièmes afin d'obtenir les courants, charges, tensions, énergies, retards, etc. Six composants principaux peuvent être identifiés:

1. **Identification géométrique:** L'entrée du processus d'extraction est une description géométrique des fils, ainsi que des constantes électriques de ce type de fils, des constantes diélectriques et des perméabilités des médias, etc. Les formats typiques pour cette description sont GDSII, Oasis, etc. À cette première étape, les dispositifs sont séparés des fils, et leurs connectivités doivent être stockées afin de récupérer une représentation ultérieure du circuit.
2. **Segmentation:** La taille des configurations des IC rend impossible un traitement direct de l'ensemble des interconnexions dans le circuit. En conséquence, l'information produite dans la première étape doit être partitionnée afin de produire des sous-problèmes maniables.

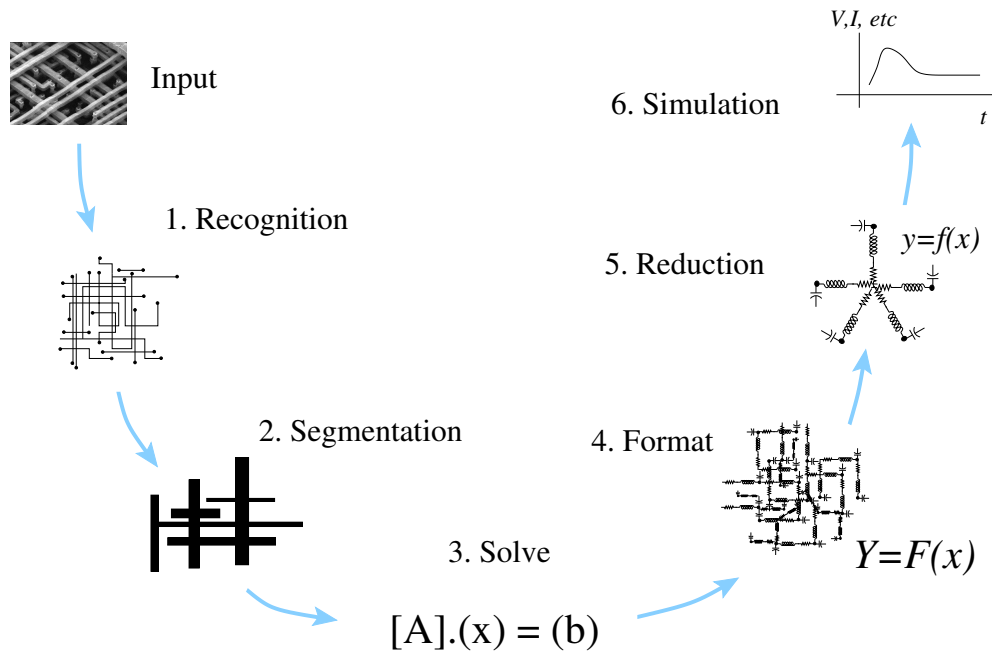


Figure 1: Composants principaux impliqués dans la modélisation des effets électromagnétiques des interconnexions dans les IC.

3. **Résolution:** Résistance  $R$ , capacitance  $C$  et inductance  $L$  sont calculés pour chaque configuration maniable créée à l'étape précédente. Généralement, ces paramètres résultent des solutions aux systèmes linéaires des équations de Maxwell. Etant le processus le plus lourd, du point de vue des coûts de calcul, l'approche choisie vis-à-vis du problème d'extraction est dictée par le type du système à résoudre, ainsi que par la méthode de résolution; ces approches seront exposées dans la prochaine section.
4. **Format du circuit RLC :** Les paramètres extraits sont transformés en circuits afin de produire des modèles significatifs. La connectivité du circuit est récupérée, des dispositifs sont inclus afin de créer une entrée valide pour le simulateur.
5. **Réduction de l'ordre du modèle (MOR) :** Dans les cas réalistes, les tailles des circuits produits par le formateur sont insurmontables pour les simulateurs de circuit. Les outils MOR les convertissent en modèles équivalents et maniables. Cette équivalence peut être atteinte soit en produisant un circuit plus petit, soit à travers d'une expression numérique plus simple.
6. **Simulation :** Magnitudes d'intérêt (courants, tensions, retard, bruit, etc.) sont obtenues après une simulation de circuit; à cette étape la modélisation des interconnexions de l'IC est effectivement couplée au reste des composants du dessin, à savoir les transistors ou

dispositifs.

## Sommaire des approches

La décomposition montrée dans 1.1 n'est pas unique; certaines de ces étapes ne sont pas toujours réalisées, ou sont groupées autrement, selon l'approche particulière au problème d'extraction. Nous détaillerons maintenant certaines des différences principales entre ces approches.

### Domaine temporel / fréquentiel

Des outils de modélisation électromagnétique peuvent être appliqués directement aux équations de Maxwell (domaine des temps); ou ils peuvent se concentrer au problème associé à une fréquence unique (domaine des fréquences).

L'avantage de travailler dans le domaine temporel est donné par le caractère compact de la description: en pratique, ils fusionnent une partie des processus décrits ci-dessus. Dans le domaine des temps, la résolution des équations de Maxwell est un problème de valeur initiale et de condition de frontière ouverte, avec une PDE hyperbolique pour les variables spatiales et temporelles.

Dans le domaine fréquentiel, le même problème est décomposé en un problème de frontière pour chaque fréquence. Chacun de ces derniers est une PDE elliptique pour les variables spatiales seulement, à savoir l'équation de Helmholtz; la fréquence demeure un paramètre pour les solutions. L'équivalence avec des méthodes du domaine temporel est récupérée après qu'un ensemble complet des solutions à fréquence unique subisse une anti-transformation de Fourier. Pour chaque fréquence, le problème est comparativement plus simple; la complexité dans le domaine fréquentiel est associée au nombre des différentes fréquences qui doivent être considérées (c.-à-d. : la signification de "complet" dans l'expression précédente dépend de chaque problème en particulier). Dans beaucoup de situations pratiques, il existe des échelles de temps d'intérêt typiques, ce qui permet de définir un ensemble réduite de fréquences associées (par exemple, dans des applications numériques, le spectre va de zéro aux fréquences de l'ordre  $1/t_{rise}$ , où  $t_{rise}$  est le temps de montée pour une rampe numérique). Par contre, pour le domaine temporel, toutes les échelles de temps significatives doivent être comprises dans la même simulation, menant à un compromis entre les petites échelles de temps qui garantissent une meilleure précision, et le coût d'avoir un grand nombre de petits pas du temps.

L'exemple typique pour des méthodes de domaine temporel est le FDTD [6]; pour le domaine fréquentiel, c'est la méthode de moments (MoM) [7]. Il y a aussi des méthodes qui peuvent être également développées dans le domaine temporel et fréquentiel, tels que la méthode des éléments finis (FEM) [8] et le circuit équivalent des éléments partiels (PEEC) [9].

Dans cette thèse, nous travaillons toujours dans le domaine fréquentiel.

## Régimes quasistatiques / d'onde complète

Dans le domaine fréquentiel, il y a fondamentalement deux approches au problème de frontière: soit une solution de l'ensemble complet des équations de Maxwell (onde complète), soit la séparation du problème en deux, résolvant le champ électrique (électro-quasi-statique, EQS) d'un côté, et le champ magnétique (magnéto-quasi-statique, MQS) de l'autre. Ce découplage simplifie énormément chacun des deux sous-problèmes par rapport au problème complet. Les charges et la capacitance sont modélisés séparément des courants et ces résistance et inductance. Les résultats obtenus avec l'hypothèse QS ne sont valides que si les échelles de temps impliquées dans les sous-problèmes sont beaucoup plus petites que l'échelle de temps pour une perturbation électromagnétique, qui est donnée par l'inverse de la fréquence. En ce sens, QS est une limite de basse fréquence; aussi, il peut-il être regardé comme une limite de large longueur d'onde, lorsque  $f \propto \lambda^{-1}$ . En tant que tels, pour des hautes fréquences, les solutionneurs QS ont besoin de décomposer les conducteurs dans un grand nombre des petites sections.

Des exemples typiques des solutionneurs d'onde complet incluent FastImp [10], HFSS [11], LargeCom [12], et plus récemment FastMaxwell [13]; pour des problèmes QS, il y a deux références standard, toutes les deux rapportées du même groupe de recherche au MIT : FastCap [14] pour EQS, FastHenry [15] pour MQS.

Une des contributions principales dans cette thèse est justement l'adaptation d'une approche très efficace pour un problème MQS à son équivalent pour le problème d'onde complet, ce qui est le sujet du chapitre 4. Dans ce dernier, nous donnerons plus de détails au sujet des liens entre QS et les solutionneurs d'onde complet.

## Méthodes intégrales / différentielles

Les équations de Maxwell peuvent être traduites et exprimées avec différentes formulations, tant sous la forme des équations différentielles que sous celle des équations intégrales.

Les solutions numériques directes à la PDE impliquent la discrétisation du domaine entier, afin de propager les conditions à la frontière en tant qu'approximations numériques aux opérateurs différentiels contenus dans les équations de Maxwell. Par conséquent, les tailles des systèmes à résoudre sont généralement très grandes; en tant que tels, ces solutions sont habituellement commodes pour des problèmes de petite taille avec beaucoup de couplage. Cependant, les composants de la description sont des cellules qui interagissent seulement avec les voisins les plus proches, afin d'exprimer les dérivés. Ceci signifie que les systèmes linéaires pour ces méthodes sont, dans le cas général, creux [16]. Autrement dit, l'inconvénient mentionné ci-dessus n'est pas de caractère fondamental, puisqu'il existe des techniques spécifiques pour manipuler de grands systèmes creux [17]. Les exemples typiques des méthodes différentielles sont ceux mentionnés ci-dessus de FDTD et de FEM ; du côté des applications, HFSS est un

exemple bien établi dans le domaine des circuit imprimés (PCB).

En utilisant des équations intégrales, il est possible de représenter le système en termes d'inconnues (les champs ou les sources) décrivant seulement les régions actives, c.-à-d. les volumes et les surfaces où les sources sont localisées. Les tailles des systèmes sont généralement plus petites que pour les équations intégrales; cependant, ces systèmes sont denses, puisqu'ils représentent l'interaction entre les sources, qui ont un caractère de longue distance (par exemple,  $1/r$  pour la fonction de Green de Coulomb). Un inconvénient commun des méthodes intégrales est lié au traitement des inhomogénéités du milieu, qui jouent le rôle des sources effectives; ceci a mené à l'introduction récente des méthodes de fonction de Green équivalentes [18, 19] afin de reproduire ces effets (du côté des applications, FastMaxwell a incorporé un tel arrangement pour traiter le substrat). Des méthodes basées sur des équations intégrales sont habituellement basées sur un schéma partant de la méthode-de-moments (MoM) afin de produire un système linéaire pour les sources [7]. Les exemples sont tous les outils du MIT mentionné ci-dessus (FastImp, FastHenry, FastCap, FastMaxwell), aussi bien que de LargeCom.

Dans cette thèse, nous utilisons des méthodes intégrales, à l'instar De la méthode MoM décrite au début du chapitre 4.

### **Inductance partielle / de boucle**

Une classification plus spécifique parmi les approches s'applique à la façon dont les champs magnétiques et les sources sont traitées dans le problème MQS, pour les outils d'extraction qui adoptent la stratégie QS. Les courants pour des systèmes de plusieurs conducteurs peuvent être modélisés sur la base des boucles ou sur celle des segments de fil; des représentations de circuit équivalentes peuvent être dérivées pour les deux types de description [20].

Des éléments partiels ont été introduits afin d'éviter l'identification à priori des boucles de courant dans un circuit, c.-à-d. le chemin de retour suivi par le courant sur chaque fil. Par contre, dans les approches d'inductance de boucle, cette détermination est la première tâche à réaliser. Les magnitudes calculées avec le traitement partiel ne représentent une réalité physique qu'au moment où les boucles sont fermées dans une étape ultérieure (par exemple par un simulateur de circuit).

En terme de calcul, cette méthode mène à des matrices denses, contenant de grands éléments hors de la diagonale. Ceux-ci représentent l'interaction non réaliste des monopoles magnétiques. Par comparaison, les éléments hors de la diagonale pour la matrice d'inductance de boucle sont beaucoup plus petits puisqu'ils représentent l'annulation numérique inhérente à une structure de boucle: le courant sur un fil est de la même magnitude, et de signe opposé, à celui de l'ensemble de ses chemins de retour. Cette différence entre les deux méthodes mène aux complications liées à la violation de passivité en essayant de rendre creuse la matrice partielle d'inductance [21].

Des exemples de traitements de boucle sont l'extracteur Calibre xL chez Mentor [22, 23],

Table 1: Outils de Mentor Graphics pour la modélisation électromagnétique

Procédé	Produit
1. Reconnaissance	Calibre LVS (layout-vs-schematics)
2-4. Segmentation, Résolution et Format	Calibre xRC/xL
5. Réduction de l'Ordre du Modèle	TICER/BMR
6. Simulation	Eldo / ADMS

ainsi que celui de Cadence, appelé Assura, [24, 25]. Les méthodes partielles proviennent du travail original de PEEC [20, 21]. Une exécution efficace, dans le domaine temporel, en utilisant des méthodes de précorrection basées sur la transformation rapide de Fourier (FFT) afin de surmonter la difficulté associée au grand nombre de produits matrice-vecteur dans la formulation partielle, a été rapportée dans [26].

Dans ce travail, nous adhérons aux traitements d'inductance de boucle; en fait, nous consacrons une partie importante du chapitre 2 à détailler les points mentionnés ci-dessus, ainsi qu'une discussion sur la façon dont les chemins de retour sont choisis dans un traitement de boucle.

## Mentor Graphics

Le travail menant à la présente thèse a été effectué aux bureaux de Mentor Graphics, situés à Montbonnot en France. Mentor est une société importante dans l'industrie du CAD, avec plus de 4000 employés dans le monde entier, répartie dans plus de 50 pays.

Ayant son siège en Orégon, aux Etats-Unis, Mentor possède 28 centres de génie, consacrant plus de 20 % de son revenu brut, qui est de l'ordre de 800 millions de dollars, aux activités de recherche et développement.

Mentor a développé des produits commerciaux pour tous les procédés discutés auparavant, et inclus dans le schéma 1. Ces produits sont énumérés dans le Tableau 1

L'équipe de travail dans laquelle ce projet a été développé est le noyau de recherche pour les outils d'extraction. Nous produisons le coeur des algorithmes insérés dans le moteur et le formateur de Calibre xL. Le rapport avec des développeurs situés au QG de Mentor mis à part, nous partageons l'espace de bureau avec le groupe principal de R&D pour les outils de simulation Eldo et ADMS. Cette proximité a mené à beaucoup de discussions fructueuses. En outre, nous coopérons avec des groupes de recherche de l'Université de Californie à Santa Barbara (UCSB), ainsi que de l'Université de l'Illinois à Urbana- Champaign (UIUC). Des

étudiants d'été provenant de ces deux établissements ont réalisé des stages durant plusieurs mois toutes les années, ce qui a stimulé énormément le cours de ce travail.

## Plan de la thèse

Pendant ce travail, nous avons touché du doigt une grande variété de problèmes liés aux procédés du schéma 1, avec une considération spéciale sur les points 3 et 4. Trois de ces problèmes constituent le contenu de la thèse, qui est en conséquence organisée en trois parties. Concernant les outils Mentor Graphics, nous nous sommes consacrés aux perfectionnements et additions pour les outils d'extraction Calibre. Dans les pages qui suivent, nous donnons une description succincte de chacun de ces problèmes, laissant des détails pour les introductions de chaque chapitre. Tous les chapitres incluent des conclusions et discussions sur des sujets de travail présents et à venir, qui seront également récapitulés en fin de thèse.

## Calcul efficace de l'inductance mutuelle

Le traitement de boucle de l'inductance implique l'identification de chaque fil ainsi que de tous les chemins de retour possibles pour chaque signal; ces boucles constituent les éléments de description pour l'extraction  $RL$ . En calculant les distributions des courants parmi les chemins de retour, nous obtenons l'inductance propre de la boucle.

Ensuite, des interactions entre toutes les paires de boucles différentes doivent être estimées. Généralement, cela exige un coût de calcul qui croît au carré du nombre de fils interagissant.

Nous présentons une méthode qui réduit nettement la complexité de ce problème. En ce qui concerne la recette générale mentionnée ci-dessus, l'avantage principal réside dans le fait que le coût devient linéaire avec le nombre de fils. La clé de cette méthode est la simplification de l'interaction entre deux boucles, en traitant chacune comme un dipôle magnétique idéal situé au centre efficace de la boucle. Nous avons dénommé ceci l'approximation dipolaire, et avons montré son efficacité pour des calculs rapides des interactions à longue distance.

Spécifiquement, les chapitres concernant cette méthode sont :

- **Chapitre 2:** Nous présentons l'approximation dipolaire pour le problème de l'extraction des parasites; ce travail est une version étendue de l'article présenté à [27] et édité dans [28] en version journal; les routines expliquées dans le texte sont incluses dans le moteur Calibre xL, et ont été classées pour une demande de brevet [29].
- **Chapitre 3:** L'approximation dipolaire est étendue afin d'inclure l'inductance mutuelle entre deux inducteurs intentionnels; ce travail a été présenté à [30] et classé pour une autre demande de brevet [31].

## Modélisation des sources aux très hautes fréquences

Aux fréquences suffisamment hautes, les courants et les champs à l'intérieur d'un conducteur ne peuvent pas être considérés uniformes. Il est bien connu que les courants se distribuent près de la surface des conducteurs, selon une chute exponentielle décrite par une échelle typique  $\delta$ , la profondeur de peau pour le conducteur. Ce paramètre diminue lorsque la fréquence croît ( $\delta \propto f^{-1/2}$ ): pour le cuivre, il va de  $6.6\mu$  à  $100\text{ MHz}$  jusqu'à  $0.21\mu$  à  $100\text{ GHz}$ .

Afin de décrire ce manque d'uniformité pour les distributions du courant, l'approche la plus directe est celle consistant à discrétiser le conducteur dans de petits éléments, tels que le courant peut être considéré uniforme pour chacun d'eux. Il est évident que cette stratégie impose un grand surcoût à l'extraction aux hautes fréquences par rapport à celles aux basses fréquences. Par exemple, un solveur MQS comme FastHenry doit décomposer chaque fil le long de sa section transversale. Le coût accru dû à cette réalité a déclenché une grande quantité de recherches dans le développement des techniques rapides de résolution, comme par exemple des expansions multipolaires rapides (dans FastHenry, FastCap, FastImp et LargeCom), la précorrection pFFT (dans FastImp et FastMaxwell), entre autre.

Nous avons choisi une stratégie complètement différente: celle qui a été présentée dans [32], où les distributions des courants sont décrites en termes d'un type spécial de fonctions, à savoir les fonctions propres de l'équation satisfaite par des courants à l'intérieur des conducteurs. Modéliser en termes de ces fonctions spécifiques, désormais appelés "modes de conduction", fournit une représentation plus compacte, bien que du même niveau d'exactitude, que les modèles de fonctions constants par morceaux.

Nos contributions dans ce domaine sont organisées comme suit :

- **Chapitre 4 :** Nous présentons le cadre formel pour ce problème, aussi bien que la méthode existante de modes de conduction, qui est limitée aux problèmes  $RL$  dans la limite QS; ensuite, nous introduisons une version  $RLC$  des modes de conduction, valide pour des structures semblables aux lignes de transmission, et montrons sa validité sur des configurations exemplaires. Ce chapitre est une version allongée du travail présenté à [33].
- **Chapitre 5:** Nous analysons, proposons, et mettons en pratique, une stratégie numérique abordant la complication principale du formalisme de modes de conduction  $RL/MQS$ , à savoir le calcul de ses éléments de matrice. Avec ces méthodes, nous arrivons à traduire une économie d'un facteur 20 pour la taille du système, comme a été rapporté dans [32] en une économie, de deux ordres de magnitude pour le temps d'exécution, par rapport au même niveau de précision avec des approches des fonctions constants par morceaux. Une version courte de ce chapitre a été présentée à [34].

- **Chapitre 6:** Ce chapitre est consacré aux questions qui doivent être posées au moment de transformer le formalisme des modes de conduction dans un solveur d'onde complète efficace. Ces questions sont: adapter les méthodes numériques du domaine  $RL$  à celui  $RLC$ ; ainsi qu'agrandir les ensembles de fonctions et de géométries de base considérés dans la version actuelle.

## Représentation large bande avec des circuits simples

Finalement, nous nous concentrons sur un problème lié aux composants du formateur dans le schéma d'extraction 1). En particulier, nous nous intéressons à la capture des variations pour la résistance et de l'inductance avec la fréquence. Plus spécifiquement, nous voulons faire ceci en utilisant seulement des composants de circuit constants.

Dans le domaine fréquentiel, des paramètres de  $R, L, C$  sont extraits fréquence par fréquence. Dans certains cas particuliers, une extraction à une fréquence unique peut suffire afin d'obtenir des limites sur le bruit ou le retard. Pour le cas général, il faut construire des circuits montrant le comportement correct sur une grande gamme des fréquences.

Puisque ce processus est réalisé à l'étape du formatage, le choix particulier de la représentation est lié au processus suivant dans le schéma, qui est la réduction de l'ordre du modèle (MOR). Dans le cas des interconnexions, il s'agit de la réduction de circuits linéaires et passifs.

Il existe fondamentalement deux lignes d'approche pour ce type de MOR: celles qui calculent une version équivalente, tandis que simplifiée mathématiquement, de la réponse du circuit; et celles qui produisent un circuit physiquement réalisable d'une plus petite dimension.

Pour le premier type de réducteurs, le point de départ est la méthode asymptotique d'évaluation de la forme d'onde (AWE) [35] en 1990, où les moments de la réponse sont ajustés aux fonctions rationnelles. Ce travail a ouvert la voie à une série d'améliorations, telles que les méthodes Padé via Lanczos [36] et PRIMA [37]. Toutes ces méthodes font partie de la catégorie des méthodes de projection de Krylov, qui constituent aujourd'hui encore un grand domaine de recherche. Le défi principal est celui d'éviter la possible perte de passivité contenue dans la formulation originale de AWE.

Calibre, l'outil d'extraction chez Mentor, a incorporé une technique qui appartient au second type de réducteurs. TICER/BMR [38, 39] se fonde sur l'élimination des noeuds du circuit. La détermination des noeuds à éliminer est basée sur des considérations locales des constantes de temps. Sans entrer dans les détails, lesquels ne relèvent pas du champ d'étude de cette thèse, nous renvoyons à [40] pour une analyse comparative et complète de ce type de méthode par rapport à celles mentionnées dans le paragraphe précédent.

Pour la représentation à large bande, TICER/BMR permet la réduction de plusieurs types de circuits comprenant des paires Foster. Ceux-ci sont des blocs simples, dont chacun se compose d'un résistor en parallèle avec un inducteur. Un de ces blocs peut reproduire une transition

*L*-décroissant/*R*-croissant en fonction de la fréquence croissante. D'un point de vue physique, ces transitions ont deux origines: le choix des chemins de retour pour le courant sur un fil de signal (effet de proximité); et la distribution non uniforme des courants sur les dimensions transversales du fil (effet de peau).

Nous organisons notre travail dans ce domaine de la façon suivante:

- **Chapitre 7:** Nous caractérisons des paires Foster et mettons en pratique une solution pour le cas d'une transition simple; cette méthode est incorporée au schéma de Calibre depuis 2005 et est protégée par une demande de brevet [41].
- **Chapitre 8:** Nous considérons le cas des paires Foster pour représenter des transitions multiples ; d'abord nous développons et analysons une stratégie pour les circuits Foster à deux paires; nous concluons en discutant brièvement des situations plus générales.



# Chapter 1

## General Introduction

Integrated Circuits (IC's) are composed of transistors and wires; the former implement the functionality of the circuit, the latter provide the necessary interconnections among the transistors. From the start of the IC industry, an exponential growth in the maximum number of transistors per chip has been verified. It has been accomplished by a reduction in the area occupied by the features to be printed, by a factor of 2 every two years. Known as Moore's law [1], it also applies to the maximum switching speed of transistors, that goes as the inverse of the scale factor; in other words, maximum speeds in IC's are doubled every two years. Faster switching transistors translates into wider frequency regimes for wire propagation. In the early days of IC logic, with maximum frequencies of  $10\text{MHz}$ , the corresponding wavelength  $\lambda$  on  $\text{SiO}_2$  was of  $15\text{m}$ , much larger than the chip dimensions, which remain fixed at  $\sim 1\text{cm}$ . Following the speed increase with scaling, (e.g. for the  $250\text{nm}$  generation, maximum frequencies of  $1\text{GHz}$  correspond to minimum wavelength of  $15\text{cm}$ ), we arrive at the current  $65\text{nm}$  generation, with frequencies in the tens of  $\text{GHz}$  associated to  $10\text{ps}$  rise-times, i.e. minimum wavelengths of the order of the millimeter, significantly smaller than some interconnect wire lengths.

Wires are the subject of this dissertation; they lead to linear systems that represent Ohm's law and Maxwell's equations. Historically, the treatment of interconnects has undergone several different phases. At the beginning, their effects could be safely neglected with respect to the ones due to transistors. The first treatment of wires were simple resistance ( $R$ ) - capacitance ( $C$ ) lumps representing for each interconnect [2]. Better  $RC$  approximations are obtained by including a distributed version of  $RC$  lumps; in the limit of an infinite number of lumps, a distributed  $RC$  circuit is equivalent to the diffusion equation [3].

More recently, as frequencies reach the  $\text{GHz}$  range, inductance ( $L$ ) effect have become important; this is a direct consequence of the form in which  $L$  enters the system equations, namely as the product  $\omega L$ , where  $\omega$  is the angular frequency. Circuits including inductance can be modeled as distributed  $RLC$  lumps, which in the limiting case lead to a transmission-line model in

the form of the telegraphist's equation [4]. Ranges of dimensions in which inductance effects are important have been discussed in [2, 5].

In this thesis, we consider different problems related to the way in which circuit parameters for wires are computed, starting from a geometrical description of wires, their electrical properties and their interconnections. The domain of application is the verification of high speed digital circuits, radio frequency (RF) and millimeter wave analog circuits, and some mixed signal circuits that incorporate passive devices as in phase-locked loop (PLL) clock generation circuits. In order to situate the contributions of our work, it is convenient to briefly describe the main processes involved in modeling electromagnetic effects in wires for these applications.

## 1.1 Electromagnetic modeling

Modeling interconnects demands computing currents and charges, or equivalently electromagnetic fields, for the enormous number of wires in an IC design. In order to do so, it is necessary to model electromagnetic effects, expressed in the form of Maxwell's set of four partial differential equations (PDE's). Needless to say, this is a very difficult task.

In the CAD industry, associated tools are known as extraction and simulation tools. In a nutshell, the first ones compute circuit parameters, which are passed on to the second ones, in order to obtain currents, charges, voltages, energies, delays etc. Six main components can be identified:

1. **Geometric recognition:** The input for extraction is a geometrical description of wires, together with electrical constants such as conductivities of wires, permittivities and permeabilities of media. Typical formats for this description are GDSII, Oasis, etc. At the first stage, devices are separated from wires, and connectivity among these must be stored in order to allow for a downstream circuit representation.
2. **Segmentation:** The size of IC configurations renders impossible a direct treatment of all the interconnects in the circuit. Therefore, the information produced in step 1 must be spanned and partitioned in order to produce manageable subproblems.
3. **Solution:** Resistance  $R$ , capacitance  $C$  and inductance  $L$  are computed for the manageable configurations created in the first step. In general, these result from solutions to linear systems representing Maxwell's equations. Usually the approach to extraction is dictated by the type of system and solution method; these approaches will be expanded in the next section.
4. **RLC circuit format:** Extracted  $R, L, C$  parameters are transformed into circuits in order to produce meaningful models. The connectivity of the circuit is recovered, components

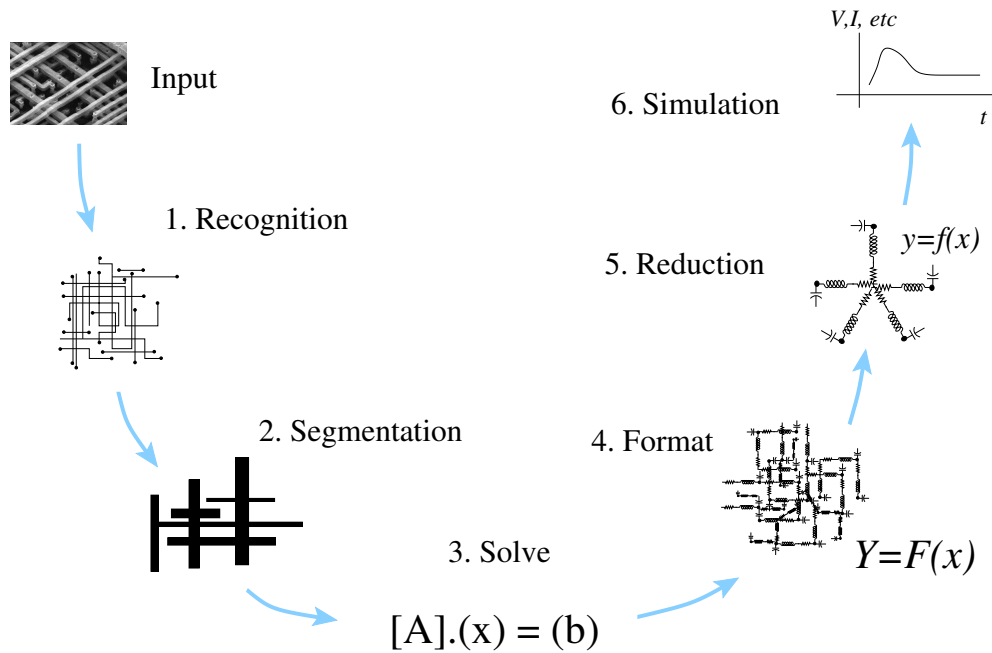


Figure 1.1: Main components involved in the modeling of electromagnetic effects in IC interconnects.

are rejoined in order to create valid input for the simulators.

5. **Model order reduction (MOR):** In realistic cases, the sizes of circuits produced by the formatter are intractable for circuit simulators. MOR tools convert them into equivalent, manageable ones; this can be done either by producing a smaller circuit, or a simpler numerical expression.
6. **Simulation:** Relevant magnitudes (currents, voltages, delays, noise, etc.) are obtained after a circuit simulation; at this stage the modeling of IC interconnects can be coupled with the rest of the components in a design, namely the transistors or devices.

## 1.2 Overview of approaches

The decomposition shown in Fig. 1.1 is not unique; some of these tasks are not always done, or are grouped differently, according to the approach of any particular method. We will now detail some of the main differences among methods.

### 1.2.1 Time / Frequency domain

EM tools can be applied directly to Maxwell's equations (time domain); or they can solve problems associated to a single frequency (frequency domain).

The advantages of working in the time domain are given by the compactness of the description: in practice, they merge some of the points in the flow described above, into one single process. In the time domain, solving Maxwell's equations is an initial-value, open boundary-condition problem, with a hyperbolic PDE for the time and spatial variables.

In the frequency domain, the same problem is decomposed into one boundary-value problem per frequency. Each of these is an elliptic PDE for the spacial variables only, namely the Helmholtz equation; the frequency is a parameter for the solutions. The equivalence with time domain methods is recovered after a complete set single-frequency solutions undergo a Fourier anti-transformation. For each frequency, the problem is comparatively simpler; complexity in the frequency domain is associated to the (problem-dependent) number of different frequencies that must be considered (i.e.: the meaning of "complete" in the previous phrase). In many practical situations, there exist typical time scales of interest, which define a reduced set of associated frequencies (e.g., in digital applications, the spectrum goes from zero to frequencies of order  $1/t_{rise}$ , with  $t_{rise}$  the rise time for a digital ramp). In the time domain, all significant time scales must be accounted for in the same simulation, leading to a trade-off between small time steps that guarantee better precision, and the cost involved in having a large number of these small.

An example for time domain methods is the Finite Difference Time Domain (FDTD) algorithm [6]; for the frequency domain, there is the Method of Moments (MOM) [7]. There are also methods which can be equally developed in the time and frequency domains, such as the Finite Element Method (FEM) [8] and the Partial Element Equivalent Circuit (PEEC) [9].

In this work, we always work in the frequency domain.

### 1.2.2 Quasistatic / Fullwave regimes

Within the frequency domain, there are basically two types of approaches to the boundary-value problem: either to approach a solution involving the full set of Maxwell's equations (fullwave), or to split the problem in two, solving the electric field on one side (electroquasistatic, EQS), and the magnetic field (magnetoquasistatic, MQS) on the other. This decoupling simplifies enormously each of the two subproblems. Charges and capacitance are modeled separately from currents and resistance/inductance.

The results obtained within the QS assumption are valid as long as the time scales involved in the subproblems are much smaller than the time scale for an EM perturbation, given by the inverse of the frequency. In this sense, QS is a low-frequency limit; also, it can be viewed as long-wavelength limit, since  $\lambda \propto f^{-1}$ . As such, for very high frequencies, QS solvers require a

decomposition of conductors into electromagnetically small portions.

Typical examples of fullwave solvers include FastImp [10], HFSS [11], LargeCom [12], and recently FastMaxwell [13]; for QS problems, there are two standard references, both coming from the same research group at MIT: FastCap [14] for EQS, FastHenry [15] for MQS. One of the main contributions in this work is precisely the adaptation of a purely MQS scheme to a fullwave problem, which is the subject of Chapter 4. Therein, we elaborate on details concerning the links between QS and fullwave solvers.

### 1.2.3 Integral / Differential methods

Maxwell's equations can be translated into many different formulations, both as differential or as integral equations.

Direct numerical solutions to PDE's involve discretizing the entire domain, in order to propagate the boundary conditions as numerical approximations to the differential operators in Maxwell's equations. The size of the systems to be solved are generally very large; as such, these solutions are usually convenient for small bounded problems. However, the components of the description are cells that only interact with nearest neighbors, as local approximations to derivatives. This means that the linear systems for these methods are, in the general case, sparse [16]. Thus the aforementioned drawback is not of a fundamental nature, since there exist a specific techniques for handling large, sparse systems [17]. Typical examples of differential methods are the aforementioned FDTD and FEM methods; in terms of applications, HFSS is a well-established example within the domain of printed circuit boards (PCB).

For integral equations, it is possible to represent the system in terms of unknowns (fields or sources) describing solely active regions, i.e. the volumes and surfaces where the sources are located. System sizes are generally smaller than for integral equations; however, these systems are in general dense, since they represent interaction between sources, which are a long-range interaction (e.g.,  $1/r$  for the Coulomb Green function). One common drawback of integral methods is related to the treatment of inhomogeneities in the medium, which play the role of effective sources; this has led to the recent introduction of equivalent Green function methods [18, 19] in order to account for these effects (in terms of applications, FastMaxwell has incorporated such a scheme for treating substrate). Methods based on integral equations are usually based on a method-of-moments (MOM) scheme in order to produce a linear system [7]. Examples are all the tools from MIT mentioned above (FastImp, FastHenry, FastCap, FastMaxwell), as well as LargeCom.

In this Thesis, we apply integral methods; such is the general method described at the beginning of Chapter 4.

### 1.2.4 Loop / Partial inductance

A more specific type of classification among approaches applies to the way magnetic fields and sources are treated in the MQS problem, for extraction tools that adopt the QS strategy. Currents in multiconductor systems can be calculated either on loops or on partial wire segments; equivalent circuit representations can be derived through either description [20].

Partial elements were introduced in order to avoid having to predetermine the current loops in a circuit, i.e. the return path followed by a current on any given wire. On the other hand, for loop inductance methods, this is the first, and most delicate, task to be carried out. The magnitudes computed within the partial treatment do not represent a physical reality, until the loops are closed further down the modeling flow (for example by a circuit simulator).

In terms of computation, this observation leads to dense matrices for partial inductance, in the sense that they contain large off-diagonal elements. These represent unrealistic monopole interaction between currents. By comparison, the off-diagonal elements in the loop inductance matrix are smaller, since they represent effectively the numerical cancellation inherent in a loop structure: the current on one wire is equal in magnitude to the ones in the return paths. This difference leads to problems of passivity violation in attempting to sparsify the partial inductance matrix [21].

Examples of loop treatments are Mentor's Calibre xL extractor [22,23], as well as Cadence's Assura tools [24,25]. Partial methods all spring from the original PEEC work [20,21]. An efficient time-domain implementation, using precorrected-FFT (Fast Fourier Transform) methods in order to overcome the difficulty associated to the large number of matrix-vector products in the partial formulation, was reported in [26].

In this work, we adhere to loop inductance treatments; in fact, we devote an important part of Chapter 2 to detailing the points mentioned above, as well as a discussion on how the return paths are selected within a loop treatment.

## 1.3 Mentor Graphics

The work leading to the present dissertation was carried out at the offices of Mentor Graphics in Montbonnot, France. Mentor is a major company in the CAD industry, with more than 4000 employees worldwide, distributed in over 50 countries. Headquartered in Oregon, USA, Mentor has 28 engineering centers and spends more than 20% of its raw income, which is in the order of 800 million US dollars, in research and development activities.

Mentor has developed commercial products for all the items described in Section 1.1. Relating to the flow in Fig. 1.1, Mentor's products are listed in Table 1.1

The workgroup in which this project was developed is the core of research for the extraction tools. We produce the kernel of the algorithms inserted into the Calibre xL engine and formatter.

Table 1.1: Mentor Graphics' tools for EM modeling

Process	Product
1. Recognition	Calibre LVS (layout-vs-schematics)
2-4. Segmentation, Solve, Format	Calibre xRC/xL
5. Model Order Reduction	TICER/BMR
6. Simulation	Eldo / ADMS

Apart from the relationship with developers at Mentor HQ, we share office space with the main R&D group for the simulation tools Eldo and ADMS. This vicinity has led to many fruitful discussions.

Also, we cooperate with research groups at the University of California in Santa Barbara, as well as the University of Illinois in Urbana Champaign. Summer visiting students from both of these institutions have been very stimulating for the course of this work.

## 1.4 Outline of this Thesis

During the course of this work, we have addressed a very large scope of problems related to the implementation of the flow described above, with special emphasis on points 3 and 4. Three of these problems constitute the contents of the present Thesis, that is accordingly organized into three parts. This work has been incorporated into an industrial tool set at Mentor Graphics, and our approaches have been used in order to enhance the Calibre extraction engine. We will now give a succinct description of each of these, leaving details for the introductions of each Chapter. All chapters include conclusions and discussions concerning present and future work, which will also be summarized at the end of the thesis.

### 1.4.1 Efficient mutual inductance calculation

Loop treatment of inductance involves recognizing each signal wire and all its possible return paths; these effective current loops constitute the building blocks of the  $RL$  extraction scheme. By computing the distributions of currents among the return paths, we obtain the loop self inductance.

Next, interactions between all pairs of two different loops must be accounted for. In general, this task requires a cost which is quadratic with the total number of interacting wires.

Our contribution in this domain is a method that significantly reduces the complexity of this problem. With respect to the general recipe mentioned above, the main advantage is that

the cost becomes linear. The key aspect is to simplify the interaction between two loops, by treating each one as an ideal magnetic dipole located at the effective center of the loop. We have denominated this the *dipole approximation*, and shown its efficiency for rapid computations of long distance interactions.

Specifically, the chapters relating to this method are:

- **Chapter 2:** We introduce the dipole approximation for the problem of parasitics extraction; this work is an extended version of the paper presented in [27] and published in [28] as a journal version; the routines explained in the text are included in the Calibre xL engine, and have been filed for a patent application [29].
- **Chapter 3:** The dipole approximation is extended in order to include mutual inductance between two intentional inductors; this work has been published in [30] and filed for another patent application [31].

### 1.4.2 High frequency modeling of sources

For very high frequencies, currents and fields inside a conductor are not uniform. It is well-known that currents distribute themselves near the surface of the conductors, according to an exponential decay within a typical scale  $\delta$ , the skin depth for the conductor. This parameter decreases with growing frequency ( $\delta \propto f^{-1/2}$ ): for copper, it varies from  $6.6\mu$  at  $100\text{ MHz}$  to  $0.21\mu$  at  $100\text{ GHz}$ .

In order to describe this non-uniformity of current distributions, the straightforward approach is to discretize the conductor into small elements, such that current can be considered uniform for each one of them. The increased cost of this procedure is self-evident, and makes high-frequency extraction a gruesome task. For example, an MQS solver like FastHenry must decompose each wire along its cross-section, including a number of piecewise-constant filaments. The increased cost due to this reality has triggered a large amount of research into developing fast solver techniques, like fast multipole expansions (in FastHenry, FastCap and FastImp, LargeCom), pFFT precorrection (in FastImp and FastMaxwell), among others.

We adhere to a completely different strategy: the one presented in [32], with current distributions described in terms of a special type of functions, named *conduction modes*, which are eigenfunctions of the differential equation satisfied by currents inside the conductors. Modeling in terms of these specific functions provides a compact representation at the same level of accuracy of piecewise constant models.

Our contributions in this domain are organized as follows:

- **Chapter 4:** We present the formal framework for this problem, as well as the existing conduction modes method, which is restricted to extraction of *RL* parameters in the QS

limit; then we introduce an *RLC* version of conduction modes, valid for structures similar to transmission lines, and validate with exemplary configurations; this chapter is an extended version of the work presented at [33].

- **Chapter 5:** We analyze, propose, and implement a numerical strategy for handling the major complication for the *RL/MQS* conduction modes formalism, which resides in the computation of its matrix elements; we are able to translate savings of a factor 20 in size, as reported in [32], into savings of two orders of magnitude in runtime with respect to similar-accuracy filament based solutions; a short version of this chapter has been published at [34].
- **Chapter 6:** This chapter is devoted to some of the issues that must be addressed in order to convert the conduction modes formalism into a complete and efficient fullwave field solver; these tasks include: adapting the numerical methods from the *RL* to the *RLC* domain; enlarging the sets of basis functions and geometries accepted.

### 1.4.3 Broadband representation with simple circuits

Finally, we concentrate on a problem related to the former part of the extraction flow (Fig.1.1): representing extracted circuits valid over a wide frequency range. In particular, we are concerned with capturing the variations of resistance and inductance with frequency. More specifically, we want to do so using only constant circuit components, namely *Foster pairs*.

Within the frequency domain, *RLC* parameters are extracted on a frequency-by-frequency basis. In some particular cases, an extraction at a single frequency is sufficient for obtaining bounds on noise or delay. In general, however, it is necessary to construct circuits exhibiting the correct behavior of parameters over a wide frequency range.

Since this task is done at the formatting stage, the particular choice of representation is linked to the subsequent process in the flow, which is Model Order Reduction (MOR). In the case of interconnects, we are dealing with reduction of passive linear circuits.

There exist basically two lines of approach for this type of MOR: those that compute a mathematically simplified equivalent version of the response of the circuit; and those that produce physically realizable circuit of smaller dimension.

For the first type of reducers, the starting point work is the Asymptotic Waveform Evaluation (AWE) method [35] in 1990, in which moments of the response are fitted to rational functions. This set the pace for a series of refinements, such as the Padé via Lanczos [36] and PRIMA [37]. These methods all fall within the category of Krylov projection methods, which constitute a large area of ongoing research. The main challenge lies in avoiding possible loss of passivity present in the original AWE formulation.

Calibre has incorporated a technique that belongs to the second type of reducers. The TICER/BMR [38, 39] method relies on elimination of circuit nodes based on local considerations of time-constants. Without going into details, which is not in the scope of this Thesis, we refer to [40] for a thorough comparative analysis of this type of method with respect to the ones mentioned in the previous paragraph.

For broadband representation, TICER/BMR permits the reduction of several types of circuits including Foster pairs. These are simple blocks consisting of one resistance in parallel with one inductance. Each of these blocks is able to reproduce one relevant frequency decreasing- $L$ /increasing- $R$  transition. From a physical point of view, these transitions have two origins: the choice of return paths for the current flowing on any given signal wire (proximity effect); and the non-uniform current crowding of currents on the cross-sectional dimensions of any wire (skin effect).

We organize our work in this area as follows:

- **Chapter 7:** We characterize Foster pairs and implement a solution to the case with one single transition; this method is incorporated into the Calibre flow as of 2005 and is protected by a patent application [41].
- **Chapter 8:** We consider the case of Foster pairs for representing multiple transitions; first we develop and analyze a strategy for two-pair serial Foster circuits; we conclude by briefly discussing more general situations.

## **Part A**

# **Efficient evaluation of mutual inductance**



# Un traitement amélioré pour l'inductance mutuelle aux longues distances

## Résumé en français

*Dans ce chapitre nous développons l'approximation dipolaire pour l'extraction de l'inductance mutuelle. Lorsqu'elle est appliquée dans des approches d'inductance de boucle, nous commençons le chapitre par une discussion étendue sur les avantages de ceux-ci par rapport aux approches d'inductance partielle (section 2.1). Cette discussion mène directement au sujet le plus délicat pour notre approche, qui est la sélection des chemins de retour pour chaque signal ; autrement dit, la détermination des boucles dans le système (section 2.2). En estimant les inductances propres de ces boucles, nous obtenons aussi des coefficients permettant le développement des formules de notre approximation dipolaire (section 2.3). Nous exposons des exemples d'application pour des configurations typiques dans le domaine de l'extraction des parasites, montrant une précision acceptable pour des distances supérieures à un seuil qui est du même ordre que les tailles des boucles (section 2.4). Finalement, nous concluons par une discussion sur les applications et les futures extensions (section 2.5). Le travail discuté en ce chapitre a été présenté à l' "International Symposium on Physical Design" (ISPD'04) [27], et développé dans un article pour les "Transactions on CAD" de l'IEEE (TCAD) [28]; c'est également le contenu d'une demande de brevet [29]. Ici, nous présentons une version légèrement modifiée du papier de TCAD.*



## Chapter 2

# An Improved Long Distance Treatment for Mutual Inductance

Extraction of electromagnetic parameters has two components: self and mutual terms. The former correspond to effects of sources upon the same component on which they are located; the latter describe effects of sources on other circuit components. Self terms must always deal with zero and short distances; the difficulty in computing them is generally associated with this observation. On the other hand, mutual terms are comparatively simpler to estimate. The complexity of their calculation lies in the large number of terms, which is quadratic with the number of wires.

The first problem we will tackle is precisely that of developing a fast yet accurate method for computing mutual inductance. A fundamental decision must be taken from the starting point: what are the components mentioned in the first phrase above? Answering this question leads to the discussion between partial and loop inductance methods.

Partial inductance, or PEEC (Partial Element Equivalent Circuit), is a term that was introduced in the world of printed circuit boards in the early 70's [20], after being widely used in applications to power line transmission from the beginning of the 20th century [42]. The main feature of this method is that it decomposes the wires in the circuit into straight segments. In other words: "inductance" is computed for pieces of wires, instead of wire loops.

It is well understood that inductance is a magnitude whose definition is valid only for closed current loops; hence the quotation marks indicating this abuse of nomenclature in partial treatments. As a matter of fact, the main result in [20] is the equivalence between PEEC and the physically correct description of currents in terms of loops. The reason PEEC was introduced in the first place is that it simplifies one part of the task on computing inductance, namely the identification of the return paths for any given wire segment.

Loop inductance methods, on the other hand, do not enjoy this benefit. The most critical step

in a loop inductance scheme is precisely that of determining which are the loops. Nevertheless, this task is tractable, and has been already implemented in various applications [22, 24, 43]. By contrast, the drawbacks of the PEEC approach are of a fundamental nature. We summarize them in Table 2.1; a thorough explanation of all these points is contained in Section 2.1.

Table 2.1: Summary of comparative advantages and disadvantages of Loop inductance methods with respect to Partial inductance ones.

	Partial inductance	Loop inductance
Advantages	Straightforward implementation;	Correct physical description; Sparsifiable matrix; Reduced circuit size;
Disadvantages	Unphysical behavior; Dense matrix; Workload pushed downstream;	Predetermination of return paths;

Once the adoption of a loop treatment has been decided upon, extraction consists in computing first the self inductance for the circuit loops, and then the mutual inductance between all pairs of elements. A general strategy has been exposed in [23], implemented inside Mentor's Calibre tools [22] and and filed for a patent application [41].

Although the use of the loop formalism introduces important savings while preserving a correct physical description, the loop inductance matrix still requires a large (quadratic) number of mutual inductance couplings. Therefore, it is desirable to have a technique that can speed up the computation of a large number of these terms.

Our contribution in this domain is the derivation of the dipole approximation, whereby we keep only the most important contributions when computing mutual inductances at large distances.

Ranges of validity of the dipole approximation are determined by the length scales of the problem. We show that, for distances that are a factor 6 or greater than the internal separation of loops, the errors of the dipole approximation are low. Thus a mixed strategy is feasible, in which the dipole approximation for far-field interactions, while retaining the (already implemented, more expensive) exact expressions for near-field interaction.

Computational gains are an order of magnitude improvement as compared to standard techniques. Apart from these gains, for parasitic extraction, the dipole approximation allows to visualize certain rules regarding the magnitude of inductance. These rules dictate when it is safe to neglect altogether some types of interactions, thus resulting in memory, as well as performance, savings.

The work discussed in this chapter was presented at ISPD'04 [27], and extended into a journal version for the IEEE Transactions on Computer Aided Design (TCAD) [28]; it is also the content of a patent application [29]. Here, we present a slightly modified version of the TCAD paper, organized as follows:

- Section 2.1 is dedicated to the detailed analysis of the entries in Table 2.1 concerning the relative advantages of loop treatments over partial ones.
- In Section 2.2, we show how to overcome the main difficulty in loop treatments, namely the determination of return paths; an important by-product is Esq.(2.12), defining coefficients to be used downstream.
- These coefficients are used in developing the Dipole Approximation, for quick evaluation of mutual inductance at long distance, in Section 2.3.
- Results and comparisons, as well as the aforementioned rules are found in Section 2.4; here, we also include an analysis of the performance of our approximations.
- Finally, in Section 2.5 we conclude with a discussion on the opportunities and possible future developments in this area.

## 2.1 Partial vs Loop Inductance treatments

To estimate the electromagnetic effects on a multi-conductor system of currents  $I_i$  running along loops  $C_i$  we consider the energy associated with a set of currents

$$\begin{aligned} W &= \frac{1}{2} \sum_i \sum_j W_{ij} \\ W_{ij} &= I_i I_j M_{ij} \end{aligned} \quad (2.1)$$

where  $M_{ij}$  is the  $i, j$  element of the inductance matrix. It can be computed from first principles, in the Magneto-Quasi-Static (MQS) domain using:

$$\begin{aligned} M_{ij} &= \frac{\Psi_{i \rightarrow j}}{I_i} \\ &= \frac{1}{I_i} \int_{S_j} \mathbf{B}^{(i)} \cdot d\mathbf{S}_j \\ &= \frac{\mu_0}{4\pi} \left\langle \oint_{C_i} \oint_{C_j} \frac{d\boldsymbol{\ell}_i \cdot d\boldsymbol{\ell}_j}{|\mathbf{r}_i - \mathbf{r}_j|} \right\rangle_{\text{Conductors' cross-sections}} \end{aligned} \quad (2.2)$$

where  $\Psi_{i \rightarrow j}$  is the magnetic flux due to the magnetic induction field  $\mathbf{B}^{(i)}$ ,  $S_j$  is the surface bounded by  $C_i$ , generated by the time varying current  $I_i$  acting on  $I_j$ . In (2.2) we are invoking the MQS regime, whereby the currents  $I_i$  are uniform over the transverse cross-sections permitting us to equalize the last two expressions. The sum in (2.1) contains as diagonal elements  $\mathcal{L}_i = M_{ii}$  the self inductance of loop  $i$ .

The integrals are evaluated over closed loops, in physical systems, and we then speak about loop inductance. The previous equations can be extended to segments [42], giving rise to the PEEC formalism, and we then speak about partial inductance. On this last formalism, conductor segments are considered to form part of loops closing at infinity.

### 2.1.1 Long distance behavior

The long distance behavior of the partial inductance matrix  $M$  elements is non-physical. In fact, for large wire separation  $r$ , its per unit length matrix elements  $m_{i,j}$  behave as

$$m_{ij}(r) \equiv \frac{M_{ij}(r)}{L} \sim -\log(r) \quad (2.3)$$

where  $L$  is their common length.

The logarithmic decrease with distance manifests itself in two dimensional  $2D$  as well as in three dimensional  $3D$  problems. The only difference between the two cases is the appearance of a constant coefficient  $\log(2L)$  in  $3D$ , which is absent in  $2D$ . Using Grover's expressions, the ratio of  $M_{ij}$  for a filament  $i$  and its neighbor  $j$  to the corresponding diagonal term  $\mathcal{L}_i$  has the following limit at large distances (large  $r$ , while  $r < L$ ):

$$\frac{M}{\mathcal{L}} \sim 1 - \frac{\log(r/w)}{\log(2L)} \rightarrow 1 \quad (2.4)$$

with  $w$ , the wire cross-section.

As a result of (2.3) and (2.4)  $M$  is dense, and not diagonally dominant. A strictly diagonally dominant real matrix is one in which the sum of the absolute value of off-diagonal elements for each row is strictly smaller than the absolute value of the diagonal counterparts. For a symmetric matrix with diagonal elements strictly positive, diagonal dominance is a sufficient condition for having real and strictly positive eigenvalues. Moreover, neglecting small off-diagonal terms in a matrix of this type does not change the sign of its eigenvalues. Matrices of this kind can be sparsified by neglecting small off-diagonal terms, without resulting in possible passivity violation. Positive definite matrices that do not satisfy the requirement of being strictly diagonally dominant, on the other hand, can display unwanted instabilities of the following kind: setting to zero seemingly negligible off-diagonal contributions can alter the sign of the eigenvalues of  $M$ , a violation of passivity for linear systems [44,45]. The system designer can be left with unwanted choices when working with  $M$  particularly in the PEEC method: either

sparsify and live with passivity violations or live with very large matrices and rapidly increase the complexity of downstream circuit simulation.

To investigate the primary source of the denseness, the following statement is useful:

**Proposition 1** *The asymptotic behavior (2.3) results from the following large distance behavior of  $\mathbf{B}$  :*

$$\begin{aligned} B(r) &\sim 1/r^2 && \text{In three dimensions} \\ B(r) &\sim 1/r && \text{In two dimensions} \end{aligned} \quad (2.5)$$

The above proposition is verified by directly substituting (2.5) into (2.2), counting powers in the integrand to estimate the asymptotic behavior, and (2.3) results.

Proposition 1 is derived from :

**Proposition 2** *The asymptotic behavior (2.5) results from the presence of unbounded current distributions.*

Consider first the 2D case of an infinitely long filament; applying Ampere's law

$$\oint \mathbf{B} \cdot d\mathbf{l} = \mu_0 I \quad (2.6)$$

and extracting  $B$

$$\begin{aligned} B(r) &= \frac{\mu_0 I}{2\pi r} \\ m(r) &= \frac{1}{I} \int B dr = \frac{\mu_0}{2\pi} \log\left(\frac{r}{w}\right) \end{aligned} \quad (2.7)$$

which gives precisely (2.3).

In 3D, consider the vector potential  $\mathbf{A}$

$$\mathbf{A}(\mathbf{r}) = \frac{\mu_0}{4\pi} \int_V \frac{\mathbf{J}(\mathbf{r}')}{|\mathbf{r} - \mathbf{r}'|} d^3 r' \quad (2.8)$$

and carry out, as in [46], a multi-pole expansion of Green's function  $1/|\mathbf{r} - \mathbf{r}'| = 1/|\mathbf{r}| + \mathbf{r} \cdot \mathbf{r}'/|\mathbf{r}|^3 + \dots$ , giving :

$$A_i(\mathbf{r}) = \frac{\mu_0}{4\pi} \left( \frac{1}{|\mathbf{r}|} \int_V J_i(\mathbf{r}') d^3 r' + \frac{\mathbf{r}}{|\mathbf{r}|^3} \cdot \int_V \mathbf{r}' J_i(\mathbf{r}') d^3 r' + \dots \right) \quad (2.9)$$

For  $B(r) \approx 1/r^2$  as demanded by (2.3), the first term in (2.9) must be different from zero. It is on the other hand well known that for any bounded current distribution in the quasi-static regime  $\partial\rho/\partial t = 0$ , with  $\rho$  the charge density, the integral in the first term of (2.9) vanishes (the volume  $V$  of integration includes the entire current distribution). Thus, under quasi-static conditions and for bounded current distributions,  $\mathbf{A}$  must decrease for large distances at least as rapidly as  $1/r^2$ . Using  $\mathbf{B} = \nabla \times \mathbf{A}$  we conclude that for bounded physical systems:

$$\mathbf{B} \sim 1/r^3, \quad (2.10)$$

Equations (2.3) and (2.5) are invalid and  $m$  decays with distance as a power law. The PEEC method violates the asymptotic behavior of Maxwell's equations in the quasistatic regime. Dropping the assumption of bounded current distributions is tantamount to the presence of monopoles in the theory, whereas dropping the quasi static assumption requires a completely new approach. The correct physical behavior of electromagnetic theory, when used in conjunction with PEEC is recovered downstream during the circuit simulation phase of the flow. During this phase circuits are necessarily closed by virtue of the Kirchoff Voltage Laws (KVL). Large cancellations involving different length scales occur, mixing short distance with long distance, an inherent result of the method. The correct theory is recovered, but the price is the size of the mutual inductance matrix needed for timing simulation. Issues related to capacity and numerical accuracy are unavoidable.

The previous are rigorous results in Electromagnetism. A loop treatment of MQS must necessarily give rise to a significantly more localized magnetic influence than what would be resulting from the PEEC approach.

### 2.1.2 Sparsification of the partial inductance matrix

There has been widespread work to improve on the PEEC formalism ([21,47–49] and references therein). The underlying goal is to sparsify the dense  $M$  matrix while preserving its positive definiteness.

One line of approach consists of including artificial currents that compensate the current of any wire segment. The goal is to cancel the monopole behavior of partial inductance for the given segment, at distances beyond the location of the compensating “current shells” [21,50].

The models generated with these techniques are shown to give accurate simulation parameters as long as the shells contain all the return paths for the original wire. This observation simply states that, if the wire loops are known to be included within the shells, then placing the compensating current, thus isolating the wire and its returns from the rest of the configuration, gives a correct value for the loop inductance. In this sense, these approaches require that all the return paths be included within these shells, a task that can be comparable to the iden-

tification of the return paths in the loop formalism. This argument would eliminate the major advantage when compared to using directly loop inductance methods.

A second strategy for sparsification of the PEEC matrix springs from the observation that the behavior (2.5) of magnetic fields within a partial inductance treatment (magnetic field produced by a magnetic monopole) is formally equivalent to that of the electrical field produced by a point charge in electrostatics. This similarity has inspired some researchers to explore the notion of double-inverse methods [51, 52]. In few words, these consist of first inverting locally the  $M$  matrix, and then sparsifying the  $K \equiv M^{-1}$  matrix. The analogy clearly extends to  $C$  and  $K$  which play similar roles in the electrostatic and magneto-static problems, respectively ( $Q = C\Delta V, j\omega I = K\Delta V$ ). This procedure introduces a new circuit element,  $K$ , whose behavior is included within simulators [51, 53].

However, there is an important difference between the two cases: for the electrostatic case, the  $C$  matrix, in the Maxwell sense, is strictly diagonal dominant by construction, and thus any truncation preserves positive definiteness; on the other hand the jury is still out regarding the diagonal dominance of  $K$  [48]. In [54], the  $K$  matrix is shown to be sparse, positive definite and symmetric, within a circuit-aware inverse extraction method that separates wires having strong inductive effects from those do not.

At variance with  $C$ , the matrix  $K$  is not physical, and it is not obvious how to extend the concept of shielding, present in the electrostatic case. Shielding of electrical fields by conductors cause the  $\mathbf{E}$  field to be localized in a dense wire environment, making the  $C$  matrix sparse. For MQS there is no physically equivalent shielding, currents and the  $\mathbf{B}$  field may penetrate the conductors. Nonetheless, it is empirically verified that  $K$  is sparse, yielding a considerable amount of strength to partial inductance followed by inverse methods [47, 55].

Another observation about the double-inverse method is that it contains an adjustable parameter, namely the size of the window for the first local inversion. The accuracy of the method depends on this parameter: as with the compensating shells, the method is accurate as long as the main contributors to the return path are contained within the window. Again, this means identification of these return paths, thus eliminating the main advantage of partial methods with respect to loop ones.

Loop inductance methods, on the other hand, have inherent localization properties deriving from (2.10), as we shall derive from (2.28), while preserving the correct physical theory.

### 2.1.3 On positive definiteness of the loop inductance matrix

In the previous section, we have discussed the denseness of partial inductance methods, and the related efforts in trying to deal with it. We claim that this is not necessary in loop inductance methods, relying on the hypothesis that the loop inductance matrix is definite positive, and therefore there is no risk of passivity violation when it is truncated.

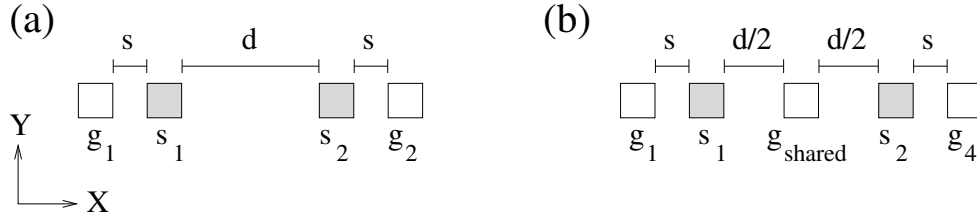


Figure 2.1: Representative worst case scenarios for diagonal-dominance of the loop inductance matrix: (a):no shared grounds; (b): with shared grounds.

The following arguments do not constitute a proof, but clearly support the above hypothesis that the loop inductance matrix  $M$  is diagonal dominant, for configurations where there are no shared return paths. Let us start by treating a seemingly worst case scenario, configurations with values of the diagonal elements that are as small as possible while the corresponding values of the off-diagonal elements are as large as possible. We take as representative example of this hypothetical worst case scenario, the configuration of Fig.2.1a.

We take the return of signal  $s_1$  to be  $g_1$ , while for signal  $s_2$ , it is  $g_2$ . To minimize loop self inductance of one signal wire, the corresponding ground return paths need to be as close as possible to the signal wire. Furthermore, to maximize mutual loop inductance between two signals is necessary to minimize the distance between the two circuits. We take values from typical 90 nm technology<sup>1</sup>. The minimum value of inter-wire separation is  $s_{min} = 0.2 \mu\text{m}$ , for representative wires of low resistance the wire width is about  $w = 1 \mu\text{m}$ . Having  $d = s = s_{min}$  and equal wire widths  $w$  in Fig. 2.1a results in the following inductance per unit length matrix:

$$M = \begin{pmatrix} 2.96 & 0.07 \\ 0.07 & 2.96 \end{pmatrix} \text{ nH/cm.}$$

The ratio  $\delta$  of self to mutual inductance is  $\delta = 42$ . The above matrix is diagonal dominant. To violate the condition of diagonal dominance, we need at least  $\delta$  worst case circuits separated by  $s_{min}$ , an unfeasible configuration. Consider now a small increase in the separation between the two initial circuits by  $1 \mu\text{m}$ . Then  $\delta$  increases to 132. This fast increase reflects the power law nature of the loop inductance variation with distance, a result we shall derive in (2.28).

For feasible wire densities, the self inductance will be larger than the sum of the magnitudes of the mutual inductances with the other circuits, i.e. the matrix  $M$  will be strictly diagonal dominant.

When different signal wires share return grounds, the above argument does not hold. Take for instance a configuration where 4 signal wires share one ground wire as return path (Fig.2.1b).

<sup>1</sup>The scaling properties of the examples in the present chapter are discussed at the beginning of Sec.2.4).

Using the same  $s_{min}$  and  $w$  as in the previous example results in a  $4 \times 4$  matrix

$$M = \begin{pmatrix} 7.8 & 3.9 & 1.6 & 2.5 \\ 3.9 & 4.9 & 1. & 1.6 \\ 1.6 & 1. & 4.9 & 3.9 \\ 2.5 & 1.6 & 3.9 & 7.8 \end{pmatrix} \text{ nH/cm.}$$

This matrix  $M$ , calculated from Grover's expressions, is positive definite but not diagonally dominant. We thus conclude that, in the absence of shared ground return paths, the inductance matrix will be diagonal dominant in the loop formalism. This is not the case in the partial inductance formalism, as can be immediately concluded from (2.4).

Our concern is the treatment of the long distance behavior of the inductance matrix, that is to say the contributions to the inductance matrix arising from signal wire segments which are separated by long distances. These wire configurations do not lead to shared ground configurations. Since the matrix is diagonal dominant, then truncation cannot lead to loss of passivity.

The general solution to the mutual inductance problem, one that incorporates short and long distance behavior, demands attention to this problem, since the presence of shared ground configurations is unavoidable albeit restricted in scope. We refer to [23] (Chapter 3) for a treatment of the general case. Therein, it is shown that the mutual inductance in the presence of shared grounds involves a term that is proportional to the partial self inductance of the shared wires. These are terms much larger than mutual ones, explaining the the lack of diagonal dominance in the matrix above.

#### 2.1.4 Size of loop and partial inductance matrices

In order to compare the sizes associated to loop and partial inductance treatments, we consider a representative IC example shown<sup>2</sup> in Fig. 2.2a. It consists of two signal lines surrounded by 4 ground lines. We construct two different netlists: the first one, extracting the  $L$  matrix with our loop inductance engine [22], and the second one with PEEC, using FastHenry [15]. Capacitance is extracted with FastCap [14]. For both cases, the presence of devices is represented by a resistor of  $R_{tr} = 50\Omega$  at nodes S1 and S2, and a capacitor to ground  $C_{load} = 1fF$  at S1\_out and S2\_out. The sizes of these netlists are as follows:

In this table, we have also included, on the last column, the runtime for the simulation of each netlist with Eldo [53], Mentor's circuit simulator. The simulations represent a step 1 Volt excitation on S1 at time  $t = 0$ , while leaving line S2 grounded at both extremes. The comparative results of the two simulations, for the far-end voltages, are shown in Fig. 2.2b.

Without any appreciable difference in the output, the gain is a factor of 5 in computation

<sup>2</sup>We acknowledge our colleague Rafael Escovar for this example, included in his Phd. Thesis [23].

	resistors	inductors	capacitors	impedance couplings	Total	Average run time (s)
PEEC	70	70	118	2415	2673	10.2
Loop	26	26	34	128	214	1.9

Table 2.2: Number of RLC elements in the PEEC and loop netlists.

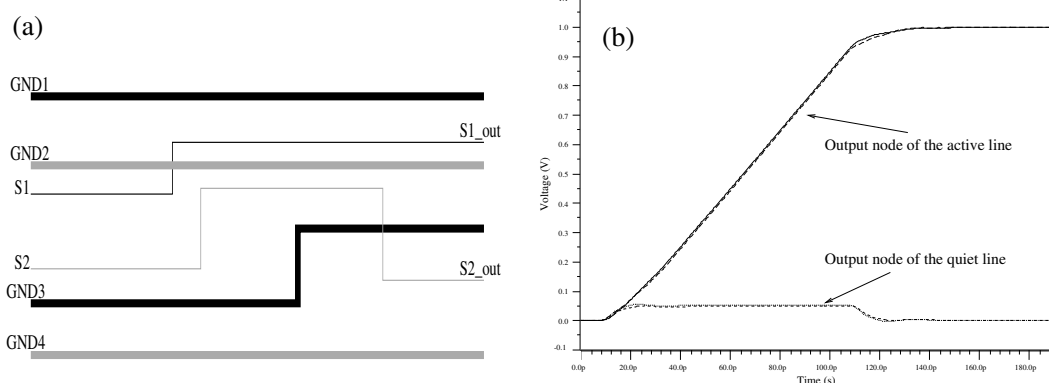


Figure 2.2: (a): Example of an IC configuration for comparison of loop and partial methods: the width of the signals S1 and S2 is  $1\mu$ , and width of grounds GND1-4 is  $5\mu$ ; wires in black are in a layer of thickness  $1\mu$ , and gray are  $0.75\mu$ , total length is  $1\text{ mm}$ . (b): Comparative results of simulation for the far-end voltages for configuration in (a).

time, and more than 10-fold in terms of space. The difference between the two factors is due to the fact that the cost of simulation is governed by both the number of nodes as well as the number of elements. While the PEEC netlist has more than 10 times the number of elements of the loop one, the nodes (70 vs. 26) are multiplied only by a factor lower than 3.

## 2.2 Return path in the loop inductance formulation

Partial inductance methods do not require *a priori* identification of which are return paths for the currents along any given signal wires. The contrary happens in the loop inductance formulation. We proceed to argue that large uncertainties related to the problem of return path selection do exist, but are limited to low frequencies, where in fact inductance effects are unimportant.

For this purpose, we introduce the concept of *bundle* [28], as the set of parallel wires of equal length consisting of one signal plus all its possible return paths. We consider a bundle as a set of closed loops with one common segment (namely the signal wire), neglecting the absence of the small segments in the orthogonal direction needed to close the loops.

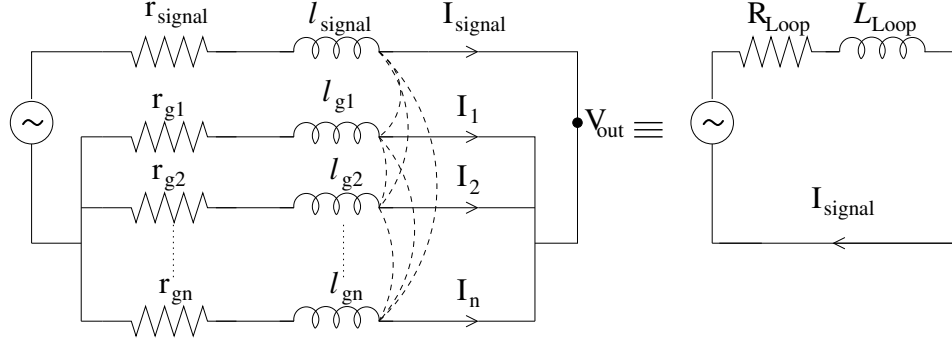


Figure 2.3: Circuit equivalence of a bundle with  $n$  return paths (for simplicity, mutual inductances between wires are depicted as dashed lines without label).

Extraction in terms of bundles is composed of the following tasks:

1. for each signal wire, we decompose its path into the union of a set of non-overlapping segments whose ends are identified by discontinuities (changes of layer or direction) either in the signal path or in the path of any of its return wire candidate neighbors;
2. for each segment, there is a set of  $n$  nearest parallel ground wire segments of the same length, that form part of the bundle;
3. a bundle's loop self impedance  $Z_{loop} = V_{in}/I_{signal}$  is computed by solving the elementary circuit in Fig.2.3, formed by the signal segment and its  $n$  return paths,

$$\Delta V = ZI \quad (2.11)$$

where

$$\Delta V = \begin{pmatrix} 1 - V_{out} \\ -V_{out} \\ \vdots \\ -V_{out} \end{pmatrix}, \quad I = \begin{pmatrix} I_{signal} \\ I_1 \\ \vdots \\ I_n \end{pmatrix}, \quad \text{such that } \sum_{i=0}^n I_i = 0$$

and  $Z$  is the  $(n+1) \times (n+1)$  matrix  $R + j\omega L$  of the elements shown at the left of Fig.2.3;

4. as a by-product of this calculation, the currents  $I_i$  give the (complex) weight of each return path within each bundle: normalized by the current  $I_{signal}$ , their sum is unity, and we define the values  $\alpha_i$ ,

$$\alpha_i \equiv \frac{I_i}{I_{signal}} \quad (2.12)$$

which will play an important role in the future sections;

5. a complete description in terms of bundles is the result of joining all the individual bundles into a single circuit representation.

Our group at Mentor has implemented this computation of self impedance in terms of bundles, empirically adjusting the parameter  $n$  to the value 9. See [23] for a thorough analysis of extraction in terms of bundles. In the following paragraphs, we will summarize the main physical characteristics related to the selection of return paths.

For this description to be accurate, we must always include the wires that the return paths are the ones that minimize the self impedance of the bundles,

$$Z_{loop}(\omega) = R_{loop} + j\omega\mathcal{L}_{loop} \quad (2.13)$$

At low  $\omega$ , this corresponds to resistance  $R$  minimization, while for large  $\omega$  it is inductance  $\mathcal{L}$  minimization. We can classify four distinct frequency regimes, according to the comparative contributions of resistance-per-unit-length  $r$  and inductance-per-unit-length  $l$ , see Table 2.3. The boundaries between regimes is determined by technology. In an order-of-magnitude estimation,  $r$  is dictated by the typical cross-section area  $wh$  as well as the material properties:  $r \sim (\sigma wh)^{-1}$ ; whereas inductance-per-unit-length is typically  $l \sim \mu_0$ . Therefore, these conditions can be stated in terms of the parameter  $\delta = \sqrt{2/\omega\mu_0\sigma}$ .

Table 2.3: Classification of frequency regimes and related physical phenomena

Regime	$r, l$ condition	Technology condition	Physical characteristics
1. Low frequencies	$r \gg \omega l$	$wh \ll \delta^2$	Many, wide return paths
2. Intermediate frequencies	$r > \omega l$	$wh < \delta^2$	$R$ - $L$ trade-off
3. High frequencies	$r \leq \omega l$	$wh \simeq \delta^2$	Only 2 or 3 nearest wires
4. Very high frequencies	$r \ll \omega l$	$wh > \delta^2$	Skin-effect current crowding

A large number of return paths are only needed in Regime 1, in which non-negligible currents may be present on far away, low resistive return paths. By keeping only the  $n$  closest wires, there is the risk of committing significant errors in the loop inductance of the bundle.<sup>3</sup> However, we point out that in this regime, the inductive part of impedance is negligible with respect to the resistive one (see Table 2.3), rendering these errors unimportant.

<sup>3</sup>On the other hand, resistance in this regime corresponds to that of the signal segment, since the contribution of all the return paths, at low frequency, is essentially their parallel equivalent resistance  $(\sum_{i \geq 1} r_{g_i}^{-1})^{-1}$ , which for  $n = 9$  is typically a very small value compared to the resistance of the signal segment  $r_{signal}$

Using the value  $n = 9$  mentioned above, we observe a monotonic decrease in inductance and increase in resistance, throughout regimes 2,3 and 4. More important, we observe no significant deviations from the values obtained with larger values of  $n$  [23]. As frequency increases, currents on far-away wires tend to zero, in order to minimize the inductive part of impedance. In fact, for frequencies in regimes 3 and 4, values of impedance are unchanged by keeping only the two or three closest return wires.

This observation plays a very important role for regime 4, where accuracy demands to account for non-uniform current distributions along the wires' cross-sections by decomposing into filaments à la FastHenry [15], or into conduction modes [32] (see Part B of this thesis). In practice, this entails a multiplicative increase in the size of the system in eq.(2.11), which is compensated by keeping only the closest wires.

From this discussion we conclude, that except for signals in region 1, where inductance does not matter, it is relatively simple to select return path configurations from a layout. The use of the physically rigorous method of loop inductance becomes for these cases reasonable and expedient.

## 2.3 Mutual inductance and the Dipole Approximation

We now develop a method to compute the *mutual inductance between bundles*  $M_{ab}$ , i.e. the off-diagonal terms in the  $Z$  matrix. The aim is to arrive at an expression analogous to (2.1), but for bundles,

$$M_{ab} = \frac{W_{ab}}{I_a I_b}$$

with currents  $I_a$  (resp.  $I_b$ ), running along the signal wires of bundle  $a(b)$ . For this purpose we begin precisely from (2.1), with subindex  $i(j)$  sweeping all wires in bundle  $a(b)$ .

Following the steps laid out in the previous section, the current  $I_b$  is divided among the return paths according to the coefficients  $\alpha$ ,

$$I_j = \alpha_{b,j} I_b \quad \text{with } \alpha_{b,0} = 1, \sum_{j \geq 1} \alpha_{b,j} = -1 \quad (2.14)$$

Consequently,  $W_{ab}$  in (2.1) can be factored as

$$W_{ab} = \frac{I_b}{2} \sum_{j \geq 1} \alpha_{b,j} \Psi_{a \rightarrow j} \quad (2.15)$$

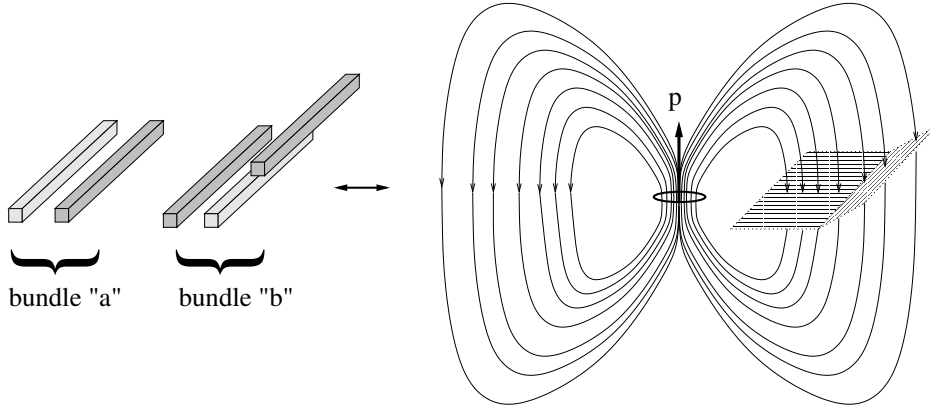


Figure 2.4: Schematic view of the dipole approximation for calculating the interaction between two bundles.

Here  $\Psi_{a \rightarrow j}$  is the magnetic flux of all wires in bundle  $a$  through the elementary surface  $S_j$  of bundle  $b$  (see Fig.2.4), which is bounded by the circuit loop  $\partial S_j$  formed by the signal wire plus the  $j$ -th return wire.

These fluxes are computed using Stokes' theorem,

$$\Psi_{a \rightarrow j} = \iint_{S_j} (\nabla \times \mathbf{A}^{(a)}) \cdot d\mathbf{S}_j = \oint_{\partial S_j} \mathbf{A}^{(a)} \cdot d\boldsymbol{\ell}_j \quad (2.16)$$

with  $\mathbf{A}^{(a)}$  the vector potential due to all wires in bundle  $a$ .

To split the closed curvilinear integral in (2.16) into two rectilinear integrals, one over the signal, the second over the return wire  $j$ , the contribution from this last one must be multiplied by -1 (since the closed integral is circulated in one definite sense). Thus, summing up all the terms, expression (2.15) becomes

$$W_{ab} = \frac{I_b}{2} \sum_{j \geq 0} \alpha'_{b,j} \int_{C_j} \mathbf{A}^{(a)} \cdot d\boldsymbol{\ell}_j \quad (2.17)$$

where  $C_j$  is the conductor  $j \geq 0$ , and  $\alpha'_{b,j} = -\alpha_{b,j} \forall j \geq 1$ .

Next we take into account the magnetic dipole approximation, whereby we consider the field due to all the circuits in bundle  $a$  as the one generated by a representative dipole moment  $\mathbf{p}_a$  [46].

To compute the value of  $\mathbf{p}_a$ , we first consider the dipole of a configuration of two parallel wires lying on the  $x - y$  plane, one being the return path of the other (Fig.2.5a). In this simple case,

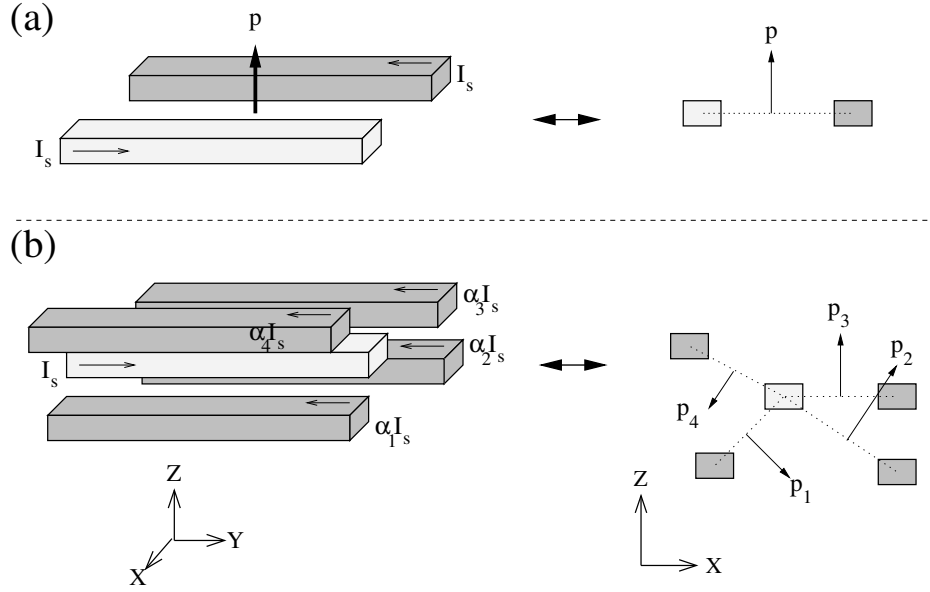


Figure 2.5: Calculation of dipole moment for a bundle: (a) simple case with one unique return path; (b) bundle with several return paths; the resulting  $\mathbf{p}$  is a weighted average of all the  $\mathbf{p}_i$ .

$$\begin{aligned}\mathbf{p}_a &= \frac{\mu_0}{8\pi} \int \mathbf{r} \times \mathbf{J}(\mathbf{r}) d^3\mathbf{r} \\ &= \frac{\mu_0}{8\pi} ILs\hat{z}\end{aligned}\quad (2.18)$$

where  $L$  is the common length of the two wires and  $s$  is the separation between them ( $p_a$  is proportional to the area spanned by the circuit and points in the direction  $\hat{z}$  perpendicular to the plane containing them.)

For bundles having multiple return paths (all oriented along the  $y$  axis, see Fig.2.5b), the integral in the first line of (2.18) is decomposed into several terms like the one in the second line. Since each of those terms is proportional to the current it carries, they are weighed again by geometrical coefficients  $\alpha_{a,i}$ ,  $i \in a$  as in (2.15).

Therefore the expression for the magnetic dipole moment becomes,

$$\mathbf{p}_a = \frac{\mu_0}{8\pi} LI_a \sum_{i \geq 0} \alpha_{a,i} (\hat{y} \times \mathbf{r}_i) \quad (2.19)$$

where  $\mathbf{r}_i$  is the position of return path  $i$  with respect to the signal wire.

Since the total current in a bundle adds up to zero, the value obtained by (2.19) is independent of where the origin of coordinates is located. We choose this origin as the position of the

“center of mass” of bundle  $a$ ,

$$\mathbf{r}_{\text{cm},a} = \frac{1}{2} \sum_{i \geq 1} \alpha_{a,i} \mathbf{r}_i \quad (2.20)$$

i.e., as the weighted average of the position of all the constituent moments of the form (2.18).

The expression for the vector potential  $\mathbf{A}$  at position  $\mathbf{r}$  due to a dipole  $\mathbf{p}_a$  at the origin is

$$\mathbf{A}^{(a)} = \frac{\mathbf{p}_a \times \mathbf{r}}{r^3} \quad (2.21)$$

The  $1/r^2$  behavior of  $\mathbf{A}$  corresponds to the  $1/r^3$  behavior for  $\mathbf{B}$  as demanded by (2.10).

Replacing expression (2.21) into (2.17), we arrive at a closed expression of the mutual inductance between bundles  $M_{ab}$ , within the dipole approximation,

$$M_{ab} = \frac{1}{I_a} \sum_{j \geq 0} \alpha'_{b,j} \int_{C_j} \frac{(\mathbf{p}_a \times \mathbf{r}_j)}{r_j^3} \cdot d\boldsymbol{\ell}_j \quad (2.22)$$

In general, the resulting  $M$  is complex, with the real part of (2.22) contributing to the mutual inductance. The imaginary part of  $M$  modifies the resistance, is effectively negligible in all the numerical examples we encountered.

Inspection of (2.19) and (2.22) shows that  $\mathbf{p}_a$  is proportional to  $I_a$ ; hence,  $M_{ab}$  does not depend on the currents, but is solely a geometric coefficient, as should be expected. For the sake of notation, from here on, we use  $\tilde{\mathbf{p}}_a$  to stand for  $\mathbf{p}_a/I_a$ .

As mentioned before, all conductors in a bundle run along the same direction, say  $\hat{y}$ . Thus  $\mathbf{p}_a$  is perpendicular to all the wires. We have the freedom to choose the  $\hat{z}$  axis parallel to the dipole moment  $\mathbf{p}_a$ , and (2.22) becomes

$$M_{ab} = \tilde{p}_a \sum_{j \geq 0} \alpha'_{b,j} x_j \int_{y_{0,j}}^{y_{1,j}} \frac{dy}{(x_j^2 + y_j^2 + z_j^2)^{3/2}} \quad (2.23)$$

where  $y_{0,j}$  and  $y_{1,j}$  are the extremes of conductor  $j$ , in a coordinate system with origin at  $\mathbf{r}_{\text{cm},a}$ . Expression (2.23) is effortlessly integrated,

$$M_{ab} = \tilde{p}_a \sum_{j \geq 0} \frac{\alpha'_{b,j} x_j y_j}{(x_j^2 + z_j^2)(x_j^2 + y_j^2 + z_j^2)^{1/2}} \Bigg|_{y_j=y_{0,j}}^{y_j=y_{1,j}} \quad (2.24)$$

Thus mutual inductance between two bundles is reduced to calculating the dipole moment and the position of the first bundle via (2.19) and (2.20), and then evaluating the simple expression (2.24) for each of the wires of the second bundle.

An important remark concerning (2.24) is that it does not strictly comply with the expected symmetry  $M_{ab} = M_{ba}$ . This is due to the fact that our treatment considers the aggressor as an

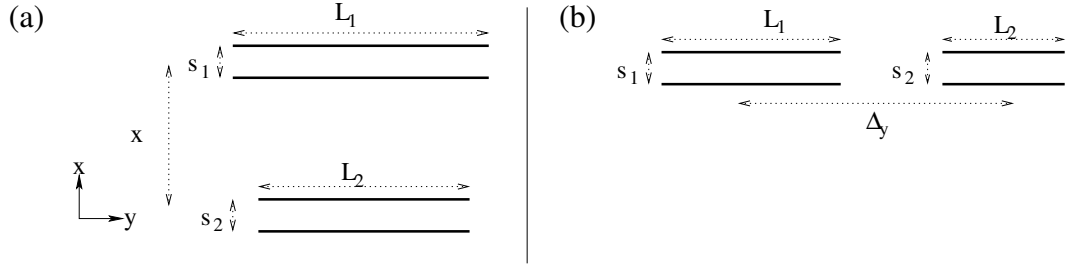


Figure 2.6: Simple configuration for the sake of comparison of (2.24) with Grover's expressions: (a) transverse coupling; (b) forward coupling.

ideal point-like dipole, whereas this is not assumed for the victim. In the next section we will show with numerical examples that in practice this asymmetry is seldom significant. In practice we enforce the expected physical symmetry by identifying  $M$  with

$$\tilde{M}_{ab} = \frac{M_{ab} + M_{ba}}{2} \quad (2.25)$$

Similarly, we can construct the expression for the interaction between wires lying along the  $x$ -axis.

In order to compare with classical Grover expressions, (2.24) would replace the one arising from the algebraic sum of filament-to-filament interactions [56],

$$M_{ab}^{grover} = \frac{\mu_0 L}{4\pi} \sum_{i \geq 0} \sum_{j \geq 0} \alpha_{a,i} \alpha_{b,j} M_{ij} \quad (2.26)$$

$$\text{where } M_{ij} = \log \left( \frac{L}{r_{ij}} + \sqrt{1 + \frac{L^2}{r_{ij}^2}} \right) + \frac{r_{ij}}{L} - \sqrt{1 + \frac{r_{ij}^2}{L^2}}$$

For example, in a very simple configuration like the one shown in Fig. 2.6a it is straightforward to see that both expressions (2.24) and (2.26), for  $x, L \gg s_1, s_2$ , give exactly the same limit, namely

$$M_{ab} \simeq \frac{\mu_0}{4\pi} s_1 s_2 L_1 L_2 \frac{2x^2 + L_2^2/4}{x^2(x^2 + L_2^2)^{3/2}} \quad (2.27)$$

As anticipated in section 2.1, once all terms are accounted for, in the loop inductance treatment, the asymptotic behavior of  $M$  is quite unlike that of (2.3). In fact, (2.27) shows two types of regimes for transverse coupling (we take  $s_1 = s_2 \equiv s$  and  $L_1 = L_2 \equiv L$  for simplicity),

$$M_{ab} \simeq \begin{cases} \frac{\mu_0}{2\pi} \frac{s^2 L^2}{x^3} \sim \frac{1}{r^3} & \text{for } x \gg L \text{ (3d case)} \\ \frac{\mu_0}{16\pi} \frac{s^2 L}{x^2} \sim \frac{1}{r^2} & \text{for } x \ll L \text{ (2d case)} \end{cases} \quad (2.28)$$

In a case of forward coupling, like the one shown in Fig.2.6b, the comparison with the Grover expressions, now in the limit  $L_1, L_2, \Delta_y \gg s_1 = s_2 \equiv s$ , gives <sup>4</sup>

$$\begin{aligned} M_{ab}^{\text{dipoles}} &\simeq \frac{\mu_0}{\pi} \frac{s^2 L^2 (\Delta_y + L)}{2(\Delta_y + L/2)^2 (\Delta_y + 3L/2)^2} \\ M_{ab}^{\text{grover}} &\simeq \frac{\mu_0}{\pi} \frac{s^2 L^2}{2\Delta_y (\Delta_y + 2L) (\Delta_y + L)} \end{aligned} \quad (2.29)$$

where we have simplified the expressions by setting  $s_1 = s_2 \equiv s$  and  $L_1 = L_2 \equiv L$ . Both expressions above have the same long distance asymptotic behavior,

$$\begin{aligned} M_{ab}^{\text{dipoles}} &\simeq \frac{\mu_0 s^2 L^2}{2\pi \Delta_y^3} \left( 1 - 3\epsilon - \frac{14}{2} \epsilon^2 \right) \\ M_{ab}^{\text{grover}} &\simeq \frac{\mu_0 s^2 L^2}{2\pi \Delta_y^3} \left( 1 - 3\epsilon - \frac{13}{2} \epsilon^2 \right) \end{aligned} \quad (2.30)$$

for  $\epsilon \equiv L/\Delta_y$ .

Although both expressions show essentially the same behavior, they have been obtained through significantly different processes:  $M_{ab}^{\text{dipoles}}$  are two direct evaluations of (2.24), whereas  $M_{ab}^{\text{grover}}$  result from a subtle cancellation of eight expressions like (2.26) [56].

## 2.4 Results

In this section, we display some numerical results that verify the validity of the dipole approximation, its applicability, and its limitations.

In the first subsection, we analyze some simple extraction rules that can be established by virtue of the dipole approximation. These rules allow for quick and very practical determination of which geometrical configurations can be automatically neglected when computing mutual inductance.

Next, we consider the question of the numerical accuracy of the dipole method. We do this by comparison of (2.24) with the results obtained with the field solver FastHenry [15].

<sup>4</sup>In the expressions that follow, we correct an errata which is present in [28].

It is self evident that calculating the mutual inductance using the dipole approximation is considerably less expensive than FastHenry. The simulations with FastHenry were carried out at the single frequency of 10 GHz. To assure good convergence with FastHenry, we empirically found that 5×5 filament partitioning suffices. In most cases, 3×3 was accurate enough.

The dipole approximation is often computationally more efficient than the direct use of Grover's expressions (2.26). An analysis of the performance is included at the end of the present section.

A good criterion to be used in considering the errors introduced in a mutual inductance extraction method is the comparison to the self inductances of the two bundles,  $L_a, L_b$ . To this effect, we choose to plot the dimensionless magnitude  $\zeta \equiv M_{ab} / \sqrt{L_a L_b}$ , whose absolute value is smaller than 1.

Observe that  $\zeta$  is scale invariant, in the following sense: if all dimensions in a given configuration are multiplied by a factor  $\lambda$ , then  $\zeta$  remains unchanged, except for minor logarithmic corrections to the self inductances<sup>5</sup>. This statement allows us to generalize the results in this section to scaled-down configurations.

### 2.4.1 Dipole selection rules

There is a number of situation-dependent rules that are exact in the dipole approximation and constitute reasonable approximations in general. They are of importance in the action of pruning geometrical configurations.

1. For perfectly symmetric bundles, the mutual inductance is negligible. An example of this kind of configuration is given by a sandwich configuration. (i.e., a perfectly symmetric coplanar ground-signal-ground bundle, see Fig.2.7). It has zero dipole moment, meaning that in the dipole approximation its signal voltage is insensitive to external noise. Verification of this rule with FastHenry, calculating the mutual inductance between two such structures, gives values of  $\zeta$  below  $10^{-5}$  for distances between bundles as small as the internal separations of the bundles. Sandwich configurations are good candidates for clock routing. This result impacts favorably on the stability of clock routing using symmetrical ground signal ground configurations [57].
2. Given two bundles with parallel dipole moments (e.g. Fig.2.8), the mutual inductance between them is minimized when their relative position forms a certain angle with the common direction of their dipole moments; the value of this angle goes from  $45^\circ$  when the bundles are much longer than the transverse dimensions, to  $\sim 35^\circ$  when this is not the

---

<sup>5</sup>In mathematical terms,  $\zeta$  is homogeneous of degree 0, while  $M_{ab}$  is homogeneous of degree 1, and  $L_a$  and  $L_b$  are "nearly" homogeneous of degree 1.

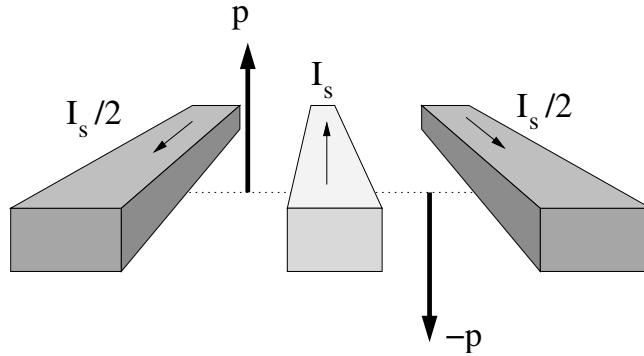


Figure 2.7: Dipole Selection Rule 1: Completely symmetric configuration, in which the return currents are balanced with respect to the signal line, having a zero net dipole moment.

case. This result derives from the following reason: since the two bundles have aligned dipole moments, then the flux of magnetic field through the second bundle due to the first one is, in first approximation, proportional to the perpendicular field of the first one (it is helpful to imagine a bundle as a coil perpendicular to its dipole moment). Thus we should analyze where the perpendicular component for the field of a dipole vanishes. For the case of long bundles, in which a 2D description is adequate, the dipole moment vanishes<sup>6</sup> at  $45^\circ$ . In the case of short bundles, this rule comes from the expression for the perpendicular component  $B_\perp$  for the field of a dipole (2.31), which is null for  $\theta = 0.5 \cos^{-1}(1/3) \approx 35^\circ$ . Numerical examples for this situation are shown in Fig.2.8.

$$\begin{aligned}
 \mathbf{B}(\mathbf{r}) &= \frac{3(\mathbf{p} \cdot \hat{\mathbf{r}})\hat{\mathbf{r}} - \mathbf{p}}{r^3} \\
 B_\perp &= \frac{1}{2}(3 \cos 2\theta + 1)\frac{p}{r^3} \\
 B_\parallel &= \frac{3}{2} \sin 2\theta \frac{p}{r^3}
 \end{aligned} \tag{2.31}$$

- Given two bundles with perpendicular dipole moments as in Fig.2.9, mutual inductance is negligible for configurations where one bundle is near the vertical axis passing through the center of the other. The reasoning is similar to the previous case, except that now we should analyze when does the parallel component  $B_\parallel$  vanish. This occurs at  $\theta = 0$  and  $\theta = 90^\circ$ . In one of the examples that will be shown in the next section (Fig.2.9) this situation manifests itself in two ways: (a) the mutual inductance drops to zero as  $D_z$

<sup>6</sup>this can be deduced from Taylor expansion of (2.24) and (2.18) under the conditions  $s \ll x, z \ll L$  where  $s$  represent generically distances within each bundle. The result is that  $M_{ab}$  exactly vanishes when  $x = z$ , i.e. when  $\theta = 45^\circ$

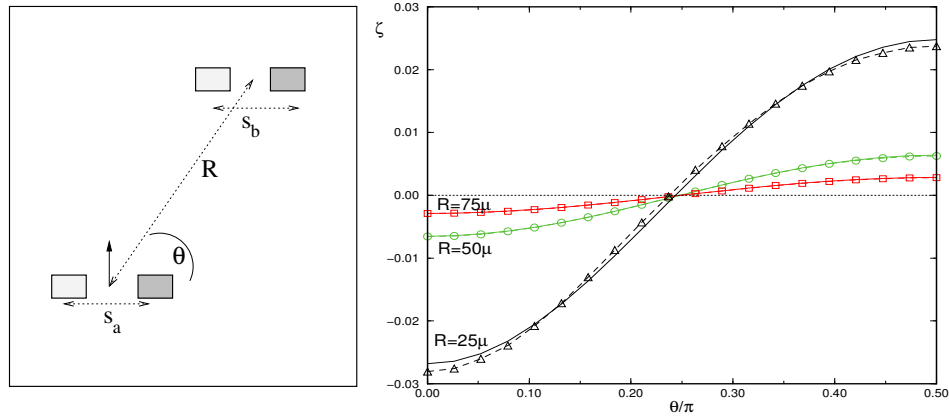


Figure 2.8: Dipole Selection Rule 2, showing the angular dependence of mutual inductance for different separation between bundles: dipole approximation (solid lines) and FastHenry (dotted lines with symbols)

does; (b) for  $D_z$  large,  $\zeta$  increases with increasing  $D_x$ . This rule is also helpful in pruning geometries.

### 2.4.2 Validation

In Fig.2.9, we display the simplest case, two bundles consisting of one signal wire with a single return path each. Notice that the relative position between signal and return is perpendicular in one bundle with respect to the other. From the results displayed in this figure, we notice that the dipole approximation shows relative discrepancies with FastHenry which are upper bounded by 10%. Considering that mutual inductance, in this case, is two or three orders of magnitude smaller than the self inductances, this means that the error introduced by the dipole approximation affects at worst, the third significant digit.

We stress that noise figures for  $\zeta$  are scale independent. For the sake of verification we reproduced all the examples that follow, scaling up and down two order of magnitudes, obtaining the same figures. This allows us to generalize the results as follows: if these typical bundle sizes of order  $5 \mu$ , and we can assure small errors for distances larger than  $\sim 30 \mu$ , then these small errors are maintained as long as the ratio of bundle size to separations is larger than 6. For this reason, we always plot distances as functions of the ratios  $\Lambda_x \equiv D_x/s$  and  $\Lambda_y \equiv D_y/s$ , where  $D_{x,y}$  are separations along  $x, y$ , and  $s$  is the typical size scale for the bundles.

Next, consider two bundles with one return path each, with their dipole moments being parallel (see Fig.2.10). Again, the resulting comparison with FastHenry also show discrepancies upper bounded by 10%. The dipole approximation holds quite accurately for mutual inductances

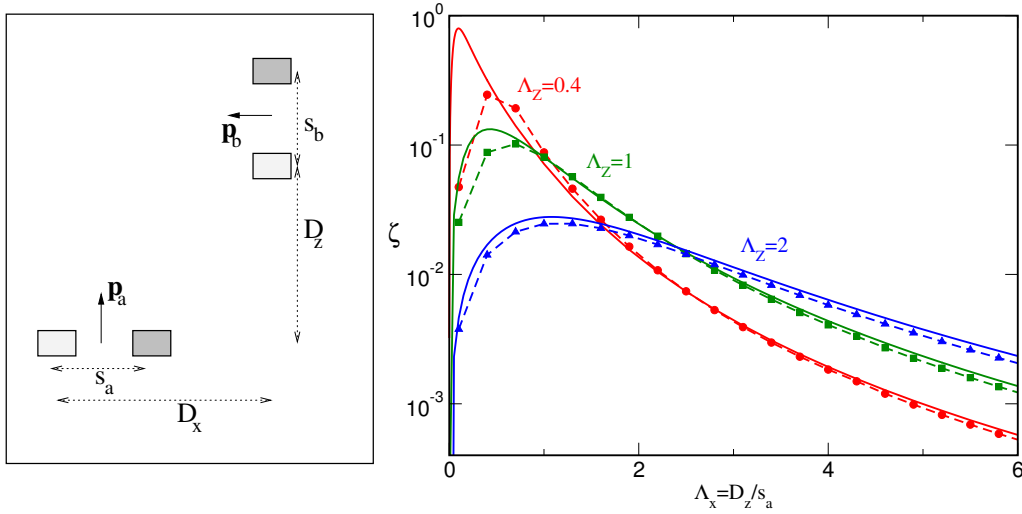


Figure 2.9: Comparison of between the dipole approximation (solid lines) and FastHenry (dotted lines with symbols) for perpendicular bundles, geometries like the one shown at left:  $\zeta$  is plotted for different values of  $\Lambda_z = D_z/s_a$  as a function of  $\Lambda_x = D_x/s_a$ . Parameters are:  $L = 500 \mu\text{m}$ ,  $s_a = s_b = 5 \mu\text{m}$  and  $h = 0.5 \mu\text{m}$ ,  $w = 0.5 \mu\text{m}$  for all conductors.

between two simple loops, irrespective of the orientation of their dipole moments.

Finally, we show a slightly more complicated geometry, consisting of two bundles with multiple return paths each. Both are asymmetric, in the widths of the return paths as well as in their positions with respect to the signal wire (see Fig.2.11).

In this example, we find that for the case of the closest configurations ( $\Lambda_x \leq 6$ ) there is a considerable difference between the two results. It should be noted, however, that even in those cases, the value of  $\zeta$  is very small, thus rendering the aforementioned errors insignificant when compared to the self inductances  $L_a, L_b$ .

In few words, the previous cases are examples that manifest the behavior that holds for arbitrary configurations: as long as distance between bundles is not too narrow ( $\Lambda \sim 6$  a seemingly worst case,  $\Lambda = 2$  being more representative), the leading dipole representation gives a good approximation to the mutual inductance.

### 2.4.3 Performance analysis

In order to analyze the efficiency of the present dipole approximation, we compare its runtimes with respect to the direct use of Grover's expressions (2.26). We mention briefly that these last expressions give basically the same results as FastHenry, meaning that the errors between the dipole approximation and Grover's expressions are as small as the ones presented in the previous sections.

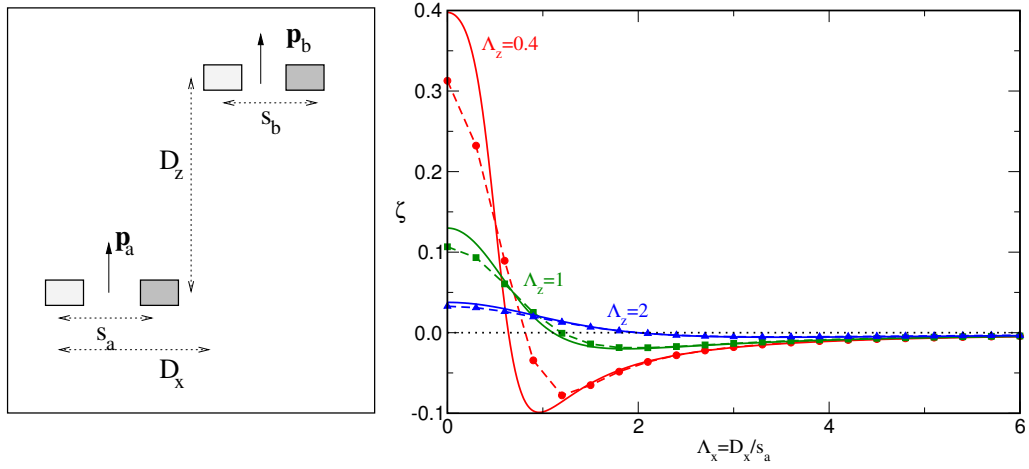


Figure 2.10: Comparison between the dipole approximation (solid lines) and FastHenry (dotted lines with symbols) for parallel bundles, geometries like the one shown at left:  $\zeta$  is plotted for different values of  $\Lambda_z = D_z/s_a$  as a function of  $\Lambda_x = D_x/s_a$ . Parameters are:  $L = 500 \mu\text{m}$ ,  $s_a = s_b = 5 \mu\text{m}$  and  $h = 0.5 \mu\text{m}$ ,  $w = 0.5 \mu\text{m}$  for all conductors.

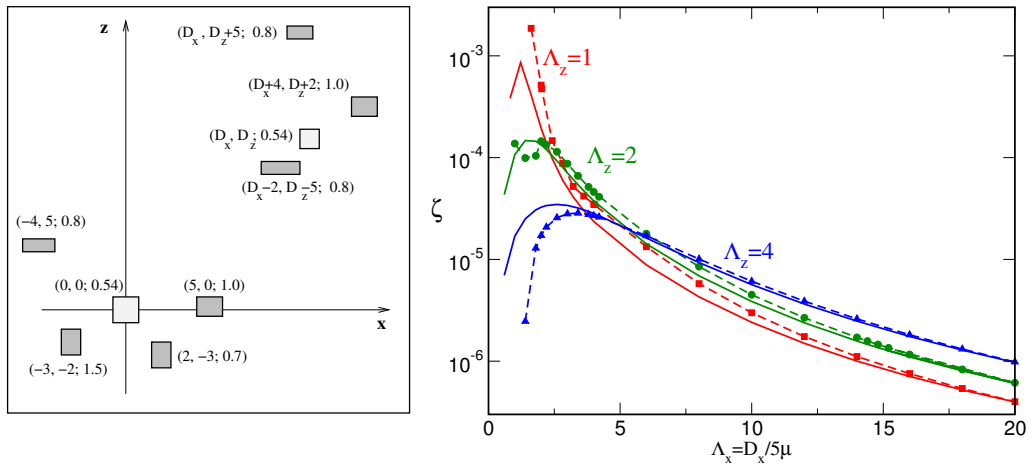


Figure 2.11: Comparison between the dipole approximation (solid lines) and FastHenry (dotted lines with symbols) for the two bundles shown at left, each of typical size  $\sim 5\mu$ :  $\zeta$  is plotted for different values of  $\Lambda_z = D_z/5\mu$  as a function of  $\Lambda_x/5\mu$ . The coordinates and widths of the wires are shown as  $(x, y; w)$  triplets, the thickness is  $h = 0.54 \mu\text{m}$ , and length is  $L = 1000 \mu\text{m}$  for all wires.

If we consider a general case, with  $N$  wires broken up into  $n_b$  bundles, Grover's expressions require  $N^2/2$  computations of terms as in the second line of (2.26). On the other hand, the dipole approximation requires a total of  $n_b N$  calculations. Thus, if there are on average considerably more than one return path per bundle (i.e., if  $n_b \ll N/2$ ), then the dipole approximation demands a much smaller number of evaluations. Moreover, each of the evaluations of Grover's expression involves a transcendental function, whereas for the dipole approximation there are  $N$  evaluations arising from the calculation of dipole moment, which are only sums and multiplications (see eq.(2.19)), plus  $(n_b - 1)N$  evaluations as in the argument in the sum of (2.24), where the most expensive operation is a half-power.

Table 2.4: Comparative runtimes for Dipole approximation (DA) and Grover's expressions (GE) as a function of the number of return paths  $N$ ; times expressed in microseconds per evaluation

N	DA	GE	Ratio GE/DA
1	0.412	1.586	3.85
2	0.544	3.343	6.14
3	0.697	5.817	8.34
4	0.784	9.052	11.54
5	1.000	13.002	13.00
6	1.092	17.902	16.39

In Table 2.4 we present a comparison between the two methods for concrete examples involving two bundles with the same number of return paths in each one. Runtimes are expressed in microseconds per mutual inductance computation ( $\sim 10^8$  similar computations are averaged for each entry of the table). All runs were carried out on a desktop PC running at 2.0 GHz, under identical situations. The approximately linear increase of the runtime ratios with bundle size (last column of Table 2.4) shows that, at least in this case, the dipole approximation is one order of magnitude faster than the use of Grover's expressions.

## 2.5 Discussion

We claim to have contributed to the understanding and simplification on the problem of mutual inductance computations relevant to IC design, in terms of simple dipole structures. For reasonable distance bounds, the dipole representation computes with good precision the behavior of the mutual inductance matrix. When the physical loops are seen in terms of dipoles, it is easier to separate what is important from what is negligible. The resulting selection rules emerge quite naturally, and further contribute to the sparsification. Considering an inductance matrix that falls

as  $1/r^2$  or  $1/r^3$  makes the problem of bounding the size of the extraction matrix manageable. This feature simplifies enormously the effort during downstream circuit simulation.

Previous work [58] have attributed to small current loops the term dipoles, without further ado. FastHenry and FastCap use effectively the multipole expansion of the Green Function in order to speed up matrix vector multiplications in their field solver [14, 15]. In fact, we have verified empirically that using FastHenry, with this expansion truncated at order 2, gives the same results as the dipole approximation [59].

Our analysis goes beyond in providing a framework for the proper extraction of the mutual inductance matrix for a wide range of distances. At very small distances, where the dipole approximation is no longer applicable, we simply need to compute the loop mutual inductances in terms of the algebraic sum of Grover-like expressions. Similarly, for interactions involving shared grounds bundles, Grover like expressions need to be used.

We stress that we are mainly interested in mutual inductance extraction at high frequencies, where the reactance part of the serial impedance is important. In this case, as discussed in Section 2.2, proximity plays a crucial role in the choice of return paths. Thus the bundles will have small spacial extensions, and the requirement that there are no shared return wires between intervening signals in the dipole approximation is fulfilled for all feasible layouts for bundles separated by distances between bundles in which the dipole approximation holds (i.e. typically 6 times the typical size of bundles).

As stated in the Introduction to this chapter, this work was carried out, published, and implemented into Mentor's Calibre tools at the early stages of this project. More recently, a collaboration with a group from University of California at Santa Barbara has re-opened the subject, in two main aspects [60, 61]:

- extending the dipole treatment to cope with short distances; this involves representing a bundle by an optimally chosen set of dipoles;
- incorporating substrate effects into the dipole treatment, based on so-called equivalent Green function methods [18, 19].



# Formules closes pour l'inductance mutuelle entre inducteurs intentionnels

## Résumé en français

*Dans ce chapitre, l'approximation dipolaire développée au chapitre antérieur est appliquée au problème du calcul de l'inductance mutuelle entre deux inducteurs intentionnels. En première instance, nous décrivons les formules standard qui seront utilisées comme référence (section 3.1), ainsi que les modifications aux formules du chapitre précédent pour le problème actuel (section 3.2). La suite du chapitre inclut un traitement pour des hautes fréquences (section 3.3), où les courants ne seront plus uniformes le long des sections transversales des segments de l'inducteur. Des exemples typiques sont exposés et analysés (sections 3.4 et 3.5), montrant le même degré de précision que dans le cas d'extraction de parasites, à savoir : cette approximation est valide pour des distances qui sont supérieures à un seuil comparable aux tailles des inducteurs. Nous finissons par une brève discussion sur des défis pour les futures recherches (section 3.6). Le travail décrit dans le présent chapitre a été présenté et publié dans les actes du "International Symposium on Circuits and Systems" (ISCAS) de l'IEEE [30], et son contenu est inclus dans une demande de brevet [31] en Mai 2006 en Kos, Grèce.*



## Chapter 3

# Mutual Inductance between Intentional Inductors: Closed Form Expressions

Intentional inductors are used as components in RF (radio frequency) analog designs, particularly in telecommunication applications [62]. Designers frequently use multiple intentional inductors. Each one of these devices occupies an amount of real estate on the chip in the order of  $10^4 \mu^2$ , at  $130nm$  technology. Design and manufacturing considerations favor placing inductors close to each other to minimize the occupied area, thereby improving the manufacturing yield. To be able to do it safely, a quantitative measure of the electromagnetic noise that one inductor generates on another one is essential. The noise figures can be evaluated in terms of the device's electrical parameters: resistance, inductance and capacitance matrices ( $R, L, C$ ). The purpose of this chapter is to provide a quick while reasonable estimate to the values of the mutual inductance as a function of separation among the inductors. Mutual inductance for moderate RF frequencies can be accurately represented with Grover like expressions integrated over the transverse dimensions. We assume low doping profiles, domain where substrate effects on inductance can be neglected [62]. Effects due to the onset of non uniform current distributions are not included in the treatment, except to verify that the correction they provide to the long distance behavior of the magnetic noise parameter is negligible.

The main results on this chapter are the derived analytical formulae, which are an extension of the dipole approximation presented in the previous chapter, and whose simplicity and linear complexity allow for quick estimates of the magnetic noise parameter. We provide detailed calculations for a number of configurations, the extensibility to other configurations being straightforward. We compare our results against Grover expressions [56] and FastHenry [15].

The computation of the mutual inductance using Grover expressions grows quadratically

with the number of segments per inductor. Using the dipole approximation we improve to linear complexity. This property makes it suitable for design explorations, whereby mutual inductance must be computed for a large number of configurations; the self inductance remains unchanged, and thus needs to be computed only once. Essentially, this method is an extension, into the domain of intentional inductors, of the one presented in the previous chapter for the problem of parasitics extraction.

Prior work within the PEEC formalism [55, 63–65] anticipated similar complexity reduction when applying the multipole expansion. We compare the two methods, ours based on the loop formalism and the other based on the PEEC formalism. In fact, we use FastHenry to obtain the PEEC results. As mentioned at the end of the previous chapter, this tool includes a multipole expansion in order to accelerate linear algebra operations. The results obtained using order 2 in these expansions are the same as the ones obtained using the dipole approximation; the difference is that FastHenry is a description based on segments (and as such, a partial treatment), whereas the dipole approximation is applied to current loops.

Neither the PEEC formalism nor the inverse method [47, 51] lead to simplified analytical results. This we take as a clear advantage of the loop formalism. The resulting expressions are given in terms of easily computable functions significantly simpler to compute than the corresponding Grover expressions for filaments.

The work described in the present chapter was published at proceedings of the IEEE International Symposium on Circuits and Systems (ISCAS) [30], and its contents were included for a patent application [31] in 2006. We organize it as follows:

- Section 3.1 describes the classical way for carrying out these calculations, that will be used as a reference to our methods;
- Section 3.2 revisits the dipole approximation presented in the previous chapter, concentrating on the application to intentional inductors;
- Section 3.3 discusses the high-frequency extensions of the method; it is also shown that these modifications are small enough to be negligible for realistic cases;
- Section 3.4 presents some basic examples, as well as estimation of errors against the classical reference;
- Section 3.5 analyzes the gains in terms of performance in the aforementioned comparison;
- Section 3.6 is a brief conclusion, as well as matters of concern for future development.

### 3.1 Classical Approach

An inductor can be considered as a circuit consisting of a concatenation of  $N$  straight segments, connecting at least two ports, laid out in one or multiple metal planes. In general, the layouts are non-Manhattan, since these provide a better figure of inductance-per-unit-area, and thus allow for better yield.

The loop self inductance of an inductor can be decomposed into:

$$L_{loop} = \sum_{i=1}^N L_{i,i} + 2 \sum_{i=1}^N \sum_{j=i+1}^N M_{i,j} \quad (3.1)$$

where  $M_{i,j}$  is the partial mutual inductance between segment  $i$  and  $j$  and  $L_{i,i}$  corresponds to the partial self inductance of segment  $i$  and the sum extends over all  $\frac{1}{2}N(N+1)$  terms.

The mutual inductance  $M$  between two inductors can be similarly computed in terms of a list of partial mutual inductance among the respective constituent segments:

$$M_{ab} = \sum_{i=1}^{N_a} \sum_{j=1}^{N_b} M_i^j \quad (3.2)$$

with  $N_a$  and  $N_b$  the number of wire segments in each inductor. The value  $M_i^j$  corresponds to the partial mutual inductance between segment  $i$  in the first inductor and segment  $j$  of the second inductor.

Under uniform current distribution, the classical approach makes use of the filament based Grover expressions [56] (equations (52)-(55)) for arbitrarily oriented filaments. For finite cross sections, the four dimensional integral required to compute the average over transverse dimensions is done numerically. For the sake of reference, we denominate this method ‘‘Classical Grover’’ (CG)

### 3.2 Dipole Approximation for inductors

The dipole approximation applied to quasi-magnetostatic problems is a general method for computing the magnetic field for an arbitrary current distribution as a function of distance, keeping only the leading term in  $1/r$  [46]. In the loop treatment, we deal exclusively with closed current loops; the leading term of the generated magnetic field is that of a dipole [28]. This is different from the PEEC approach to the dipole approximation, which contains monopole contributions. The monopole contribution vanishes for quasistatic closed loop current distributions, in a finite domain. In the loop inductance approach, we replace the field produced by each of the elementary current filaments within an inductor with one of a representative point-like dipole at

the center. The computation then proceeds following first principles in Electromagnetic Theory. The mutual inductance between two inductors  $a$  and  $b$  is given by:

$$M_{ab} = \frac{\Psi_{a \rightarrow b}}{I_a} = \sum_{S_j \in b} \int_{S_j} \mathbf{B}^{(a)} \cdot d\mathbf{S}_j = \frac{1}{I_a} \oint_C \mathbf{A}^{(a)} \cdot d\boldsymbol{\ell} \quad (3.3)$$

with  $\Psi_{a \rightarrow b}$  the magnetic flux resulting from the field generated by inductor  $a$  over the area sustained by inductor  $b$ . In addition,  $S_j$  are the surfaces subtended by the turns of inductor  $b$ ,  $C$  is the union of all segments of inductor  $b$ ,  $\mathbf{B}^{(a)}$  is the magnetic induction field generated by inductor  $a$  and  $\mathbf{A}^{(a)}$  is its vector potential that satisfies  $\mathbf{B}^{(a)} = \nabla \times \mathbf{A}^{(a)}$ . We now introduce the dipole approximation:

- computation of the vector potential  $\mathbf{A}^{(a)}$  for a magnetic dipole, in terms of the magnetic dipole moment  $\mathbf{p}^{(a)}$ ;

$$\mathbf{A}^{(a)} = \frac{\mathbf{p}^{(a)} \times \mathbf{r}}{r^3} \quad (3.4)$$

- computation of the dipole moment of inductor  $a$ , divided by its current;

$$\tilde{\mathbf{p}}^{(a)} \equiv \frac{\mathbf{p}^{(a)}}{I} = \frac{\mu}{8\pi I} \int \mathbf{r} \times \mathbf{J}(\mathbf{r}) d^3\mathbf{r} \quad (3.5)$$

- computation of the magnetic flux  $\Psi_{a \rightarrow b}$  of the field produced by the magnetic dipole of inductor  $a$  on the area sustained by inductor  $b$ ;
- replacing  $a$  with  $b$  in the above steps to compute the resulting mutual inductance as the average  $M = (M_{ab} + M_{ba})/2$  to ensure that the inductance matrix is symmetric.

For a single planar current distribution, representative of single metal layer intentional inductors, the dipole moment (3.5) reduces to:

$$\tilde{\mathbf{p}}^{(a)} = \frac{\mu}{8\pi} S \hat{\mathbf{z}} \quad (3.6)$$

where  $S$  is the total area bounded by the wire loop, and  $\hat{\mathbf{z}}$  is an unitary vector perpendicular to the plane containing the loop. The calculation of the dipole moment of the whole inductor  $\mathbf{p}^{(a)}$ , i.e. the vector sum of the dipole moments of each filament loop, reduces to computing the sum of the areas “trapped” inside each turn of the inductor  $a$ . In what follows we define:  $t \equiv$  number of turns;  $n \equiv$  number of sides per turn;  $N \equiv$  total number of segments ( $n \times t$ );  $d \equiv$  separation between vertices on successive turns;  $s = d \cos\left(\frac{2\pi}{n}\right) \equiv$  separation between sides on successive turns.

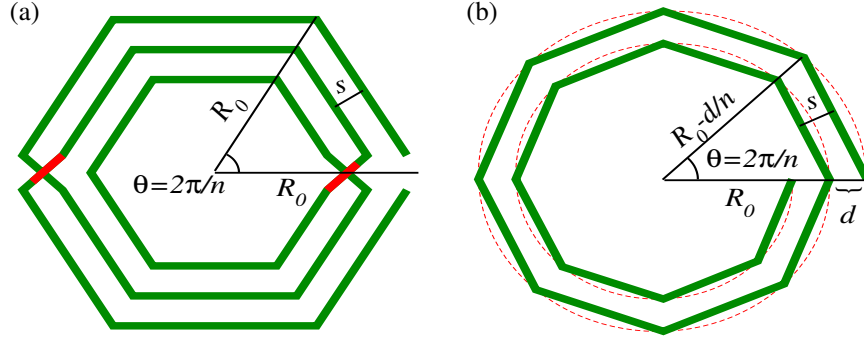


Figure 3.1: Polygonal inductors: (a) symmetric; (b) spiral.

We exemplify the calculation of area (magnetic dipole) for some common single layer polygonal inductors.

1. **Symmetric inductors**, built as concentric rings of regular polygons joined at every half turn, as shown in Fig. 3.1(a).
2. **Spiral inductors**, constructed such that the vertices of the inductor are situated along a linear spiral (i.e. a curve defined by  $r(\theta) = R_0 - \theta d/2\pi$ , where  $R_0$  is the distance from the center to the farthestmost vertex of the inductor, and  $d$  is the separation between corresponding vertices on two successive turns of the inductor, see Fig. 3.1(b).
3. **Arbitrary planar inductors**, general single layer inductor.

For a symmetric inductor,  $S$  is the sum of the areas of all the concentric polygons (e.g., the hexagons in Fig.3.1a), which is

$$S^{(sym)} = \frac{n}{2} \sin\left(\frac{2\pi}{n}\right) \sum_{\text{polygon}_i}^t R_i^2 \quad (3.7)$$

For a spiral inductor, we split its area into triangles as shown in Fig. 3.1(b). The resulting total area is

$$S^{(spiral)} = \frac{1}{2} \sin\left(\frac{2\pi}{n}\right) \sum_{\text{triangle}_i}^N R_i \left(R_i - \frac{d}{n}\right) \quad (3.8)$$

Expressions (3.7) and (3.8) have been obtained for inductors whose segments can be treated as filaments. The extension to finite cross section, for uniform current distribution within each

segment, is done by averaging over its transverse dimensions. Note that, given the simple combination of algebraic expressions and trigonometrical functions in (3.7) and (3.8), direct integration is easily obtainable leading to:

$$\tilde{S} = \frac{1}{wh} \int_{R-w}^R \int_0^h S(R', h') dR' dh' \quad (3.9)$$

The resulting expressions for finite cross section are

$$\tilde{S}^{(sym)} = \frac{N}{2} \sin\left(\frac{2\pi}{n}\right) \left[ R_0^2 + \left(R_0 + \frac{s}{6}\right)s - \left(R_0 - \frac{w}{3} + \frac{s}{2}\right)(st + w) + \frac{1}{3}(st)^2 \right] \quad (3.10)$$

$$\tilde{S}^{(spiral)} = \frac{N}{2} \sin\left(\frac{2\pi}{n}\right) \left[ R_0^2 - \frac{s^2}{3n^2} - \left(R_0 - \frac{w}{3}\right)w - \left(R_0 - \frac{w}{2}\right)st - \frac{1}{3}(st)^2 \right] \quad (3.11)$$

For an arbitrary planar inductor, the dipole moment can be computed as a sum of the areas of the triangles bounded by each inductor segment and the segments joining its extremes with the origin  $r = 0$ , where we locate the dipole moment. Each area is averaged over its finite transverse dimensions. The cost increase of performing this decomposition is small compared to the total cost (see analysis in Section 3.5).

Our next step is to compute the magnetic flux, through the surfaces bounded by the wiring of inductor  $b$ , for the field generated by the collection of dipoles representing inductor  $a$ . This part of the computation is common to all three types of inductors analyzed before. Combining expressions (3.3) and (3.4) we obtain, for the dipole located at  $\mathbf{r} = \mathbf{0}$ :

$$M_{ab} = \tilde{p}^{(a)} \sum_{j=1}^{N_b} \int_{\text{segment } j} \frac{-y_j dx_j + x_j dy_j}{(x_j^2 + y_j^2 + z_j^2)^{3/2}} \quad (3.12)$$

This last expression is trivially integrable giving:

$$M_{ab} = \tilde{p}^{(a)} \sum_{j=1}^{N_b-1} \frac{c_j}{b_j^2 - a_j^2} \left( \frac{L_j + a_j}{(b_j^2 + a_j L_j + L_j^2)^{1/2}} - \frac{a_j}{b_j} \right) \quad (3.13)$$

where we introduced for each segment  $j$  starting at  $(x_0, y_0)$  and ending at  $(x_1, y_1)$ , the coefficients:

$$\begin{aligned} L_j &\equiv \sqrt{(x_1 - x_0)^2 + (y_1 - y_0)^2}; \\ a_j &\equiv 2(x_0(x_1 - x_0) + y_0(y_1 - y_0)) / L_j; \\ b_j &\equiv \sqrt{x_0^2 + y_0^2 + z_b^2}; \\ c_j &\equiv (x_0 y_1 - x_1 y_0) / L_j \end{aligned}$$

Equations (3.10) to (3.13), properly symmetrized by replacing  $a$  with  $b$  and averaging, constitute our basic results for the evaluation of the mutual inductance between two intentional inductors.

### 3.3 High frequency extensions

The derivation of the previous results demands that the currents be uniform across the wires' cross-section. This approximation ceases to be valid at higher frequencies (above 5-7 GHz), wherein skin and proximity effects sensibly modify the current distribution inside the wires.

At higher frequencies we compute the distribution of currents across the cross section of each wire segment. The natural way to do so is to discretize the wire segments into  $m$  filaments, each one carrying uniform current. In Fig.3.2 we show schematically a discretized inductor, represented in terms of filaments. Solving for the filament currents, from the Kirchoff equations for one inductor we obtain the following coefficients:

$$\alpha_{j,k} \equiv \frac{I_{j,k}}{I}, \quad 1 \leq j \leq m, 1 \leq k \leq N \quad (3.14)$$

where

$$I = \sum_{i=1}^m I_{i,k} \quad (3.15)$$

is the total inductor current common to all segments. Notice that the values in (3.14) are frequency dependent complex numbers. The dependence of  $\alpha_{i,k}$  on the second subindex  $k$  simply expresses the fact that we allow for current redistribution in going from segment to segment.

The above discretization procedure is carried out only once per frequency and per inductor. It provides the high frequency self impedance of the inductor, which is defined as  $\Delta V/I$ , with  $\Delta V$  the difference of potential between the input and output nodes and  $I$  given by (3.15).

The implicit approximation is that the current distribution in one inductor is unaffected by the presence of the other inductor. This assumption still holds for small distances, even for separations between inductors much smaller than the inductors' sizes, as we have verified with

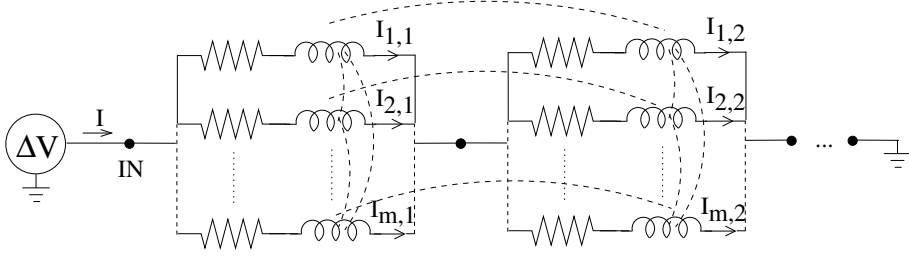


Figure 3.2: Circuit equivalent of a filament discretization of an inductor; for the sake of clarity, the inductive interaction between filaments of different segments are not drawn, but they are included in the calculation.

FastHenry which does not incorporate this assumption. Two different results can be derived from this approximation. The first one applies to the classical approach. Within the classical approach we obtain the following expression for the mutual inductance in the filament decomposition, under the above mentioned approximation:

$$M_{ab} = \Re e \left( \sum_{k_a=1}^{N_a} \sum_{k_b=1}^{N_b} \sum_{i_a=1}^{m_a} \sum_{i_b=1}^{m_b} \alpha_{i_a, k_a} \alpha_{i_b, k_b} M_{i_a k_a, i_b k_b} \right) \quad (3.16)$$

The imaginary part of the above expression is in fact the mutual resistance between the inductors divided by  $2\pi f$ , with  $f$  the frequency. We have verified with simulations that the mutual resistance is in general negligible.

In other words, in the filament decomposition, (3.2) is replaced by (3.16). We have verified with FastHenry that the results obtained in this fashion are accurate and computationally less expensive than FastHenry for non negligible separations.

Similarly, in the dipole method, the extension of the dipole moment in (3.5) consists of a weighted sum over filaments:

$$\tilde{\mathbf{p}}^{(a)} = \sum_{k=1}^{N_a} \sum_{i=1}^{m_a} \alpha_{i, k} \tilde{\mathbf{p}}_{i, k} \quad (3.17)$$

with  $I\alpha_{i, k} \tilde{\mathbf{p}}_{i, k}$  the contribution of filament  $i$  in the  $k$ -th segment to the total dipole moment and  $\tilde{\mathbf{p}}_{i, k}$  proportional to the area spanned by the filament.

The total magnetic flux through the victim inductor is the weighted sum over the fluxes through the surfaces spanned by each filament, giving

$$M_{ab}^{(HF)} = \Re e \left( \sum_{k=1}^{N_b} \sum_{j=1}^{m_b} \alpha_{j, k} M_{a, jk} \right) \quad (3.18)$$

with  $M_{a, jk}$  calculated as in (3.13) for segments.

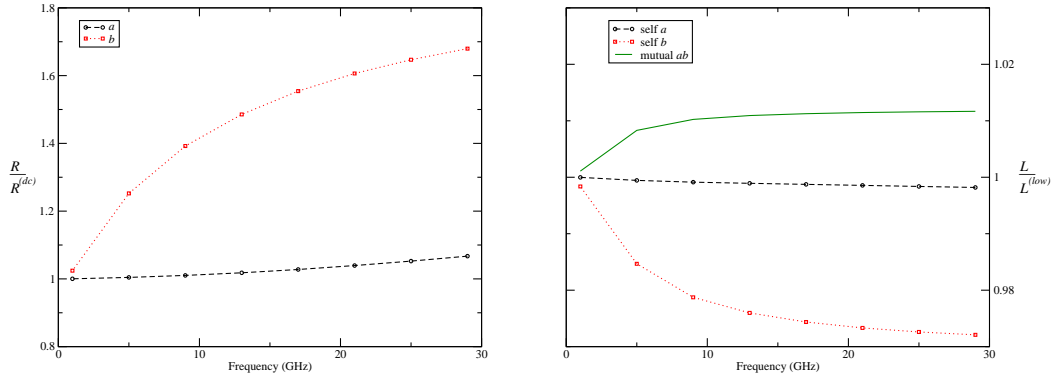


Figure 3.3: Frequency variation of resistance (left), self inductance, and mutual inductance (right) for a configuration of: square inductor  $a$  ( $R_0 = 100\mu\text{m}$ ,  $s = 1\mu\text{m}$ ,  $w = 1\mu\text{m}$ ,  $t = 0.65\mu\text{m}$ ); spiral inductor  $b$  ( $R_0 = 100\mu\text{m}$ ,  $s = 1\mu\text{m}$ ,  $w = 10\mu\text{m}$ ,  $t = 0.65\mu\text{m}$ ); with a border-to-border separation of  $50\mu\text{m}$  between them. We plot the ratio of the frequency dependent values to the low frequency ones.

Concerning the necessity of implementing this discretized version of the dipole approximation, we study a typical configuration in Fig. 3.3. These graphs show that frequency-dependent variations for mutual inductance are negligible, at least up to a frequency of  $30\text{ GHz}$ .

### 3.4 Validation

We compare our simple analytical results to those obtained using standard references. The key parameter for magnetic noise analysis is the ratio  $\zeta$  defined as:

$$\zeta \equiv \frac{M_{ab}}{\sqrt{L_a L_b}} \quad (3.19)$$

with  $L_a$ ,  $L_b$  the self inductances of inductors  $a$  and  $b$ , respectively. The geometric mean between  $L_a$  and  $L_b$  is a normalization factor for noise estimates, which needs to be computed once. This calculation is unrelated to the Dipole Approximation: we use either Grover's formulas or FastHenry to calculate it, with no significant difference between the two methods.

While using FastHenry, we apply it in its default mode, i.e. with multipole expansions up to order 2. In Fig. 3.4 we plot  $\zeta$  as a function of the horizontal border-to-border separation  $d_x$  for different values of the center to center separation  $\Delta_y$ . The calculations with FastHenry are made at  $5\text{GHz}$ , its results are insensitive to the number of filaments, uniform current distribution being valid at this frequency for these geometries. Except for very large separations, the results from FastHenry and CG sit on top of each other as expected. The minor differences at very large

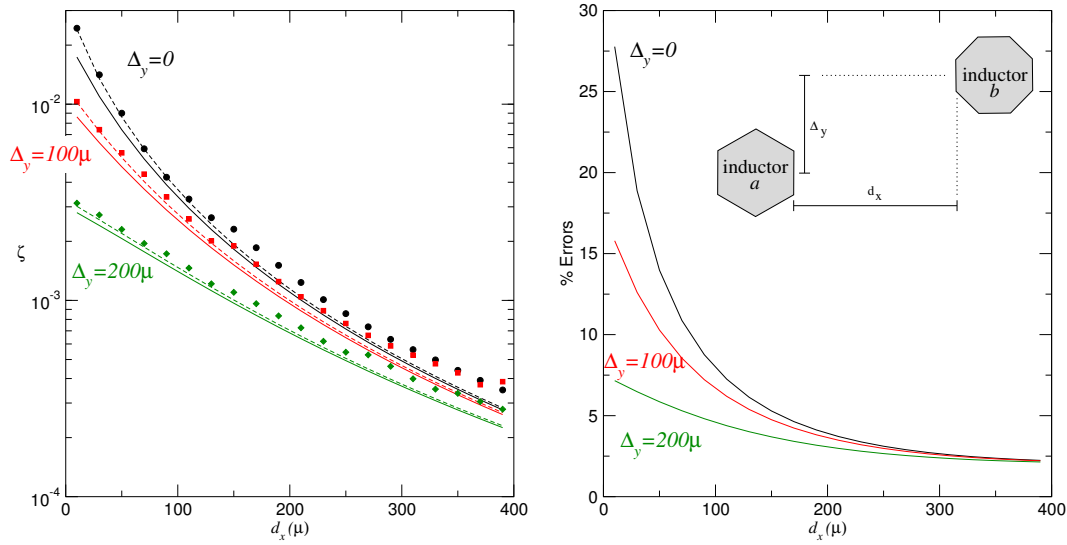


Figure 3.4: Mutual inductance coupling for Dipole approximation (solid lines), Classical Grover (dashed lines), FastHenry (symbols). Configuration consisting of a 6-turn hexagonal symmetric inductor ( $R_0 = 50\mu\text{m}$ ,  $s = 1\mu\text{m}$ ) and a 5-turn octagonal symmetric inductor ( $R_0 = 80\mu\text{m}$ ,  $s = 0.5\mu\text{m}$ );  $\Delta_y$  and  $d_x$  are defined in the inset, and errors for DA with respect to CG are presented at right

separations are interpreted as possible numerical instabilities for very small values of  $\zeta$  within FastHenry, totally harmless for relevant calculations. The dipole approximation (DA) and CG agree with each other and, for completeness, also agree with ASITIC [66] at large distances. Concerning the short distance behavior of DA, region where the approximation breaks down, it turns out to provide order of magnitude approximation, useful for first order estimates of noise figures at short distance.

The value of  $\zeta$  in the DA is scale invariant, with small logarithmic deviations arising from the self inductances in the Grover approximation. This result can be immediately concluded from a cursory examination of the above formulae in Sec.3.2. This permits us to express our estimates in terms of the ratio of separation to mean radius, rather than minimum separation. In this and other examples we verify that when this ratio is larger than 1/10 reasonable agreement between is obtained. It also allows us to predict noise estimates after scaling. In Fig.3.4 we display the relative error using the DA method for the example shown in Figure 2 as a function of horizontal separation. Different configurations have given similar results to the ones presented above.

Our approach is naturally extensible to a filament decomposition to study modifications due to non uniformity in the current distribution. Nevertheless, we verified with FastHenry computing self and mutual inductance for the examples presented above, among others, using extensive filament decomposition, and noticed that in going up to 30GHz the variations in  $\zeta$

amount to less than 3%. Therefore, the predictive power of the method presented here is not substantially affected by skin effect considerations, up to 30GHz.

### 3.5 Performance analysis

A basic property emerging from the dipole approximation introduced for computing the mutual inductance among two intentional devices is its linear growth with the number of segments. It results in general as a consequence of the multipole expansion and is valid to any order in this expansion. Algorithms that grow asymptotically as fast as  $N \log N$ , and even linear algorithms are properly discussed by Beatson and Greengard [67]. The classical Grover expression in (3.2) is quadratic in the number of segments.

Given two inductors with  $N_a$  and  $N_b$  number of segments, the linear behavior for the dipole approximation emerges in a natural way from: one evaluation of (3.5) using (3.10) or (3.11), or a worst case of  $N_a$  evaluations of the areas of triangles if no specific formula for the total area can be obtained; plus  $N_b$  evaluations of (3.13). Given two inductors with  $N_t = N_a + N_b$  total segments, the dipole approximation in the loop formalism, requires a maximum  $2N_t$  operations (the factor of 2 is due to symmetrization), as opposed to  $\frac{1}{2}N_t^2$  operations in the classical approach (see eq.(3.2)).

Furthermore, all the terms appearing in the computation of  $M_{ab}$  in the dipole approximation involve simple functions, i.e. there is a single transcendental function to evaluate, the  $\sin(2\pi/n)$  in the expressions for the area which is evaluated once per inductor, irrespectively of the separation. There are no further integrals to be computed for finite cross sections.

To evaluate the results of a PEEC analysis to the same order in powers of  $1/r$  we must include contributions to  $\mathbf{A}(\mathbf{r})$  that behave as  $1/r$  at large distances [55, 63–65], in addition to the dipole behavior  $1/r^2$  in the vector potential  $\mathbf{A}(\mathbf{r})$ . Both approaches being fundamentally equivalent, once we include all contributions, the  $1/r$  contributions of partial methods cancel out, leaving the dipole term as the dominant one. This equivalence has been verified using FastHenry with its multipole expansion for filament interactions, retaining up to the dipole level.

In Table 3.5 and Fig. 3.5 compare the total average runtimes for the three methods, for two symmetrical octagonal inductors as a function of the number of turns of one of them, for a fixed separation. These were performed according to the following criteria:

For the CG and the loop dipole method, we break the computation into a setup step (reading input files, memory allocation, etc.), common to both, and a computation part. For FastHenry, we only display the total runtimes, with a single filament per segment, and the default dipole approximation for the long distance computation. For each datapoint we run 1000 samples, all of them on a Sun workstation with an Opteron processor clocked at 2.39 GHz and 2 GB of physical memory. To avoid the influence of outliers, the highest and lowest 1% of runtimes for

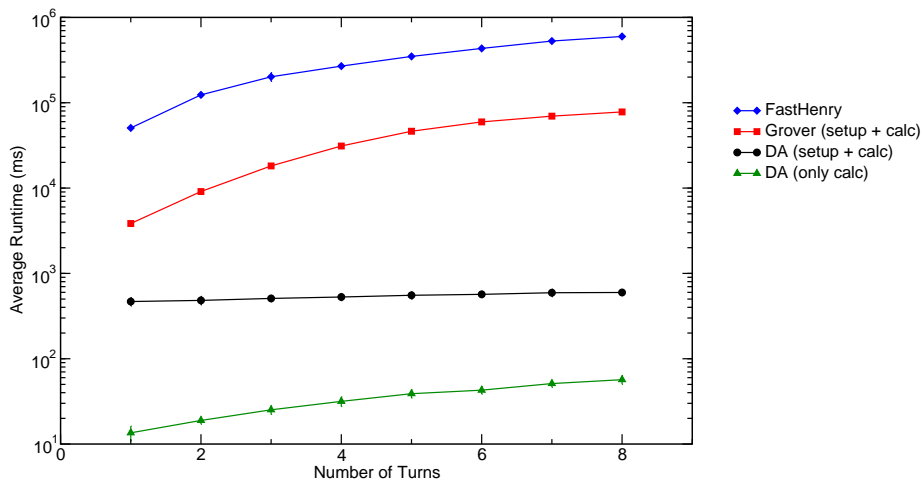


Figure 3.5: Comparative runtimes for the methods described in the text, as a function of the number of turns  $N_{turns}$ , for two identical octagonal symmetric inductors.

each configuration are discarded.

The Dipole Approximation in the loop treatment is two and one half orders of magnitude faster than the Classical Grover approach. The common set-up time in DA and CG is roughly one order of magnitude larger than the time for the DA calculation. The total runtime using the DA method is dominated by the set up time. The opposite holds when using CG. The overall effect, is to render the DA total runtime to be two orders of magnitude faster than the runtime using CG. These estimates were presented for a single separation distance  $s$ . For noise driven synthesis applications, we are interested in the computational cost for a number of separations. Thus in general we anticipate further gains while using the DA method to compute  $\zeta(s)$  since the dipole moment and the self inductance of each device are computed only once.

### 3.6 Conclusions

We introduced a method for calculating mutual inductance between intentional devices based on first principles on closed loop configurations, resulting from a multipole expansion starting with a dipole term  $A(r) \approx 1/r^2$ . This is conceptually different from the PEEC method, that contains  $A \approx 1/r$  behavior. Reasonable levels of accuracy are obtained in the computation of the noise parameter  $\zeta$  for a wide spectrum of geometries, separations and frequencies up to 30GHz. The resulting analytical expression with linear complexity in  $N$  and moderate accuracy, can be useful for a number of applications.

The computed magnitudes are essentially frequency-independent, as shown in Sec.3.3 and thus can be used to estimate the inductive part of interactions between intentional devices. Self

$N_{turns}$	$CG DA^{(setup)}$	$CG^{(calc)}$	$DA^{(calc)}$	$FH$
	$10^2 \times$	$10^3 \times$		$10^5 \times$
1	$4.68 \pm 0.52$	$3.8 \pm 0.2$	$13.5 \pm 2.6$	$5.1 \pm 0.1$
2	$4.82 \pm 0.54$	$9.1 \pm 0.5$	$18.9 \pm 1.8$	$12.4 \pm 0.3$
3	$5.09 \pm 0.43$	$18.2 \pm 0.5$	$25.2 \pm 2.9$	$20.2 \pm 0.2$
4	$5.29 \pm 0.50$	$31.1 \pm 0.6$	$31.6 \pm 4.1$	$26.9 \pm 0.3$
5	$5.54 \pm 0.55$	$46.3 \pm 0.7$	$38.9 \pm 4.4$	$34.9 \pm 2.2$
6	$5.68 \pm 0.47$	$59.6 \pm 0.8$	$42.8 \pm 4.4$	$43.3 \pm 0.5$
7	$5.93 \pm 0.59$	$69.6 \pm 0.8$	$51.1 \pm 4.9$	$52.9 \pm 0.9$
8	$5.98 \pm 0.49$	$78.1 \pm 0.9$	$56.8 \pm 6.6$	$59.8 \pm 0.5$

Table 3.1: Comparative runtimes for Loop Dipole approximation (DA), Classical Grover expressions (CG), and FastHenry (FH) as a function of the number of turns  $N_{turns}$  for two identical octagonal symmetric inductors; times expressed in microseconds per calculation

parameters, which determine the presence of resonant peaks, must be computed with a method that couples resistance, inductance and capacitance of all the elements in the inductor; an example of this type of modeling is carried out in our group, as reported in [23].

The resonances in the self impedance of an inductor are the result of cancellations between the capacitive and inductive effects. Between different inductors, electric effects play a minor role when compared to magnetic ones, due to shielding. In other words, mutual capacitive coupling between inductors can be roughly estimated, or neglected altogether, since this coupling is mainly of inductive nature.

Exploration of a design consisting of several intentional inductors requires testing and comparing a large number of different configurations. Among these, self inductance remains essentially unchanged, meaning that self parameters need to be computed only once. On the other hand, noise (mutual) parameters, which are the output of our calculation, must be recomputed for each configuration. This task can be done significantly less expensive by using the dipole approximation, as shown in this chapter.

Concerning present and future work, we state that the same comments found at the end of the previous chapter, concerning the dipole approximation, apply to this one.



## **Part B**

# **High-frequency modeling of currents and charges using conduction modes**



# Modélisation *RLC* avec des modes de conduction

## Résumé en français

*Ce chapitre est consacré aux modélisations des courants et charges sur la base de modes de conduction. Nous présentons d'abord le cadre général selon lequel l'ensemble original des équations de Maxwell est converti à un système linéaire pour les sources (sections 4.1), tant pour une description quasistatique et découplée  $RL + C$  (section 4.2.1), que pour une description d'onde complète  $RLC$  (section 4.2.2). Ensuite, nous introduisons les modes de conduction comme une base qui permet une caractérisation efficace des courants pour le cas  $RL$  déjà existant dans la littérature (sections 4.3.1) et des courants et charges pour l'extension au domaine  $RLC$ , ce qui constitue une innovation originale (sections 4.3.2). Nous continuons en discutant le choix des modes et son rapport avec une classe particulière des problèmes, à savoir la propagation des ondes quasi-TEM (transverse électromagnétique) en présence des conducteurs non parfaits (section 4.4). Un schéma des algorithmes liés à l'implémentation de cette méthode est inclus et brièvement discuté en section 4.6. En section 4.7, se trouvent des exemples d'application, montrant des résultats très précis par rapport aux références standard, avec une réduction significative pour la taille des systèmes linéaires. Les conclusions en section 4.8 sont succinctes, car la discussion approfondie sur ce sujet fait l'objet d'un traitement plus systématique au chapitre 6. Le présent chapitre est une prolongation du papier présenté lors de la dernière réunion de l' "International Conference on Computer-Aided Design" (ICCAD) en Novembre 2006 [33].*



## Chapter 4

# *RLC* conduction modes formalism and examples

Obtaining electromagnetic parameters for IC interconnects implies solving, in an approximate manner, Maxwell's equations for the circuit components in a layout. For configurations with a very large number of conductors, this task is difficult. In order to cope with this complexity, long distance interactions among wires must be neglected (at the first level of approximation), so as to produce smaller coupled problems, for which a solution is possible. The task of performing this separation, computing the EM parameters for the smaller problems, and later including the long-distance interactions neglected above, is the function of an extractor.

In the market of commercial extractors, there are four major competitors: Assura (Cadence) [25], Raphael (Synopsys) [68], Columbus (Sequence) [43], and Calibre (Mentor Graphics) [22]. All of them perform a full-chip sweep, isolating a large number of manageable configurations that must be solved individually.

Fast solvers are a necessity for each one of these subproblems. We distinguish between fullwave and decoupled solvers. The first ones treat the complete set of four Maxwell equations, producing *RLC* parameters. The second type of solvers split the problem in two, solving for charges and producing *C* parameters on one side; for currents and producing *R* and *L* on the other. Each of these two subproblems are comparatively simpler than the fullwave ones. For validity of this decomposition, dimensions of the components must be small compared to the EM wavelength in the medium.

In Table 4.1, we include a (non-exhaustive) list of tools for solving these problems. We include academic as well as commercial programs<sup>1</sup>. For most of these solvers, sources and/or fields are treated as piecewise constant functions. For example, charge distribution can be

---

<sup>1</sup>Concerning these last ones, we point out that we ignore the details of each implementation; we know broadly what type of solution is proposed.

represented by a set of surface panels (FastCap, FastMaxwell), currents by a set of filaments (FastHenry, FastMaxwell), the  $\mathbf{E}$ ,  $\mathbf{H}$  field on conductors' surfaces by piecewise-constant panels (FastImp, LargeCom).

The number of such piecewise-constant elements depends on two main factors: geometry and fields' variations. The impact of geometry, for any given configuration, is independent of the method to be used. Geometry is an unavoidable constraint, in the following sense: if many relevant small wires are present, many small elements are required.

Instead, the second factor depends on frequency. It is well known that, for high enough frequencies, currents cease to be uniform along the conductors' cross-sections. The shape of this non-uniformity of currents on the conductor is not arbitrary; they have exponential decays of order  $\delta$ , the skin depth for a conductor. This establishes a length scale, that decreases as the inverse square root of frequency, determining the minimum size in which currents can safely be considered uniform along the transverse dimensions.

Table 4.1: List of well-known electromagnetic solvers and their characteristics

Name	Origin	Type	Volume elements	Surface elements	Description
FastHenry	MIT [69]	<i>RL</i>	✓		Filament decomposition for skin effects
FastCap	MIT [69]	<i>C</i>		✓	Panel discretization of Laplace's equation
FastImp	MIT [69]	Fullwave or <i>RL</i>		✓	Fullwave surface using Green's identities
FastMaxwell	MIT [69]	Fullwave	✓	✓	Integrated panel+filament mesh model
LargeCom	U.of Illinois [70]	Fullwave or <i>RL</i>		✓	Surface formulation in Fourier $k$ -space
HFSS	Ansoft [11]	Fullwave	✓		Volume differential finite element method (FEM)
Sonnet Suites	Sonnet [71]	Fullwave	✓		FFT-based planar wave decomposition
IE3D	Zeland [72]	Fullwave		✓	Surface-mesh fullwave solver

Knowledge of how currents decay inside the conductor is used by tools like FastHenry [15] and Calibre [22, 23], in order to discretize the conductors' cross-section in an efficient way, with fine filaments near the borders and wider ones toward the center. But this knowledge also suggests an idea that avoids altogether the need of fine discretization: describing currents in terms of distribution functions with the appropriate behavior. These functions, named "conduction modes", are non other than the eigenfunctions to the differential equation for the system, which is the Helmholtz equation. If the set of expansion functions is well chosen, the conduction modes produces an important reduction in the system size.

Choosing these type of functions is reminiscent of the separation-of-variables techniques used in electrostatics for solving Laplace's equation, given boundary conditions on a closed surface [46]. The same problem can be solved by discretizing the boundary and applying any finite element method for solving this elliptic PDE. However, this would neglect the gains to be made in using the more adequate eigenfunctions to the Laplace equation.

This analogy with electrostatics ends here, since we are concerned with a different type of

problem and therefore a different kind of approach. Instead of solving Laplace's equation within a closed surface, we construct and solve a linear system based on a chosen set of functions that describe the current distribution. The success of this technique depends on the quality of this choice.

Conduction modes were first introduced in 60's [73], and resurfaced in 2001 [32], for *RL* problems involving only longitudinal currents, and short wires compared to the wavelengths. As such, this formulation was presented as a reduced-size replacement for a piecewise-constant approaches, like FastHenry. Size reductions of factor 20 were reported for several examples [16]. Another application of conduction modes was put forward by the same group in 2003 [74], in which these functions are used as boundary conditions in order to reduce the size of FastImp (see Table 4.1), a surface mesh fullwave solver.

There are two main disadvantages of the conduction modes method. The first one is that the conduction modes are defined only for simple geometries, namely rectangular or cylindrical cross-sections [73]. This restriction does not play an important role in the IC domain, where most structures fall into this category [75].

The second disadvantage is that, although there is an important reduction in size, this is not immediately reflected in the overall runtime. The reason is that the computation of the matrix elements, for the conduction modes method, is computationally more expensive than their piecewise constant counterparts. We will show that this limitation is not fundamental; in fact, we have developed a comprehensive study on these matrix elements, demonstrating that significant runtime savings are attainable.

Our contribution to the conduction modes method has two main components:

1. We have generalized the original formulation, which was valid only for *RL* extraction under the Magneto-Quasi-Static (MQS) assumption, into a fullwave *RLC* methodology; we have shown its validity for transmission-line type of structures.
2. We have systematically tackled the problem of calculating nontrivial  $n$ -dimensional integrals inherent to the conduction modes method, thus rendering it not only efficient in terms of size, as well as in terms of performance.

The present chapter deals with point 1 above, restricted to a special type of subproblem which will be described in the text. Next chapter is devoted exclusively to point 2 above, restricted to the *RL* formulation. Chapter 6 deals with the generalizations of these two aspects, namely the formulation to a more ample set of problems, as well as the speed-up for the calculation of matrix elements for the *RLC* method.

In detail, in this chapter we cover the following aspects:

- general framework, by which we pass from the original set of Maxwell's equations to a

linear system (Sections 4.1), first for a separate *RL* + *C* description (Section 4.2.1), and then for a mixed *RLC* one (Section 4.2.2);

- introduction of conduction modes as a basis for expanding and solving these linear systems, for the *RL* and *RLC* cases (Sections 4.3.1 and 4.3.2, respectively);
- choice of conduction modes and relationship to a particular class of problems, namely the quasi-TEM wave propagation in the presence of non-perfect conductors (Section 4.4);
- different solution schemes for the conduction modes method (Section 4.6) and outline of the implementation of algorithms (Section 4.6);
- examples of application, showing very precise results when compared to some of the tools described above, with a considerable reduction in size (Section 4.7);

We mention that the present chapter is an extension, as well as an upgrade, of the paper presented at the last meeting of ICCAD in November 2006 [33]; the following chapter is the analogous for a paper accepted to ISVLSI 2007 [34]; and chapter 6 is a description of ongoing work, as well as proposals for the future.

## 4.1 From Maxwell's equations to a MPIE

Electromagnetic fields, currents and charges are governed by Maxwell's equations:

$$\nabla \cdot \epsilon \mathbf{E} = \rho \quad (4.1a)$$

$$\nabla \times \mathbf{E} = -\frac{\partial \mathbf{B}}{\partial t} \quad (4.1b)$$

$$\nabla \cdot \mathbf{B} = 0 \quad (4.1c)$$

$$\nabla \times \frac{\mathbf{B}}{\mu} = \mathbf{J} + \frac{\partial \epsilon \mathbf{E}}{\partial t} \quad (4.1d)$$

where  $\mathbf{E}$  is the electric field,  $\mathbf{B}$  is the magnetic induction vector field,  $\mathbf{J}$  and  $\rho$  are the current and charge distribution functions respectively,  $\epsilon$  is the dielectric permittivity of the medium and  $\mu$  its magnetic permeability, with  $\epsilon\mu = c^{-2}$ , and  $c$  the velocity of light in the medium.

It is standard practice to define the scalar and vector potentials, by observing that: from (4.1c),  $\mathbf{B}$  is divergence-free, and can be derived as the curl of some vector potential  $\mathbf{A}$ ; then this expression for  $\mathbf{B}$  is inserted into (4.1b), obtaining a curl-free magnitude,  $\mathbf{E} + \partial\mathbf{A}/\partial t$ , which can be derived as the gradient of some scalar potential  $\phi$ ,

$$\begin{aligned}\mathbf{B} &= \nabla \times \mathbf{A} \\ \mathbf{E} + \frac{\partial \mathbf{A}}{\partial t} &= -\nabla \phi\end{aligned}\quad (4.2)$$

Replacing these two expressions in (4.1a) and (4.1d), the equations for the potentials become,

$$\nabla^2 \mathbf{A} - \frac{\partial^2 \mathbf{A}}{\partial t^2} - \nabla \left( \nabla \cdot \mathbf{A} + \frac{1}{c^2} \frac{\partial \phi}{\partial t} \right) = -\mu \mathbf{J} \quad (4.3a)$$

$$\nabla^2 \phi + \frac{\partial \nabla \cdot \mathbf{A}}{\partial t} = -\frac{\rho}{\epsilon} \quad (4.3b)$$

Vector potential  $\mathbf{A}$  has been defined only by its curl; this contemplates a freedom in the choice of its divergence. This property of EM potentials is called the gauge invariance; in this work we adopt the Lorentz gauge, whereby  $\nabla \cdot \mathbf{A} = -\frac{1}{c^2} \frac{\partial \phi}{\partial t}$ , so as to cancel the second term in (4.3a),

$$\nabla^2 \mathbf{A} - \frac{1}{c^2} \frac{\partial^2 \mathbf{A}}{\partial t^2} = -\mu \mathbf{J} \quad (4.4a)$$

$$\nabla^2 \phi - \frac{1}{c^2} \frac{\partial^2 \phi}{\partial t^2} = -\frac{\rho}{\epsilon} \quad (4.4b)$$

These second-order differential equations are in fact wave equations, having the retarded-potential solutions,

$$\mathbf{A}(\mathbf{r}, t) = \frac{\mu}{4\pi} \int_V \frac{\mathbf{J}(\mathbf{r}', t_{ret})}{|\mathbf{r} - \mathbf{r}'|} d^3 r' \quad (4.5a)$$

$$\phi(\mathbf{r}, t) = \frac{1}{4\pi\epsilon} \int_V \frac{\rho(\mathbf{r}', t_{ret})}{|\mathbf{r} - \mathbf{r}'|} d^3 r' \quad (4.5b)$$

where  $t_{ret} = t - |\mathbf{r} - \mathbf{r}'|/c$  is the retarded time, such that an EM perturbation at position  $\mathbf{r}'$  and time  $t_{ret}$  reaches position  $\mathbf{r}$  at time  $t$ ; and  $V$  is the entire space containing the sources  $\mathbf{J}$  and  $\rho$  (in this last statement, we consider that sources are bounded, so that we have open boundary conditions:  $\mathbf{A}, \phi \sim 1/r \rightarrow 0$  as  $r \rightarrow \infty$ ).

We work in the frequency domain, whereby all sources and fields have a time harmonic behavior  $\mathbf{X} = \mathbf{X}_0 e^{-j\omega t}$ , with  $\omega$  the common angular frequency<sup>2</sup>. Within this framework, time

<sup>2</sup>We neglect the sub-index "0", in favor of a clearer notation; this is valid because we assume the same behavior

derivatives in (4.1) are replaced by  $-j\omega$ , and the effect of evaluating at  $t_{ret}$  translates into multiplication by a phase factor  $\exp(-jk_0|\mathbf{r} - \mathbf{r}'|)$  with  $k_0 = \sqrt{\epsilon\mu_0}\omega = 2\pi/\lambda$  the wave number and  $\lambda$  the wavelength.

Another important relationship among fields and sources is Ohm's law which states that, in the interior of conductors,  $\mathbf{J}$  is proportional to  $\mathbf{E}$ . The constant of proportionality  $\sigma$  is called the conductivity of the medium,

$$\mathbf{J} = \sigma\mathbf{E} \quad (4.6)$$

With this last expression, the Mixed Potential Integral Equation (MPIE) is reached:

$$\frac{\mathbf{J}(\mathbf{r})}{\sigma} + \frac{j\omega\mu_0}{4\pi} \int_V \mathbf{J}(\mathbf{r}') \frac{e^{-jk_0|\mathbf{r}-\mathbf{r}'|}}{|\mathbf{r}-\mathbf{r}'|} d\mathbf{r}' = -\nabla\phi(\mathbf{r}) \quad (4.7a)$$

$$\frac{1}{4\pi\epsilon} \int_V \rho(\mathbf{r}') \frac{e^{-jk_0|\mathbf{r}-\mathbf{r}'|}}{|\mathbf{r}-\mathbf{r}'|} d\mathbf{r}' = \phi(\mathbf{r}) \quad (4.7b)$$

The common kernel  $\exp(-jk_0|\mathbf{r} - \mathbf{r}'|)/|\mathbf{r} - \mathbf{r}'|$  is the Green function for this problem in the Lorentz gauge.

## 4.2 From the MPIE to a linear system

In addition to the MPIE (4.7), the sources  $\mathbf{J}$  and  $\rho$  are related by the continuity equation:

$$\nabla \cdot \mathbf{J} + \frac{\partial \rho}{\partial t} = 0 \quad (4.8)$$

Charges inside the conductors' volume, in the absence of time-varying external fields, have a time dependence  $\exp(-t/\tau)$ , where  $\tau = \epsilon/(4\pi\sigma)$  is the relaxation time [76]. For good conductors, this is of order  $10^{-18}$  s; consequently, it is safe to assume that, for frequencies in the range 10-1000 GHz, with typical times periods of  $10^{-11} - 10^{-13}$  s, charge inside the conductors' volume is null. However, the same cannot be said for surface charges on the conductors, where there is a discontinuity in the constituent relationships of the materials [77]. Therefore, we impose the absence of volume charge distribution,

$$\nabla \cdot \mathbf{J} = 0 \quad \text{inside the conductors} \quad (4.9)$$

This condition implies a distinction must be made between surfaces of conductors that are properly frontiers and those that are not (see Fig.4.1):

---

for all magnitudes.

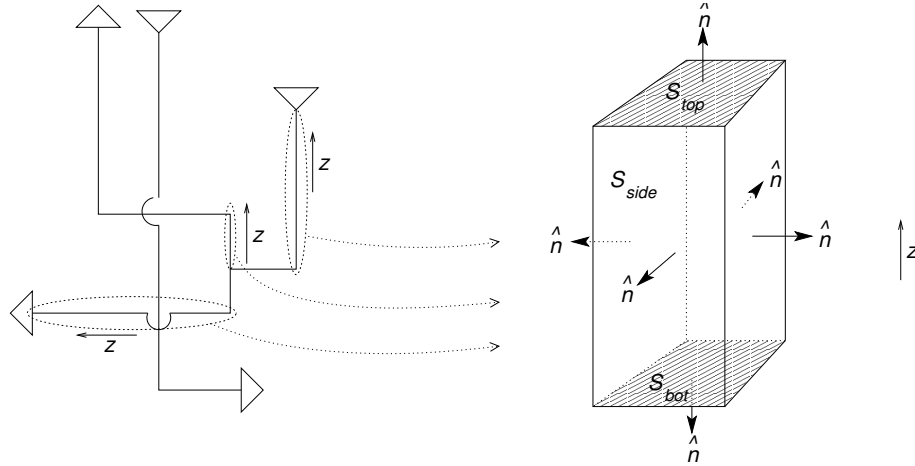


Figure 4.1: Conductors' surface  $S(V)$  with its normal vectors  $\hat{\mathbf{n}}$ , decomposed into two contact surfaces  $S_{top}$  and  $S_{bot}$ , and one non-contact surface  $S_{side}$  composed of four faces (right); these surfaces are determined by the role their electrical placement in the circuit (left).

- **Contact surfaces**, which represent the terminations of the conductors, and are surrounded by conducting material, so that they are effectively in the interior of the conductor; they do not support charge distribution, and they allow for normal current distribution on both sides; in a circuit representation, these surfaces correspond to the ports, where external conditions are imposed, either in the form of voltage or current sources, or as continuity from other conductors;

$$\phi(\mathbf{r}) = \phi_{S_i} \quad \text{on conductors' contact surfaces} \quad (4.10)$$

- **Non-contact surfaces**, on the other hand, are those that face non-conducting material, or materials with very low conductivity; these surfaces contain non-zero charge distributions; the value of this surface charge is not arbitrary: due to the condition  $\rho = 0$  inside the conductor, it is related to the normal component of the current; thus the charge distributions in (4.7b) are in fact surface distributions given by,

$$\mathbf{J} \cdot \hat{\mathbf{n}} = j\omega\rho \quad \text{on conductors' non - contact surfaces} \quad (4.11)$$

In order to approximate a solution to (4.7a) and (4.7b), we adopt the Galerkin method of moments. This is a standard procedure whereby an integral equation is transformed into a linear system [78].

The first step consists in expanding the vector current density  $\mathbf{J}$  and surface charge density  $\rho$ , in terms of two sets of functions  $\mathbf{w}_i(\mathbf{r}), i = 1 \dots n_v$ , defined on the conductors volumes, and

$v_j(\mathbf{r})$ ,  $j = 1 \dots n_s$  defined on the conductors' surfaces,

$$\mathbf{J}(\mathbf{r}) \approx \sum_{j=1}^{n_v} I_j \mathbf{w}_j(\mathbf{r}) \quad \mathbf{r} \in V \quad (4.12a)$$

$$\rho(\mathbf{r}) \approx \sum_{j=1}^{n_s} q_j v_j(\mathbf{r}) \quad \mathbf{r} \in S_{non-contact} \quad (4.12b)$$

To determine the coefficients  $I_i$  and  $q_j$  for these expansions, (4.12) is replaced into (4.7a) and (4.7b). Orthogonality between the residual of this replacement and the basis functions is imposed. These constraints on the inner products with  $\mathbf{w}_i(\mathbf{r})$ ,  $1 \leq i \leq n_v$  for (4.7a), and  $v_j(\mathbf{r})$ ,  $1 \leq j \leq n_s$  for (4.7b), are represented by a  $N^2$  linear system, with  $N \equiv n_v + n_s$ :

$$\left[ \begin{array}{c|c} R + j\omega L & 0 \\ \hline 0 & P \end{array} \right] \begin{pmatrix} I \\ q \end{pmatrix} = \begin{pmatrix} - \langle \mathbf{w}_i, \nabla \phi \rangle \\ \langle v_j, \phi \rangle \end{pmatrix} \quad \left. \begin{array}{l} \} \ n_v \\ \} \ n_s \end{array} \right\} \quad (4.13)$$

with the matrix elements given by:

$$R_{ij} = \frac{1}{\sigma} \int_V \mathbf{w}_i^*(\mathbf{r}) \cdot \mathbf{w}_j(\mathbf{r}) \, d^3r \quad (4.14a)$$

$$L_{ij} = \frac{\mu_0}{4\pi} \int_V \int_V \mathbf{w}_i^*(\mathbf{r}') \mathbf{w}_j(\mathbf{r}) \frac{e^{-jk_0|\mathbf{r}-\mathbf{r}'|}}{|\mathbf{r}-\mathbf{r}'|} \, d^3r \, d^3r' \quad (4.14b)$$

$$P_{ij} = \frac{1}{4\pi\epsilon} \int_S \int_S v_i^*(\mathbf{r}') v_j(\mathbf{r}) \frac{e^{-jk_0|\mathbf{r}-\mathbf{r}'|}}{|\mathbf{r}-\mathbf{r}'|} \, d^2r \, d^2r' \quad (4.14c)$$

and the subindices  $i, j$  ranging from 1 to  $n_v$ , in the first two lines, and from  $n_v + 1$  to  $N$  in the last one. The volume  $V$  is the union of all the conductors' volumes, whereas  $S$  is the set of all the conductors' non-contact surfaces. The inner products appearing on the right hand side (rhs) of (4.13) are given by:

$$\langle \mathbf{w}_i, \nabla \phi \rangle = \int_V \nabla \phi \cdot \mathbf{w}_i^* \, d^3r \quad i = 1 \dots n_v \quad (4.15a)$$

$$\langle v_i, \phi \rangle = \int_S \phi v_i^* \, d^2r \quad i = n_v + 1 \dots N \quad (4.15b)$$

The effectiveness of the method will be assessed by the level of precision obtained in using a relatively small number of functions for each conductor, as well as the difficulty associated

with computing (4.14).

### 4.2.1 Quasi-static approximation

The linear system in (4.13) is coupled through its right-hand-side (rhs). In computational electromagnetics, there is a standard framework known as the quasistatic (QS) limit [79], whose main characteristic is the decoupling of charges and currents in the description of the system. In terms of the unknowns  $q_i, I_i$  for the expansion (4.12), this means splitting the two blocks in (4.13), and solving two different subproblems: the electroquasistatic (EQS) and magnetoquasistatic (MQS). In Table 4.2, we list the main ingredients of each of these type of problems, as well as their relationship to the solution of (4.13).

Table 4.2: Electroquasistatic (EQS) and Magneto-quasi-static (MQS) approximations and relationship to linear system in (4.13)

	EQS	MQS
Principal quantities	$\mathbf{E}, \rho$	$\mathbf{H}, \mathbf{J}$
Approximation	$\nabla \times \mathbf{E} \simeq 0$	$\nabla \times \mathbf{H} \simeq \mathbf{J}$
Typical time scale	$\tau_e \equiv \epsilon/\sigma$	$\tau_m \equiv \mu\sigma d^2$
Example tool	FastCap	FastHenry
Unknowns	$q_i$ in (4.12b)	$I_i$ in (4.12a)
System matrix	Second block in (4.13)	First block in (4.13)
Boundary conditions	$\phi = const$	$\Delta\phi = V_{top} - V_{bot}$
Output	Capacitance $C$	Resistance $R$ , inductance $L$

Once these two incomplete problems have been solved, meaningful quantities (e.g., voltages, currents, noise, delay, etc.) are obtained through a circuit representation involving  $R, L$  and  $C$  elements. Thus in the QS approach, the coupling between  $RL$  effects on one side, and  $C$  on the other, is carried out at a later phase, by a tool that is independent of the solvers<sup>3</sup>. This means that the  $RL$  parameters on one side, and the  $C$  parameters on the other, are computed independently of each other. Full physical meaning of these parameters is recovered after the generation of the complete circuit, combining both magnetic and electric effects and accounting for displacement currents.

Under which conditions is this decomposition valid? The answer to this question is problem dependent; there is no general rule that can be applied to every problem.

Physically, we must analyze the different time scales involved in the problem. For EQS fields, these are given by the charge relaxation time  $\tau_e \equiv \epsilon/\sigma$ ; for MQS, the characteristic times

<sup>3</sup>Relating to the general flow in Fig. 1.1 described in the Introduction, this task is done either by a circuit simulator or a model order reduction tool.

result from solutions to diffusion equation for currents in a conductor,  $\tau_m \equiv \mu\sigma d^2$ , where  $d$  is a typical dimension of the system [79]. The two problems can be treated independently as long as both of these time scales are small compared to the time scales for full electromagnetic fields,  $\tau_{em} \equiv 1/\omega$ . In other words, as long as it is valid to consider the sources of the “other” problem as stationary, we may neglect their time derivatives (see second line in Table 4.2). Thus, the quasi-static assumption is a high- $\tau_{em}$  / low frequency regime.

Conditions of validity for the QS decomposition can also be analyzed in terms of length scales, related to the essential difference between the two boundary conditions in the MQS and EQS problems (see Table 4.2). As long as the dimensions of these two problems are electrically small, these differences are not relevant in the results of the simulation. Quantitatively, electrically small refers to the typical spacial variations for electromagnetic fields in the surrounding medium<sup>4</sup>, of order  $\lambda$ . Here, the quasistatic assumption is a short-conductor, or long-wavelength, limit.

Within this nearly infinite wavelength approximation  $\lambda \gg \ell$  (with  $\ell$  the conductor’s length) it is admissible to replace the phase factors by 1 inside the integrals in (4.14), an assumption that is very practical in terms of computational cost (see following Chapter).

#### 4.2.2 *RLC* mixed representation

If the quasistatic approximation is not used, then it is possible to derive a system of equations that retains the coupling between (4.7a) for currents and (4.7b) for charges. Our goal in this section is to reduce the linear system on (4.13) expressing the unknowns solely in terms of currents. The corresponding charge unknowns will be related to the previous ones through the continuity condition. To this effect, we start from Green’s theorem:

$$\oiint_{S(V_i)} \mathbf{F} \cdot \hat{\mathbf{n}} \, d^2r = - \int_{V_i} \nabla \cdot \mathbf{F} \, d^3r \quad (4.16)$$

with  $S(V_i)$  a closed surface that encloses volume  $V_i$  (a single conductor) and we use it on  $\mathbf{F} = \phi \mathbf{w}_i^*$ . We then use the identity  $\nabla \cdot (\phi \mathbf{u}) = \mathbf{u} \cdot \nabla \phi + (\nabla \cdot \mathbf{u})\phi$  to obtain,

$$\oiint_{S(V_i)} (\mathbf{w}_i^* \cdot \hat{\mathbf{n}}) \phi \, d^2r + \int_{V_i} \mathbf{w}_i^* \cdot \nabla \phi \, d^3r + \int_{V_i} (\nabla \cdot \mathbf{w}_i^*) \phi \, d^3r = 0 \quad (4.17)$$

We use divergence-free functions  $\mathbf{w}_i$ , as demanded by the continuity equation inside the volume, thus the last term in (4.17) vanishes. The first integral in the last expression is decomposed

<sup>4</sup>Inside the conductors, the length scales are given by the decay of fields/currents in the interior, and the distribution of charges on the surface; the first one is given by the skin depth  $\delta$  (see (4.21)) and the second one depends on the shape of the surface. The capacity to capture these scales depends on the precision level for the solution of each of the decomposed problems (*RL* and *C*), and not on the QS decomposition itself.

into integrals over the two contact surfaces  $S_{top}$ ,  $S_{bot}$  plus the integral over the side walls  $S_{side}$  (non-contact surfaces, see Fig.4.1). On the side walls, we adopt the following choice for  $v_i$  to describe the surface charge distribution functions:

$$v_i = \mathbf{w}_i \cdot \hat{\mathbf{n}} \quad \text{On side face } S_{side} \quad (4.18)$$

resulting in  $n_v = n_s$  and

$$\int_{V_i} \mathbf{w}_i^* \cdot \nabla \phi \, d^3\mathbf{r} + \sum_{sides} \int_{S_{side,i}} v_i^* \phi \, d^2r = \int_{S_{top,i}} (\mathbf{w}_i^* \cdot \hat{\mathbf{n}}) \phi \, d^2r + \int_{S_{bot,i}} (\mathbf{w}_i^* \cdot \hat{\mathbf{n}}) \phi \, d^2r \quad (4.19)$$

The left hand side on this last expression is the sum of the two right hand sides of (4.13), which we replace by the respective left hand sides.

Consistency between the continuity conditions (4.9)-(4.11) and this choice of functions  $v_i$  in (4.18) implies that the values  $q_i$  in the solution must be such that  $j\omega q_i = I_i$ .

As to the rhs of (4.19), the factors  $\mathbf{w}_i \cdot \hat{\mathbf{n}}$  act as weights for the average potential on each contact surface. On each of these, we identify the average potential with the excitation voltage on that end of the conductor. Between the two terms in the rhs of (4.19), there is a difference of sign given by the orientation of the normal vectors (see Fig.4.1); there also is a factor identical to the  $z$ -dependence  $f_i(z)$  of the  $z$  component for the function  $\mathbf{w}_i(\mathbf{r})$ . Thus we obtain the following equation for the system:

$$\left[ R + j\omega L + \frac{P}{j\omega} \right] \begin{pmatrix} I \end{pmatrix} = \begin{pmatrix} \Delta \tilde{V} \end{pmatrix} \quad (4.20)$$

with  $(\Delta \tilde{V})_i = f_i(\ell_i)V_{f,i} - f_i(0)V_{0,i}$

with the size of the system being  $n \times n$ . This equation, with the matrix elements defined in (4.14), is the basis of the *RLC* formulation for extraction.

### 4.3 Definition of conduction mode functions

The conduction modes are eigenfunctions of the homogeneous vector Helmholtz equation that the current density  $\mathbf{J}$  satisfies inside the conductors.

$$(\nabla^2 + \kappa^2)\mathbf{J}(\mathbf{r}) = 0 \quad (4.21)$$

$$\text{with } \kappa^2 = -k_0^2 + \frac{j}{\delta^2}, \quad \delta = \sqrt{\frac{2}{\omega\mu\sigma}}$$

where we have introduced the skin depth  $\delta$ , which is the fundamental length scale for penetration currents and fields inside a conductor [46, 76]. We emphasize its frequency dependence,  $\delta \sim f^{-1/2}$ : fields penetrate less as frequency is increases.

Equation (4.21) is the differential form of (4.7). We will now introduce solutions to this equation, and the conditions that must be imposed on them, that constitute the expansion functions for the conduction modes formalism. We distinguish between the *RL* special case, presented in [32], and the *RLC* general one, which we have presented in [33].

### 4.3.1 *RL* functions

In the *RL* version of conduction modes, as published in [32], currents are assumed to be unidimensional, with their spacial variation independent of the current direction. In other words:

$$\mathbf{J}(\mathbf{r}) = J_z(x, y)\hat{\mathbf{z}} \quad (4.22)$$

Furthermore, this method is developed under the *MQS* hypothesis, in which it is valid to decouple the *RL* and *C* problems; for its validity,  $\lambda_{min} \gg \ell \iff k_0d \ll 1$  must hold for all dimensions  $d$  in the problem. This last condition allows for setting  $k_0 = 0$  in the integrals (4.14b), thus simplifying enormously their computation (details of this procedure are the subject of the following chapter).

The *RL* conduction mode eigenfunctions of (4.21) are:

$$\mathbf{w}_i(\mathbf{r}) = \begin{cases} \hat{\mathbf{z}}A_i e^{-[\alpha_i(x-x_i)+\beta_i(y-y_i)]} & \text{if } \mathbf{r} \in V_{n_i} \\ 0 & \text{else} \end{cases} \quad (4.23)$$

with

$$\alpha_i^2 + \beta_i^2 = -\left(\frac{2\pi}{\lambda}\right)^2 + \left(\frac{1+j}{\delta}\right)^2 \quad (4.24)$$

and  $x_i, y_i$  indicate the corner, on the cross section, from which the conduction mode decays. Since  $\delta \ll \lambda$ , one can neglect<sup>5</sup> the first term in the rhs of (4.24). For the rhs of (4.13), the above assumptions lead to:

<sup>5</sup>For the 10-100 GHz range, and typical materials,  $\lambda$  is in the *mm* to *cm* scale, and  $\delta$  is of order  $1\mu\text{m}$ .

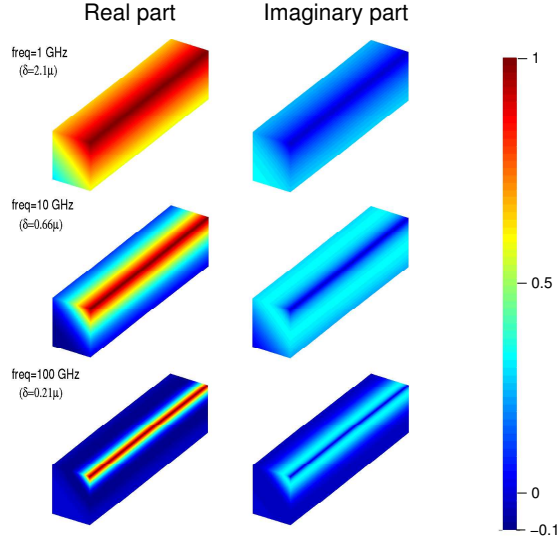


Figure 4.2: Distribution of currents for a corner  $RL$  conduction mode, for a wire of dimensions  $1\mu \times 1\mu \times 50\mu$  and the frequencies such that the skin depth is larger, comparable and smaller than the cross-sectional dimensions (color scale is normalized so that the maximum of current is 1 for each frequency).

$$\langle \mathbf{w}_i, \nabla \phi \rangle = \int_{V_i} \frac{\partial \phi(z)}{\partial z} w_i^*(x, y) d\mathbf{r} = \int_{V_i} \frac{\partial \phi}{\partial z} dz = \phi(L) - \phi(0) = \Delta V \quad (4.25)$$

with the normalization  $\int w_i(x, y) dx dy = 1$  over the cross section of the conductor. Either  $\alpha_i$  or  $\beta_i$  can be zero, in which case we speak of a side mode. In Fig. 4.2 we show the current distributions for a corner conduction mode.

Although (4.24) allows for an infinite number of solutions, the purpose of this method is to show that using only a few is sufficient to accurately represent current redistributions. The author in [16] obtains the same accuracy, for  $RL$  effects in the regime of small penetration  $\delta$ , using 3 modes per conductor, as the one obtained with 252 filaments. In this sense, the  $RL$  conduction modes is an efficient replacement for filament-based methods like FastHenry, which adopt the same conditions (4.22).

### 4.3.2 $RLC$ functions

For the coupled  $RLC$  mixed representation shown in section 4.2.2, we introduce a broader set of eigenfunctions to the vector Helmholtz equation, as compared to the  $RL$  case of the previous section. Given that the equation separates in cartesian coordinates the extension is straightfor-

ward:

$$\mathbf{w}_i(\mathbf{r}) = \begin{cases} (a_{xi}\hat{\mathbf{x}} + a_{yi}\hat{\mathbf{y}} + a_{zi}\hat{\mathbf{z}})e^{-[\alpha_i(x-x_i)+\beta_i(y-y_i)]+\eta_i(z-z_i)} & \text{if } \mathbf{r} \in V_{n_i} \\ 0 & \text{else} \end{cases} \quad (4.26)$$

with

$$\alpha_i^2 + \beta_i^2 + \eta_i^2 = -\left(\frac{2\pi}{\lambda}\right)^2 + \left(\frac{1+j}{\delta}\right)^2 \quad (4.27)$$

Enforcing the continuity condition (4.9) leads to,

$$a_{xi}\alpha_i + a_{yi}\beta_i + a_{zi}\eta_i = 0 \quad (4.28)$$

This last condition restricts the spatial direction for basis functions  $\mathbf{w}_i$

$$(a_{xi}, a_{yi}, a_{zi}) = A_i \left( \frac{1}{\alpha_i}, \frac{1}{\beta_i}, -\frac{2}{\eta_i} \right) + B_i \left( \frac{1}{\alpha_i}, -\frac{1}{\beta_i}, 0 \right) \quad (4.29)$$

for arbitrary  $A_i, B_i$  complex numbers.

The direction of the second vector in the rhs of (4.29) represents solutions with no current flow along the  $z$  axis, direction of the applied gradient of the potential. These solutions carry no net charge, and represent redistribution of currents along the cross section of a conductor. We neglect their contribution, and keep only a vector that is perpendicular to it<sup>6</sup>.

We thus determine the *RLC* conduction modes, up to an arbitrary normalization constant  $A_i$ . In order to normalize the basis functions, we impose that the total current entering the conductor at the bottom face be represented as the sum of all the coefficients in (4.12) corresponding to that conductor  $I_{conductor\ k} = \sum_{i \in k} I_i$ .

This choice fixes the arbitrary constant remaining in (4.29) :

$$(a_{xi}, a_{yi}, a_{zi}) = \left( \frac{\alpha_i}{e^{\alpha_i w_i} - 1} \right) \left( \frac{\beta_i}{e^{\beta_i h_i} - 1} \right) \left( \frac{j\delta^2 \eta_i \alpha_i}{2}, \frac{j\delta^2 \eta_i \beta_i}{2}, 1 \right) \quad (4.30)$$

with  $w_i$  and  $h_i$ , the width and thickness of the conductor, respectively. In general, a conduction mode will have both  $\alpha_i, \beta_i \neq 0$ , and we will refer to it as a corner mode. If one of these parameters is zero, we will call it a side mode, as in the *RL* case. If, for example,  $\alpha_i = 0$ , then the first fraction in the expression above should be replaced by  $w_i^{-1}$ . Likewise, the second fraction is replaced by  $h_i^{-1}$  ( $\alpha_i$  and  $\beta_i$  cannot both be zero due to (4.24)).

For every current conduction mode  $\mathbf{w}_i$ , there is a corresponding surface charge function  $v_i$  computed using (4.18). The link between the charge and current distribution functions arises

---

<sup>6</sup>An analysis of the significance of this assumption is left for Section 6.4, in which we discuss limitations and possible extensions of our present formulation.

solely from the continuity conditions and the properties of good conductors. This link represents numerically the coupling between *RL* and *C* effects within the full *RLC* representation. In the present work, we have used a particular set of these *RLC* modes, which we denominate quasi-TEM. Physical details concerning this choice is the subject of the following section. In few words, these modes are appropriate for a certain type of geometry. A discussion on the limitations of this choice of modes, as well as the effects of using a larger set of modes, is included in Section 6.4.

## 4.4 *RLC* conduction modes and TEM waves

In many applications, we are concerned with the problem of extracting *RLC* parameters for configurations that are long wires with electrically small cross-sectional dimensions. These type of structures are found, for example, in clock-tree designs [5, 80]. The parameters we extract will often be used in transmission line (TL) models, or else in a distributed lumped model approximation to TL. We refer to these long (comparable to a wavelength) and thin (of the order of the skin depth) structures as TL-like structures. In this section, we discuss which values of conduction mode parameters are compatible with this description.

### 4.4.1 TEM fields and transmission line behavior

Transverse Electromagnetic (TEM) waves are the dominant propagation mode of fields, for transmission line structures [81]. The main characteristic of these waves is that the electric and magnetic components of the field lie in the plane orthogonal to the direction of propagation, and are orthogonal to each other [46]. TEM propagation relies on the following assumptions [4]:

1. wires are perfect conductors;
2. very long wires, with symmetry along the corresponding axis;
3. homogeneous medium surrounding the conductors;
4. small transverse dimensions;

Variations from these conditions induce non-TEM modes; analytical studies of these high-order terms are found in [82–85]. For the TL-like structures defined above, conditions 1 and 2 are met approximately, whereas we assume 3 and 4 to be valid. Therefore we expect to have quasi-TEM behavior for the waves in the medium. In chapter 6, we will discuss the necessary amendments to our formulation in order to capture non-quasi-TEM responses.

In the TEM treatment of transmission lines, the conditions above simplify the relationship between the capacitance and inductance matrix, setting  $LC = (\mu\epsilon)^{-1} = c^2$ . In fact, the perfect-conductor assumption must be dropped, in order to allow for bounded currents to flow along

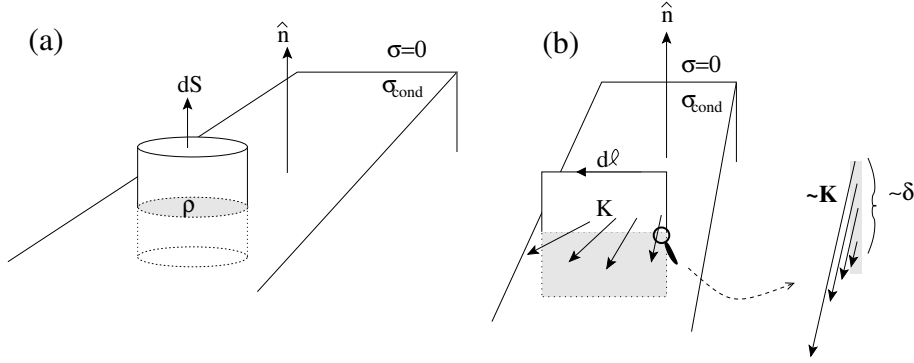


Figure 4.3: Geometry for the analysis of fields at the boundary between conducting and non-conducting media (non-contact surfaces).

the  $z$ -axis. Physical contradictions are avoided by including an *ad-hoc* (small) resistance-per-unit length to describe ohmic losses, but neglecting the effect that these voltage drops have in “bending” the fields. Refer to the discussion on pp 28-9 and 46 of [4], and references therein, for a detailed discussion of the assumptions of transmission line analysis.

#### 4.4.2 Boundary conditions for conduction modes

In any integral method-of-moments approach, EM waves in the medium are not explicitly modeled. Instead, these are determined by the boundary conditions on the non-contact surfaces. To compute the normal component of the fields at the boundaries of the medium surrounding the conductors, consider an infinitesimally small cylinder on the frontier, use Maxwell’s divergence laws and Gauss’s theorem, in order to relate the flux of the fields through the cylinder’s lids with the charge inside the cylinder 4.3a; for the tangential components, a similar procedure is carried out for a small rectangle, using Maxwell’s curl laws and Stokes’ theorem 4.3b.

$$\begin{aligned} (\mathbf{D}^{(out)} - \mathbf{D}^{(in)}) \cdot \hat{\mathbf{n}} &= \rho & (\mathbf{E}^{(out)} - \mathbf{E}^{(in)}) \times \hat{\mathbf{n}} &= 0 \\ (\mathbf{B}^{(out)} - \mathbf{B}^{(in)}) \cdot \hat{\mathbf{n}} &= 0 & (\mathbf{H}^{(out)} - \mathbf{H}^{(in)}) \times \hat{\mathbf{n}} &= \mathbf{K} \end{aligned} \quad (4.31)$$

where  $\hat{\mathbf{n}}$  is the unit normal vector pointing from the conductor into the medium, and  $\rho$  and  $\mathbf{K}$  is the superficial charge and current at the discontinuity, respectively.

The tangential component of the electric field is continuous,

$$\mathbf{E}_{\parallel}^{(out)} = \mathbf{E}_{\parallel}^{(in)} = \frac{\mathbf{W}_{\parallel}}{\sigma} \quad (4.32)$$

On the other hand, the normal component of  $\mathbf{E}$  has a discontinuity due to the surface charge

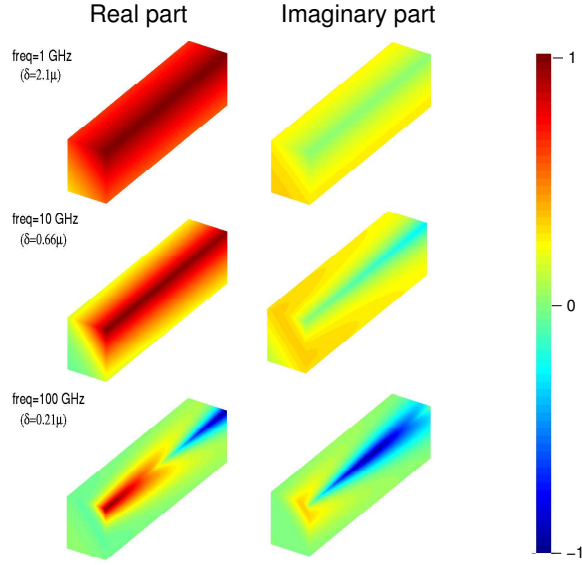


Figure 4.4: Distribution of currents for a corner *RLC* conduction mode, for a wire of dimensions  $1\mu \times 1\mu \times 1500\mu$  and at frequencies such that the skin depth is larger, comparable and smaller than the cross-sectional dimensions (color scale is normalized so that the maximum of current is 1 for each frequency).

distribution. Assuming there is no change in  $\epsilon$  across the surface,

$$\begin{aligned} \mathbf{E}_{\perp}^{(\text{in})} &= \sigma^{-1} \mathbf{w}_{\perp} \\ \mathbf{E}_{\perp}^{(\text{out})} &= \frac{\rho}{\epsilon} - \sigma^{-1} \mathbf{w}_{\perp} \end{aligned} \quad (4.33)$$

As to the magnetic induction  $\mathbf{B}$ , all components are continuous across the non-contact surface, since the modes  $\mathbf{w}_i$  in our model are volume currents, and not superficial<sup>7</sup>.

#### 4.4.3 Conduction mode parameters and quasi-TEM fields

In [33], we presented an implementation of the *RLC* conduction mode formalism. Therein, we adopted a particular choice of modes:

<sup>7</sup>Surface currents exist for the limiting case  $\sigma \rightarrow \infty$  (or  $\omega \rightarrow \infty$ ), in which  $\delta \rightarrow 0$ ; for real situations, there is a sharp exponential attenuation of the volumetric currents inside the conductor, over a length scale of  $\delta$ . If  $\delta$  is small enough, this can be viewed as an equivalent surface current  $\mathbf{K}_{\text{eff}} = \int \mathbf{J} dn$ , leading to a discontinuity in the tangential magnetic field [46]. These deviations from perfect conductivity are precisely the object of the CM model.

$$\begin{aligned}\eta_i &= \pm j \frac{2\pi}{\lambda} \\ \alpha_i^2 + \beta_i^2 &= \left( \frac{1+j}{\delta} \right)^2\end{aligned}\quad (4.34)$$

From a practical point of view, when selecting  $\alpha, \beta, \eta$  in (4.27) we no longer neglect the  $(2\pi/\lambda)^2$  term in the rhs, as was done in (4.24) for *RL/MQS*, since we are modeling dimensions comparable with the wavelength  $\lambda$ . We associate the  $\lambda$  scale in (4.34) with the  $z$  dependence. This particular choice stems from the observation that for realistic configurations, the wire length is the only length scale that can be comparable to the wavelength, while the wire cross sections are much smaller than  $\lambda$ , making  $\lambda$ -sensitivity in  $x$  or  $y$  unnoticeable.

The resulting picture is: we represent the  $\delta$ -order exponential current crowding, common to the *RL* conduction modes, along the current cross-sectional dimensions; and a sinusoidal  $\lambda$ -order wave traveling on the  $z$ -axis (the different signs in (4.34) correspond to forward- and backward-traveling waves). A schematic of these functions is shown in Fig. 4.4.

We will now show that, for this particular choice of  $(\alpha, \beta, \eta)$ , the fields at the boundaries of the conductors are quasi-TEM. In other words, we want to analyze the ratios of the electric  $\mathbf{E}^{(out)}$  and magnetic  $\mathbf{H}^{(out)}$  fields on the non-conducting side of the surface in Fig. 4.3

Consider, without loss of generality, the non-contact surface along perpendicular to the  $x$ -direction,  $\hat{\mathbf{n}} = \hat{\mathbf{x}}$ , so that in the medium neighboring the conductors:

$$\begin{aligned}E_z|_{x=0}^{(out)} &= \frac{w_z}{\sigma} \\ E_y|_{x=0}^{(out)} &= \frac{w_y}{\sigma} = \frac{j\delta^2\eta\beta w_z}{2\sigma} = O\left(\frac{\delta}{\lambda}\right) \frac{w_z}{\sigma} \\ E_x|_{x=0}^{(out)} &= \frac{\rho}{\epsilon} - \frac{w_x}{\sigma} = -\left(\frac{2}{\omega\epsilon} - \frac{1}{\sigma}\right)\delta^2\eta\alpha w_z = \left(O\left(\frac{\delta}{\lambda}\right) + O\left(\frac{\lambda}{\delta}\right)\right) \frac{w_z}{\sigma}\end{aligned}\quad (4.35)$$

where we have used our choice of modes (4.34) in order to express the order-of-magnitude of the  $E_y$  and  $E_x$  fields. Given that  $\lambda \gg \delta$ , we can say that

$$\left| \frac{E_{long}^{(out)}}{E_{trans}^{(out)}} \right| = \left| \frac{E_z}{\sqrt{E_x^2 + E_y^2}} \right| = O\left(\frac{\delta}{\lambda}\right) \ll 1 \quad (4.36)$$

i.e., the TEM conditions are nearly satisfied.

The longitudinal magnetic field  $H_z$  vanishes inside the conductor, independently of the choice (4.34). This can be seen by taking the curl of the electric field, which is proportional to the current  $\mathbf{w}$  in (4.30),

$$\mathbf{B}^{(in)} = \frac{j\mu}{\omega} \left( \nabla \times \frac{\mathbf{W}}{\sigma} \right) = \frac{(2j + \delta^2 \eta^2) w_z}{2\omega\sigma} (\beta, -\alpha, 0) \quad (4.37)$$

Given the continuity of the magnetic field at the non-contact surface,  $B_z^{(out)}$  must also vanish. This states that the small non-TEM effects modeled with the present formalism are in fact transverse electric (TE) modes. For perfect conductors, the  $\delta$ -thick current distribution reduces to a superficial current  $\mathbf{K}$  (see footnote page 89 and inset Fig.4.3). Then there is a jump in the tangential magnetic field which is mainly oriented on  $y$ , because the  $\mathbf{K}$  runs mainly on the  $z$  axis ( $w_z \gg w_y$ ).

Variations from (4.34) for the choice of conduction mode parameters are discussed in Section 6.4. Basically, more modes introduce degrees of freedom which are expected to be negligible for transmission line type of configurations.

Another important issue is the choice of  $\alpha$  and  $\beta$  for any given geometry. It is evident that the second line in (4.34) has an infinite number of solutions. For every conductor, there are four side modes, as well as a continuum of corner modes. Our aim is to choose a subset of these solutions such that they capture the behavior of currents and charges in the conductors. The number of modes in this subset is a trade-off between precision and performance. We will show that four side modes, and eventually four corner modes at  $45^\circ$ , are sufficient for a variety of configurations.

## 4.5 Solvers

We now consider the rhs of equation (4.20). In Section 4.2.2 this array is defined as the difference between the average potential, multiplied by a factor representing the  $z$ -dependence, on each contact surface. For the quasi-TEM modes of (4.34), this factor is a phase  $\exp(\pm jk_0 \ell)$ .

For a given geometry, the rhs of this equation contains the information on how the wires are connected. As such, we could say that the "circuit analysis" is contained in the rhs. We will discuss, in the first subsection, how to obtain the most general information available, which is the admittance matrix among the wires. In most cases, the interest is to obtain a reduced amount of information. The other subsections will focus on two such cases. Similar approaches to the ones exposed therein, can be adopted for any particular circuit topology. A general treatment demands implementation of nodal or mesh analysis, as in FastHenry or FastMaxwell.

For matrix solvers, we use standard LU Decomposition adapting the algorithm in [86] to complex algebra. We recall that the main feature of the conduction modes method is that of producing representations significantly smaller, and with the same modeling capacity, than the piecewise-constant counterparts. In this sense, the choice of matrix solver is not a critical one: savings result from having smaller systems for the same problem.

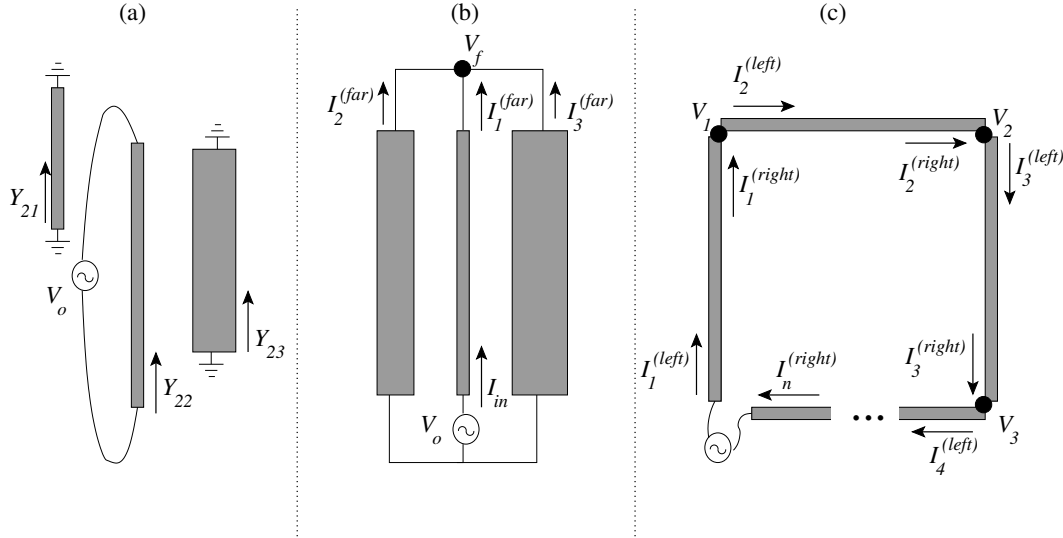


Figure 4.5: Different solution schemes for different types of problems: (a) admittance matrix calculation; (b) shorted transmission line; (c) serial circuit.

In the examples analyzed, solving the linear system entails a cost no larger than 1% of the total. The main component of computation cost is always in the filling of the matrix, a subject that will be thoroughly analyzed in the next two chapters.

#### 4.5.1 Admittance matrix

In the most general case, we are interested in obtaining the admittance matrix  $\mathbf{Y}$ , i.e. an  $n \times n$  array with  $n$  the number of conductors, representing the electromagnetic interaction between conductors. The elements  $Y_{ik}$  are defined as the current on conductor  $i$  when conductor  $k$  is subject to a unitary voltage drop and all others are grounded at both ends:

$$Y_{ik} = \sum_{p \in \text{cond}_i} I_p^{(k)}; \quad \mathbf{I}^{(k)} = \mathcal{Z}^{-1} \mathbf{B}^{(k)}; \quad B_i^{(k)} = \begin{cases} 1 & \text{if } i \in \text{cond}_k \\ 0 & \text{else} \end{cases} \quad (4.38)$$

where  $\mathcal{Z}$  is the conduction modes matrix, given by the first block of (4.13) for *RL/MQS*, and by (4.20) for *RLC*.

From the admittance matrix, all relevant magnitudes (impedance, S-parameters, etc.) can be computed through elementary circuit theory. For example, in the *RL/MQS* implementation, the currents at both ends of a conductor are identical, and we can refer unequivocally to the current along a conductor. In this case, the impedance matrix is,

$$\mathbf{Z}^{(MQS)} = \left( \mathbf{Y}^{(MQS)} \right)^{-1}$$

In words, the element  $Y_{ik}$  is the total current on conductor  $k$  when conductor  $i$  is excited by a voltage source between its contact surfaces, and all the others are grounded at both ends (see Fig. 4.5a). For the *RLC* problem, currents at opposite ends do not coincide, so that both input and output admittance/impedance matrices can be defined, according to whether the currents are excitations are considered at the near or the far end. The currents at the far end are multiplied by the  $f_i(\ell)$ , representing the  $z$ -dependence of the conduction modes (see eq.(4.20)).

### 4.5.2 Shorted transmission line

Now we study a commonly encountered situation in extraction, namely a configuration as in a bundle (see Section 2.2)<sup>8</sup>, in which the  $n$  wires are composed of one signal wire plus  $n - 1$  return paths, such that all wires are shorted at the far end, the return paths are shorted at the near end, and the source is placed between this node and the near end of the signal. For quasi-TEM conduction modes, this kind of configuration represents a shorted transmission line, as in Fig.4.5b.

The impedance of this shorted circuit is defined as  $V_o/I_{in}$ , with  $I_{in}$  the total current at the shorted (far) end of the signal and  $V_o$  is the amplitude of the voltage source at the open (near) end. We point out that there exist a plethora of different magnitudes to be computed, according to how the conductors and source(s) are connected, as well as the location of the ports (i.e., where are the currents to be extracted). We show the example of the shorted T-line, as it is a common case in the literature, but a scheme similar to the one exposed in this section can be effortlessly devised for any arbitrary circuit.

In this case, we have  $N + 1$  unknowns, given by the  $N$  conduction mode currents, plus the unknown potential  $V_f$  at the far end. The extra equation is Kirchoff's law at the far end,

$$\sum_{i=1}^N I_i^{(far)} = 0 \quad (4.39)$$

Although this solution can be computed from the impedance matrices in the previous section, it is more efficient to write a specific system for this circuit,

$$\mathcal{Z}\mathbf{I} = V_f \mathbf{B}^{(far)} - V_o \mathbf{B}^{(near)}; \quad B_i^{(far)} = e^{n_i \ell_i}; \quad B_i^{(near)} = \begin{cases} 1 & \text{if } i \in \text{cond}_1 \\ 0 & \text{else} \end{cases} \quad (4.40)$$

Thus, we can solve two systems (as opposed to  $n$ , if we were to generate the whole impedance matrix) with the same matrix  $\mathcal{Z}$ , and then impose the Kirchoff condition:

<sup>8</sup>In Sec. 2.2, we considered the *RL* version of bundles; the only difference for *RLC* is that the currents are not constant along the  $z$  axis.

$$\begin{cases} \mathbf{I}^{(far)} = \mathcal{Z}^{-1} \mathbf{B}^{(far)} \\ \mathbf{I}^{(near)} = \mathcal{Z}^{-1} \mathbf{B}^{(near)} \\ \mathbf{I} = V_f \mathbf{I}^{(far)} - V_o \mathbf{I}^{(near)} \end{cases} \Rightarrow V_f = \frac{\sum_{i=1}^N I_i^{(far)}}{\sum_{i=1}^N I_i^{(near)}} V_o \quad (4.41)$$

Once  $V_f$  is determined, we obtain the currents  $I_i$ , enabling us to determine the total current for any conductor.

This kind of solution scheme, translated to the  $RL/MQS$  domain, is precisely what is referred to in Section 2.2 for solving the self inductance of a bundle, (2.11), and obtaining the coefficients in (2.12) proportional to the participation of each return wire in the total current.

### 4.5.3 Serial circuit / inductors

Another particular case of interest is that where all conductors form a serial circuit, as in an intentional inductor. Again, this example can be computed from the admittance matrices in Section 4.5.1, but this would imply the solution and storage of unwanted quantities.

As in the previous case, we concentrate on the input impedance, i.e. the ratio  $V_o/I_{in}$ , where now  $I_{in}$  represents the current at the open end of the first segment of the inductor.

For an inductor, we have to impose a Kirchoff law (4.39) at each node of the inductor. The voltages of all the intermediate nodes are the added unknowns (see Fig.4.5c). In each node with voltage  $V_i$ , we must cancel the right current  $I_i^{(right)}$  of the previous segment with the left current  $I_{i+1}^{(left)}$  of the following segment. Each of these currents is the sum of the contributions of all the modes for that segment. For segment  $i$ , the charge  $q_i$  on its non-contact surfaces results from the displacement current  $I_i^{(disp)}$ , which is the difference between the longitudinal currents at the two extremes:  $j\omega q_i = I_i^{(disp)} = I_i^{(right)} - I_i^{(left)}$ .

We avoid the tedious algebra and give a recipe to solve this problem:

1. Solve, for each  $k = 0, 1, \dots, n$

$$\mathbf{H}^{(k)} = \mathcal{Z}^{-1} \mathbf{B}^{(k)}; \quad B_i^{(k)} \equiv \begin{cases} e^{\eta_i \ell_i} & \text{if } i \in \text{cond}_k \\ -1 & \text{if } i \in \text{cond}_{k+1} \\ 0 & \text{else} \end{cases} \quad (4.42)$$

2. Construct the matrices  $\mathbf{A}, \mathbf{C} \in \mathbb{C}^{n \times n}$ ,

$$A_{ik} \equiv \sum_{m \in \text{cond}_i} H_m^{(k)}; \quad C_{ik} \equiv \sum_{m \in \text{cond}_i} H_m^{(k)} e^{\eta_m \ell_m} \quad (4.43)$$

for  $i, k = 1, \dots, n$ , as well as the vectors  $\mathbf{J}$  and  $\mathbf{K}$  which correspond to setting  $k = 0$  in the above definitions,

$$J_i \equiv A_{i0}; \quad K_i \equiv C_{i0} \quad (4.44)$$

3. Define the incidence matrix  $\mathbf{M} \in \mathbb{R}^{n-1 \times n}$ , whose elements are given by  $M_{ik} = \delta_{i-1,k}$ <sup>9</sup>, and use this matrix to construct,

$$\mathbf{Y} \equiv [\mathbf{E}_1 | \mathbf{C} - \mathbf{M}\mathbf{A}] \in \mathbb{C}^{n \times n} \quad (4.45)$$

with  $\mathbf{E}_1$  the first column of the identity matrix.

4. Solve the matrix equation,

$$\mathbf{Y}\tilde{\mathbf{V}} = -(\mathbf{C} - \mathbf{M}\mathbf{A}) \quad (4.46)$$

where  $\tilde{\mathbf{V}} \in \mathbb{C}^n$  is a vector whose first element is  $y_{in}$ , the left current entering segment 1, and the rest of the elements are the voltages of the intermediate nodes,  $\tilde{V}_i = V_{i+1}$ ,  $i = 2, \dots, n$ .

5. Obtain the closed-end input impedance of the inductor:

$$Z = \frac{1}{y_{in}} = \frac{1}{\tilde{V}_1} \quad (4.47)$$

The above procedure can be trivially modified if we wish to compute other magnitudes, e.g. open-ended impedance, or output instead of input impedance. With this recipe, we are able to account for *RLC* effects for inductors, with a cost of solving  $n$  systems with the same matrix of size  $N$  (i.e., we need only repeat the back-substitution, and not the decomposition), plus one more solve of size  $n$ .

## 4.6 Code organization: global structure

Development of the algorithm for the methods exposed in this chapter has been the major effort of the present work. Although this code has undergone several different iterations, it has always maintained the structure shown in the flowchart in Fig.4.6.

The components of this code are:

- Input: we can either run the tool as a stand-alone or integrated into the Calibre xRC/xL family; in either case, we receive information on the geometry of the wires (widths,

---

<sup>9</sup> $\delta_{ik}$  here represents the Kronecker symbol, equal to 1 if  $i = k$ , and 0 if they are different.

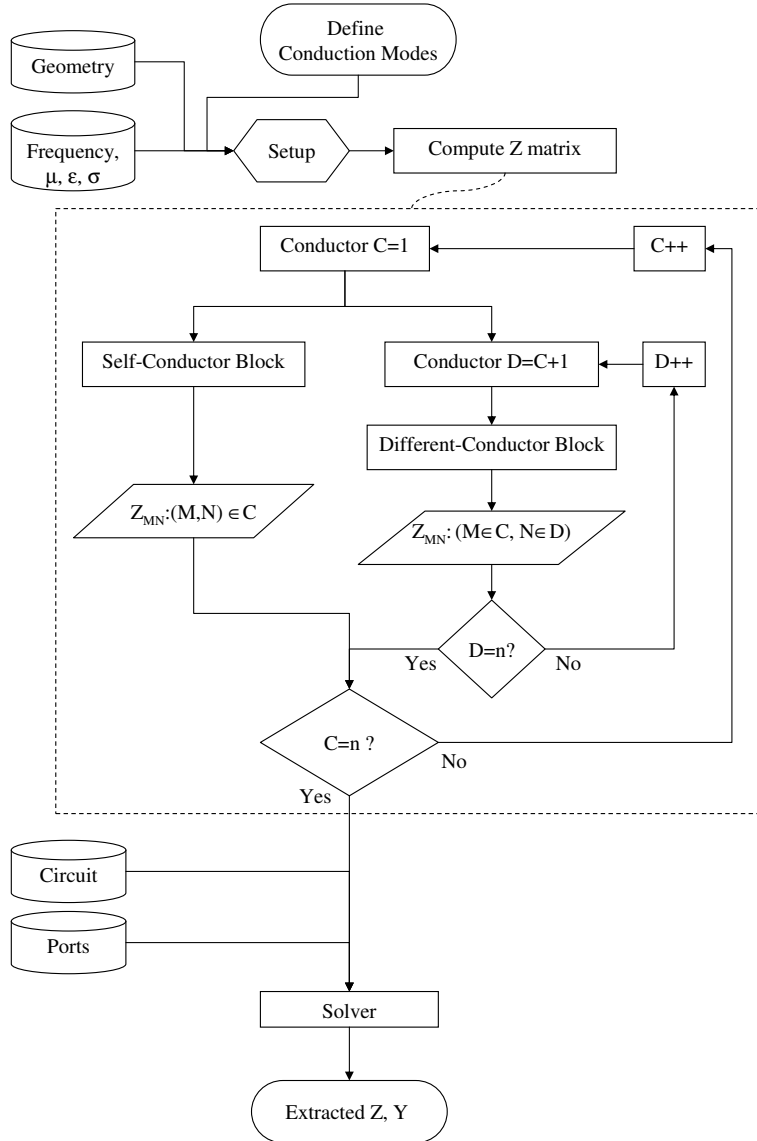


Figure 4.6: Conduction modes flow.

lengths, thicknesses, and relative positions); and the electrical parameters (frequency, conductivities  $\sigma$ , electrical permittivities  $\epsilon$ , magnetic permeabilities  $\mu$ ).

- Setup: the method begins by determining which conduction modes are to be created; and allocating space, establishing magnitudes which will be used throughout (e.g. reading or calculating the Gaussian quadratures).
- Matrix calculation: this is the most intensive part of the calculation, in which we construct the  $\mathcal{Z}$  matrix for the conduction modes; in this flow we only sketch the loops involved, and refer to next chapter for details on this calculation (see Figs.5.7,5.8).
- Solve: the final step is solving the system, as shown in Section 4.5, in order to determine the conduction mode current and thus the electrical parameters; for this step, we need further information concerning the interconnections among wires (i.e. how is the underlying circuit), as well as which are the ports (i.e. where are the currents to be modeled).

All the code was developed in C++, using complex arithmetic. For the numerical integrations we have developed fast and efficient methods specific for the conduction modes applications (see Section 5.6); these coexist, and can be used alternatively, with adapted algorithms contained in [86] and [87].

## 4.7 Examples

In this section, we will show different situations in which the *RLC* conduction modes formalism is capable of rendering accurate magnitudes, showing a significant reduction in size. These examples evidence the capacity of the method to capture resonances: in the first case we study a shorted transmission line composed of two copper wires; then we switch to a more complicated example, consisting of a square three-turn intentional inductor.

- FastImp used in the fullwave mode [10]
- Numerical solution of circuits with parameters obtained via separate *RL* and *C* computations under quasistatic conditions.

The examples in the section were included in the presentation of this work at [33]. We do not discuss in this section the runtimes involved, because at this stage, some features of the *RLC* method are at a development phase. One such feature is the optimal calculation of the matrix elements for the  $\mathcal{Z}$  matrix in (4.20). This kind of optimization strategy has been developed in full detail for the *RL* case, and is the subject of the following chapter. Extensions to the *RLC* case, though straightforward, are lengthy. Some aspects of this generalization are discussed in

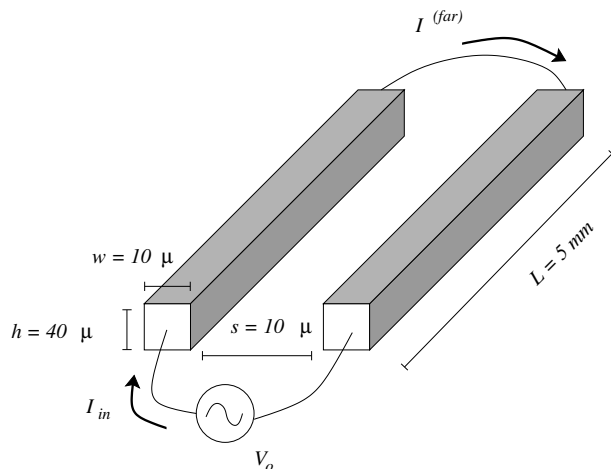


Figure 4.7: Shorted Transmission Lines example configuration.

Chapter 6. For the interest of the present section, it suffices to say that the runtime involved in the following examples are unrealistically of the same order as the other methods.

#### 4.7.1 Shorted transmission line

Our first example is drawn from [74], consisting of two *Cu* wires *5mm* long, of cross sections  $10\mu \times 40\mu$ , separated by a distance of  $10\mu$ , shorted at the far end, and with an input excitation  $V_o$  at the near end (Fig.4.7). The solution of this system in terms of *RLC* conduction modes is explained in Section 4.5.2. We employ 16 modes per conductor: 4 side plus 4 corner for each possible  $z$ -propagation.

Comparison against the mentioned references is standard: FastImp contemplates a transmission line option; concerning the number of panels, we varied the discretization until stable values were reached, at  $3 \times 5 \times 100$  panels along width, thickness, and length, respectively. The total number of panels is 3260.

For the  $RL + C$  representation, we resort to a W-model [53] for transmission line simulation with per-unit-length  $RL$  values tabulated at different frequencies. Extraction of these parameters was carried out with FastHenry at a fine  $9 \times 9$  discretization on the cross-section<sup>10</sup>. Per-unit-length  $C$  values stabilize with FastCap using 272 panels. Issuing from an electrostatics solution, these capacitance parameters are frequency-independent.

In Figs. 4.8 and 4.8 we compare the admittance ( $V_o/I_{in}$ ), as well as the shorted current  $I^{(far)}$ , defined in Fig. 4.7.

<sup>10</sup>Note: we use FastHenry without the multipole acceleration, computing direct matrix products, and therefore avoiding a subdivision of filaments along their lengths; for these size of problem, this is the optimal use for this tool, both in terms of size and performance. This point will be expanded upon in the following chapter.

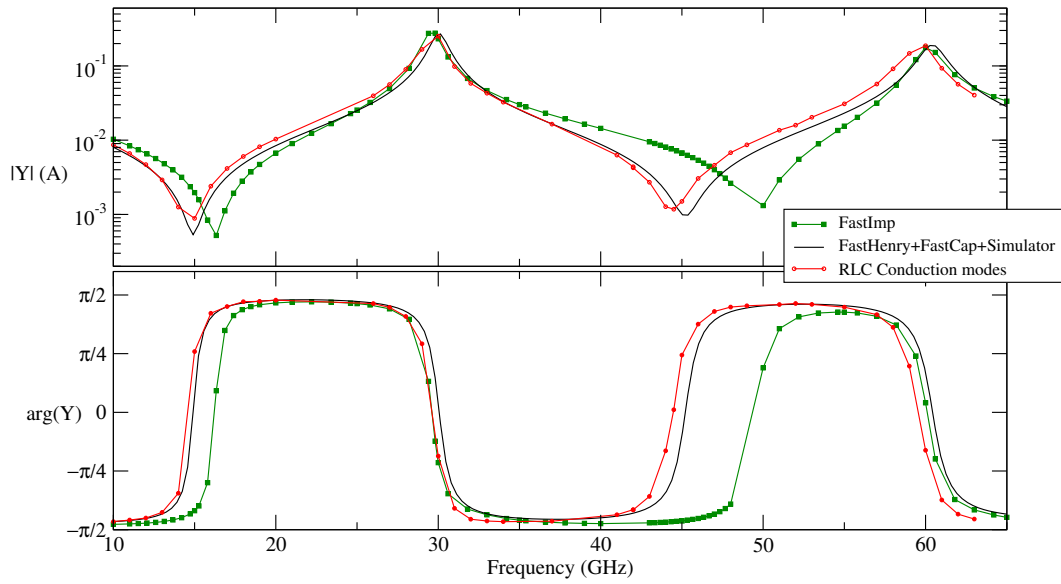


Figure 4.8: Admittance for the shorted transmission line in Fig.4.7: modulus (top) and argument (bottom), comparing Conduction Modes against the other methods described in text.

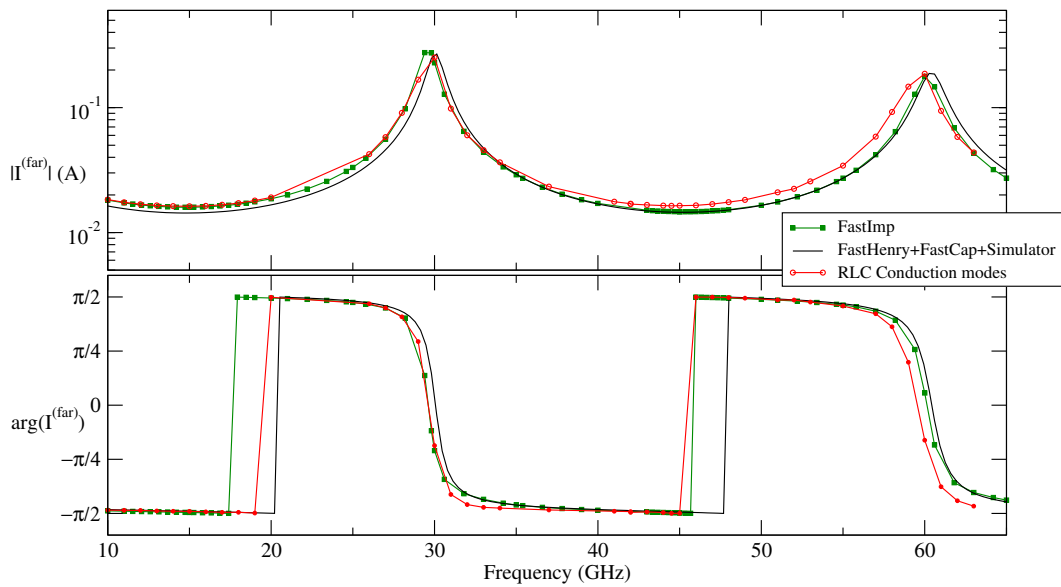


Figure 4.9: Shorted current for the transmission line in Fig.4.7: modulus (top) and argument (bottom), comparing Conduction Modes against the other methods described in text.

We observe the expected resonance peaks at frequencies multiples of quarter wave lengths. Qualitatively, the merged *RLC* conduction modes model shows the correct physical behavior. The location of the minima for the admittance is significantly different on FastImp compared to ours as well as the transmission line model<sup>11</sup>. To determine this discrepancy, we turned to LargeCom [12] from Univ.of Illinois, which confirmed our results [88]. We ignore the origin of these discrepancies.

### 4.7.2 *RLC* inductor

Next we consider a square 3-turn inductor, with the parameters shown in Fig.4.10a. All the wires are Cu, and we neglect substrate effects.

For conduction modes, we use 8 modes per segment: 4 side modes for each sense of propagation along its length. Thus the total current and charge distributions has a dimensionality of 96. These conduction modes are the entries for matrix  $\mathcal{Z}$  in (4.20), whose elements are defined in (4.14). The underlying circuit is shown in Fig. 4.10c, where each  $Z$  element represents the collection of conduction modes for that segment. Solution of this model follows the recipe in Section 4.5.3.

On the other hand, we compute a decoupled *RL + C* extraction; the corresponding circuit is shown in Fig. 4.10b. The resistor and inductor on each segment represent in fact a collection of piece-wise constant filaments. Since the total lengths of wires is much smaller that the wavelength, it is sufficient to represent each segment as one branch of lumped *R, L, C* elements. The *RL* extraction is carried out with Calibre xL using a  $5 \times 3$  discretization along the cross-sections, and capacitance is computed with FastCap. Stability was reached for 11904 panels. Solution to this circuit is similar to the one for the *RLC* circuit described in Section 4.5.3, with two differences: currents are the same at both ends of each segment; the total currents at a node do not cancel out, the difference representing the time-derivative of the charge ( $j\omega q$ ) transferred to the capacitors at that node. A routine for this solution is integrated into the Calibre engine [22, 23].

Impedance computation for this example is shown in Fig. 4.11. Accuracy near the resonance is remarkable. In Table 4.3 we compare the sizes of the problems solved by the two different approaches<sup>12</sup>.

Attempts to obtain stable output from FastImp, for this example, have been unfruitful. We have raised the number of panels along the length of each up to 400 (with a total of panels above  $10^5$ , total system size  $8 \times 10^5$ ) without obtaining stable results. Again, we ignore the source of

<sup>11</sup>This is not the case for the shorted current  $I^{far}$ , where the discrepancies in the jumps of the argument (bottom graph in Fig. 4.9) are due to insignificant differences for a smooth change of sign in the real part; we are using a definition of the argument function  $\arg(z) \in [-\pi, \pi]$ .

<sup>12</sup>We separate the *RL* and *C* contributions, since the complexity associated to each problem is of a different nature; for example, the system with more than 11000 panels in FastCap was solved very fast, as compared to comparable sizes for FastHenry.

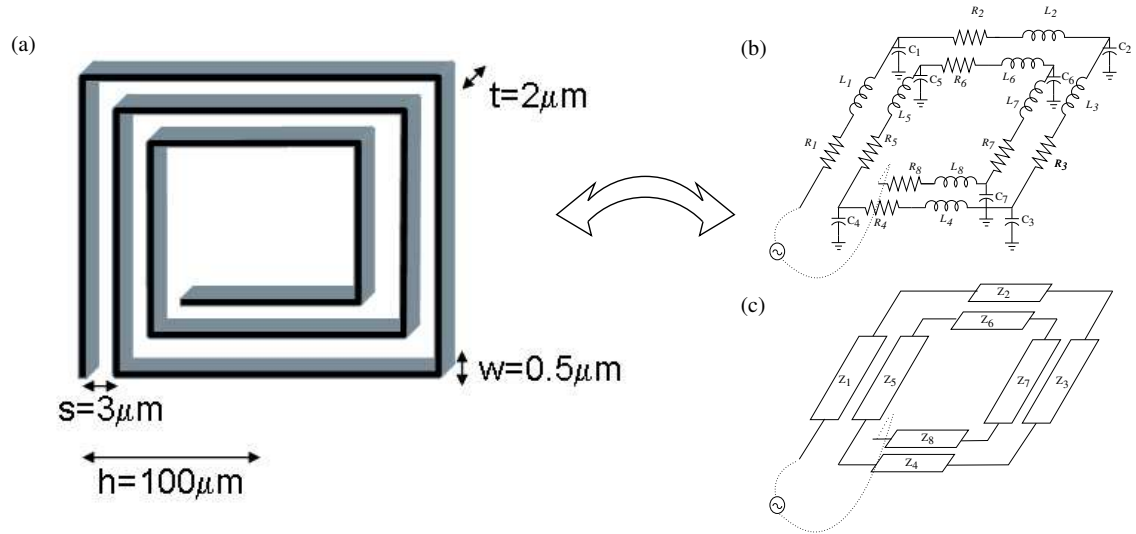


Figure 4.10: (a): Example 3-turn square inductor; (b):  $RL + C$  circuit representation for decoupled extraction; (c):  $RLC$  circuit representation for fullwave extraction with conduction modes (for the sake of clarity, we omit the coupling elements, and we reduce one turn).

this difficulty.

As in the previous example, the capacitive effects are coupled to the inductive-resistive ones through the nature of the conduction modes, which model charges and currents within the same mathematical function. The only assumption we are making is that these functions apply to the whole extent of each wire segment. In practice, this neglects border effects (mainly capacitive) near each corner of the inductor. Taking these into account is tantamount to enlarging the set of conduction modes, a subject which will be discussed in Section 6.4.

Table 4.3: Comparative sizes for the different methods

Method	Transmission Line	Inductor
RLC Conduction Modes	32	96
FastImp	3260	N/A
RL+C+Simulator	162+272	300 + 11904

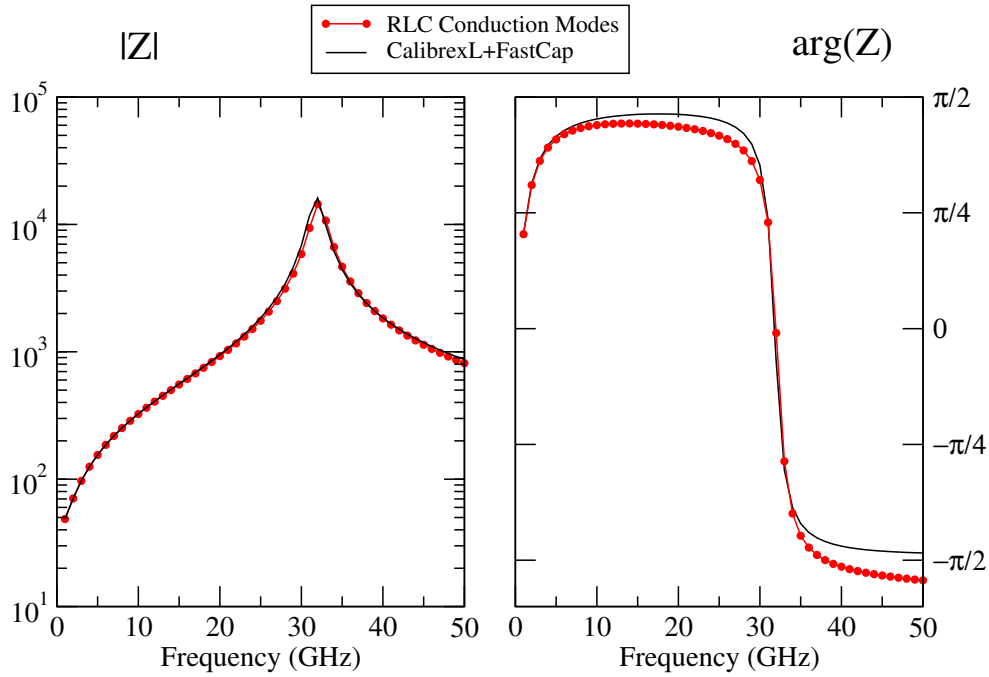


Figure 4.11: Comparison between *RLC* conduction modes and mixed *RL + C* results for the square inductor example in the vicinity of its first resonant frequency.

## 4.8 Conclusions

We have presented the essence of a new simulation approach to study *RLC* fullwave modeling of conductors in terms of a small set of conduction basis functions. We have been able to capture the interplay between the electric and magnetic energy content that gives rise to resonances, while keeping a very concise description of the geometry.

This formulation consists of using a generalized version of the conduction modes basis functions presented originally in [32], which only account for current distribution functions, and therefore solves the quasi-static *RL* problem. Our functions include also charge distributions, with built-in continuity, which are proper for the full *RLC* statement. The resulting model resembles a transverse electromagnetic (*TEM*) model with frequency dependent parameters.

The main feature of this approach is that capacitive and inductive couplings are coupled together by these functions. Solution of the full equation (4.20) gives the same results, for the total impedance of the system, as those produced with the *RL+C* decomposition. By comparison, this involves solving two different quasi-static problems, broken up such that all dimensions are small compared to the wavelength, and then joining them through a circuit simulator or analogous model. The gains in size are considerable, as shown in Table 4.3.

The usefulness of this type of approach depends on two main factors: performance and the

extensibility to more general types of configurations. The first point is the subject of the next chapter, where we address the main performance issue related to conduction modes formalism, i.e. the extensive algebra associated with the matrix elements in (4.14). The generalization of the method presented here is addressed in Chapter 6, where we outline and discuss the main tasks involved in developing a fullwave field solver based on the concept of conduction modes.



# Éléments de matrice pour les modes de conduction : cas $RL$

## Résumé en français

*Dans ce chapitre, nous proposons une solution au problème principal de la formulation  $RL/MQS$  des modes de conduction, qui est celui du calcul des intégrales multidimensionnelles pour les éléments  $L_{ij}$  définis par eq.(4.14). La première partie du chapitre décrit des considérations générales qui sont valables pour toutes les intégrales 5.2. Ici, nous réduisons la dimensionnalité de 6 à 2. À la section 5.3, nous considérons les intégrales pour la situation où l'élément  $L_{ij}$  de matrice correspond à deux modes du même conducteur; les difficultés trouvées sont principalement liées à une singularité intégrable présente dans le domaine d'intégration. Les intégrales associées aux modes de conducteurs différents sont analysées dans la section 5.4 ; les complications, dans ce cas, sont plutôt liées à la grande quantité d'éléments, ainsi qu'au manque de symétrie permettant des simplifications pour les fonctions à intégrer. Néanmoins, l'absence de la singularité mentionnée ci-dessus permet un calcul très efficace sur la base des approximations de Taylor. Nous montrons un schéma de l'organisation des algorithmes pour ce calcul dans la section 5.5, ce qui complète le diagramme global présenté dans le chapitre précédent. Dans la section 5.6, nous étudions en profondeur la précision et l'efficacité de nos méthodes en fonction de ces paramètres de contrôle. En conclusion, nous analysons des exemples comparatifs (sections 5.7 et 5.8), montrant une économie de deux ordres de magnitude pour le temps de calcul, par rapport à FastHenry d'un côté, et à l'application des modes de conduction avec des méthodes d'intégration standard de l'autre. Une version succincte de ce chapitre a été publiée à l' " International Symposium on Very Large Scale Integration " (ISVLSI), tenue en mai 2007 à Porto Alegre en Brésil. Aussi, les algorithmes de ce chapitre sont en train d'être fusionnés dans l'outil d'extraction Calibre xL chez Mentor Graphics.*



## Chapter 5

# Calculation of Matrix Elements for *RL* Conduction Modes

In the previous chapter, we have shown how to expand sources in terms of conduction modes basis functions, in a way that renders this method very efficient in terms of size savings. However, we have purposefully avoided to comment on the runtimes. Discussion of computational costs are also absent in the literature on conduction modes [16, 32, 33, 74].

The reason for this omission is simply that, in adopting this strategy, the burden of the calculation is transferred, from the cost of having a large linear system of easily computed elements, to that of having a much smaller system whose elements are difficult to obtain.

Matrix elements for conduction modes are the 6- and 4-dimensional integrals in (4.14). They extend over the whole volume and surface of the conductors, and are composed of two very distinct components: on one side, the Green function  $\exp(-jk_0r)/r$ ; on the other, exponential decays of order  $\delta$  for the conduction modes  $\mathbf{w}_i^*$  and  $\mathbf{w}_j$ . This duality renders difficult a standard numerical integration of these matrix elements.

In this chapter, we immerse ourselves precisely in these complications. We restrict ourselves to the *RL* case, so that only  $L_{ij}$  integrals are studied. Furthermore, we work within the Magneto-Quasi-Static (MQS) approximation, whereby we are safe to set  $k_0 = 0$  thus neglecting the phase factor in Green's function. The generalizations to the full *RLC* case are treated in the next chapter.

Chronologically, the work displayed in this chapter was developed in order to replace the standard numerical integration methods that were incorporated into the early versions of our general conduction modes formulation.

The first of these methods was the Monte Carlo (MC) implementation given by [89]. This algorithm was designed for use in quantum field theory calculations, and is targeted for dimensions of the order of 10 or larger, as well as situations in which little detailed information about

the integrand is known. For our purposes, it gives a very reliable estimate of the integral values, but its performance is far from optimal. Concerning the accuracy/performance payoff, it has a single control parameter corresponding to the maximum number of function calls. On output, we obtain an estimate of the error committed.

At a later stage, this component of the calculation was replaced by the so-called Adaptive Quadrature (AQ) algorithms [87], which target integrands of lower dimensionality. The accuracy/performance is controlled by either of two parameters, the maximum number of calls and/or the desired precision, which is estimated at each refinement. The drawback of AQ, with respect to MC, is that some particular integrals have a very slow convergence rate. The number of such occurrences is very low, and it is possible to implement the method in such a way as to avoid a standstill in the computation, by incrementally modifying the number of calls for those particular cases.

Both methods above belong to the class of importance sampling methods, meaning that they must develop a heuristic in order to evaluate the integrand at the regions where it, and/or its gradient, is peaked. The difference between them relies in the way they sample the space: MC does a stochastic sampling, whereas AQ is deterministic.

Importance sampling is the only option when we do not possess a detailed information on the integrand. For conduction modes, this information is hidden within complicated forms for the integrands. In a nutshell, this chapter is about how to capture and use this information for evaluating the conduction mode integrals. We organize this chapter as follows:

- Sections 5.1 and the first part of 5.2 are devoted to exposing the general setup and considerations valid for all integrals; here, we reduce the dimensionality from 6 to 2.
- Section 5.3 considers the integrals for the situation in which the matrix element  $L_{ij}$  corresponds to two modes for the same conductor; the difficulties in this case are mainly due to an integrable singularity in the integration domain.
- The integrals for different conductors are analyzed in Section 5.4; the complications, in this case, are related to the more general geometry, but the task is enormously simplified by the absence of the singularity mentioned above.
- We show a flow for the organization of the algorithms in Section 5.5, thus completing the global diagram presented in the previous chapter.
- A thorough study of the precision and performance of these methods is carried out in Section 5.6, including comparisons against the aforementioned methods for multidimensional integration [86, 87, 89].
- Finally, in 5.7 we conduct examples of *RL* extraction, and compare the results with the

well-established standard FastHenry [15], observing up to two order of magnitude in performance gains without loss of accuracy.

A distilled version of this chapter has been published at the IEEE International Symposium on Very Large Scale Integration (ISVLSI), held in May 2007 in Porto Alegre, Brazil. The algorithms in this chapter are in the process of being merged into Mentor's Calibre xL extraction tool.

## 5.1 Statement of the problem

In this chapter, we concentrate on the matrix elements  $L_{ij}$  represented in (4.14b), for  $RL$  current modes under Magneto-Quasi-Static (MQS) conditions. This means that currents are treated as one-dimensional, along the  $z$ -axis (which is defined as that of the voltage drop along the conductor), and that the modes are independent of  $z$ . Thus the integrals are written as<sup>1</sup>,

$$L_{ij} = \frac{\mu A_i^* A_j}{4\pi} \int_V \int_{V'} \frac{e^{\alpha_i^* x + \alpha_j x' + \beta_i^* y + \beta_j y'}}{|\mathbf{r} - \mathbf{r}'|} d^3 r d^3 r' \quad (5.1)$$

where  $V, V'$  refer to the volumes of two conductors while  $i$  and  $j$ , refer to CM modes, and  $A_{i,j}$  are the normalization constant for the conduction modes, defined in Section 4.3.1.

This matrix  $L$  is clearly hermitian, hence only  $N(N + 1)/2$  of the total  $N^2$  integrals need to be computed, with  $N$  the total number of degrees of freedom  $N = mn$ ,  $n$  and  $m$  the number of conductors and the number of modes per conductor, respectively.

A natural classification of these integrals corresponds to whether the two conduction modes belong to the same or different conductors. Either case has particular characteristics that favor distinct integration techniques; on broad terms, these are:

- When both volumes cover the same conductor, there is a higher degree of symmetry, so that fewer terms need to be computed; for these integrals, the integration domain contains an integrable singularity at zero separation which demands special attention.
- When both  $V, V'$  refer to different conductors, the integrand is non-singular and smooth within the full integration domain, thus permitting the use of Taylor expansions, which reduce significantly the cost of evaluating the integral.

In a typical multi-conductor configuration, the number  $N_{same}$  of same-conductor matrix elements is much smaller than the one for different conductors,  $N_{diff}$ : for  $n$  conductors with  $m$  the number of conduction modes per conductor, there are  $n.m^2$  same-conductor elements while

<sup>1</sup>For the expressions in this chapter we shorten the notation by omitting the border factors  $e^{-\alpha_i^* x_b - \beta_j y_b}$ , which are simply a factor common to the whole integral.

$(n^2 - n).m^2$  different-conductor ones. Due to hermiticity, the number of integrals that must be computed reduces to:

$$\begin{aligned} N_{same} &= \frac{1}{2}(m^2 + m).n \\ N_{diff} &= \frac{1}{2}(n^2 - n).m^2 \end{aligned} \quad (5.2)$$

It has been shown empirically [16] that  $m$  values can reasonably be assumed to be independent of  $n$ , and small; thus  $N_{diff}$  is significantly larger than  $N_{same}$ . The quadratic growth of  $N_{diff}$  with  $n$  is the dominant contributions for configurations containing three or more conductors.

Furthermore, symmetries further reduce the number of independent contributions to  $N_{same}$  (see Fig.5.1):

- For a conductor containing four side modes, only 5 integrals (out of 10) need to be computed, namely: (E,E) (E,W) (N,N) (N,S) (E,N)
- For a conductor containing four corner modes of equal angles, only 4 integrals (out of 10) need to be computed, namely: (NE,NE) (NE,NW) (NE,SE) (NE,SW)
- For a conductor containing four side modes and four corner modes, only 4 mixed integrals (out of 16) need to be computed, namely: (E,NE) (E,NW) (N,NE) (N,SE)

We will first discuss some general aspects of our integration strategy applicable to both domains, to be followed by a detailed analysis that relies on the above mentioned classification.

## 5.2 General considerations

The first and obvious simplification results from the observation that, except for the exponentials representing each conduction mode, the variables enter in the combination  $x - x', y - y', z - z'$  contained in the Green function for this system. Therefore, we apply the change of variables shown in Fig.5.2:

$$\begin{cases} \mathbf{r}_+ = \mathbf{r} + \mathbf{r}' \\ \mathbf{r}_- = \mathbf{r} - \mathbf{r}' \end{cases} \quad (5.3)$$

with  $\mathbf{r} = (x, y, z)$ ; the Jacobian for each dimension is  $1/2$ , giving a total factor of  $1/8$ .

In the new variables, the integrals over  $x_+, y_+, z_+$  are performed analytically:

$$L_{ij} = N_{ij} \int_{-w'}^w \int_{-h'}^h \int_{-\ell'}^\ell \frac{\xi_x(x_-)\xi_y(y_-)\xi_z(z_-)}{r} dx_- dy_- dz_- \quad (5.4)$$

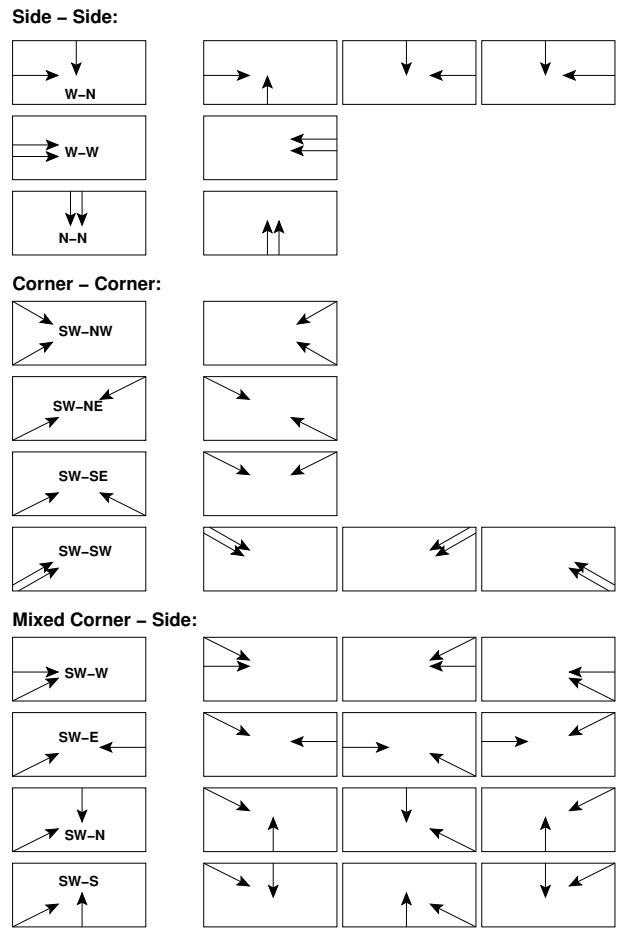


Figure 5.1: Examples of Mode equivalence for same-conductor integrals.

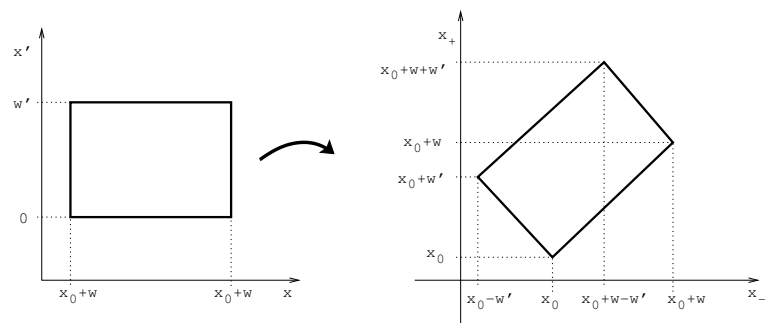


Figure 5.2: Change of variables in eq.(5.3), exemplified for the x-integration.

with  $r = \sqrt{(x_- + x_0)^2 + (y_- + y_0)^2 + (z_- + z_0)^2}$  and the functions  $\xi_{x,y,z}$  are the result of the analytical integrals in  $x_+, y_+, z_+$ ;  $x_0$  is the separation between the two left extremes of each conductor (without loss of generality, we assume the conductor with primed variables to be located at the origin, see Fig.5.2), and  $y_0, z_0$  are the corresponding values for the other axes. In (5.4), we have also defined the proportionality constant  $N_{ij} \equiv \frac{\mu A_i^* A_j}{32\pi}$ .

Functions  $\xi_{x,y,z}$  act as weight functions for the integration of the  $r^{-1}$  Coulomb kernel over the relative (“-”) variables. In order to illustrate the variety of weight functions, according to each possible pair of conduction modes, we illustrate on the the  $x$  variable:

$$\xi_x(x) = \begin{cases} w + w' - |x| - |x - x_1| & \text{if } \alpha_i^* + \alpha_j = 0 \\ (\alpha_i^* + \alpha_j)^{-1} (\gamma_1 e^{\alpha_i^* x} + \gamma_2 e^{-\alpha_j x}) & \text{if } \alpha_i^* + \alpha_j \neq 0 \end{cases} \quad (5.5)$$

with  $x_1 \equiv w - w'$ , and the piecewise-constant functions<sup>2</sup>

$$\begin{aligned} \gamma_1 &\equiv e^{(\alpha_i^* + \alpha_j)w'} \Theta(x_1 - x) - \Theta(x) \\ \gamma_2 &\equiv e^{(\alpha_i^* + \alpha_j)w} \Theta(x - x_1) - \Theta(-x) \end{aligned} \quad (5.6)$$

For the  $\xi_y(y)$  weight function,  $\alpha$  is replaced by  $\beta$  and  $x_0, x_1$  by  $y_0, y_1 = h - h'$ . Since we are within the *MQS* regime, the  $z$ -integral can be done analytically leading to:

$$L_{ij} = N_{ij} \int_{-w'}^{+w} \int_{-h'}^{+h} \xi_x(x) \xi_y(y) F(\rho(x + x_0, y + y_0)) dx dy \quad (5.7)$$

where  $\rho(x, y) = \sqrt{x^2 + y^2}$  and  $F(\rho)$  is a cumbersome expression, which in the case of both conductors sharing the  $z$ -extension (i.e:  $z_0 = 0; \ell = \ell'$ ), is

$$F_\ell = \ell \left( \sinh^{-1} \left( \frac{\ell}{\rho} \right) - \sqrt{1 + \frac{\rho^2}{\ell^2} + \frac{\rho}{\ell}} \right) \quad (5.8)$$

with  $\ell$  the common length of the conductors.

The general case is a combination of four same-length expressions (5.8) evaluated at four different values [56]:

$$F = \frac{1}{2} [F_{|z_0+\ell} + F_{|z_0-\ell'} - F_{|z_0} - F_{|z_0+\ell-\ell'}] \quad (5.9)$$

with the same notation as the one for  $x$ , Fig. 5.2, replacing  $x_0 \leftrightarrow z_0, w \leftrightarrow \ell, w' \leftrightarrow \ell'$ .

---

<sup>2</sup>We use  $\Theta(x) \equiv \begin{cases} 1 & \text{if } x \geq 0 \\ 0 & \text{if } x < 0 \end{cases}$ , the Heaviside step function.

We are left with two dimensional integrals, which we classify according to the different weight functions. Each conduction mode can either be a “corner” (both  $\alpha, \beta \neq 0$ : e.g. the  $SW$ ,  $SE$ ,  $NE$  or  $NW$  in Fig. 5.1) or a “side” mode (only one non-zero exponential component:  $E$ ,  $N$ ,  $S$  or  $W$ ). Therefore, any integral can contain 0,1 or 2 exponential decays along each of the cross-sectional dimensions. The integrals belong to the following types (see Fig. 5.3):

- [H,V]** (or **[V,H]**): One horizontal side mode and one vertical side mode, the corresponding integral has one exponentially decaying contribution along each integration axis.
- [H,H]** (or **[V,V]**): Two horizontal (or vertical), the integral has two exponentially decaying contributions along one axis, and none along the other.
- [H,C]** (or **[C,H]** **[V,C]** **[C,V]**): One corner mode and one side mode (in any combination), the integral has two exponentially decaying contributions along one axis, and one along the other.
- [C,C]** : Two corner modes, the integral has two exponentially decaying contributions along each axis.

For any of the two integration variables,  $x$  or  $y$ , the number of exponentially decaying functions on that variable classifies the contribution of this integration variable to the total integral. Rearranging expressions in (5.5), we can decompose each integral into terms that have a definite behavior (exponential or linear) along each axis. In Table 5.1, we show a representative set identifying the dimensions of the different sub- domains for each type of integral described above.

Table 5.1: Decomposition of the total integration domain into exponential ( $E$ ) and linear ( $L$ ) contributions along the  $x$  and  $y$  integration coordinates (e.g.:  $E - L$  is exponential in  $x$ , linear in  $y$ ), for different types of integrals.

Type	$E - E$	$L - E$	$E - L$	$L - L$
<b>[H,V]</b>	✓	✓	✓	✓
<b>[H,H]</b>	-	-	✓	-
<b>[V,V]</b>	-	✓	-	-
<b>[H,C]</b>	✓	-	✓	-
<b>[V,C]</b>	✓	✓	-	-
<b>[C,C]</b>	✓	-	-	-

This decomposition permits us to apply appropriate methods of integration according to the functional behavior of the integrand, as well as the integration domain.

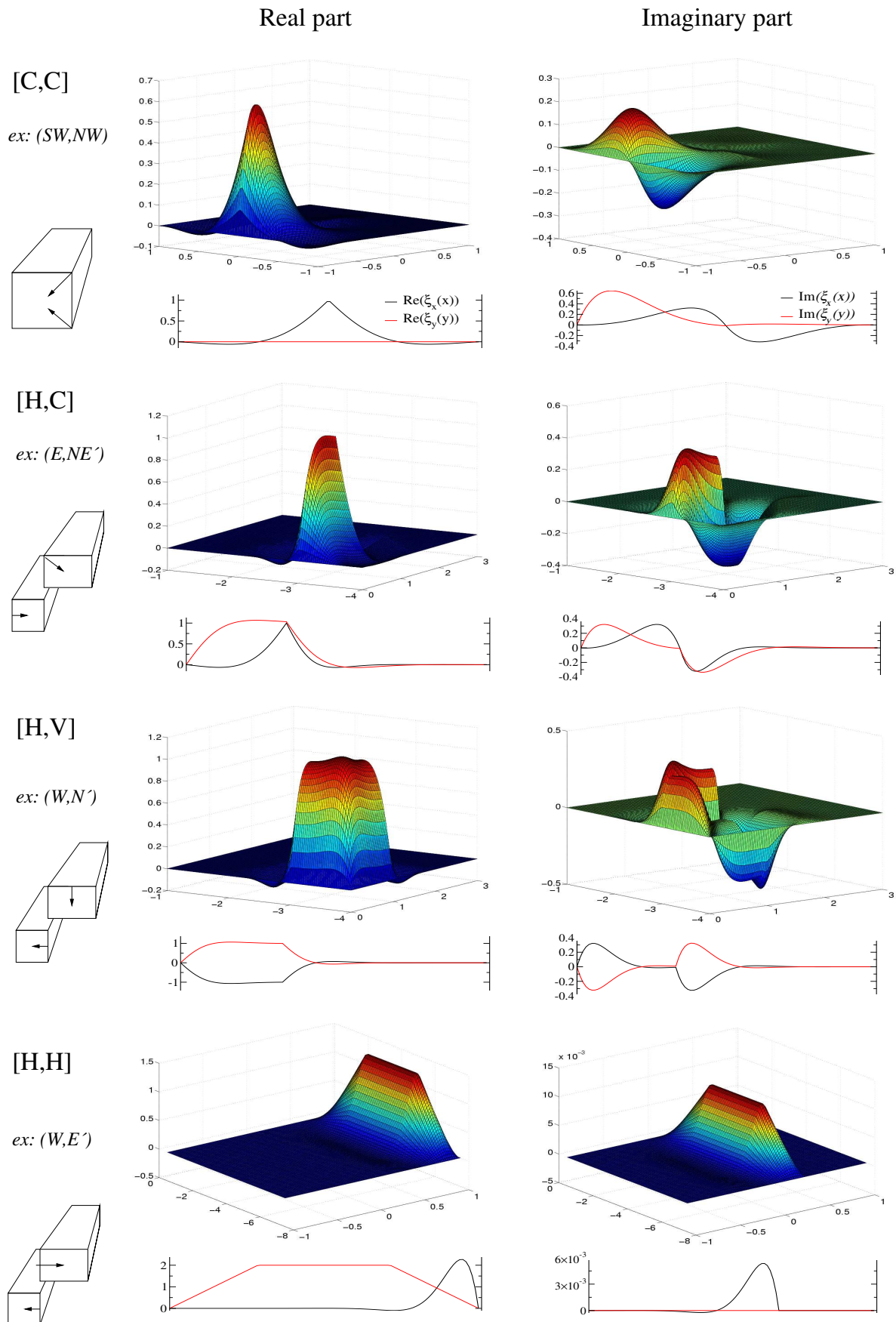


Figure 5.3: Examples of total weight functions  $\xi_x \xi_y(x, y)$  (3-d plots); and the corresponding separate  $\xi_x(x)$  and  $\xi_y(y)$  (2-d plots) for different types of integrals.

### 5.3 Same-conductor integrals

For matrix elements between two modes belonging to the same conductor, we have  $x_0 = y_0 = 0$  and  $w = w', h = h'$ . Therefore, the integration domain simplifies to  $x \in [0, w]; y \in [0, h]$ .

The expression for the  $x$ -weight function in this interval is,

$$\xi_x = \begin{cases} 2e^t \left( \sinh(\alpha_j x - t) + \sinh(\alpha_i^* x - t) \right) & \text{if } \alpha_i^* + \alpha_j \neq 0 \\ 2(w - x) & \text{if } \alpha_i^* + \alpha_j = 0 \end{cases} \quad (5.10)$$

where  $t \equiv (\alpha_i^* + \alpha_j)w/2$ ; analogous expressions hold for  $\xi_y$ .

#### 5.3.1 Exponential decays: $E$ -type contributions

When both  $\alpha_i^*, \alpha_j \neq 0$ , the expression on the first line of (5.10) is a sum of two or four decaying exponentials. In particular, for  $[\mathbf{H}, \mathbf{H}]$  type integrals, we have

$$\xi_x = \begin{cases} 2 \cos\left(\frac{x}{\delta}\right) \left( e^{-\frac{x}{\delta}} - e^{-\frac{2w-x}{\delta}} \right) & \text{if } \alpha_i = \alpha_j \\ 2j \sin\left(\frac{w-x}{\delta}\right) \left( e^{-\frac{w-x}{\delta}} + e^{-\frac{w+x}{\delta}} \right) & \text{if } \alpha_i = -\alpha_j \end{cases} \quad (5.11)$$

Here the first line corresponds to two modes decaying from the same side, i.e. (E,E) or (W,W); while the second one is for modes decaying from opposite sides, (E,W) or (W,E). Similar expressions as the ones in (5.11) exist for the other integrals with double exponential contributions, namely the types  $[\mathbf{H}, \mathbf{C}]$  and  $[\mathbf{C}, \mathbf{C}]$  in Table 5.1.

Once the exponential decays are written explicitly as in (5.11), we proceed to estimate the  $x$ -integral by using a Gauss-Laguerre quadrature rule [86]. This is a tabulated set of  $G_{lag}$  points and weights  $\{x_i^{lag}, w_i^{lag}\}$  that best approximate the integral,

$$\int_0^\infty e^{-x} f(x) dx \simeq \sum_{i=1}^{G_{lag}} w_i^{lag} f(x_i^{lag}) \quad (5.12)$$

We point out that these tabulated values exist for the integrals in the  $[0, \infty]$  range, whereas we have finite integrals in the  $[0, w]$  interval. Therefore, we must transform each exponential as:

$$\int_0^w e^{-\frac{x}{\delta}} f(x) dx = \delta \left[ \int_0^\infty e^{-x} f(\delta x) dx - e^{-\frac{w}{\delta}} \int_0^\infty e^{-x} f((x+w)\delta) dx \right] \quad (5.13)$$

Each exponential term over a finite range is replaced by two infinite-range integrals, that can each be approximated by (5.12)<sup>3</sup>. Taking into account all the contributions for the exponentials,

<sup>3</sup>The inclusion of this extra term can be avoided according to the relative importance of the second integral in (5.13) with respect to the first one: as frequency increases, the skin depth  $\delta$  decreases, and for frequencies such that  $\delta$  is an order of magnitude smaller than  $w$ , the factor  $\exp(-w/\delta)$  makes the second integral negligible.

the  $x$ -contribution to  $[\mathbf{H}, \mathbf{H}]$  integrals in (5.11) is approximated as

$$\int_0^w \xi_x(x) F(x, y) dx \simeq \delta \sum_{i=1}^{G_{lag}} w_i^c \left( F(u_i) - K_c (F(u_i') + F(u_i'')) - (K_c + K_s) F(u_i) \right) + w_i^s K_s \left( F(u_i') - F(u_i'') - (K_c - K_s) F(u_i) \right) \quad (5.14)$$

for  $\alpha_i = \alpha_j$ , and

$$\int_0^w \xi_x(x) F(\rho(x, y)) dx \simeq \delta \sum_{i=1}^{G_{lag}} w_i^s \left( F(u_i') - 2K_c F(u_i) + (K_c^2 + K_s^2) F(u_i'') \right)$$

for  $\alpha_i = -\alpha_j$ , where we have defined

$$\begin{aligned} u_i &= \sqrt{(x_i^{lag}/\delta)^2 + y^2}, & w_i^c &= w_i^{lag} \cos(x_i^{lag}), & K_c &= e^{-w/\delta} \cos(w/\delta) \\ u_i' &= \sqrt{((w - x_i^{lag})/\delta)^2 + y^2}, & w_i^s &= w_i^{lag} \sin(x_i^{lag}), & K_s &= e^{-w/\delta} \sin(w/\delta) \\ u_i'' &= \sqrt{((w + x_i^{lag})/\delta)^2 + y^2} \end{aligned}$$

In Section 5.6 we will analyze in detail the convergence and cost of this techniques, as a function of the parameter  $G_{lag}$ .

### 5.3.2 Linear decays: $L$ -type contributions

When both  $\alpha_i^* = \alpha_j = 0$ , there is no exponential contribution on  $x$ , and  $\xi_x$  is lineal. Its contribution is best approximated by a Gauss-Jacobi quadrature rule [86]. As in the previous case, this consists of another set of  $G^{jac}$  tabulated points and weights  $x_i^{jac}$ ,  $w_i^{jac}$  such that

$$\int_{-1}^1 (1-x)^a (1+x)^b f(x) dx \simeq \sum_{i=1}^{G_{jac}} w_i^{jac} f(x_i^{jac}) \quad (5.15)$$

By setting  $a = 1$ ,  $b = 0$  and performing a linear shift in  $x$  for  $x_i$  in (5.11), we obtain the rule:

$$\int_0^w (w-x) F(x, y) dx \simeq \frac{w^2}{4} \sum_{i=1}^{G_{jac}} w_i^{jac} F\left(\frac{w}{2}(x_i^{jac} + 1), y\right) \quad (5.16)$$

The exponential decay dominates the behavior of the whole integrand. Therefore, as long

as there is one exponential decay along any axis, the integral is well approximated if the exponentials are. In other words, the overall quality of the fit is not greatly affected by the accuracy with which the linear part is approximated, i.e. the number  $G_{jac}$ . In practice, we have observed that using  $G_{jac} \simeq 10$  suffices for the desired precision; we study in depth this cost/accuracy relationship in Section 5.6. These arguments apply to the  $x$ -component of the  $[\mathbf{V},\mathbf{V}]$  integrals, as well as one term of the  $[\mathbf{V},\mathbf{C}]$  integrals (see Table 5.1).

### 5.3.3 Flat terms: $L - L$ integral types

For the  $[\mathbf{H},\mathbf{V}]$  integrals, the weight functions are,

$$\begin{aligned}\xi_x &= e^{\alpha_i^*(w-x)} - e^{\alpha_i^*x} - \kappa_x \\ \xi_y &= e^{\beta_j(h-y)} - e^{\beta_jy} - \kappa_y\end{aligned}\quad (5.17)$$

where  $\kappa_x \equiv 1 - \exp(\alpha_i^*w)$ ,  $\kappa_y \equiv 1 - \exp(\beta_jh)$ .

The product  $\xi_x\xi_y$  can be split up three ways:

- an  $E - E$  term due to the product of the two exponentials of these weight functions;
- an  $E - L$  and an  $L - E$  terms coming from the cross-products of the two exponentials of one function and the constant of the other;
- an  $L - L$  term springing from the product of the two constants in each function (in fact, it is "flat-flat").

Note that the  $L - L$  term is the most significant one among the three contributions above. This is because for this term, the weight function is a constant close to 1, whereas the other terms have exponential decays which confine the integrand to a region of order  $\delta$  (for  $E - L$ ) or  $\delta^2$  (for  $E - E$ ). These two terms are handled with the techniques described in the two previous sections. For  $L - L$ , using a double Gauss-Jacobi rule would result in large errors due to the integrable singularity at the origin (in the previous section, these errors were mitigated by the presence of exponential decays).

In order to circumvent this complication, we switch to a polar coordinate system (Fig.5.4)

$$\begin{cases} \rho &\equiv \sqrt{x^2 + y^2} \\ \phi &\equiv \arctan(y/x) \end{cases} \Leftrightarrow \begin{cases} x &= \rho \cos(\phi) \\ y &= \rho \sin(\phi) \end{cases}\quad (5.18)$$

with the Jacobian given by  $\rho$ . Therefore, the integrand goes to zero near  $\rho = 0$ , thus explicitly removing the integrable singularity at the origin. The price for this change of variables is the

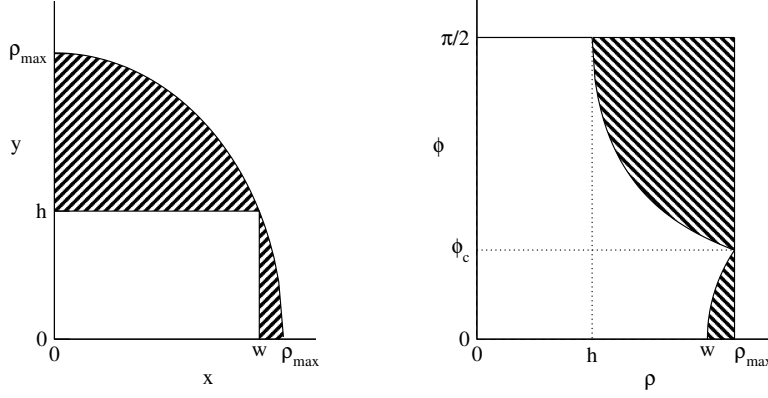


Figure 5.4: Integration domains for  $L - L$  same-conductor in cartesian (left) and polar variables (right); the shaded regions are the excess that must be deduced from the total value (see text).

irregular shape of the new integration domain, represented by the unshaded region of Fig.5.4 (right).

To deal with this domain, we first integrate over the square  $\rho \in [0, \rho_{max} \equiv \sqrt{w^2 + h^2}]$ ,  $\phi \in [0, \pi/2]$  domain, i.e. the quarter-circle in the original variables. Next, we need to estimate the value of the contributions of the excess regions (shaded sections of Fig.5.4)

$$L_{ij}^{(L-L)} = N_{ij} \kappa_x \kappa_y (C_1 - C_2) \quad (5.19)$$

with

$$\begin{aligned} C_1 &\equiv 3t^2 \sinh^{-1}\left(\frac{1}{t}\right) + (t^2 - 2)\sqrt{1+t^2} + 2t^3 + 2; & (t \equiv \ell/\rho_{max}) \\ C_2 &\equiv \int_h^{\rho_{max}} \cos^{-1}\left(\frac{h}{\rho}\right) \rho F(\rho) d\rho + \int_w^{\rho_{max}} \cos^{-1}\left(\frac{w}{\rho}\right) \rho F(\rho) d\rho \end{aligned} \quad (5.20)$$

Each of the integrals in  $C_2$  is dealt with in the following manner (see Fig.5.5):

- $\rho F(\rho)$  is replaced by its Taylor approximation at  $\rho = w$  and at  $\rho = h$ , and the product of these polynomials with the inverse trigonometric functions is analytically integrable;
- $\rho \cos^{-1}(w/\rho)$  and  $\rho \cos^{-1}(h/\rho)$  are replaced by their Taylor expansions at  $\rho = \rho_{max}$  and the product of these polynomials with  $F(\rho)$  is analytically integrable;
- the cutting point  $\rho_c$  is determined, for each branch, as the intersection of the two poly-

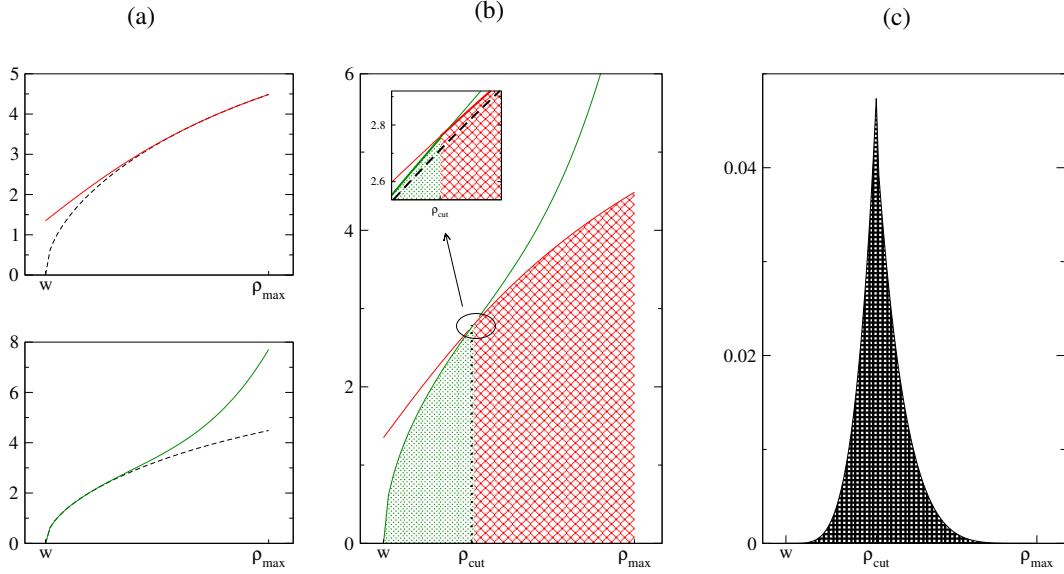


Figure 5.5: Taylor approximation for the polar-variable integration of same-conductor  $L - L$  terms (a); the resulting integrals (b, with inset showing detail); and error committed (c).

mials above<sup>4</sup>.

We exemplify point 1 above applied to the second integral in (5.20), being all the other integrals (tedious but) similar in nature. In this case, we write

$$\rho F(\rho) \simeq \sum_{n=0}^{T_s} p_n (\rho - w)^n \quad (5.21)$$

where the coefficients  $p_n$  are combinations of  $\sinh^{-1}(\ell/w)$ ,  $\sqrt{1 + w^2/\ell^2}$  and powers of  $w/\ell$ . In other words, this Taylor expansion demands only one transcendental function call. This expansion is replaced in the example integral,

$$\int_{\rho_c}^{\rho_{max}} \cos^{-1}\left(\frac{w}{\rho}\right) \rho F(\rho) d\rho \simeq \sum_{n=0}^K p_n I_n \quad (5.22)$$

where we have defined

<sup>4</sup>In practice,  $\rho_c$  is a function of the ratios  $w/h$  and  $\rho_{max}/\ell$  which can be effortlessly tabulated and interpolated for any arbitrary geometry; we will show this dependence in detail in Section 5.6.3.

$$\begin{aligned}
I_n &\equiv \int_{\rho_c}^{\rho_{max}} \cos^{-1}\left(\frac{w}{\rho}\right) (\rho - w)^n d\rho \\
&= h^{n+1} \sum_{i=0}^n \binom{n}{k} (-1)^{n-i} \int_{u_c}^1 u^{-(i+2)} \cos^{-1}(u) du
\end{aligned} \tag{5.23}$$

and  $u_c \equiv w/\rho_c$ .

The integrals inside the sum have analytical solutions which involve combinations of  $\sqrt{1 - u_c^2}$ ,  $\tanh^{-1}(\sqrt{1 - u_c^2})$  and powers of  $u_c$ . Again, only one transcendental function call is necessary.

Hence, this recipe enables us to compute the  $L - L$  term in (5.17) with as few as 9 transcendental function evaluations, 9 square roots, plus a limited number of elementary arithmetic (additions and multiplications).

The key to the success of this scheme is that the Taylor expansions are carried out at a distance far away from the singularity, which itself is "softened" by the Jacobian of the transformation  $\rho$ , forcing the whole integrand to go to zero at the origin; also important is the observation that extending the order of these polynomials,  $T_s$  does not represent an important computational burden, since only additional elementary arithmetic is added. Presently, we are working on extensions of this method in order to cover integrals with exponential decays (i.e.: to replace the Gauss-Laguerre and Gauss-Jacobi techniques of the previous section).

## 5.4 Different-conductor integrals

Compared to the same-conductor case, the integration domain for different conductors does not share the symmetries that allow for the simple expressions as the ones shown in (5.10), except for some limited situations<sup>5</sup>.

For example, the  $x$ -integral on the interval  $[x_0 - w', x_0 + w]$  is divided into four terms: two terms, ranging  $[x_0 - w', x_0 + w - w']$  and  $[x_0, x_0 + w]$  of length  $w$  whose behavior (exponential or linear) is given by  $\alpha_j$ ; plus two other terms,  $[x_0 - w', x_0]$  and  $[x_0 + w - w', x_0 + w]$  of length  $w'$  whose behavior is given by  $\alpha_i^*$ . Thus the cost associated with each different-conductor integral will be multiplied by a factor of 16 (worst-case, no symmetry on any axis) compared to the same-conductor case.

Integrals for different conductors, however, permit more efficient approximations, as compared due to same-conductor integrals, due to the absence of the singularity. Each of the potentially 16 terms are significantly less expensive to compute. In practice, we apply the following

<sup>5</sup>For example, when both conductors belong to the same metal layer, then  $y_0 = 0$  and  $h = h'$ , thus simplifying the integration domains for the  $y$ -integration as if it were same-conductor.

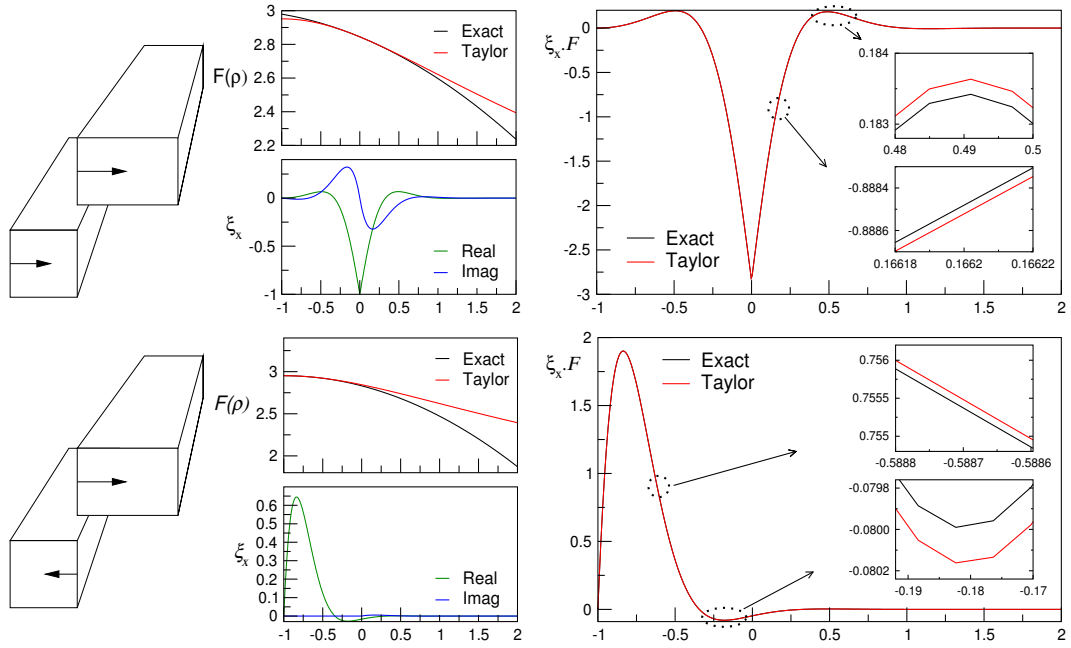


Figure 5.6: Taylor approximations for exponential terms in different-conductor integrals.

strategy:

### 5.4.1 Exponential contributions

Exponential contributions are integrated by carrying out a Taylor expansion of everything but the exponential term. This a reasonable strategy, if we observe that, in the presence of an exponential decay, the integrand will be very peaked at the maximum value of the exponential.

In this section, we analyze integrands with a double exponential contribution along an axis, such as the  $x$ -integral for  $[\mathbf{H},\mathbf{H}]$  and  $[\mathbf{H},\mathbf{C}]$  types, the  $y$ -integral for  $[\mathbf{V},\mathbf{V}]$  and  $[\mathbf{H},\mathbf{V}]$  types, and both integrals for  $[\mathbf{C},\mathbf{C}]$  types. The case of a single exponential contribution is described briefly in Section 5.4.3

For example, consider an  $x$ -integral with a double exponential (see Fig.5.6): we expand  $F(x, y) \approx \sum p_n(x - x_p)^n$  around the  $\rho_p = \rho(x_p, y)$ ; the location of the peaks  $x_p$  depend on the side from which the two modes decay<sup>6</sup>:

<sup>6</sup>The value of  $y$  in the definition for  $\rho_p$  depends on whether the  $y$ -integration has an exponential decay or not: in the first case, we are actually dealing with a 2-d Taylor expansion; in the second case,  $y$ -dependence is linear (or flat), and the integral is evaluated at certain discrete points (see Sec.5.4.2).

$$\begin{aligned}
(E, E) &\leftrightarrow x_p = x_0 \\
(W, W) &\leftrightarrow x_p = x_0 + w - w' \\
(E, W) &\leftrightarrow x_p = x_0 + w - \varepsilon \\
(W, E) &\leftrightarrow x_p = x_0 - w' + \varepsilon
\end{aligned} \tag{5.24}$$

In other words, the peak is located at  $x_0$  if both modes decay from the left, and is shifted by  $w$  if the  $\alpha_i^*$  decays from the opposite side, and by  $-w'$  if  $\alpha_j$  does so. The displacements  $\varepsilon$  for the "mixed" cases occur because the integration domain is of area zero at the location of these peaks: the change of coordinates forces  $\xi_x$  to vanish at the extremes  $x_0 - w'$  and  $x_0 + w$ . Hence, the peaks cannot be located exactly at the extremes. Instead, they correspond to the maxima of  $\xi_x$  in the vicinity of the corresponding extreme, given by the solution to the equation,

$$e^{\pm(\alpha_i^* + \alpha_j)\varepsilon} = \frac{\alpha_i^*}{\alpha_j} \tag{5.25}$$

where the "-" is for (E,W) and the "+" is for (W,E) integrals.

The  $x$ -integral along this axis reduces to:

$$\int_{-w'}^w \xi_x(x) F(\hat{\rho}(x + x_0, y + y_0)) dx \simeq \sum_{n=0}^{T_d} p_n J_n \tag{5.26}$$

where the expansion coefficients are,

$$\begin{aligned}
p_n &\equiv \frac{1}{n!} \left. \frac{\partial^n F(x, y)}{\partial x^n} \right|_{x=x_p} \\
p_0 &= \ell \left( \log(t + \sqrt{1 + t^2}) - \frac{t}{1 + \sqrt{1 + t^2}} \right) \\
p_1 &= -\frac{c_p t^2}{1 + \sqrt{1 + t^2}} \\
p_2 &= \frac{t}{2\ell} \left( \frac{(1 - c_p^2)t^2}{1 + \sqrt{1 + t^2}} + \frac{c_p^2 t^2}{\sqrt{1 + t^2}} \right); \quad \text{etc.}
\end{aligned} \tag{5.27}$$

with  $t \equiv \ell/\rho_p$  and  $c_p \equiv x_p/\rho_p$ ; in (5.26) we have also defined:

$$J_n \equiv \int_{-w'}^w (x - x_p)^n (\gamma_1(x)e^{\alpha_i^* x} + \gamma_2(x)e^{-\alpha_j x}) dx \tag{5.28}$$

The functions  $\gamma_1, \gamma_2$  are defined in (5.6), and are responsible for the "peaked" behavior.

Concerning the integrals in (5.26), they are computed analytically using the following recursion:

$$\begin{aligned}
 J_n &= C_n + C'_n \\
 C_n &\equiv \int_{-w'}^w (x - x_p)^n \gamma_1 e^{\alpha_i^* x} dx = \frac{1}{\alpha} (K_n - nC_{n-1}) \\
 C'_n &\equiv \int_{-w'}^w (x - x_p)^n \gamma_2 e^{-\alpha_j x} dx = \frac{1}{\alpha'} (K_n - nC'_{n-1})
 \end{aligned} \tag{5.29}$$

with

$$K_n = \delta_{n0} - w^n e^{\alpha_i^* w} - (-w')^n e^{\alpha_i^* w} + (w - w')^n e^{\alpha_i^* w + \alpha_i^* w}$$

This simple expansion permits the computation of these integrals with very few transcendental function evaluations (notice that the coefficients  $p_n$  in (5.27) contain only one logarithm and one square root, and evaluation of all the  $J_n$  demand only two exponentials). A detailed analysis of the cost and performance of this method is contained in Sections 5.6 and 5.7.

#### 5.4.2 Linear or Flat contributions

Weight functions  $\xi_x$  corresponding to integrals of type **[V,V]** are trapezoidal, composed of two linear intervals of length  $w_{<}$  plus one flat one of length  $w_{>}$ , where  $w_{>(<)}$  is the larger (smaller) of  $w, w'$ , eq. (5.5).

In contrast to the case of exponential decays, these integrals do not contain peaked weight functions. Therefore the arguments leading to a Taylor approximation do not hold.

Nevertheless, since we are in the case of different conductors, the function  $F$  is very regular, and thus we are safe to adopt quadrature rules in order to estimate these integrals. Linear intervals are integrated with a  $G$ -point Gauss-Jacobi quadrature rule, as in Section 5.3.2, whereas flat contributions are integrated with a  $G_d$ -point Gauss-Legendre quadrature rule [86], which is a simplified version of Gauss-Jacobi with  $a = b = 0$  in (5.15).

Due to the smooth behavior of  $F$ , we found that the required number  $G_d$  is generally very small ( $G_d = 3$  turned out to be sufficient for all of the examples we studied). In Section 5.6, we support this claim rigorously.

#### 5.4.3 Mixed Flat/Exponential

Special care must be taken for integrals that contain both flat and exponential terms, such as the  $x$ -integral for **[H,V]** or **[V,C]** types.

Here, we must separate the different kinds of terms in order to capture the correct behavior for each, and apply the corresponding method. The complication is in discriminating exponential terms from and the linear/flat ones, in order to isolate them and apply the appropriate techniques: Taylor approximations as in Section 5.4.1 for the first ones, Gaussian quadratures as in Section 5.4.2 for the second. For example, consider the (E,S) integral, belonging to type [H,V], i.e.  $\alpha_i^* = 0, \beta_j = 0$ . We can write the whole integrand as,

$$\begin{aligned}
L = N_{ij} \left\{ \right. & \int_{-w'}^0 \int_0^h [F(\rho) - F(\rho_w) - F(\rho_{-h'}) + F(\rho_{w,-h'})] e^{-\alpha_j x + \beta_i^* y} dx dy \\
& + \int_0^w \int_0^h [F(\rho) - F(\rho_{-h'}) + (F(\rho_{-w',-h'}) - F(\rho_{-w'})) e^{\alpha_j w}] e^{\beta_i^* y} dx dy \\
& + \int_{-w'}^0 \int_{-h'}^0 [F(\rho) - F(\rho_w) + (F(\rho_{w,h}) - F(\rho_h)) e^{\beta_i^* h}] e^{\alpha_j x} dx dy \\
& \left. + \int_0^w \int_{-h'}^0 [F(\rho) - F(\rho_h) e^{\beta_i^* h} + (F(\rho_{-w',-h'}) e^{\beta_i^* h} - F(\rho_{-w'})) e^{\alpha_j w}] e^{\beta_i^* y} dx dy \right\} \quad (5.30)
\end{aligned}$$

where we have introduced a notation with subindices for displaced distances: for example  $\rho_{-w'} = \sqrt{(x + x_0 - w')^2 + (y + y_0)^2}$ ,  $\rho_{w,-h'} = \sqrt{(x + x_0 + w)^2 + (y + y_0 - h')^2}$ , etc.

In this last expression, we are showing explicitly the different contributions: the first term is a double-exponential  $E - E$ , the second is  $L - E$ , the third  $E - L$  and the fourth  $L - L$ . Thus, the whole integral is decomposed into 16 terms: 4 Taylor-Taylor, 8 mixed Taylor-Gaussian, and 4 Gaussian-Gaussian types of integrals. In terms of performance, this decomposition is not expensive compared to the global runtime, since the Taylor expansions are evaluated extremely fast, and it is sufficient to take as low as 3 evaluation points for different-conductor Gaussian quadratures; a thorough analysis of these costs is included in Section 5.6.

## 5.5 Code organization: Integral calculation blocks

We are now able to complete the description of the flow of the conduction modes method, by expanding in detail the two integration blocks contained in the flow in Fig.4.6.

These details are contained in the flows in Figs.5.7 and 5.8. They reflect the calculations that have been detailed, for the *RL/MQS* case, in this chapter. Extensions to the *RLC* case will be discussed in the following chapter.

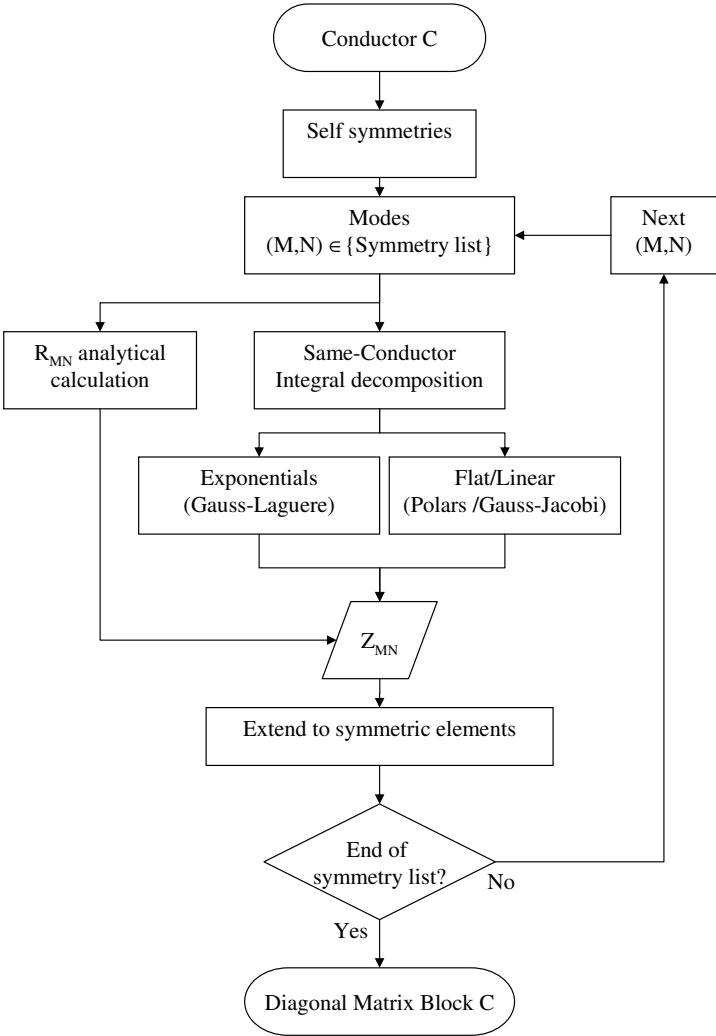


Figure 5.7: Flow for the computation of a matrix block for the same conductor.

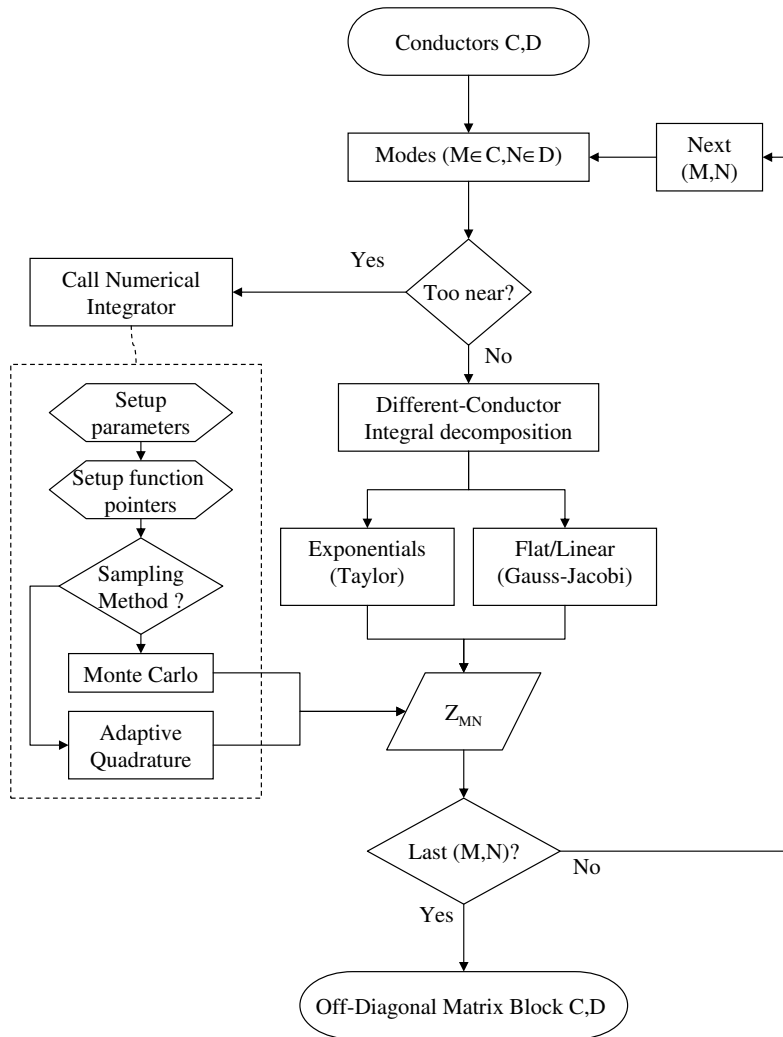


Figure 5.8: Flow for the computation of a matrix block for the different conductors.

## 5.6 Performance/accuracy analysis

Throughout the previous section, we have introduced several techniques for dealing with specific integrals. All of these techniques involve some parameter that determines the performance/accuracy trade-off for that particular calculation.

These parameters are:

- $G_{lag}$ : number of points in the Gauss-Laguerre quadrature rule for same-conductor integrals with exponential decays; we will discriminate between  $G_{lag}^{(s)}$  for the case when there is exponential decays in only one dimension, and  $G_{lag}^{(d)}$  when the decay is on both dimensions.
- $G_{jac}$ : number of points in the Gauss-Jacobi quadrature rule for linear/flat contributions.
- $T_s$ : order of Taylor polynomials for the  $L-L$  term in the same-conductor integrals of type [H,V].
- $T_d$ : order of Taylor polynomials for the different-conductor integrals.
- $G_d$ : number of points in the Gauss-Jacobi and Gauss-Legendre quadrature rules for linear and flat terms in different-conductor integrals.
- $\rho_{cut}$ : the cut-off value where the two polar expansions are joined for same-integral flat terms.

The impact of these parameters must also be weighted by the number of times they appear in evaluation of integrals. For example, we have seen that using the methods in Section 5.4 we can account for all the contributions for each type of integral in table (5.1). The number of calls to transcendental functions  $N_{calls}$  is given by,

$$N_{calls} = 4 \left( G_{jac} N_L + G_{jac}^2 N_{LL} + N_{EE} \right) = \begin{cases} 4 + 8G_{jac} + 4G_{jac}^2 & [\text{H, V}] \\ 16G_{jac} & [\text{H, H}] \\ 4 + 8G_{jac} & [\text{H, C}] \\ 16 & [\text{C, C}] \end{cases} \quad (5.31)$$

where  $N_E$  is the number of terms with a single linear ( $L-F, F-L$ ) contribution,  $N_{LL}$  is the number of  $L-L$  terms, and  $N_{EE}$  is the number of  $E-E$  terms. (Taylor contributions cost only one call, since the exponentials for each mode  $j$  can be evaluated once per mode at setup time, stored and reused for every matrix element  $L_{ji}$ ). Similar decompositions hold for same-conductor integrals.

In this section, we will analyze in detail the convergence of integrals with respect to these parameters. In carrying out these analyses, we will compare against the two different references mentioned in the introduction to this chapter: Monte Carlo (MC) [89] and Adaptive Quadrature (AQ) [87].

In order to avoid bias associated with different integration method, as well as the overheads they incur, we will use, for comparison of performance, the number of CPU cycles. This number is obtained using standard tools; we adopt the *quantify* package from IBM/Rational [90]. Although this cycle count is both machine- and compiler-dependent, it provides an easily implementable way of avoiding an expensive comprehensive search through all the instructions and sub-instructions of each of the methods.

Concerning the source of improvements in runtimes with respect to these standard methods, they have two distinct components:

1. the main source of savings derives from the approximation of the integrals for different conductors, which is controlled by the parameters  $G_d$  and  $T_d$  (see Section 5.4);
2. the reduced runtime is then dominated by the same-conductor integrals, and further gains are obtained by applying the approximations for same-conductor integrals, with  $G_{lag}$  as the critical parameter (see Section 5.3).

In the rest of this section, we will analyze, separately and in detail, the impact of the integrals and parameters enumerated above. Overall runtimes are found in next section.

### 5.6.1 $T_d$ and $G_d$ sensitivity

Approximation of integrals for different conductors involves two parameters that determine the performance/accuracy trade-off (see Section 5.4):  $T_d$ , the order of the Taylor expansions for the function  $F(\rho)$  for exponential contributions; and  $G_d$ , the number of values taken for each linear interval. In this section, we show that for our purposes, it suffices to set  $G_d = 3$  and  $T_d = 2$ .

Computing this integral demands the evaluation of an order- $T_d$  Taylor polynomial at  $3G_d$  points on the  $x$ -axis, according to the Gauss-Legendre  $G_d$ -point rules:  $G_d$  within  $[x_0 - w', x_0]$ , plus  $G_d$  in  $[x_0, x_0 + w - w']$ , and  $G_d$  in  $[x_0, x_0 + w]$ .

In terms of cost, parameter  $T_d$  has no incidence on the total cost of integration, for the range  $0 \leq T_d \leq 3$ . This was verified by obtaining exactly the same number of cycles in *quantify* [90] for all values of  $T_d$  in this range. The reason is that, for  $n > 0$ , the Taylor coefficients  $p_n$ , eq.(5.27), and the analytic integrals  $J_n$ , eq.(5.29), only require transcendental function evaluations already included in  $p_0$  and  $J_0$ . They only add more elementary arithmetic that does not affect the total CPU cycle count<sup>7</sup>.

<sup>7</sup>This is an empirical observation, tested on several different processors, as well as compilers.

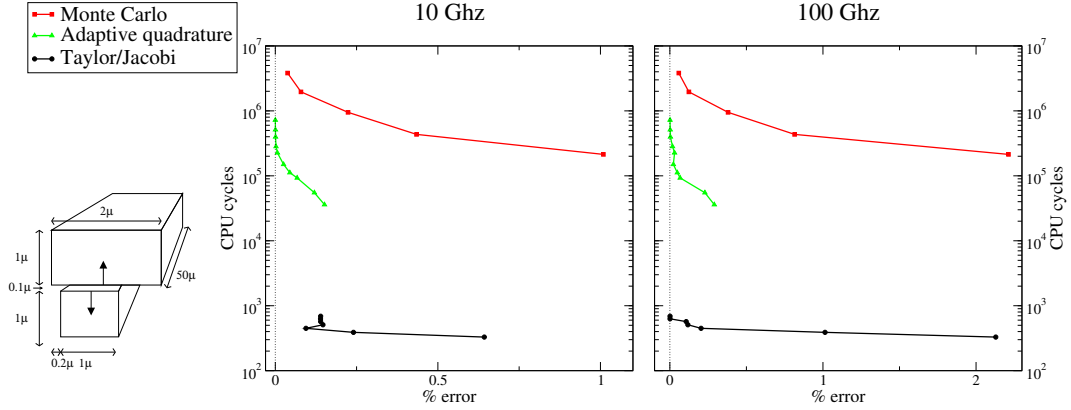


Figure 5.9: Accuracy/cost trade-off of Taylor-Jacobi integration for different-conductor integrals, varying the parameter  $G_d \in [1, 7]$  and fixing  $T_d = 3$ , compared to adaptive quadrature and Monte Carlo methods: at 10 GHz (left) and 100 GHz (right), for the configuration shown at right.

On the other hand, the CPU cycle count depends linearly on  $G_d$ , which is evident from observing that each point in the Gauss-Jacobi rule demands one Taylor expansion.

Fig. 5.9 displays an extreme situation, whereby the two modes participating in the integral show exponential decays from borders separated by  $0.1\mu$ . The integrals are computed at 10 GHz and 100 GHz and the material of both wires is copper, i.e.  $\delta \approx 0.66\mu$  and  $\delta \approx 0.21\mu$  respectively.

For this configuration, we compare the cost and accuracy of our approximations against the standard references: fixing  $T_d = 3$ , we vary  $G_d$  in the range  $1 \leq G_d \leq 7$ , and plot the error, defined as the variation from a reference obtained with AQ in high precision mode. For AQ, we modify the maximum number of calls to the integrand within the allowed ranges<sup>8</sup> and compute the error in the same manner.

Both of these methods are deterministic, and therefore the error for a value at a certain precision level is the difference between this value and the asymptotic exact value. On the other hand, MC is stochastic; for any level of precision (i.e number of function calls, which we vary from  $10^4$  to  $2 \times 10^5$ ), we compute the same integral a large number of times<sup>9</sup> and define the error as the standard deviation for the distribution of values.

The plots in Fig. 5.9 show more than 2 orders of magnitude improvement, with respect to AQ, by applying the Taylor/Jacobi method, and more than 3 orders of magnitude with respect to MC. The detailed behavior of errors with respect to the parameters  $G_d, T_d$  is shown in Fig. 5.10. We observe the following:

<sup>8</sup>For 2-dimensional integrals, the minimum number of calls in BDCUHRE [87] is hard-wired at 195, which correspond to the minimum precision/lowest CPU cycles of the AQ data in Figs. 5.9 and 5.12.

<sup>9</sup>Nearly normal distributions are always obtained, with as few as 1000 values.

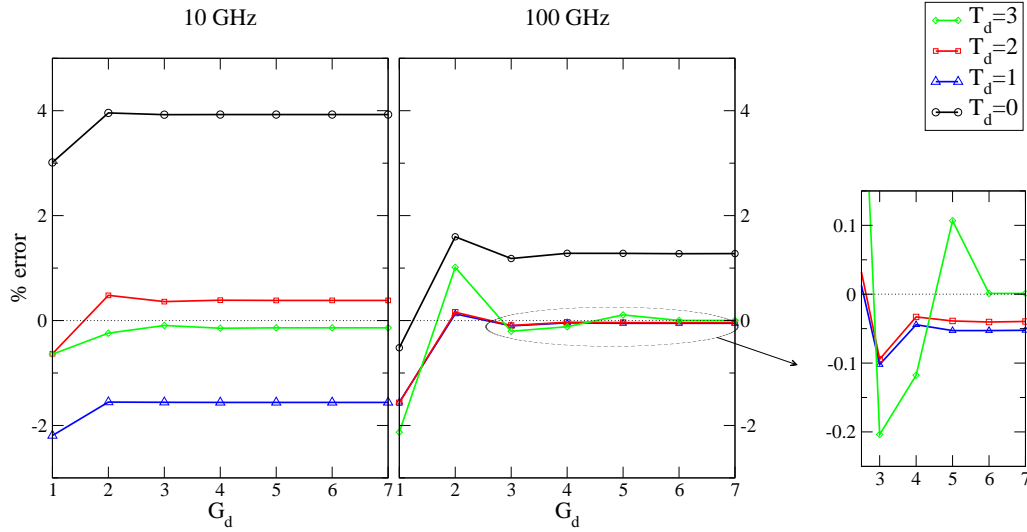


Figure 5.10: Convergence of Taylor-Jacobi as a function of the number of points for the Gauss-Jacobi rules ( $G_d$ ), and the order of the Taylor polynomial ( $T_d$ ), for the configuration in Fig. 5.9, at 10 GHz (left) and 100 GHz (right, with detailed blow-up).

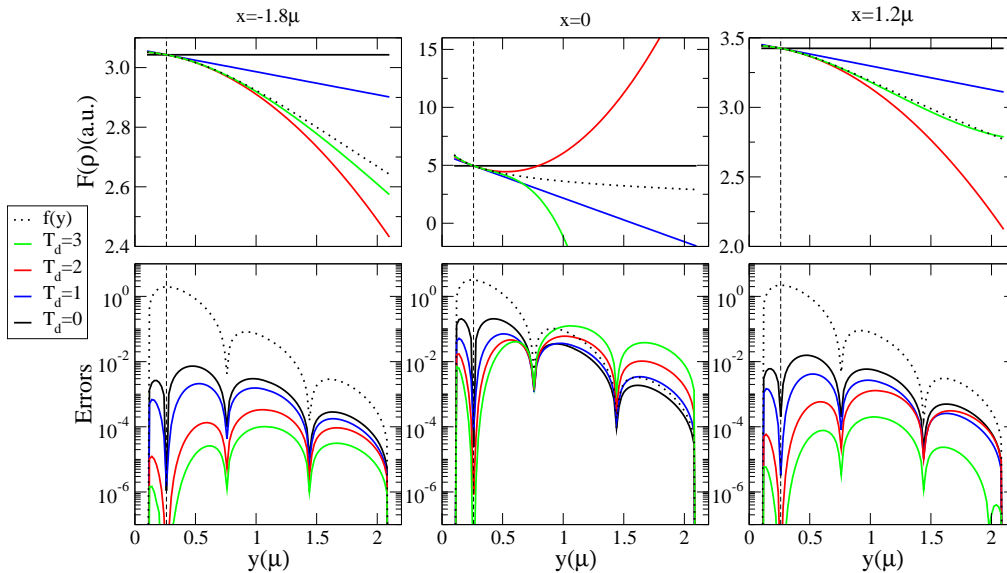


Figure 5.11: Taylor approximations for  $F(\rho)$  (top graphs); and errors for  $\xi_y F(\rho)$ , with dotted lines indicating the value (bottom), as a function of  $y$  and for three different values of  $x$ ; the configuration is the one shown in Fig.5.9, at 100 GHz; dashed vertical lines show the location of the peak for  $\xi_y$  at  $y_p \approx 0.657\mu$  (see Fig.5.6).

- errors become insensitive to  $G_d$  for  $G_d \geq 3$  at 10 GHz; the same holds with  $T_d=0,1,2$  at 100 GHz;
- order-2 and order-1 Taylor expansions show insignificant differences at 100 GHz (where  $\delta \ll w, h$  for both conductors);
- at 100 GHz, and for low values of  $G_d$ , order-3 Taylor deviated further than order-2 and order-1;
- for practical purposes, we are satisfied with errors smaller than 1%, so that setting  $G_d = 3$  and  $T_d = 2$  is appropriate for all cases.

The apparent contradiction of the second and third points above are explained by analyzing in detail the origin of errors for the Taylor approximation. As mentioned in Section 5.4, the weight function  $\xi_y$ , is peaked at  $y_p = y_0 + h - \varepsilon$  (see eq.(5.25) and Fig.5.6b). For the configuration we are presently considering,  $y_p \simeq 0.53\mu$  at 10 GHz and  $y_p \simeq 0.26\mu$  at 100 GHz. Taylor coefficients are evaluated at this value.

In Fig.5.11, we investigate in detail the behavior of these approximations for different regions of the integration domain. First we choose three values of the  $x$ -variable (i.e. the “linear” dimension, in the sense that there is no exponential decay on  $x$ ). These three values correspond to  $x_0 - w'$ ,  $0$ ,  $x_0 + w$  (the two extremes of the interval, and the minimum value). For each of these values, we plot - on the top graphs of Fig.5.11 - the different orders of Taylor approximations centered at  $y_p$ , ranging from the constant ( $T_d = 0$ ) to the cubic function ( $T_d = 3$ ). We point out that, in the vicinity of  $y_p$ , the approximation always improves with increasing order, as expected.

However, for large  $y$ -separations from the peak, and particularly for the smallest value of  $x$ , the higher-order Taylor approximations deviate more than the lower-order ones. This is expected, since  $F(\rho)$  becomes steeper as  $x$  decreases, thereby raising the contributions of the higher-order derivatives, and thus the errors in the Taylor approximations. Strictly speaking, the radius of convergence for this expansion at  $x = 0$  is  $y_p$ : the Taylor series does not converge to the original function for  $|y - y_p| > y_p$ .

Since we are concerned with approximating the whole integrand, which includes the peaked weight function  $\xi_y$ , we also plot - on the lower graphs of Fig.5.11- the incidence of the errors discussed above<sup>10</sup>. The values of the original integrand are included as dashed lines, in order to compare magnitude of the errors with the value being estimated. We can observe that all errors vanish at  $y_p$  and the zeroes of  $\xi_y$  (these occur at intervals of  $\pi\delta \simeq 0.657\mu$ ). For the  $x = 0$  plots, there is a second peak contributing to the error for the higher-order approximations. These errors, associated to the higher-order approximations, can be reduced by carrying out another

<sup>10</sup>The relationship between the errors in these graphs and the ones at the bottom graph of Fig.5.10 is that the latter are a numerical integration of the former, using a  $3 \times G_d$  Gauss-Legendre rule.

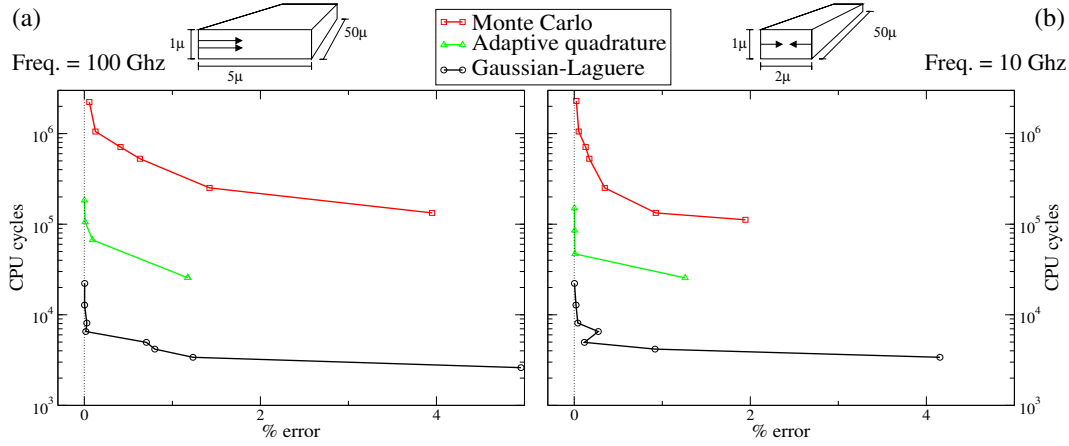


Figure 5.12: Accuracy/cost trade-off of Gauss-Laguerre integration for same-conductor integrals, varying the parameter  $G_{lag} \in [3, 28]$ , compared to adaptive quadrature and Monte Carlo methods: (a) at 100 GHz, for modes decaying from the same side and an aspect ratio of 5; (b) at 10 GHz, modes decaying from opposite side, aspect ratio of 2.

Taylor expansion at these secondary peaks, and joining the two expansions at the intermediate zero of  $\xi_y$ . The cost increase is a factor 2. The main conclusion from this discussion is that higher-order Taylor terms do not necessarily improve the convergence, and can actually deteriorate it, if they are included “blindly”. Although we have not encountered such situations, the necessity of the second-peak expansion depends on the relationship between the abscissas at the first and second peaks. We have repeated the exercise in this figures for separations as low as  $10^{-3}\mu$ , (i.e. less than 1/100th of a skin depth at 100 GHz), and errors remain bounded by 1%.

### 5.6.2 $G_{lag}$ sensitivity

For same-conductor integrals, we concentrate on the sensitivity to  $G_{lag}$  (the number of points in the Gauss-Laguerre rules, eq. (5.12)). By increasing this number, we increase also the number of calls to the function, as well as the precision.

In Fig.5.12 we compare, against the standard AQ and MC methods, the convergence of the Gauss-Laguerre integration method for values of  $G_{lag}$  ranging from 3 to 28, for the (W,W) integral of a conductor of dimensions  $1\mu \times 5\mu \times 50\mu$ , at a 10 GHz and 100 GHz. The determination of the errors in these graphs is the same as in the previous section.

From the results in Fig.5.12a, we conclude that the Gauss-Laguerre approximation of Section 5.3 improves one order of magnitude with respect to the better of the two standard integration methods.

As mentioned in Section 5.3.2, the efficiency of the Gauss-Laguerre strategy relies on the dominance of the order- $\delta$  exponential decay inside the conductors. Therefore, we expect the

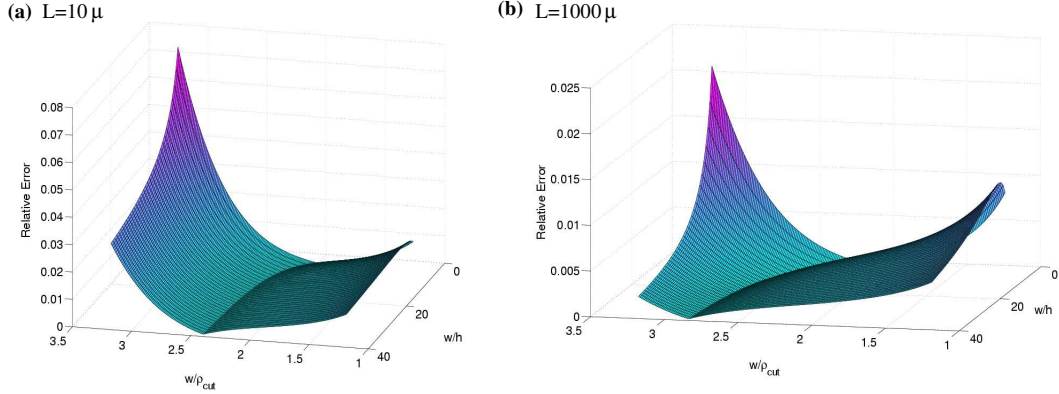


Figure 5.13: Errors for polar variables method applied to the flat integrals for [H,V] types, as a function of  $\rho_c$  and aspect ratio  $w/h$ , and for two different lengths:  $L = 10\mu$ (a) and  $L = 1000\mu$ (b).

savings shown in the previous graphs to increase with frequency. This is in fact the case: in Fig.5.12b we show that the savings are inferior when we decrease one decade. Also, we point out that the aspect ratio for this second example is 2 (instead of 5 for the previous case); we have observed that the standard integration methods improve as the aspect ratio decreases.

Other parameters that affect same-conductor integrals are:  $G_{jac}$ , number of points for Gauss-Jacobi in the case of same conductors, which plays the same role as  $G_d$  above, so we omit a special treatment (in practice  $G_{jac} \simeq 7$  is sufficient for any desired level of accuracy); and  $T_s$ , the order of Taylor approximations for the polar-variable integrals, which does not affect the cost (same argument as for  $T_d$  above), and we keep fixed at 4; and  $\rho_c$ , which is analyzed next.

### 5.6.3 $\rho_c$ sensitivity

In computing the flat  $L - L$  term for [H,V] same-conductor integrals, we carry out two Taylor expansions in the polar variable  $\rho$ , and joined these expansions at a value  $\rho_c$  (see Sec. 5.3.3).

As in the previous Taylor expansions for different conductors, the cost of the expansions does not vary significantly with the order of the polynomials. Again, this is because higher orders only add elementary arithmetic, but do not require new transcendental function evaluations. For all our calculations, we set the order of these expansion to 4, incurring in 13 such evaluations, 7 square roots, plus sums and multiplications in a number that does not exceed 100.

By comparison, the AQ method needs, on average several thousand integrand evaluations, with one transcendental function call for each of these. In terms of CPU cycles, we observe three orders of magnitude improvement, from  $O(10^5)$  to  $O(10^2)$ . We do not plot these comparisons, since there are no control parameters to regulate the number of calls in our approximation.

Concerning the errors for this calculation, we point out that they are sensitive to the choice

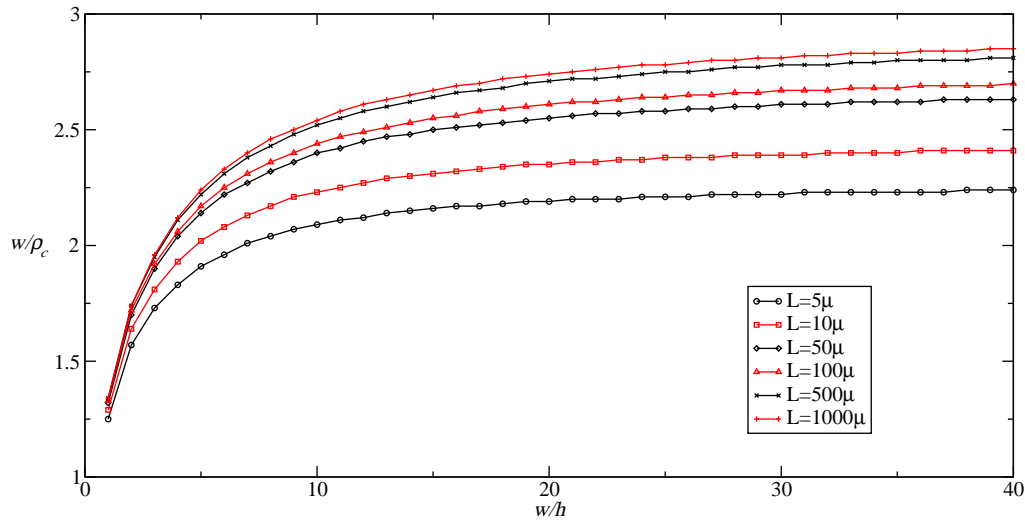


Figure 5.14: Curves  $\rho_c(w/h)$  for different  $L$ , result of minimizing errors in graphs 5.13.

of  $\rho_c$ . There are basically two variables that determine the optimal choice of  $\rho_c$ : length  $L$  and the aspect ratio  $w/h$ .

In Fig. 5.13 we plot these errors for two different values of  $L$ , as a function of  $\rho_c$  and  $w/h$ . Reference data is obtained with AQ integration. We observe that errors are minimized along a curve  $\rho_c(w/h)$  (in fact, they vanish, due to a change of sign). Minimization of errors defines a functional dependence for  $\rho_{cut}(w, L)$ , which we plot in Fig. 5.14. The smoothness of these functions suggest that they can be tabulated for interpolation at arbitrary geometries, or also fitted to a model<sup>11</sup>. Using linear interpolation, we are able to obtain errors below 0.1 % for a wide spectrum of aspect ratios and lengths.

## 5.7 Examples

For *RL/MQS* extraction, we will always compare our results and runtimes against FastHenry [15]. It is a filament-based approach that decomposes conductors into a user-specified number of filaments whose dimensions can be tuned so as to capture greater detail near the conductors' surfaces. Concerning the use of FastHenry, we clarify that there are two options for tuning its performance:

- Solver type: can be either GMRES iterative, or LU decomposition; the advantage of the first ones is that for very large sizes, the cost grows, as a function of size  $N$ , like  $kN^2$ ,

<sup>11</sup>No satisfactory fit has been found yet; on the other hand, tabulation of the curves in Fig. 5.14 is straightforward.

where  $k$  is the average number of iterations; this is to be compared to the  $N^3$  growth of direct methods [86].

- Multipole acceleration: FastHenry can avoid direct matrix product by carrying out a multipole expansion; for very large system size, this can lead to significant space and performance improvements; this expansion conserves accuracy as long as wires are short; in practice, this condition demands a refinement which increases the total number of filaments<sup>12</sup>.

Optimal choice of these options depends on the size and structure of the underlying linear system. For small number of closely-packed filaments, it is advantageous to use LU decomposition, and to avoid the size increase due to the multipole refinement. With growing number of filaments, the comparative cost of solving the system becomes dominant, and it is convenient to switch to iterative methods. Since these carry out a large number of matrix-vector multiplications, it may be also be convenient to perform the multipole acceleration, despite the size increase demanded by the refinement. Another important feature of the multipole refinement is that it also produces, as a by-product, a preconditioner for the system matrix, which decreases the number  $k$  of iterations.

The first example is a large exploration of simple configurations, in order to validate the use of 4 side conduction modes per conductor; we use FastHenry in its default mode so as to assure accurate values; the other two examples are of two different sizes: first we show a small example of one signal wire with three parallel return paths; then we show a large power-and-ground grid example consisting of 215 wires. For the first one, the multipole acceleration is counterproductive, due to the increase in size. For the second one, this decision depends on the level of discretization. Choice of solvers depends, in both cases, on the number of filaments.

### 5.7.1 Configuration space exploration

First, we concentrate on the validity of the conduction modes method, by randomly exploring a large configuration space and computing the error of our method. As such, this verification does not concentrate on the specific numerical expressions developed in the previous sections, but is rather a “proof of concept” for the method. We obtain the same figures whether we use our approximation or a numerical integrator, such as the Adaptive Quadrature method [87] described above; FastHenry is used in its default mode. The following two examples focus on the gains accomplished by the recipes in this chapter.

We consider, as a “building block” for this exploration, loops of two wire, since any arbitrary configuration can be described in terms of these blocks. The guidelines are as follows:

<sup>12</sup>In FastHenry, the total size of the system  $N$  is the number of meshes, which is related to the number of filaments through  $N = n_f + n_s + n_c - 1$ , where  $n_f$ ,  $n_s$  and  $n_c$  are the numbers of filaments, sources, and conductors, respectively.

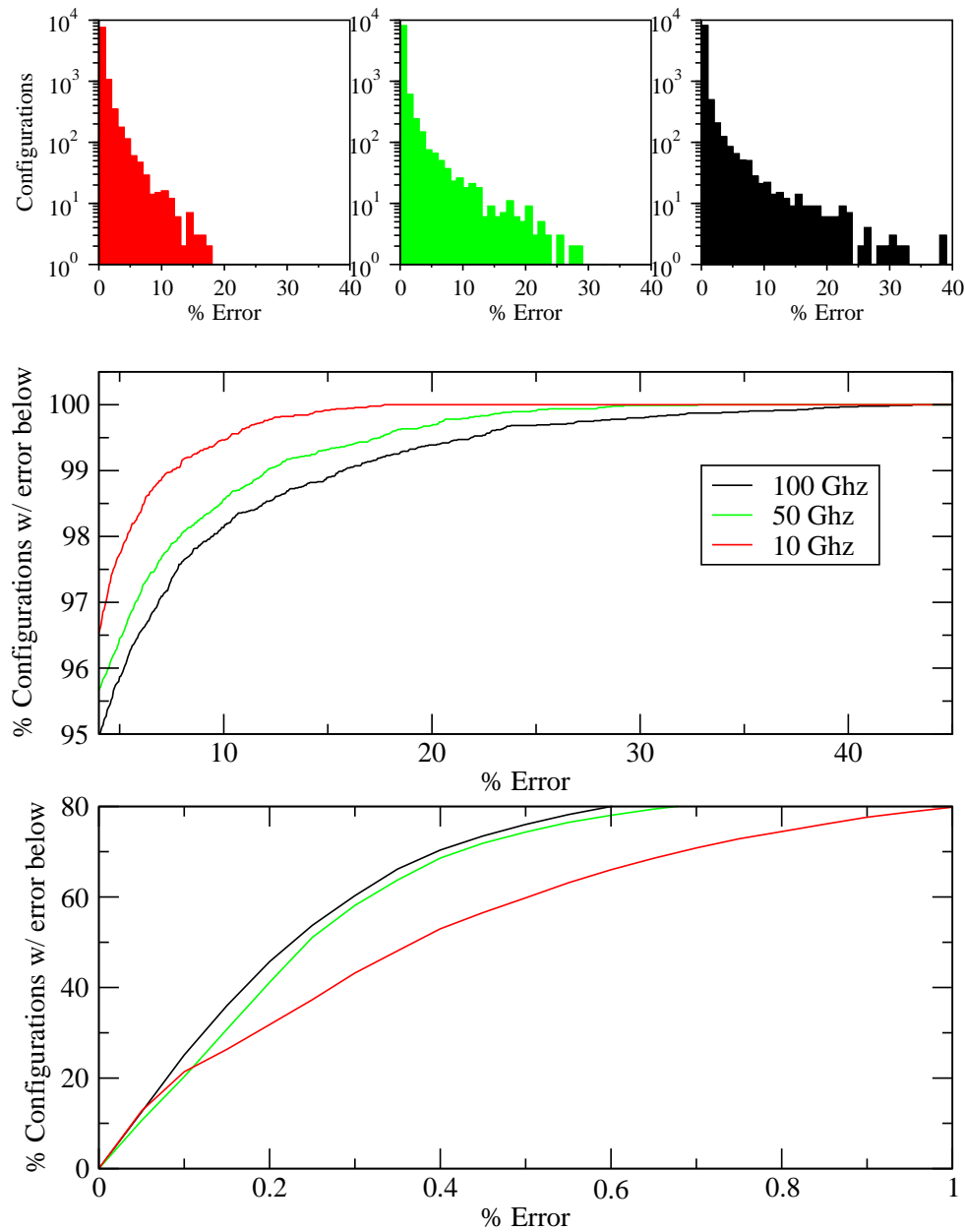


Figure 5.15: Distribution of errors for the random parameter space exploration: we show the normalized error histograms for 10000 two-wire configurations, at 10 GHz (top left), 50 GHz (top middle), 100 GHz (top right); as well as a detail of low-and high-error tails of the cumulative histograms, showing that, for all three frequencies, more that 95% of the configurations have errors lower than 5% (Note the logarithmic scale on the y-axis of the histograms).

1. We restrict to two-wire configurations, and establish  $|Z_{loop}| = |R_{loop} + j\omega L_{loop}|$ , the modulus of the impedance of the loop formed by these two wires, as the magnitude of reference ( $Z_{loop}$  is the impedance computed for a bundle in eq.(2.11), section 2.2).
2. We fix the thickness of the two conductors at  $1 \mu$ , material copper, and three frequencies: 10, 50 and 100 GHz (i.e.:  $h$  is approximately  $1.5\delta$ ,  $3\delta$ , and  $5\delta$ , respectively).
3. We construct 10000 configurations at random, by choosing random values for the widths, lengths, and separations, within the ranges to<sup>13</sup>:

$$w_{1,2} \in [1, 10]\mu; x_{sep}, y_{sep} \in [0, 25]\mu; \ell_{1,2} \in [10, 50]\mu$$

4. For each configuration, we compute the relative error in  $Z_{loop}$ , using the conduction modes method, with respect to FastHenry at high precision.
5. We plot the histogram of these errors, as well as the percentile errors.
6. We investigate in depth the origin of the outliers.

In Fig.5.15 we show the distribution of errors for these parameter sweeps. We carry out the exploration for 10, 50 and 100 GHz, and observe that for all three cases, very few configurations show significant errors. Quantitatively, we can say that less than 5% of the configurations have significant errors, at 100 GHz; this number improves for lower frequencies: about 3% for 50 GHz and less than 2% for 10 GHz.

We have found that the outliers of these histograms correspond to configurations in which there is a large difference between the widths of the two wires, as well as a non-negligible overlap in the  $x$ -extensions. This situation, which further deteriorates with increasing frequency, is related to the major drawback within the conduction modes method: since they are functions defined for the whole conductor, they cannot capture effects due to the localization of currents at intermediate positions along a cross-sectional dimension. Typical example for this picture are the ground planes. The solution to this problem requires splitting the wide conductors in order to capture these details. This is a necessary task that is not yet developed; we discuss in Section 6.5 the issues concerning such an implementation.

We also observe that, on the low-error region of the distributions, the values for 100 GHz are slightly better than the ones for the lower frequencies. This is compatible with the fundamental concept behind conduction modes, which is to efficiently capture high frequency current crowding.

---

<sup>13</sup>Apart from these restrictions, we also impose the physical constraint that the volumes of the conductors do not overlap

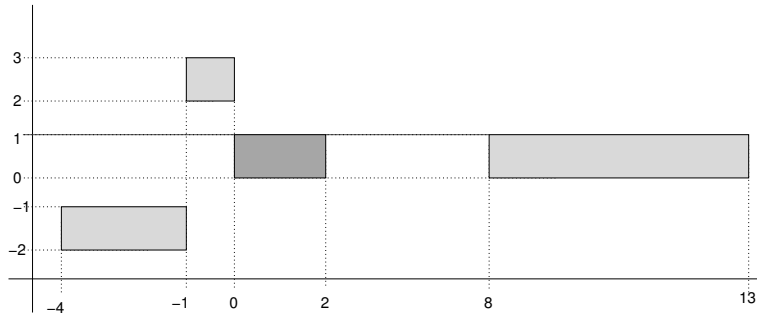


Figure 5.16: Bundle example configuration; all dimensions in  $\mu$ , lengths are  $50\mu$ .

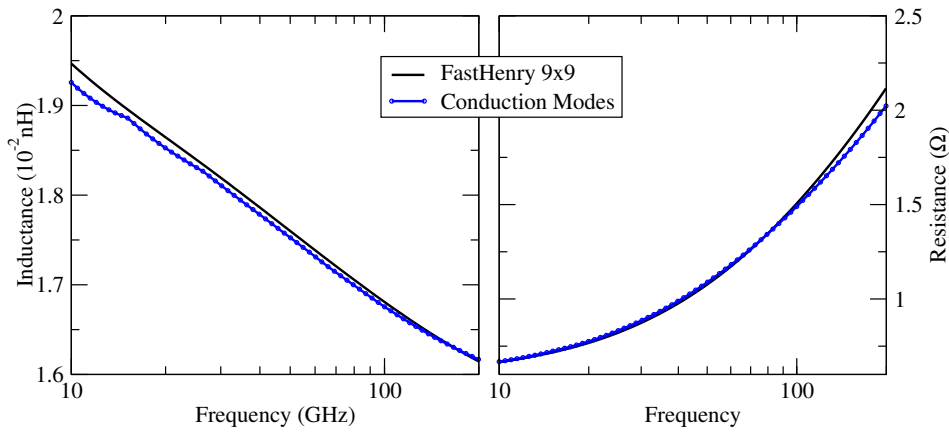


Figure 5.17: Loop inductance and resistance behavior for the example 5.16, comparing 4 conduction modes against FastHenry at high precision.

### 5.7.2 Bundle example

Consider the test example shown in Fig.5.16. It corresponds to a typical bundle example, consisting of one signal wire (darker shading in the figure) and three return paths.

We compute the loop impedance and use FastHenry, with each wire decomposed into 81 filaments as reference for accuracy; this comparison is shown in Fig.5.17. The total size of the linear system contains 324 unknowns in FastHenry vs 16 for CM. The graphs on Fig.5.18 contain the percentage error for this curve, compared against data issuing from FastHenry with increasing precision levels.

Note that errors for the CM method are small for inductance at high frequencies and for resistance at low. This corresponds to the relative importance of each magnitude: for this example,  $\omega L/R \approx 1$  at 10 GHz and  $\omega L/R \approx 0.1$  and at 100 GHz. The precision of CM, using only 4 modes per conductor, is comparable to that of  $7 \times 7$  for high frequency inductance, where it is important.

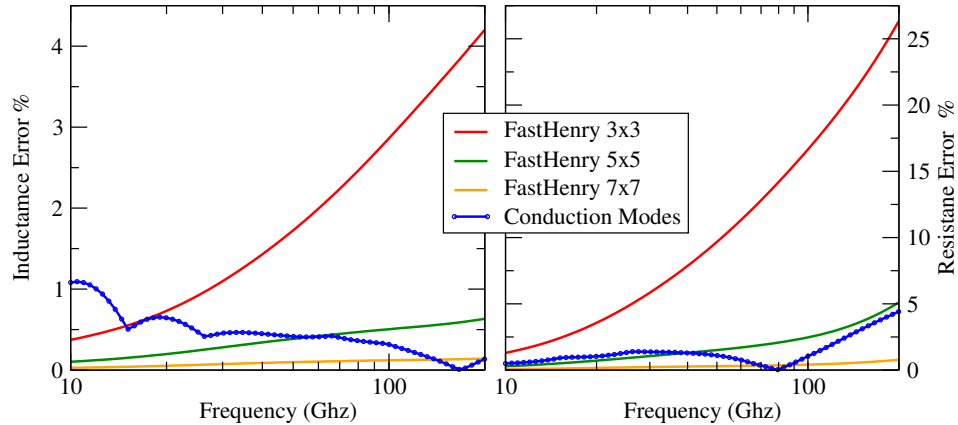


Figure 5.18: Relative errors against reference, for different levels of FastHenry precision and 4 conduction modes per conductor.

Run times for the above example, comparing against different levels of accuracy for FastHenry, are displayed in the first column of Table 5.2. They were all computed on a Xeon 3.0GHz processor, averaging over 100 identical calls for each method, for the configuration at 100 GHz (runtime values are insensitive to frequency). The runtimes show less than 0.5% dispersion. Concerning the FastHenry computations, they were all performed without the multiple refinement, owing to the observation that, for this configuration, refinement involves a multiplication in size by a factor 8. For the solver, the first three entries in the table were done with LU decomposition, whereas the last one was done with GMRES.

For the conduction modes runtimes, we observe that one order of magnitude is gained, with respect to the AQ numerical integration, in applying the Taylor approximations for different conductors; with respect to this reduced runtime, a further order of magnitude is obtained by applying the same-conductor methods. Compared to the same-precision level of FastHenry, there is an improvement of two orders of magnitude in total runtime.

### 5.7.3 Power and ground grid

We next consider a larger example, consisting of a configuration representing a power and ground grid, Fig. 5.19. Total dimensions are  $1\text{mm} \times 1\text{mm}$ , with 5 wires in each grid. The orientation of the wires in the top grid is perpendicular to the orientation of wires for the lower grid. The cross sectional dimensions are  $5\mu \times 2\mu$  for the top grid, and  $10\mu \times 2\mu$  for the lower one. Separation between the two grids is  $10\mu$ .

In order to model a power glitch for this structure, we place an AC current source between one node of the grid, e.g. the one located on the second wire of the top grid and the third wire of the lower one ( $x = 500\mu, y = 250\mu$ ). This excitation is the input for a circuit simulation

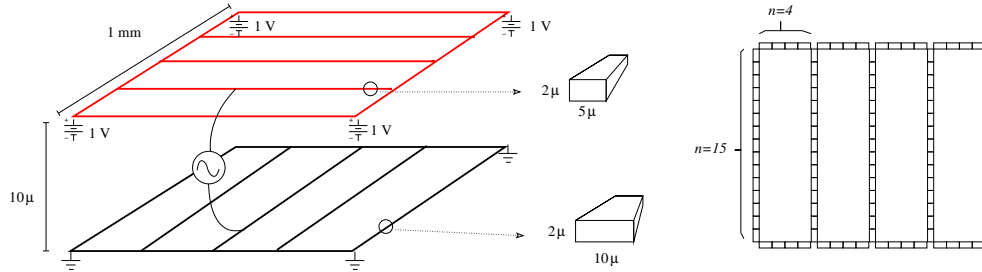


Figure 5.19: Configuration for the power and ground grid example of *RL* extraction.

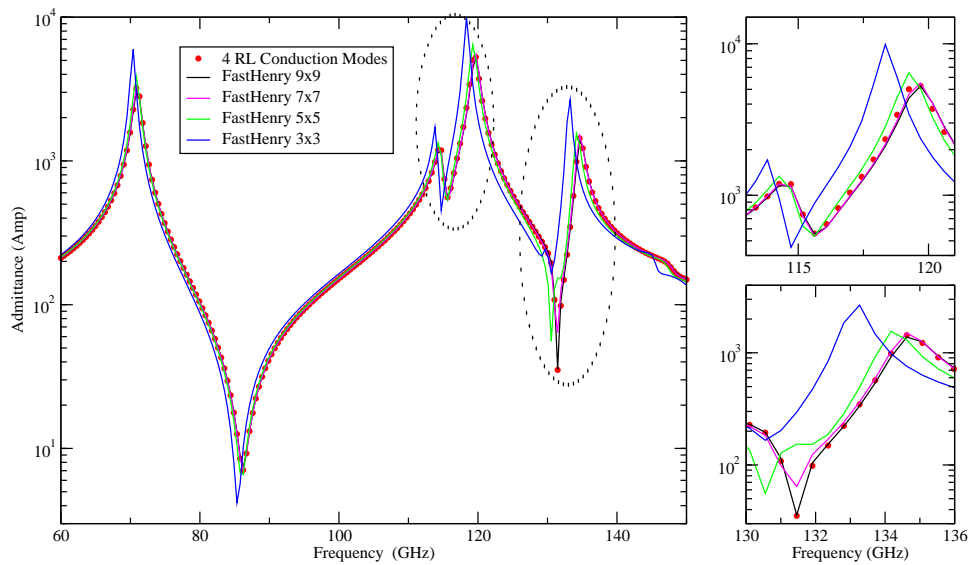


Figure 5.20: Input impedance for the power and ground grid example in Fig. 5.19, showing the first resonant peaks. Data for *RL* Conduction Modes is compared against FastHenry for different filament discretizations; insets at right show details near the peaks. Capacitance is extracted with FastCap.

using Eldo [53], consisting of 214 segments joining 208 nodes, resulting from the discretization shown in Fig. 5.19, with long wires split up into 15 segments and short ones into 4. This discretization assures that all segments are electrically small up to frequencies of order 100 *GHz* (i.e.  $\lambda \approx 3mm$ ). We compute the impedance of the grid as the ratio between the voltage at the excited node and the input current.

Capacitance among these segments is extracted with a discrete ES solver, FastCap [14] with a total number of 67584 panels. We compare for different methods of *R* and *L* extraction. In Fig. 5.20, we observe that CM precision for this case is better than that of FastHenry at 7×7 filaments per conductor (as in the previous example, we consider the 9×9 discretization as reference).

Runtimes for this example are shown in the last two columns of Table 5.2. FastHenry computations, for this case, were done with multipole acceleration and GMRES, for the three more accurate cases; for the 3×3 discretization, LU decomposition without multipole acceleration was optimal.

As in the previous case, we obtain two orders of magnitude improvement in runtimes, with respect to numerical integrations as well as compared to similar-accuracy FastHenry results. Contrary to the previous example, the gains for performing only the different-conductor approximations are very close to the ones for the full approximations. This is due to the fact that the savings for same-conductor integrals grow linearly with the number of conductors, whereas the ones for different-conductor integrals grow quadratically; a detailed cost estimation is included at the end of next section.

Table 5.2: Sizes and Runtimes for the different methods considered: "CM Taylor" refers to the savings obtained with the different-conductor approximations (Section 5.4); "CM Taylor/Gauss" refers to the complete approximations in this chapter; "CM - AQ" is using AQ algorithm for all integrals.

Method	Size Bundle	Runtime (ms) Bundle	Size Grid	Runtime (s) Grid
FastHenry 9x9	324	1185.3	21,834	4199
FastHenry 7x7	196	500.1	12,936	1718
FastHenry 5x5	100	150.9	6,600	633
FastHenry 3x3	36	25.6	1944	62
CM - AQ	16	949.0	860	2925.11
CM Taylor	16	130.1	860	31.65
CM Taylor/Gauss	16	6.5	860	23.19

## 5.8 Discussion

In the previous section, we have verified empirically that conduction modes introduces two orders of magnitude improvement with respect to similar-accuracy filament-based methods; similar comparison is established against the use of conduction modes with standard numerical integration methods.

An important difference between the two examples lies in the impact of solve runtime  $t_{solve}$  with respect to the total runtimes expressed in Table 5.2. For the bundle example,  $t_{solve}$  is completely negligible (less than 1% and therefore difficult to measure); whereas for the grid, it is 6.67 sec, i.e. 30% of total runtime. This is expected, since this contribution grows cubically with increasing number of conduction modes. For 860 modes, this contribution is still not critical, but for much larger configurations, an iterative solver should be considered.

On the other hand, for a filament-based approach, and for equivalent levels of accuracy, the size of the system is such that cost is dominated by  $t_{solve}$ .

The most relevant feature of the conduction modes method is the savings in size, which are a factor 15 for the conduction modes with respect to FastHenry. This is similar to the ones reported in [32]. These savings are of a fundamental nature, as they respond to the fact that the conduction modes functions represent a more compact model, compared to piecewise-constant filaments, of the physical phenomenon related to skin effect.

Here, we have effectively translated these gains in system size into gains in runtime. For larger systems, with runtimes dominated by  $t_{solve}$ , these gains will depend on the solver method: if a factor 15 is maintained in size savings, then a factor  $15^k$  is expected for runtimes, with  $k$  the order of complexity for the solve method. This explains the two orders of magnitude improvement, for runtimes, with respect to FastHenry.

For very large problems, accelerated solvers are necessary even when using conduction modes. As mentioned above, these cost linearly in  $t_{solve}$ , i.e.  $k \simeq 1$ . The arguments of the previous paragraphs indicate that we would expect, when using conduction modes for these cases, to obtain a linear relationship between the savings in size and in runtime. However, these savings should in fact be larger, owing to the fact that accelerated solvers must always treat a certain number of closely-interacting wires in the direct manner, with  $k = 3$  for that part of the calculation [91]. Modeling with conduction modes reduces the size of all the components of the model, whether they interact closely or not. Assuming a factor 15 in size savings, the total runtime savings will result from a (geometry-dependent) average between a factor 15 for the cost of the accelerated interactions, and  $15^3$  for the non-accelerated ones. Thus, conduction modes obtains better-than-linear improvements in performance, even in the presence of accelerated solvers.

With respect to standard numerical integration methods, the origin of the runtime savings shown in Table 5.2 can be illustrated in the following manner: consider, for the sake of simplic-

ity, that each element computed with the numerical AQ integration has a cost  $Q$ , and that the savings for each different-conductor approximation reduces this cost by a factor  $K_d$ , whereas this factor is  $K_s$  for the case of same-conductor integrals (we have shown representative examples in Section 5.6, where  $K_d \geq O(10^2)$  and  $K_s = O(10)$ ). Then the costs associated with each of the conduction modes implementations are:

$$\begin{aligned} C^{(AQ)} &= \frac{Q}{2} (N^2 + N) \\ C^{(D)} &= \frac{Q}{2K_d} (N^2 + K_d N(m+1)) \\ C^{(S/D)} &= \frac{Q}{2K_d} \left( N^2 + \frac{K_d}{K_s} N(m+1) \right) \end{aligned} \quad (5.32)$$

where the supraindices indicate the different approximation methods presented in this chapter: “D” is for only different-conductor, and ”S/D” is for both the full acceleration scheme;  $N$  is the total number of modes, and  $m$  is the number of modes per conductor, as in (5.2). Thus the savings, are

$$\begin{aligned} S^{(D)} &= \left( \frac{1 + N^{-1}}{1 + K_d(m+1)N^{-1}} \right) K_d \\ S^{(S/D)} &= \left( \frac{1 + N^{-1}}{1 + K_d(m+1)(K_s N)^{-1}} \right) K_d \end{aligned} \quad (5.33)$$

For very large  $N$ , both of these values go asymptotically to  $K_d$  with a  $N^{-1}$  behavior; the rate of this tendency is a factor  $K_s$  larger for  $S^{(S/D)}$  than for  $S^{(S)}$ . This is precisely the situation for the power and ground grid example.

Instead, for relatively small values of  $N$  (compared to  $K_d$ ), the savings are of order  $N/(m+1)$  for  $S^{(S)}$  and  $K_s N/(m+1)$  for  $S^{(S/D)}$ . This represents the figures for the bundle example<sup>14</sup>. The two order of magnitude savings for this example have a great impact in the cost of high-frequency extraction, where a large number of configurations with few wires must be considered.

Concerning future work, further savings can be obtained, specifically for the same-conductor integrals, in precomputing them and applying an interpolation or parametrization techniques. We briefly discuss this subject in Section 6.3. Also, a systematic treatment of the outliers in Fig. 5.15 is necessary; this will be briefly discussed in Section 6.5.

<sup>14</sup>In fact, these values are enhanced by the application of the symmetries discussed in Section 5.1, having the effect of eliminating the factors  $(m+1)$  in the second and third lines in eq.(5.32).



# Généralisation des modes de conduction

## Résumé en français

*Ce chapitre est consacré au sujet de l'implémentation de la méthode RLC des modes de conduction, avec l'objectif de voir si celle-ci peut être étendue pour atteindre un solveur électromagnétique d'onde complète très efficace. Les modifications et/ou additions nécessaires pour cette tâche se situent à trois niveaux : en première instance, l'adaptation des méthodes efficaces d'intégration développées au chapitre 5 dans le domaine RL/MQS à celui RLC-onde complète (sections 6.1-6.3) ; deuxièmement, la description d'une gamme plus étendue des phénomènes que ceux présentés au chapitre 4, ce qui demande l'extension des bases des modes de conduction (section 6.4); finalement, la compréhension des géométries arbitraires (section 6.5). Une quatrième source de modifications, qui n'est pas discutée dans cette thèse est celle associée aux médias multicouches tels que le substrat ou les configurations à diélectriques multiples. Nous renvoyons, pour cette tâche, à la littérature portant sur des méthodes de fonction de Green équivalente. Le contenu de ce chapitre est la traduction d'un travail en cours, aussi bien que des propositions de travail pour l'avenir. En tant que tels, nous utiliserons souvent des arguments intuitifs résultant du raisonnement physique d'un côté, et de notre expérience avec les modes de conduction de l'autre. En ce sens, ce chapitre peut être considéré comme une discussion générale sur les méthodes présentées dans les deux chapitres précédents.*



## Chapter 6

# Generalization of conduction modes

This chapter is dedicated to issues concerning implementation of *RLC* conduction modes. The objective is to address the question of whether this methodology can be expanded into an efficient fullwave Electromagnetic solver. So far, we have developed a method for modeling currents inside the conductors' volume and charges on its surfaces, and presented examples of significant savings for a certain type of structure, namely the TL-type of configuration. Furthermore, we have shown in the previous chapter that, for *RL/MQS* extraction, this can be implemented in an extremely efficient manner. The aim is to be able to obtain savings, in size and computation, for more general type of problems.

The modifications and/or additions necessary for upgrading this tool into an EM solver come in three general categories:

- ***RLC* efficiency:** going from the *RL/MQS* to *RLC* demands inclusion of  $P$  elements, as well as an increase in the complexity in computing the  $L$  matrix elements; in Sections 6.1, 6.2 and 6.3, we immerse into this complexity, and devise an efficient strategy to carry out these calculations.
- **Generalized waves:** in Chapter 4 we constructed the *RLC* conduction mode basis retaining only quasi-TEM-type modes with net current entering the conductors; we consider, in Section 6.4, what kind of modes must be included in order to obtain a more general description.
- **Arbitrary geometry:** only Manhattan-type geometry has been developed so far; the general case is more complex. Another complication arises from configuration in which the dimensions of the conductors differ dramatically (typical example: ground planes). In Section 6.5 we briefly discuss the solutions needed for these types of problems.

Another issue which deserves special attention, and will not be discussed in this Thesis, is the incorporation of effects of inhomogeneous media. Examples in the IC domain include multi-

layered dielectrics and substrate. At present, our team is cooperating with researchers from the University of California in Santa Barbara [61], investigating on Green-function methods for this task [18, 19, 92]. In a nutshell, they consist in considering the effect of the multiple media by an equivalent Green function, that replaces the kernel  $\frac{e^{-jk_0r}}{r}$  for our homogeneous space formulation. Applications of this type of technique are found in FastMaxwell [13]. For the adaptation of these methods to the conduction modes method, we expect similar complications to the ones outlined in [93].

The contents of this chapter constitute ongoing work, as well as propositions for future lines of work. As such, we will often be indulging in intuitive arguments arising from physical reasoning on one side, and our experience with the conduction modes on the other. In this sense, this chapter can be considered as a general discussion on the methods presented in the previous two chapters; therefore, we omit conclusions at the end of the present one.

## 6.1 $L$ - and $P$ -matrix elements for $RLC$ extraction

While computing matrix elements for conduction modes, we noticed the following property: the capacitive ( $P$ ) contribution nearly cancels out with the inductive ( $L$ ) one for the case where the two modes  $i, j$  correspond to waves traveling in the same sense on the  $z$ -direction (in other words, when  $\eta_i = \eta_j$ ), and are practically the same when the modes are opposing waves in  $z$  ( $\eta_i = -\eta_j$ ).

This is strictly a high frequency phenomenon. In fact, in the (infinite-frequency) limit  $\delta \rightarrow 0$ , the  $L_{ij}$  and  $P_{ij}$  contributions with  $\eta_i = \eta_j$  exactly cancel each other out. This limit can also be seen as the perfect conductor condition, leading to the familiar relationship  $LC = c^{-2}I$  ( $I$  is the identity matrix) [4, 80].

The origin of this near cancellation and doubling stems from the observation that the  $L$  contribution for these modes may be written as

$$L = \iint_{y,z} \left( \int_0^d e^{-x/\delta} f(x, y, z) dx \right) dy dz, \quad (6.1)$$

whereas the  $P$  contribution becomes:

$$P/\omega^2 = \pm \iint_{y,z} f(0, y, z) dy dz, \quad (6.2)$$

both with the same integrand function  $f(x, y, z)$ ; the  $\pm$  corresponds to same- or different-orientation on the  $z$  axis.

In other words: the  $P$  matrix elements, divided by  $\omega^2$ , are a zero-th order version of the

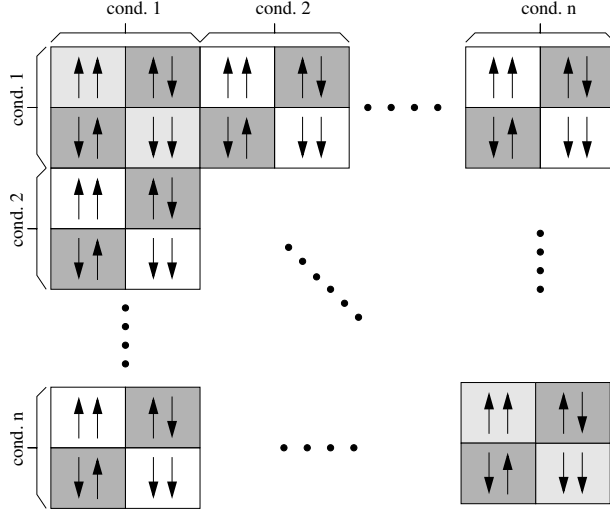


Figure 6.1: Structure of the matrix in (4.20) according to the propagation in  $z$  (arrows). The darker boxes represent larger elements in that part of the matrix (multiplied by a phase factor  $e^{\pm jk_0\ell}$ ); the diagonal elements contain the contribution of the  $R$  elements.

$L$  ones. This collapse is carried out by the peaked form of the weight functions  $\xi_x, \xi_y$ . These weight functions can be seen as quasi-Dirac<sup>1</sup>  $\delta_D$  for the  $L_{ij}$  integral, whereas the  $P_{ij}$  is the same integrand multiplied by an exact Dirac  $\delta_D$ .

Given this state of affairs, we always pair up the combination  $j\omega(L_{ij} - P_{ij}/\omega^2)$  (see (4.20)). Otherwise, we would be incurring in large numerical errors by computing them separately and canceling out two similar magnitudes, each with a certain numerical error.

Apart from being larger, the  $\uparrow\downarrow$  and  $\downarrow\uparrow$  elements are also dominated by a phase factor  $e^{\pm jk_0\ell}$ , which result from the  $z$ -weight functions,

$$\xi_z(z) = \begin{cases} (\ell - z) \cos(k_0 z) & (\uparrow\uparrow), (\downarrow\downarrow) \\ \frac{e^{\pm jk_0\ell}}{k_0} \sin((\ell - z)k_0) & (\uparrow\downarrow), (\downarrow\uparrow) \end{cases} \quad z \in [0, \ell] \quad (6.3)$$

(the weight functions, defined in eq.(5.5) are the result of reducing from two variables to one; here, we have exemplified with a same-conductor integral on  $z$ , the general case being similar in nature.)

Therefore, decomposing into forward- and backward-traveling waves results in a matrix  $Z = R + j\omega(L - P/\omega^2)$  in (4.20), that has a checker-board structure as shown in Fig.6.1.

<sup>1</sup>The Dirac  $\delta_D$  is a generalized function defined as:  $\int_a^b \delta_D(x) dx = \begin{cases} 1 & \text{if } 0 \in [a, b] \\ 0 & \text{else} \end{cases}$

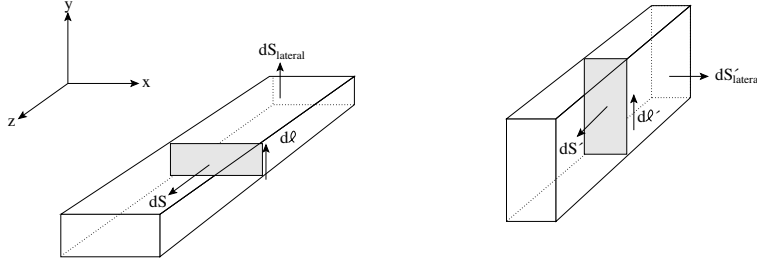


Figure 6.2: Schematic of geometry for calculation of  $P$  elements using Stokes' theorem.

### 6.1.1 $P$ integrals for different conductors using Stokes' Theorem

When computing a  $P_{ij}$  matrix element of the form (4.14c), it is convenient to transform the surface integrals into volume ones. This is done by successively applying Stokes' theorem twice. The reasons for the convenience mentioned above will be evident at the end of this calculation. The calculation that follows is valid only for the case of different conductors.

The  $P$  integrals for surface charge functions that are given by (4.18), are written as

$$\begin{aligned}
 P_{ij} &= \frac{1}{4\pi\epsilon} \int_{S'} \int_S \frac{e^{-jk_0 d}}{d} (\mathbf{w} \cdot \mathbf{dS}_{lateral}) (\mathbf{w}' \cdot \mathbf{dS}'_{lateral}) \\
 &= \frac{1}{4\pi\epsilon} \int_0^L \oint_C \int_0^{L'} \oint_{C'} \frac{e^{-jk_0 d}}{d} (\mathbf{w} \cdot (\mathbf{dz} \times \mathbf{d\ell})) (\mathbf{w}' \cdot (\mathbf{dz}' \times \mathbf{d\ell}')) \\
 &= \frac{1}{4\pi\epsilon} \int_0^L \oint_C \int_0^{L'} \oint_{C'} \frac{e^{-jk_0 d}}{d} (\mathbf{d\ell} \cdot (\mathbf{w} \times \mathbf{dz})) (\mathbf{d\ell}' \cdot (\mathbf{w}' \times \mathbf{dz}')) \quad (6.4)
 \end{aligned}$$

where  $d = |\mathbf{r} - \mathbf{r}'|$  and the elements of area  $\mathbf{dS}_{lateral}$  and length  $\mathbf{d\ell}$  are shown in Fig6.2. With respect to the original expression (4.14c) we have adopted here the more compact notation  $\mathbf{w} \equiv \mathbf{w}_i^*(\mathbf{r})$ ,  $\mathbf{w}' \equiv \mathbf{w}_j(\mathbf{r}')$ .

In the final expression in (6.4), we have expressed the integrals on the lateral faces of the conductors as a decomposition of one along the  $z$ - axes plus one along a closed loop that contours the conductors' cross-section.

Stokes' Theorem states,

$$\oint_C \mathbf{d\ell} \times \mathbf{f} = \iint_{S(C)} \mathbf{dS} \cdot (\nabla \times \mathbf{f}) \quad (6.5)$$

for  $S(C)$  a surface subtended by path  $C$  and  $\mathbf{f} : \mathcal{R}^3 \rightarrow \mathcal{R}^3$  non-singular on  $S(C)$ .

This theorem can readily be applied to the non-primed variables for the last expression in (6.4)<sup>2</sup> with  $\mathbf{f} = \mathbf{w}(\mathbf{r}) \exp(-jk_0d)/d$ ,

$$P_{ij} = \frac{1}{4\pi\epsilon} \int_0^L \iint_S \int_0^{L'} \oint_{C'} (\mathbf{dS} \cdot (\nabla \times (\mathbf{f} \times \mathbf{dz}))) (\mathbf{d\ell}' \cdot (\mathbf{w}' \times \mathbf{dz}')) \quad (6.6)$$

The first vector product in this integrand gives  $(-f_y, f_x, 0)$ , whose curl is,

$$-\frac{\partial f_x}{\partial z} \hat{\mathbf{x}} - \frac{\partial f_y}{\partial z} \hat{\mathbf{y}} + \left( \frac{\partial f_x}{\partial x} + \frac{\partial f_y}{\partial y} \right) \hat{\mathbf{z}} \quad (6.7)$$

Since the area element  $\mathbf{dS} = dx dy \hat{\mathbf{z}}$  is parallel to the  $z$ -axis (see Fig. 6.2), we retain only the last component of this curl; moreover, the un-primed integration is simply a 3-d integral over the volume of this conductor,

$$P_{ij} = \frac{1}{4\pi\epsilon} \int_V \int_0^{L'} \oint_{C'} d^3r \left( \frac{\partial f_x}{\partial x} + \frac{\partial f_y}{\partial y} \right) (\mathbf{d\ell}' \cdot (\mathbf{w}' \times \mathbf{dz}')) \quad (6.8)$$

Next, we perform the same procedure for the primed variables, with the difference that the function  $\mathbf{f}$  will be replaced by

$$\tilde{\mathbf{f}} = \left( \frac{\partial f_x}{\partial x} + \frac{\partial f_y}{\partial y} \right) \mathbf{w}' \quad (6.9)$$

After some lengthy algebra, and using the divergence-free condition<sup>3</sup> for both  $\mathbf{w}$  and  $\mathbf{w}'$  we obtain the final expression,

$$\begin{aligned} P_{ij} = & \frac{1}{4\pi\epsilon} \iint_{V, V'} \left[ \frac{\partial w_z}{\partial z} \frac{\partial w'_z}{\partial z'} \right. \\ & + \left( w_x w'_x + w_y w'_y - \left( w_x \frac{\partial w'_z}{\partial z'} + w'_x \frac{\partial w_z}{\partial z} \right) \tilde{x} - \left( w_y \frac{\partial w'_z}{\partial z'} + w'_y \frac{\partial w_z}{\partial z} \right) \tilde{y} \right) \frac{1 + jk_0d}{d^2} \\ & \left. - (\tilde{x}w_x + \tilde{y}w_y)(\tilde{x}w'_x + \tilde{y}w'_y) \frac{3 + 3jk_0d - k_0^2d^2}{d^4} \right] \frac{e^{-jk_0d}}{d} d^3r d^3r' \quad (6.10) \end{aligned}$$

where we have defined  $\tilde{x} \equiv x - x'$ ,  $\tilde{y} \equiv y - y'$ , i.e. the same relative variables  $x_-$ ,  $y_-$  that were used in the transformation (5.3).

We observe that all the terms in expression (6.10) contain a product of a component of  $\mathbf{w}'$  with a component of  $\mathbf{w}$  (or, in the original notation,  $\mathbf{w}_i^*$  and  $\mathbf{w}_j$ ). Hence, all terms contain the

<sup>2</sup>We are dealing with different conductors, therefore  $d \neq 0$  and the integrand is well-behaved.

<sup>3</sup>For example:  $\frac{\partial f_x}{\partial x} + \frac{\partial f_y}{\partial y} = \frac{e^{-jk_0d}}{d} \left( \frac{\partial w_z}{\partial z} + ((x - x')w_x + (y - y')w_y) \frac{1 + jk_0d}{d^2} \right)$

same exponential dependence  $e^{(\alpha_i^*x + \beta_i^*y + \eta_i^*z + \alpha_jx' + \beta_jy' + \eta_jz')}$ , that is common to the  $L_{ij}$  integral. This enables us to perform, at this stage, the same transformation as in Sec.5.2: adopt the variables  $\mathbf{r}_- = \mathbf{r} - \mathbf{r}'$ ,  $\mathbf{r}_+ = \mathbf{r} + \mathbf{r}'$  and obtain,

$$P_{ij} = \frac{1}{4\pi\epsilon} \int_V \left[ \eta_i^* \eta_j + ((t_i^* \eta_j + t_j \eta_i^*)x + (s_i^* \eta_j + s_j \eta_i^*)y - (t_i^* t_j + s_i^* s_j)) \frac{1 + jk_0 r}{r^2} - (t_i^* x + s_i^* y)(t_j x + s_j y) \frac{3 + 3jk_0 r - k_0^2 r^2}{r^4} \right] \xi_x \xi_y \xi_z \frac{e^{-jk_0 r}}{r} d^3 r \quad (6.11)$$

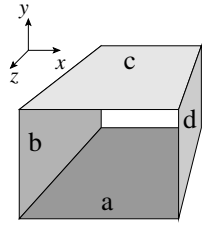
for the  $\mathbf{r}_-$  variables, where  $\xi_{x,y,z}$  are as in (5.5),  $t_{i,j}$  are the  $x$ -components and  $s_{i,j}$  are the  $y$ -components for modes  $i, j$  respectively (eq.(4.30)):

$$(t_i, s_i) = \left( \frac{\alpha_i}{e^{\alpha_i w_i} - 1} \right) \left( \frac{\beta_i}{e^{\beta_i h_i} - 1} \right) \frac{j\delta^2 \eta_i}{2} (\alpha_i, \beta_i)$$

Though this expression seems cumbersome, there are important advantages gained in using it instead of the usual surface integrals (4.14c):

1. We have observed that, when using the Adaptive Quadrature [87] method for numerical integration, the convergence of integrals that mix 2-d and 3-d terms is very poor. If we decompose the surface  $P$  integral into all its components, there are 2-d as well as 3-d contributions<sup>4</sup>. In that case, it is necessary to calculate them separately. Using expression (6.11) avoids this extra partitioning.
2. Expression (6.11) exhibits, at least for the case of different conductors, the property discussed in the previous section:  $L \simeq |P|/\omega^2$ . Effectively, if we form the combination  $j\omega(L - P/\omega^2)$ , then the constant factor in the  $P$  term is  $\frac{1}{4\pi\epsilon\omega^2} = \frac{\mu}{4\pi k_0^2}$ . Considering the first term in (6.11), plus the definition for the  $\eta = \pm jk_0$  in (4.34), we see that, in the case where the product  $\eta_i^* \eta_j > 0$  (i.e., when  $\eta_i = \eta_j$ ) then this first term cancels out with the  $L$  contribution. The following terms in (6.11) all contain at least one order of  $s$  or  $t$ , rendering them of order  $(k_0\delta)$  or higher. This explains the cancellation mentioned above.
3. Moreover, the argument in the previous paragraph can be extended to group all terms in (6.11) by the order  $n$  in which  $(k_0\delta)^n$  appears. This permits an  $RLC$  integration scheme for the  $z$ - component in terms of a series expansion in terms of powers of  $k_0 r$  and  $k_0 z$  (see Section 6.2.2). Coupled with the integration methods for  $x, y$ , shown in the previous chapter, we can use this result to efficiently compute all different-conductor integrals in the  $RLC$  formulation.

<sup>4</sup>This is precisely what is shown in the next section, for same-conductor elements, where Stokes' theorem does not hold.



$P^{(xx)}$			$P^{(xy)}$			$P^{(yy)}$			$P^{(yx)}$		
aa'	$r_a$	$I$	ab'	$r$	$I$	bb'	$r_b$	$I$	ba'	$r$	$I$
ac'	$r_c$	$e^{\alpha w}$	ad'	$r$	$e^{\beta h}$	bd'	$r_d$	$e^{\beta h}$	bc'	$r$	$e^{\alpha w}$
ca'	$r_c$	$e^{\alpha w}$	cb'	$r$	$e^{\alpha w}$	db'	$r_d$	$e^{\beta h}$	da'	$r$	$e^{\beta h}$
cc'	$r_a$	$e^{\alpha w + \alpha w}$	cd'	$r$	$e^{\alpha w + \beta h}$	dd'	$r_b$	$e^{\beta h + \beta h}$	dc'	$r$	$e^{\beta h + \alpha w}$

Figure 6.3: Diagram for same-conductor *P* integrals; the table at right shows the decomposition of the 16 surface terms for the two surface charge distributions.

### 6.1.2 *P* integrals for same conductors

When two conduction modes belong to the same conductor, then the integrand contains an integrable singularity, and Stokes' theorem does not apply.

Therefore, a different approach is needed. In fact, for same conductors, we adopt the straightforward decomposition of all terms having charge  $v_i^*$  on one face and  $v_j$  on another. There are 16 such terms, which we group into the types of surface integrals,  $P^{(xx)}$ ,  $P^{(xy)}$ ,  $P^{(yx)}$ ,  $P^{(yy)}$ , shown in Fig.6.3. For example,  $P^{(xx)}$  contains the four terms coming from  $v_i^*$  and  $v_j$  on sides "a" and "c".

Both  $P^{(xx)}$  and  $P^{(yy)}$  reduce to 2d integrals, performing the  $\mathbf{r}_- = \mathbf{r} - \mathbf{r}'$ ,  $\mathbf{r}_+ = \mathbf{r} + \mathbf{r}'$  transformation as in (5.3), for variables  $x$  and  $z$  in the first case, and for  $y$  and  $z$  in the second:

$$\begin{aligned}
 P_{ij}^{(xx)} &= \frac{s_i^* s_j}{4\pi\epsilon} \int_{-w}^w \int_0^L \left[ \left(1 + e^{(\beta_i^* + \beta_j)h}\right) \frac{e^{-jk_0 r_a}}{r_a} - \left(e^{\beta_i^* h} + e^{\beta_j h}\right) \frac{e^{-jk_0 r_c}}{r_c} \right] \xi_x \xi_z \, dx \, dz \\
 P_{ij}^{(yy)} &= \frac{t_i^* t_j}{4\pi\epsilon} \int_{-h}^h \int_0^L \left[ \left(1 + e^{(\alpha_i^* + \alpha_j)w}\right) \frac{e^{-jk_0 r_b}}{r_b} - \left(e^{\alpha_i^* w} + e^{\alpha_j w}\right) \frac{e^{-jk_0 r_d}}{r_d} \right] \xi_y \xi_z \, dy \, dz \quad (6.12)
 \end{aligned}$$

where  $r_a \equiv \sqrt{x^2 + z^2}$ ,  $r_b \equiv \sqrt{y^2 + z^2}$ ,  $r_c \equiv \sqrt{x^2 + h^2 + z^2}$ ,  $r_d \equiv \sqrt{w^2 + y^2 + z^2}$  and  $\xi_x, \xi_y$  are the same weight functions defined in the previous chapter, eq.(5.5).

On the other hand,  $P^{(xy)}$  and  $P^{(yx)}$  cannot be reduced in the same manner; only the  $z$  variable is reducible with the  $z_+, z_-$  transformation, and we obtain 3d integrals:

$$\begin{aligned}
P_{ij}^{(xy)} &= \frac{s_i^* t_j}{4\pi\epsilon} \int_{-w}^w \int_{-h}^h \int_0^L \frac{e^{-jk_0 r}}{r} e^{\alpha_i^* x + \beta_j y} \gamma_x \gamma_y \xi_z \, dx \, dy \, dz \\
P_{ij}^{(yx)} &= \frac{t_i^* s_j}{4\pi\epsilon} \int_{-w}^w \int_{-h}^h \int_0^L \frac{e^{-jk_0 r}}{r} e^{\alpha_j x + \beta_i^* y} \gamma_x \gamma_y \xi_z \, dx \, dy \, dz
\end{aligned} \tag{6.13}$$

where we have used the piecewise constant functions of (5.6) which, for the same-conductor case have the property  $\gamma_x(x) \equiv \gamma_2(x) = \gamma_1(-x)$ :

$$\begin{aligned}
\gamma_x &= \Theta(x) - e^{(\alpha_i^* + \alpha_j)w} \Theta(-x) \\
\gamma_y &= \Theta(y) - e^{(\beta_i^* + \beta_j)h} \Theta(-y)
\end{aligned} \tag{6.14}$$

If one of the modes is a side mode, then the transverse current has only one component, and two of the integrals above vanish. For example, if  $\mathbf{w}_i$  is a horizontal mode, then  $P_{ij}^{(xy)} = P_{ij}^{(xx)} = 0$  because  $s_i^* = 0$ .

Unlike the different-conductor case, these terms cannot be grouped together into one single integral. The comparison with the  $L$  integral, showing the basic property that  $L \simeq |P|/\omega^2$  must be proved on a case-by-case basis. This involves a large number of lengthy expressions, which we omit for the sake of brevity. Basically, this compensation results from<sup>5</sup>:

- For an **[H,H]** type of integral, only  $P^{(yy)} \neq 0$ ; the 2-d integrals in (6.12) are exactly the subtraction between the evaluations of  $L$  integrals at  $x = 0$  and at  $x = w$  (resp.  $y = 0$  and  $y = h$  for **[V,V]** type, only  $P^{(yy)} \neq 0$ ).
- For an **[H,V]** type of integral, only  $P^{(yx)} \neq 0$ ; the 3-d integrals in (6.13) cancel exactly with “flat” term exposed in (5.17), leaving only terms multiplied by factors  $e^{-w/\delta}$  and/or  $e^{-h/\delta}$ ,
- For a **[C,C]** type of integral, we have not been able to isolate the origin of the cancellation; this involves all four integrals in (6.12) and (6.13), and therefore a combination of the two mechanisms described above; we have verified, with the numerical integration tools described in the previous chapter, that this property holds in all our calculations (similarly for **[H,C]**, **[V,C]**, with contributions from three of the integrals).

<sup>5</sup>Refer to classification in Section 5.2 for the definition of integral types based on the exponential decays along the cross-sections.

## 6.2 Accelerated *RLC* integral calculations

The expressions shown in the two previous sections form the basis that allow us to calculate, in an accurate and efficient way, the *RLC* conduction mode matrix elements. In Chapter 5, we discussed the computation of  $L$  matrix elements in the *RL/MQS* domain. The techniques differ for two distinct cases, depending on whether the two modes correspond to the same or to different conductors. This distinction persists in the *RLC* integrals, and is further amplified by the observation in the previous section: for different conductors, the  $P$  integrals can be transformed "as a block" into 3d integrals that resemble the  $L$  integrals; on the other hand, for same-conductor integrals, this transformation is not possible.

Compared to the *RL/MQS* situation, the first observation is that the integrals are 3-d, because the  $z$ -integration cannot be done analytically. This is for two reasons: the  $z$ -dependence  $\exp(\eta z)$ ; and because we cannot set  $k_0 = 0$  in the Green function  $\frac{e^{-jk_0 r}}{r}$ .

We perform the  $\{z, z'\} \leftrightarrow \{z_-, z_+\}$  transformation, as in (5.3); after integration over the  $z_+$  variable, the result is a weight function  $\xi_z$  for the interval  $[z_0 - \ell', z_0 + \ell]$  that multiplies the Green function. The algebra is exactly the same as in eqs.(5.4)-(5.6). For the quasi-TEM implementation of *RLC* conduction modes, we have chosen  $\eta = \pm jk_0$ , so that these weight function are combinations of  $\cos(k_0 z)$ ,  $\sin(k_0 z)$  and linear functions in  $z$ . For example, if we consider the simplified case  $z_0 = 0$  and  $\ell = \ell'$  (i.e., wires with the same  $z$ -extension), the weight functions become:

$$\xi_z(z) = \begin{cases} (\ell - z) \cos(k_0 z) & \text{if } \eta_i = \eta_j \quad (\uparrow\uparrow) \text{ or } (\downarrow\downarrow) \\ \frac{\mp j}{k_0} \sin(k_0(\ell - z)) & \text{if } \eta_i = -\eta_j \quad (\uparrow\downarrow) \text{ or } (\downarrow\uparrow) \end{cases} \quad (6.15)$$

where the  $\pm$  distinguishes between  $\uparrow\downarrow$  and  $\downarrow\uparrow$ . The general case is represented by similar expressions for each of the four subintervals:  $[-\ell', 0]$ ,  $[-\ell', \ell - \ell']$ ,  $[0, \ell]$ ,  $[\ell - \ell', \ell]$  (setting  $r = \sqrt{(x_- + x_0)^2 + (y_- + y_0)^2 + (z_- + z_0)^2}$  in the Green function). This form of  $z$ -dependence induces the following strategy for the 3d integrals:

1. Replace  $\exp(-jk_0 r)$  and  $\xi_z(z)$  by their Taylor series in powers of  $k_0 r$  and  $k_0 z$  respectively.
2. Integrate along the  $z$ -axis, separately for each power of the expansions.
3. Perform, for the integration along the cross-sectional variables  $x$  and  $y$ , the same recipes as for the *RL/MQS* case:
  - Taylor for different conductors (as in Sec.5.4);
  - Gaussian quadratures/Polar variables for same conductors (as in Sec.5.3).

For the first step above, the expansions are,

$$\begin{aligned}
\frac{e^{-jk_0 r}}{r} &= \frac{1}{r} - jk_0 - \frac{k_0^2 r}{2} + \frac{jk_0^3 r^2}{6} + \dots \\
\cos(k_0 z) &= 1 - \frac{k_0^2 z^2}{2} + \frac{k_0^4 z^4}{24} - \dots \\
\sin(k_0 z) &= k_0 z - \frac{k_0^3 z^3}{6} + \frac{k_0^5 z^5}{120} \dots
\end{aligned} \tag{6.16}$$

Therefore each appearance of  $\exp(-jk_0 r) \cos(k_0 z) r^{-1}$  is replaced by several terms, combining all the products up to a given power of  $k_0$ . In this manner, we reduce these expressions to a sum of products of whole powers of  $r$  and  $z$ :

$$\begin{aligned}
\frac{e^{-jk_0 r}}{r} \xi_z^{\uparrow\uparrow} &= (\ell - z) \left[ \frac{1}{r} - jk_0 - \frac{k_0^2}{2} \left( r + \frac{z^2}{r} \right) + \frac{jk_0^3}{6} (r^2 + 3z^2) \right. \\
&\quad \left. + \frac{k_0^4}{24} \left( r^3 + \frac{z^4}{r} + 12rz^2 \right) - \frac{jk_0^5}{120} (r^4 + 5z^4 + 10r^2 z^2) - \dots \right] \\
\frac{e^{-jk_0 r}}{r} \xi_z^{\uparrow\downarrow} &= (\ell - z) \left[ \frac{1}{r} - jk_0 - \frac{k_0^2}{2} \left( r + \frac{(\ell - z)^2}{3r} \right) + \frac{jk_0^3}{6} (r^2 + (\ell - z)^2) \right. \\
&\quad \left. + \frac{k_0^4}{24} \left( r^3 + \frac{(\ell - z)^4}{5r} \right) - \frac{jk_0^5}{120} \left( r^4 + (\ell - z)^4 + \frac{10}{3} r^2 (\ell - z)^2 \right) - \dots \right]
\end{aligned} \tag{6.17}$$

Note that all these terms can be integrated analytically in  $z$ . For carrying out this integration, we separate same-conductor from different-conductor matrix elements.

### 6.2.1 Same-conductor integrals

When both modes correspond to the same conductor, all the  $z$ -dependence is given by expressions (6.17). We exemplify for the  $\uparrow\uparrow$  weight functions, the other one being essentially the same type of calculations.

Replacing  $z^2 = r^2 - \rho^2$  for all but the  $\ell - z$  factor in (6.17), and defining,

$$H_n \equiv \int_0^\ell (\ell - z) r^n dz \tag{6.18}$$

we can write the result of the  $z$ -integration as

$$\Phi(\rho) = \sum_{n=-1}^{M-1} G_n(\rho) H_n(\rho) \tag{6.19}$$

with  $\rho = \sqrt{x^2 + y^2}$ , and  $M$  is the maximum order of  $k_0$  retained in the Taylor expansion; for example, setting  $M = 5$  we obtain:

$i$	$G_i$	$H_i$
-1	$1 + \frac{1}{2}\tilde{\rho}^2 + \frac{1}{24}\tilde{\rho}^4$	$\ell \left( \sinh^{-1} u - \frac{u}{1 + \sqrt{1+u^2}} \right)$
0	$-jk_0 \left( 1 + \frac{1}{2}\tilde{\rho}^2 + \frac{1}{24}\tilde{\rho}^4 \right)$	$\frac{\ell^2}{2}$
1	$-k_0^2 \left( 1 + \frac{1}{3}\tilde{\rho}^2 \right)$	$\frac{\ell^3}{3} \left( (1 + u^2)^{3/2} - 1 \right) u^{-3}$
2	$jk_0^3 \left( \frac{2}{3} + \frac{1}{6}\tilde{\rho}^2 \right)$	$\frac{\ell^4}{4} (1 + 2u^{-2})$
3	$\frac{1}{3}k_0^4$	$\frac{\ell^5}{5} \left( (1 + u^2)^{5/2} - 1 \right) u^{-5}$
4	$-\frac{j}{15}k_0^5$	$\frac{\ell^6}{6} (1 + 3u^{-2} + 3u^{-4})$

(6.20)

where we have used  $\tilde{\rho} \equiv k_0\rho$  and  $u \equiv \ell/\rho$ . Keeping higher order terms results in similar expressions, slightly more lengthy, without adding in any new transcendental function evaluation.

Function  $\Phi(\rho)$  in (6.19) plays the same role, for RLC integration, as the function  $F(\rho)$  in (5.8) for the RL/MQS counterpart: it reduces by one the dimensionality of the integrals, and defines the kernel of the integrand in  $(x, y)$ -plane, to be multiplied by functions of  $x, y$ . These functions are the combination of the  $P$  integrals presented in Section 6.1.2, and the weight functions  $\xi_{x,y}$  for  $L$ , which are the same as for the RL/MQS case studied in the previous chapter. The techniques of Section 5.3 are valid for performing the  $x, y$  integration:  $L$  contributions are replaced by a Gauss-Jacobi expansion, whose principal values are canceled by the  $P$  terms ( for  $\uparrow\uparrow$  integrals), or doubled (for  $\uparrow\downarrow$ ).

For these same-conductor integrals, we are presently developing an interpolation approach that will replace the one shown herein; this new technique is the subject of Section 6.3.

### 6.2.2 Different-conductor integrals

For different-conductor integrals, the full  $z$ -dependence is composed of (6.17) multiplied by the sum of the  $L$  and  $P$  contributions,

$$L_{ij} - \frac{1}{\omega^2} P_{ij} = \frac{\mu}{4\pi} \int_{-w'}^w \int_{-h'}^h \xi_x(x) \xi_y(y) \left\{ \int_0^\ell \frac{e^{-jk_0 r}}{r} \xi_z \left[ 1 \mp \left( f_0 + f_1 \frac{1 + jk_0 r}{r^2} + f_2 \frac{3 + 3jk_0 r - 3k_0^2 r^2}{r^4} \right) \right] dz \right\} dx dy \quad (6.21)$$

where the  $x, y$  polynomials  $f_0 = \eta_i^* \eta_j$ ,  $f_1 = (t_i^* \eta_j + t_j \eta_i^*)x + (s_i^* \eta_j + s_j \eta_i^*)y - (t_i^* t_j + s_i^* s_j)$ , and  $f_2 = (t_i^* x + s_i^* y)(t_j x + s_j y)$  are the expression inside the brackets of (6.11).

Again, we consider the  $\uparrow\uparrow$  example, with the other possibilities being similar. Keeping terms

up to order- $M$  in  $k_0$  we obtain, after  $z$ -integration, an expression similar to the same-conductor case,

$$\Phi(x, y) = \sum_{n=-5}^{M-3} G_n(x, y) H_n(\rho) \quad (6.22)$$

with  $\rho = \sqrt{(x + x_0)^2 + (y + y_0)^2}$ , and setting for example  $M = 5$ :

$i$	$G_i$	$H_i$
-5	$(3 + \frac{3}{2}\tilde{\rho}^2 + \frac{1}{8}\tilde{\rho}^4)f_2$	$\frac{1}{3}\rho^{-3} \left( \frac{1+2u^2}{\sqrt{1+u^2}} - 1 \right)$
-4	-	$\frac{1}{2}\ell\rho^{-3} \tan^{-1} u$
-3	$(1 + \frac{1}{2}\tilde{\rho}^2 + \frac{1}{24}\tilde{\rho}^4)f_1 - k_0^2 f_2$	$\rho^{-1}(\sqrt{1+u^2} - 1)$
-2	-	$\ell\rho^{-1} \tan^{-1} u - \frac{1}{2} \log(1 + u^2)$
-1	$\frac{1}{6}k_0^2\tilde{\rho}^2 f_1$	$\ell \left( \sinh^{-1} u - \frac{u}{1+\sqrt{1+u^2}} \right)$
0	$-\frac{jk_0^3}{3}((1 + \frac{1}{2}\tilde{\rho}^2)f_1 + \frac{1}{5}k_0^2 f_2)$	$\frac{1}{2}\ell^2$
1	$-\frac{k_0^4}{3}f_1$	$\frac{\ell^3}{3} \left( (1 + u^2)^{3/2} - 1 \right) u^{-3}$
2	$\frac{jk_0^5}{5}f_1$	$\frac{\ell^4}{4} (1 + 2u^{-2})$

(6.23)

with the same notation as in (6.20).

As in the same-conductor case  $\Phi(x, y)$  reduces the dimensionality of the integrals, so that (6.21) becomes:

$$L_{ij} - \frac{1}{\omega^2} P_{ij} = \int_{-w'}^w \int_{-h'}^h \Phi(x, y) \xi_x(x) \xi_y(y) dx dy \quad (6.24)$$

Having performed the  $z$  integration, we are now in a position to apply the methods of Section 5.4 in order to calculate this 2-d integral. Basically, this consists in Taylor expansions for every exponentially decaying interval and Gauss-Legendre rules for every flat/linear interval.

Although the expressions in (6.23) contain more terms than the ones for  $RL$ , they do not entail an important increase in computational cost. Both cases consist of one-time evaluations of transcendental functions, plus a certain number of elementary arithmetic. Both the number of transcendental functions and elementary arithmetic is greater for the  $RLC$  case; however, this difference is slight when compared against the savings obtained therein.

### 6.2.3 Preliminary examples

As mentioned at the beginning of the present chapter, this strategy is presently under development, hence we cannot show global results for the methods in this section. Instead, we present, in Fig. 6.4 a brief analysis of the  $k_0$ -approximation: we consider integrals for different conduc-

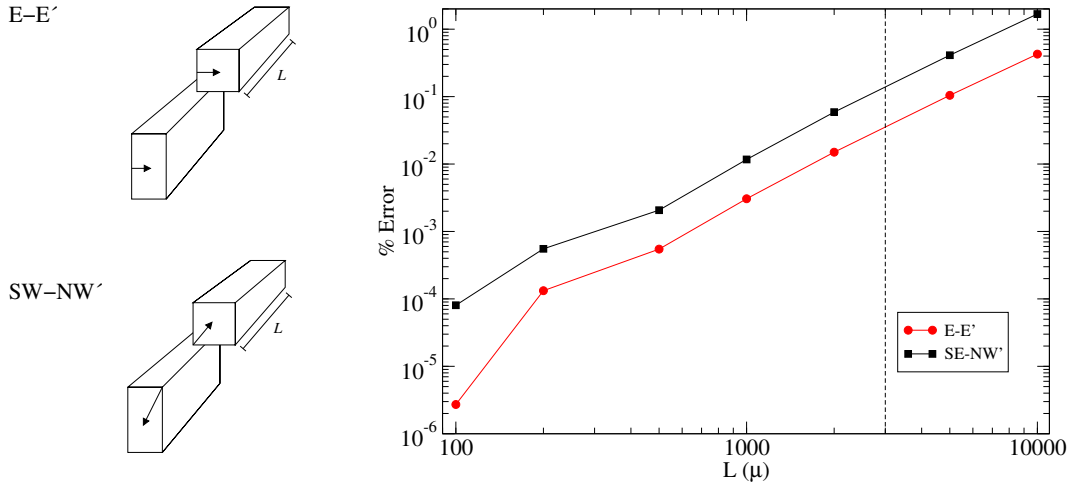


Figure 6.4: Approximation errors for Taylor on  $k_0$ ; dimensions of wires are  $1\mu \times 1\mu \times L$ ,  $2\mu \times 3\mu \times L$ , and the separation is  $2\mu$  on  $x$  and  $1\mu$  on  $y$ ; material is copper, and frequency is  $100\text{GHz}$ . The wavelength  $\lambda = 3000\mu$  is indicated by the dashed vertical line.

tors, replace the  $z$ -dependence by the order-2 Taylor approximation in (6.22), and compare the results for this 2d integral (6.24) against the original 3d integrals (6.21). We use the Adaptive Quadrature (AQ) [87] method for both the 2d and 3d integrals<sup>6</sup>.

Errors for this Taylor approximation remain below 1% for values of length significantly larger than the wavelength. The reason for this behavior is given by the  $\frac{1}{r}$  factor, which dampens the value of the integrand for values of  $z$  where the approximation errors are large. For large  $L$ , errors grow with the expected  $L^3$  dependence (the remainder  $R_2 \propto z_m^3$  for some  $z_m \in [0, L]$ ).

In terms of cost, we mention that, in approximating the  $z$  integral in this manner, the number of function calls is reduced, on average, by a factor 20: for these 3d integrals, the number of calls is of order  $8 \times 10^5$ , whereas the 2d ones, for the same AQ accuracy parameters, demand an order  $4 \times 10^4$ .

Nevertheless, we expect the savings mentioned above to be increased by two additional orders of magnitude when the Taylor expansions on  $x, y$  are implemented. This is a consequence of applying the methods shown in Section 5.4, with the runtimes of Section 5.6 and errors of Section 5.7. Runtimes are expected to be slightly longer than the ones in Fig. 5.11, since the RLC Taylor expansions contain more transcendental functions than the RL/MQS ones.

<sup>6</sup>The full strategy includes the Taylor and Gauss-Legendre expansions on  $x, y$  for (6.23); this part of the code is currently under development (although it is computationally inexpensive, it is "developmentally" very expensive).

### 6.3 Interpolation/Parametrization of self matrix elements

In the previous chapter, we presented a systematic approach to the problem of computing matrix elements in the *RL* conduction modes matrix. Therein, we showed that by performing certain approximations, we could reduce one order of magnitude in calculation of the elements for different conductors. For the *RLC* problem, the analogous savings are obtained by combining the methods in Sections 6.1 and 6.2 above.

For *RL*, we also obtained a further order of magnitude savings by approximating the same-conductor elements, by using Gaussian and polar variables integrations on the cross-sectional dimensions. Comparatively, the savings for each same-conductor integral are less significant than the ones for different-conductor integrals. For *RLC*, we expect the same-conductor savings to compare worse, because the Taylor expansion in  $k_0$  breaks down when the origin is contained in the integration domain.

A far more interesting alternative is that of avoiding these calculations altogether, by pre-computing them offline; at runtime we can obtain the value of the matrix elements by either of the following methods:

- Creating a large library (or several distributed small ones) of precomputed values at certain specified nodes, spreading out over all the possible configurations, and interpolating among the nodes of this lookup library for any arbitrary configuration. The choice of interpolation method must be done carefully, according to the distribution of node; a survey on multidimensional interpolation is found in [94].
- Parametrizing the function dependence of the matrix elements, thus creating a numerical model for each. In this case, the difficulty of the problem lies in capturing the correct model for each of the dimensions of the problem.

In [95], an interpolation approach was presented for *RL* extraction of inductance among interconnects. The nodes of the library consist of a predetermined set of current distribution functions for two-wire configurations, denominated “proximity templates”. More recently, this technique was refined by requiring orthogonality among these functions, as well as inclusion of these within a multilayered complex image formulation [96]. The main advantage is that the matrix elements for the templates are computed “offline”, avoiding the burden of computing non-trivial integrals.

The efficiency of creating such library is dominated by  $\Pi$ , the number of degrees of freedom for the interpolation. For two-wire configurations,  $\Pi = 10$ : the three dimensions of each conductor, the three separations, and the frequency. In the most general case, the proximity templates method implies constructing, bookkeeping, and scanning (online), a number of 10-dimensional lookup libraries. The complexity of this method is exponential in  $\Pi$ , with the basis

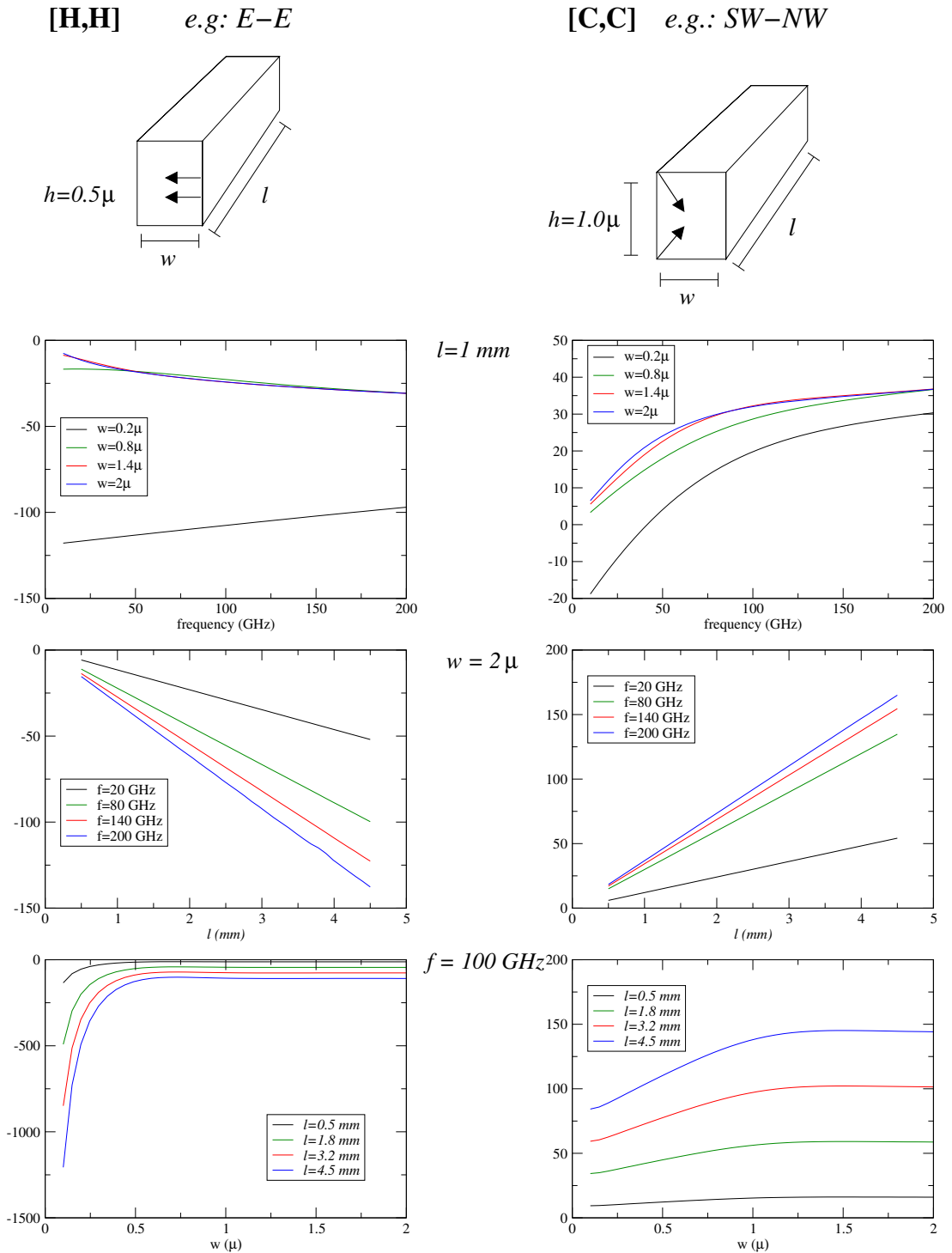


Figure 6.5: Typical values for same-conductor  $Z = j\omega(L - P/\omega^2)$  integrals, expressing variations with respect to  $(l, w, f)$  parameters; for the two different types of integrals shown above, we show:  $Z(f)$  for different  $w$  and fixed  $L = 1 \text{ mm}$  (top);  $Z(L)$  for different  $f$  and fixed  $w = 2 \mu\text{m}$  (center);  $Z(w)$  for different  $L$  and fixed  $f = 100 \text{ GHz}$  (bottom).

of the exponential determined by the number of nodes along each of the dimensions. Furthermore, the number of such libraries is given by the product between the number of templates for each of the participating conductors.

For these reasons, we do not consider an interpolation scheme in computing matrix elements for different conductors.

However, for elements for the same conductor, this number reduces drastically, to  $\Pi = 4$  (the three dimensions plus the frequency), which is manageable. Moreover, the number of libraries required is much smaller, because symmetries reduce the effective number of different matrix elements (see Section 5.3). This scheme is also appropriate for different-conductor matrix elements, in configurations where there is a large degree of symmetry among wires (e.g.: planar inductors, where it is common for all long segments to be on the same layer and have the same width, or ground planes that have been partitioned into several subregions, with a large degree of symmetry among them).

Furthermore, in ICs some of these 4 dimensions do not necessarily have a continuous variation. For example, the thickness of wires is related to the thickness of the metal layers. These thicknesses are restricted to a small number of discrete values [75, 97]. For our interpolation scheme, this reduces the dimensionality by one, setting  $\Pi = 3$ , with the proviso that we must construct one set of libraries for each value of the thickness.

For the three remaining parameters ( $l, w, f$ ), we show in Fig.6.5, the dependence of some matrix elements. These are the functions to be either interpolated or parametrized. A first glance at these graphs shows that the  $l$ -dependence is linear. This means that, along the  $l$ - dimension of  $\Pi$ -space, two values suffice for parametrization/interpolation. In practice, the dimensionality is reduced to 2.

The dependences on  $w$  and  $f$  require a more delicate inspection. The fact that  $\Pi$  is reduced to 2 allows for a large amount of nodes in an interpolation scheme, which leads to the possibility of adopting simple algorithms (e.g. a bi-cubic splines [86] for equally-spaced nodes; [94] and [98] give recipes for arbitrarily spaced nodes). If a parametrization scheme is adopted, the lower dimensionality permits an efficient isolation the behavior of each dimension as in Fig.6.5, in order to fit these curves with analytical expressions. At present, we are analyzing the advantages and disadvantages of either one of the two methods (or a combination of them), applied to these integrals.

## 6.4 Enlarging the conduction modes basis

The conduction modes method is based on a particular choice of modes for the expansion basis. Obviously, the goal is to capture as much of the physics as possible, with as few functions as possible.

In this section, we discuss the implications of enlarging the conduction modes basis, i.e. the set of functions  $\mathbf{w}_i$  in (4.12) (the surface charge functions are always defined by (4.18)). For the *RLC* examples shown in Chapter 4, we made certain assumptions in order to reduce the number of modes. In particular:

- in Section 4.4, only quasi-TEM modes were considered, leading to a reduction in the size of the parameter space for the conduction modes;
- in Section 4.3.2, we neglected one of the possible directions for the quasi-TEM conduction modes.

Dropping each of these two assumptions leads to the inclusion of new sets of conduction modes, which we denominate “dissipation” and “reacomodation” modes, respectively. They constitute the subject of the two subsections that follow.

Although these ideas have not been implemented, we can combine our experience in conduction modes with physical intuition, to predict the effects that these future inclusions may lead to. This intuition is a useful guide in determining if and when to implement these additions. In the following two subsections, we detail each of the assumptions above.

Another type of concern is related to the difficulty, reported in [74] within the *RL* case, for conduction modes to describe low-frequency behavior. This drawback is related to the fact that, as frequency decreases, the skin-depth increases, and therefore all the modes corresponding to the same conductor are nearly degenerate, leading to ill-conditioned matrices. A way out of this problem was proposed and implemented, in the same article, by defining localized conduction modes, which are defined over a subregion of the entire cross-section. The analogous solution for *RLC* modes would imply a further enlargement of the modes basis (localization also along the  $z$ -axis).

For *RL* examples, we have always observed a smooth transition between the low frequency model, e.g. FastHenry with one filament per wire, and the high frequency model based on conduction modes, when matrix elements are computed with a high level of accuracy<sup>7</sup>. Determination of the cut-off frequency, below which conduction modes must be “switched off”, is a crucial issue for a secure implementation of this method for wide frequency spectra. This cut-off frequency is configuration-dependent, and is a function of the comparison between the smallest cross-sectional dimensions and separations on one side, and the skin-depth on the other.

#### 6.4.1 Dissipative modes

The particular choice of parameters  $\alpha, \beta, \eta$  for *RLC* conduction modes of Section 4.4 corresponds to quasi-TEM modes of propagation for the waves in the medium surrounding the con-

<sup>7</sup>This was not the case in earlier versions of the method, with integrals computed stochastically using Monte Carlo (see Chapter 5), obtaining significant statistical noise at low frequencies.

ductors (see discussion in Section 4.4). As a consequence, we have set a sinusoidal dependence along the  $z$ -axis, with  $\lambda = 2\pi k_0^{-1}$ , i.e. the natural wavelength for EM waves in the medium.

In terms of the conduction mode parameters, relation (4.27) states that, if  $\eta$  ceases to be  $\pm jk_0$ , then it must contain some  $\delta^{-1}$ -order component. Given that, for the frequencies and materials of interest,  $\delta \simeq 10^{-3}\lambda$ , this means that we can safely neglect the  $-k_0^2$  in (4.27), and concentrate only on the first term in the rhs<sup>8</sup>:

$$\alpha_i^2 + \beta_i^2 + \eta_i^2 = \left(\frac{1+j}{\delta}\right)^2 \quad (6.25)$$

Thus, inclusion of non-TEM modes involves including  $\eta$  in the redistribution of the rhs in (6.25). We recall that, both for *RL/MQS* and *RLC* conduction modes, this redistribution was limited to  $\alpha$  and  $\beta$ . We thus obtain a description with exponential terms along all three spatial directions.

Computationally, the evaluation of matrix elements for these new modes is not expected to add a significant amount of cost. This is due the fact that the  $z$ -exponentials localize the integrands for these elements (in contrast to the sinusoidals for the quasi-TEM modes), so that we may set  $\exp(-jk_0 r) = \exp(-jk_0 r_0)$  in the Green function for the corresponding integrals (with  $r_0$  defined as the distance between the maxima of the exponential decays). Then, the familiar Taylor expansion and Gaussian quadrature techniques for exponential decays, which were previously used only for cross-sectional dimensions, can be applied to the longitudinal one. The difficulty in the implementation relies mainly in the mixing of these new modes with old ones. Before embarking on this course, it is instructive to attempt to forecast when these modes can be important.

Physically, these “dissipation” modes are such that capacitive effects are much larger than the inductive ones. This observation results from estimating the magnitudes of longitudinal and transverse currents; from the continuity equation imposed on the definition of conduction modes, which was shown in eq. (4.30),

$$\left. \begin{array}{l} \frac{w_x}{w_z} = \frac{j}{2}(\delta^2 \eta \alpha) \\ \frac{w_y}{w_z} = \frac{j}{2}(\delta^2 \eta \beta) \end{array} \right\} \Rightarrow \frac{w_{trans}}{w_{long}} = O(1) \quad (6.26)$$

where we have imposed  $\eta$  to be order  $\delta$ . We recall that the cancellation between  $L$  and  $P$  in Section 6.1, for quasi-TEM modes, relies on the ratio at the right of eq.(6.26) being of order  $O(\delta/\lambda)$ . Not having this relationship is tantamount to having  $|\omega^2 P/L| = O(\lambda^2/\delta^2)$  for dissipative modes.

Furthermore, these modes have a typical length scale of  $\delta$ , whereas the quasi-TEM modes extend all over the conductor. As such, we expect their effects to be negligible if  $\ell \gg \delta$ .

<sup>8</sup>For the validity of this statement, we also need  $w, h \ll \lambda$ , an assumption which is most generally the case.

Conversely, these modes should be appropriate for representing border effects for geometries with small scales, i.e. vias and small connecting wire. Unfortunately, these statements can only be verified in practice: including these modes and observing that the solution is not affected; this task involves implementing the difficulties mentioned above.

### 6.4.2 Charge reaccomodation modes

The second type of modes neglected in the *RLC* formulation of Chapter 4 are those that carry no net current along the  $z$ -axis. They represent a redistribution of charge along the transverse dimensions of the conductor.

These neglected modes are quasi-TEM with no transverse divergence,

$$\left. \begin{aligned} \alpha_i^2 + \beta_i^2 + \eta_i^2 &= -\left(\frac{2\pi}{\lambda}\right)^2 + \left(\frac{1+j}{\delta}\right)^2 \\ \eta_i &= \pm jk_0 \\ \nabla \cdot \mathbf{w}^{(reac)} &= 0 \\ \nabla_{trans} \cdot \mathbf{w}^{(reac)} &= 0 \end{aligned} \right\} \Rightarrow \mathbf{w}_i^{(reac)} = B_i \left( \frac{1}{\alpha_i}, -\frac{1}{\beta_i}, 0 \right) \quad (6.27)$$

where  $\nabla_{trans} = \hat{\mathbf{x}}\partial_x + \hat{\mathbf{y}}\partial_y$ .

The main distinction, between these modes and the ones we have been using, is that  $w_z^{(reac)} = 0$ : currents only flow on the transverse direction. We cannot normalize these modes in the same manner as the usual ones, because there is no current entering the conductor. Also, for any value of  $z$ , the total charge for these modes is zero, so we cannot normalize according to the value of charge. For the sake of having comparable elements in the description, we borrow the same normalization as for the modes in (4.30), defining the proportionality constant as,

$$B_i = \left( \frac{\alpha_i}{e^{\alpha_i w_i} - 1} \right) \left( \frac{\beta_i}{e^{\beta_i h_i} - 1} \right) \delta \eta_i \quad (6.28)$$

with the same comment as in (4.30), namely that, if it is a side mode with, say,  $\alpha_i = 0$ , then the first fraction above is replaced by its limit  $w$ . In this manner, the currents  $I_i$  and corresponding charges  $q_i = (j\omega)^{-1}I_i$  to these modes have the same scale factor as the ones for the usual conduction modes in Chapter 4.

There are two important consequences related to the absence of  $z$ -currents:

1. the rhs of the system equations for these modes vanishes (see eq.(4.19));
2. the  $L$  contribution is negligible with respect to the one coming from  $P$  elements, thus avoiding the cancellation discussed in Section 6.1; all the elements corresponding to  $\mathbf{w}_i^{(reac)}$  (including those on the diagonal) are much larger than the ones for “normal” modes.

The combination of the two statements above suggests that contribution from these modes is negligible. As in the previous case, these statements can only be verified through trial and error.

## 6.5 Arbitrary 3-d geometries

Concerning the geometry of the wires that can be treated by our conduction modes method, there exist certain associated limitations. We now examine two of them.

### 6.5.1 Non-Manhattan configurations

For two currents running on wires at  $90^\circ$ , inductance effects are negligible. In this case, only capacitance needs to be computed. At  $90^\circ$ , the application of Stokes' theorem runs very similar to the calculation for parallel wires, Section 6.1.1. The resulting expression is the same as (6.11) with appropriate exchanges of  $x, y$  parameters and the corresponding ones for  $z$ . Taylor expansions as is Section 6.2.2 can be applied in a straightforward manner.

Collectively termed Manhattan geometry, parallel and perpendicular configurations cover a large set of IC interconnect applications; typical exceptions are given by multi-sided inductors. Concern for non-Manhattan geometries is more important in PCB and package applications.

When the angle between the two conductors is not  $90^\circ$ , the calculation in Section 6.1.1 becomes very cumbersome. Even for the case of inductance of infinitesimal filaments, this computation involves the non-trivial combination of no less than 15 transcendental functions (page 56, [56]). For non-negligible cross-sections, these complicated expression must be integrated over the two cross-sections [23]. In practice, though, it is appropriate to approximate wires as filaments located at the centers of the cross-sections [59].

In our case, the conduction modes are helpful, as they concentrate the value of the integrand within a narrow region, allowing for Taylor expansions as in 5.4. Obtaining the expressions ready to be used for these Taylor expansion is not an easy task. An analysis of the necessity for inclusion of this case must be done before embarking on this road.

### 6.5.2 "Fat" wires

Any description in terms of localized current distribution method encounters difficulties when dealing with wires that have significant difference in their dimensions, e.g., when we have one wire on top of another with a larger width, as in a ground plane; or when two wires have very different lengths. The reason for this difficulty is due to a well-known phenomenon: the current returning on the wide wire tends to concentrate on the "shadow" of the thinner one.

In filament-type approaches to  $RL/MQS$  inductance extraction, the problem is solved by applying a specific discretization for ground planes [15, 23], with many narrow filaments, for the wide wire, at the shadow of the thin one. These kind of solutions, when applied to a large system of wires, can be a double-edged blade: if this *ad hoc* discretization is carried out for all wires above the ground plane, then the size of the system will grow accordingly. Clearly, some heuristic is needed in order to contain this growth; pondering the importance of each particular discretization.

For conduction modes, the analogous solution is to decompose the wide conductor into a collection of sub-conductors, occupying the same total volume and being able to reproduce the “shadow” currents mentioned above. As in the filament approach, we must avoid an explosion in system size, by determining when and how to make this decomposition, and which modes to use in the process.

For the  $RLC$  formulation, this situation can also occur along the length: if two wires have significantly different lengths, then the strategy of decomposing into same-length wires can lead to an explosion in the size of the system.

Such a strategy is in the process of being implemented for  $RL/MQS$  extraction, within the Calibre engine. Basically, two main tasks are involved in this development [99]:

- Optimal automatization and tuning of schemes for decomposing wide wires into narrower sub-conductors, where the local conduction modes are defined. This task is quite straightforward for individual cases, but leads to cumbersome issues when developing a full-proof method for the general case.
- The difficulties springing from the fact that integrals for two adjacent sub-conductors, corresponding to a decomposition of a single wide wire, contain the origin within the integration domain. This breaks down the Taylor schemes developed in Chapter 5 for different conductors. Dealing with these difficulties implies modifications to the numerical integration methods. The new integration schemes are based on partial interpolation of the integrands.



## **Part C**

# **Broadband representation of *RL* behavior**



# Pairs Foster pour des transitions simples

## Résumé en français

*Ici, nous nous intéressons au problème lié à la représentation des effets RL en fonction de la fréquence. Suite au choix de méthode de réduction de l'ordre du modèle effectué chez Mentor, méthodologie cf. Introduction Générale, nous utilisons des pairs Foster. Dans la section 7.1, nous analysons en détail la réponse d'un pair Foster, définissant son paramètre principal, c.-à-d. la fréquence caractéristique. Dans la section 7.2 nous montrons comment calculer les paramètres d'un circuit avec un seul pair Foster, en garantissant la passivité du circuit. L'équivalence entre un pair Foster et un élément d'un circuit échelle est exposée dans la section 7.3. La section 7.4 contient une description de l'implémentation de cette stratégie dans les outils d'extraction chez Mentor. Finalement, nous montrons et analysons des exemples des transitions simples qui sont modélés avec des circuits d'un pair Foster (section 7.5). Les méthodes de ce chapitre sont contenues dans le formateur Calibre, et font partie du contenu de la demande de brevet correspondant [41].*



## Chapter 7

# Single-transition Foster pairs

We now address the question of how to represent broadband frequency dependent resistance and inductance effects for IC interconnects. As discussed in the Introduction, we wish to do so using realizable circuit elements, compatible with the node-elimination, model order reduction (MOR) scheme. The main goal in this type of modeling is to capture the relevant variations of resistance and inductance, with only very few data input values (and hence few circuit elements).

Resistance always increases, and inductance always decreases, as frequency grows. To understand this in physical terms, we must consider that currents always reaccommodate themselves so as to minimize the total impedance,  $Z = R + j\omega L$ . The weight of the frequency for the imaginary part of  $Z$  causes the importance of  $L$  to grow with respect to that of  $R$ .

Empirically, we have already seen two cases in which this phenomenon presents itself: the selection and distribution of return paths for a signal wire (Sec. 2.2); and the current crowding within conductors due to skin effects (Chapters 4-6). For any given configuration, there is a frequency threshold that determines the onset where inductive effects become important. Below this frequency, impedance can be considered frequency-independent. For very high frequencies, currents are nearly superficial, constrained within a width  $\delta \propto f^{-1/2}$ , so that inductance stabilizes at a fixed value, and resistance grows as  $f^{1/2}$ . In general, we are interested in modeling the response of a system at intermediate frequencies, where these transitions appear.

A Foster pair is a simple circuit, with constant parameter values, whose response as a function of frequency resembles the one described above. It consists of one resistance in parallel with one inductance, as in Fig.7.1. At very low frequencies, the impedance  $j\omega L$  of the inductive branch is negligible, so the current will flow mainly through it; as frequency increases, this contribution becomes more important, while the impedance of the resistance remains unchanged. For high enough frequencies, current flows mainly through the resistive branch. The value of frequency at which this transition takes place is called the characteristic frequency of the Foster pair.

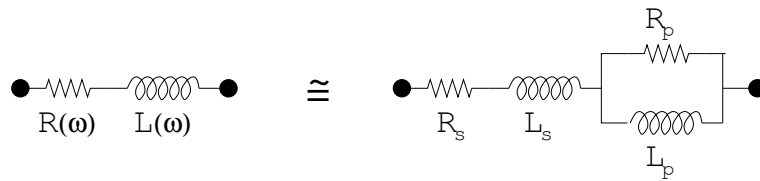


Figure 7.1: Basic circuit: a resistance and inductance in series with one Foster pair, as a representation of a frequency-dependent  $RL$  circuit.

Circuits with Foster pairs for representing frequency-dependent effects were used already in the sixties. At the beginning, these studies were of a theoretical nature: [100] is a thorough comparative analysis of different  $RL$  structures with respect to Foster and Cauer ones; [101] shows applications to network synthesis; and [102] treats equivalence transformations between Cauer and Foster networks. More recently, applications appear in the literature: in [103] Foster pairs are used for a finite-pole approximation within a full 2-d modeling approach, and [104] include Foster pairs for a transmission line model; Model Order Reduction (MOR) applications of Foster pairs are found in [105] and [40]. Alternatives to Foster pairs, namely the ladder networks, are reported in [106] and [107].

We follow [40]: therein several recipes for including Foster pairs into the Mentor's MOR scheme TICER/BMR [38,39] are presented. We will construct Foster pairs for a specific case of the Arbitrary Frequencies Branch Merge method (page 235 of [40]), which allows the freedom to choose the characteristic frequencies for the Foster pair circuit. Reduction of these computed circuits is described in the same reference.

The two typical frequency-dependent transitions found in IC's can occur either at distinct frequency ranges, or at overlapping ones. In practice, the response can be modeled well with one or two Foster pairs, depending on how many types of phenomena are contained in the original data (current crowding and/or skin effect). In this chapter we show how to determine the parameters of one-pair Foster circuits, leaving the more general case for the following chapter.

We organize the contents of the present chapter as follows:

- in Section 7.1, we analyze in detail the response of a Foster pair, defining its main parameter, i.e. the characteristic frequency;
- in Section 7.2 we show how to compute a one-pair Foster circuit for a set of 4 input data points, coming from two different frequencies;
- we prove in Section 7.3 that a one-pair Foster circuit is identical to a corresponding ladder circuit;
- Section 7.4 deals with issues regarding the implementation of Foster pairs within Mentor's

extraction tool, Calibre xL;

- Section 7.5 analyzes basic examples of one-pair Foster modeling.

The contents of these two chapters constitute a working example of the difficulties encountered in an industrial application. The issues herein discussed are mainly related to assuring a simple yet robust solution to the problem of representing broadband  $RL$  effects, in a manner compatible with a decision made at a higher level (i.e., the adoption of the TICER/Branch Merge Reduction (BMR) scheme, discussed in Chapter 1). Compared to the previous chapters, they do not contain highly innovative concepts, from a scientific point of view<sup>1</sup> except for the future issues described at the final discussion in Chapter 8. Nevertheless, they exhibit a systematic and scientific approach to the implementation and extension of an existing method, based on simple physical concepts, for modeling and synthesizing data in order to comply with these constraints.

## 7.1 Characterization of Foster pairs

The frequency dependent impedance for the Foster pair in Fig.7.1 is:

$$Z^{(FP)}(\omega) = \left( \frac{1}{R_p} + \frac{1}{j\omega L_p} \right)^{-1} = \left( \frac{\omega^2 L_p^2}{R_p^2 + \omega^2 L_p^2} \right) R_p + \left( \frac{R_p^2}{R_p^2 + \omega^2 L_p^2} \right) j\omega L_p \quad (7.1)$$

This can be written in terms of the characteristic frequency of the Foster pair,

$$\Omega \equiv \frac{R_p}{L_p} \quad (7.2)$$

$$Z^{(FP)}(\omega) = \left( 1 - \frac{1}{1 + \left(\frac{\omega}{\Omega}\right)^2} \right) R_p + \left( \frac{1}{1 + \left(\frac{\omega}{\Omega}\right)^2} \right) j\omega L_p \quad (7.3)$$

Separating real and imaginary parts, we see that the equivalent resistance and inductance for the Foster pair are given by,

$$Z^{(FP)} = R^{(FP)} + j\omega L^{(FP)}, \quad \begin{cases} R^{(FP)}(\omega) &= (1 - \psi(\omega)) R_p \\ L^{(FP)}(\omega) &= \psi(\omega) L_p \end{cases} \quad (7.4)$$

In Fig. 7.2 we plot the general form for the characteristic function  $\psi(\omega) \equiv (1 + (\omega/\Omega)^2)^{-1}$ , having the following properties:

- $\lim_{\omega \rightarrow 0} \psi(\omega) = 1$ ;

---

<sup>1</sup>e

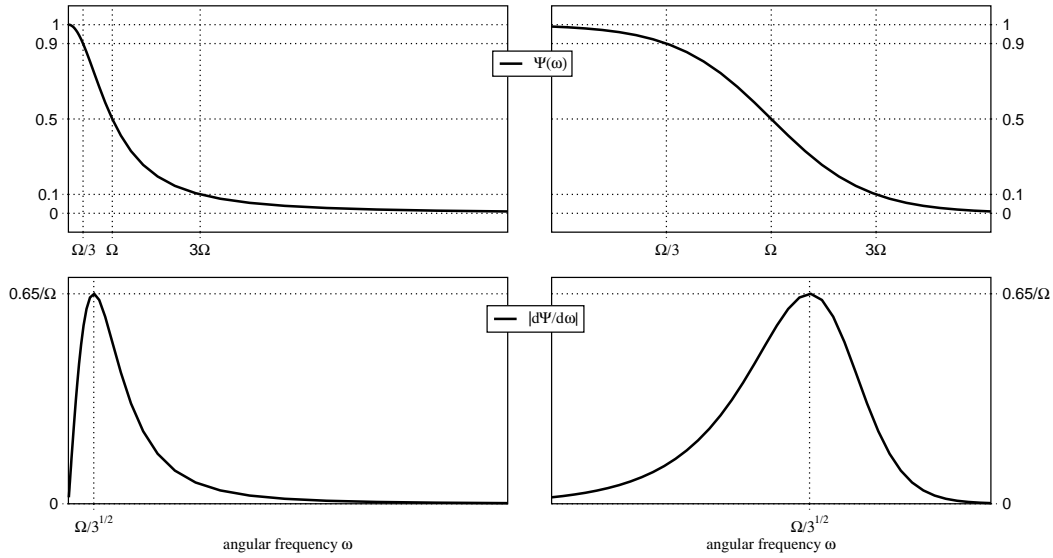


Figure 7.2: Characteristic function  $\psi(\omega)$  and its derivative  $d\psi/d\omega$  for a Foster pair, in linear (left) and logarithmic (right) scales.

- $\lim_{\omega \rightarrow \infty} \psi(\omega) = 0$ ;
- $\psi(\Omega) = \frac{1}{2}$ ;
- $\psi(3\Omega) = 0.9$  and  $\psi(\Omega/3) = 0.1$ .
- the derivative  $\psi'(\omega) < 0 \forall \omega$  with a peak at  $\omega_p = \Omega/\sqrt{3}$ , and  $\Psi'(\omega_p) = \frac{3\sqrt{3}}{8\Omega} \approx \frac{0.65}{\Omega}$ .

In other words,  $\psi(\omega)$  is a soft decreasing unit step function, occurring in the vicinity of  $\Omega$ . The typical “width” of the transition in the frequency domain is approximately one decade. In fact,  $\psi(\omega)$  has a symmetric shape to the right and left of  $\Omega$ , if we use a logarithmic scale for the frequency (as is common practice when analyzing broadband behavior).

For a Foster pair, the equivalent resistance and inductance are both subject to this type of transition, the first one being multiplied by a factor  $-R_p$  and the second one by a factor  $L_p$ , so that the desired increasing- $R$ /decreasing- $L$  characteristic is modeled.

## 7.2 One-pair Foster circuit parameters

The simplest realization of a circuit with these characteristics is the one shown in Fig.7.1, composed of only one Foster pair in series with a resistor and an inductor.

Such a circuit contains four parameters to be determined. Namely, the two series values  $R_s, L_s$  plus the Foster pair  $R_p, L_p$ . These four parameters are determined by giving extraction

values at two different frequencies  $\omega_\ell = 2\pi f_\ell$  and  $\omega_h = 2\pi f_h$ , satisfying the consistency conditions:

$$\omega_\ell < \omega_h \iff \begin{cases} R(\omega_\ell) < R(\omega_h) \\ L(\omega_\ell) > L(\omega_h) \end{cases} \quad (7.5)$$

The equations to solve in this case are :

$$\begin{aligned} R_s + \frac{R_p \omega_\ell^2 L_p^2}{R_p^2 + \omega_\ell^2 L_p^2} &= R_\ell \equiv R(\omega_\ell) & R_s + \frac{R_p \omega_h^2 L_p^2}{R_p^2 + \omega_h^2 L_p^2} &= R_h \equiv R(\omega_h) \\ L_s + \frac{R_p^2 L_p}{R_p^2 + \omega_\ell^2 L_p^2} &= L_\ell \equiv R(\omega_\ell) & L_s + \frac{R_p^2 L_p}{R_p^2 + \omega_h^2 L_p^2} &= L_h \equiv L(\omega_h) \end{aligned} \quad (7.6)$$

This system has an analytic solution, given by:

$$\begin{aligned} R_p &= (R_h - R_\ell)K; & R_s &= R_\ell - \frac{\beta_\ell^2}{1 + \beta_\ell^2} R_p \\ L_p &= (L_\ell - L_h)K; & L_s &= L_\ell - \frac{1}{1 + \beta_\ell^2} L_p \end{aligned} \quad (7.7)$$

with

$$\begin{aligned} K &= \frac{(1 + \beta_\ell^2)(1 + \beta_h^2)}{\beta_h^2 - \beta_\ell^2} = \frac{1}{\psi(\omega_\ell) - \psi(\omega_h)} \\ \beta_{\ell,h} &= \frac{\omega_{\ell,h}}{\Omega} \end{aligned}$$

Here, we have set,

$$\Omega = \frac{R_h - R_\ell}{L_\ell - L_h} \quad (7.8)$$

Equation (7.8) expresses the essence of this solution: it is the result of equating the characteristic frequency of the Foster pair to the characteristic frequency implied by the data, given by the ratio between the variations of  $R$  and  $L$ .

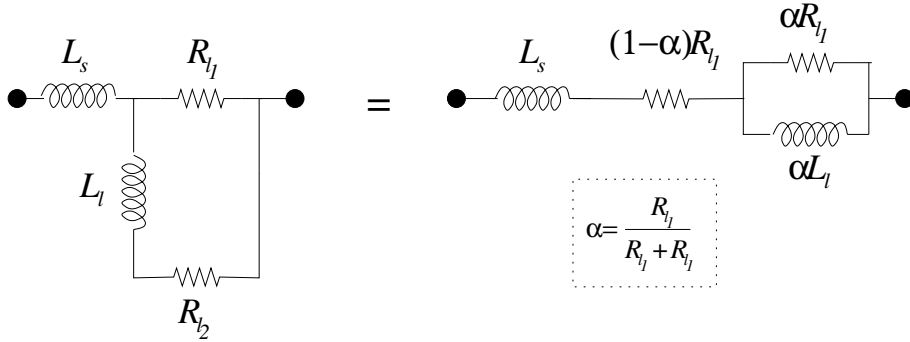


Figure 7.3: Equivalence between a ladder circuit and a corresponding Foster pair circuit.

### 7.3 Equivalence between ladder and Foster pairs

As mentioned in the introduction to the present chapter, several authors have used ladder circuits, instead of Foster pairs, in order to represent frequency-dependent  $RL$  behavior [106, 107]. A ladder element is a “cousin” of a Foster pair: it also has two parallel branches, with a resistance in one branch and an inductance *plus* an inductance on the other, as in the circuit at lhs of the equivalence in Fig.7.3. In this section, we will prove that this ladder circuit has identical behavior as the Foster pair shown as the rhs of this equivalence.

The impedance for the ladder element is:

$$Z^{(L)}(\omega) = \left( \frac{1}{R_{l_1}} + \frac{1}{R_{l_2} + j\omega L_l} \right)^{-1} \quad (7.9)$$

(parameters defined in Fig.7.3) Performing the same procedure as done for Foster pairs, the response for the ladder circuit is:

$$Z(\omega) = R(\omega) + j\omega L(\omega), \quad \begin{cases} R(\omega) &= (1 - \alpha\psi(\omega)) R_{l_1} \\ L(\omega) &= L_s + \alpha^2\psi(\omega)L_l \end{cases} \quad (7.10)$$

where  $\psi$  is the same function as before, with the characteristic frequency given by,

$$\Omega^{(L)} \equiv \frac{R_{l_1} + R_{l_2}}{L_l} \quad (7.11)$$

and we have an additional parameter,

$$\alpha \equiv \frac{R_{l_1}}{R_{l_1} + R_{l_2}}; \quad 0 \leq \alpha \leq 1 \quad (7.12)$$

Like in the Foster circuit, the system with two pairs of input data at  $\omega_\ell$  and  $\omega_h$  has an

immediate solution given by,

$$\Omega = \frac{R_h - R_\ell}{L_\ell - L_h}; \quad \alpha = \frac{R_h - R_\ell}{\psi_\ell R_h - \psi_h R_\ell} \quad (7.13)$$

(obtaining the original parameters  $(R_{l_1,2}, L_l, L_s)$  is trivial from here on).

For the sake of comparison, we rewrite (7.10) in the following way:

$$\begin{cases} R^{(L)}(\omega) &= (1 - \alpha)R_{l_1} + (1 - \psi(\omega))\alpha R_{l_1} \\ L^{(L)}(\omega) &= L_0 + \psi(\omega)\frac{\alpha R_{l_1}}{\Omega} \end{cases} \quad (7.14)$$

Compared to a Foster pair, (7.4) says that the magnitude of the step in  $R^{(FP)}(\omega)$  is  $R_p$ , and the one in  $L^{(FP)}(\omega)$  is  $-L_p$ , which can be written as  $-R_p/\Omega$ . In other words: the step for the ladder is exactly the same as the one for a Foster pair, multiplied by a factor  $\alpha$ . Thus the response of a ladder circuit with solution given by (7.7) is identical to that of a Foster pair with parameters,

$$\begin{aligned} L_s &= L_0 & L_p &= \alpha L_l \\ R_s &= (1 - \alpha)R_{l_1} & R_p &= \alpha R_{l_1} \end{aligned} \quad (7.15)$$

(Note:  $R_s^{-1} = R_{l_1}^{-1} + R_{l_2}^{-1}$ , stating that the series resistance of the equivalent Foster pair is simply the parallel between the resistances of the two ladder branches.)

The difference between the two systems relies in how the sensibility is tuned. For the ladder, parameter  $\alpha$  controls the low-frequency resistance by establishing the relative weight of the purely resistive branch with respect to the mixed; in Foster pairs this role is carried out by the series resistance  $R_s$ .

Two limiting situations exist:

- $\alpha \rightarrow 1$ : gives a Foster pair with  $(R_{l_1}, L_l)$  and no series resistance; this is coherent with the fact that  $\alpha = 1 \leftrightarrow R_{l_2} = 0$ .
- $\alpha \rightarrow 0$ : corresponds to  $R_{l_1} = 0$ , which is tantamount to shorting the ladder structure; only inductance  $L_s$  survives, and there is no corresponding Foster pair.

As a conclusion: for a single-transition picture, there is no difference between using one type of representation or the other. We anticipate that, for systems with more than one transition, the situation is quite different, because the ladder circuits can be cascaded to produce non-trivial behavior (this will be analyzed in the following Chapter).

## 7.4 Implementation

Determining the characteristic frequency in (7.8) is the main difference between our method and the ones discussed in [40], whereby all the characteristic frequencies are pre-established. From the MOR point of view, this predetermination of all possible  $\Omega$ 's in a circuit is a desired property. Instead, from the extraction side of the flow, it is computationally convenient to let  $\Omega$  be determined by the data, as in (7.8). This choice determines the Arbitrary Frequencies Branch Merge variant of MOR mentioned earlier [40].

However, before accepting this solution, we must be certain that it is a representative model of the original data. In other words, we must verify that the transition of the produced Foster pair takes place in the vicinity of the frequencies corresponding to the data we possess. Failing to do so, solution (7.7) is unstable and may lead to unphysical parameters<sup>2</sup>.

Graphically, we want to avoid the situation in which the two data points are on the same branch of the function  $\psi(\omega)$  in Fig. 7.2, meaning that they are not both to the left of the 10%-transition mark, nor both to the right of the one for 90%. This condition reads:

$$[\omega_\ell, \omega_h] \cap [\Omega/3, 3\Omega] \neq \emptyset \quad (7.16)$$

i.e.:

$$\frac{\omega_\ell}{3} \leq \omega_c \leq 3\omega_h \quad (7.17)$$

In arithmetic terms, this statement is equivalent to requiring the denominator in (7.7) not to be small. This denominator is factored as  $(\beta_\ell + \beta_h)(\beta_h - \beta_\ell)$ ,

$$\beta_h - \beta_\ell \ll 1 \iff \omega_h - \omega_\ell \ll \Omega \quad (7.18)$$

If the input data does not comply to these conditions, it is because no significant transition occurs in the given frequency range. Thus, fixed average values of resistance and inductance are appropriate for the whole range.

Returning to the discussion between fixed- $\Omega$  and free- $\Omega$  methods, we point out that the former must impose *ad hoc* the non-negativity of circuit parameters at computation time (generally, a Gauss-Seidel triangulation), whereas condition (7.17) is sufficient for the latter.

In Fig.7.4 we show the implementation of the Foster pair synthesis method included in the actual version Mentor's Calibre tools [22, 41, 108]. Only those aspects that are relevant to broadband extraction are pointed out. The major blocks of the calculation are the one-frequency extraction call to Calibre xL and the call to the TICER/BMR MOR tool, which are documented in the references. With respect to the flow in Fig.7.4, we make the following comments:

<sup>2</sup>Namely, the series parameters  $R_s$  and/or  $L_s$  may take negative values.

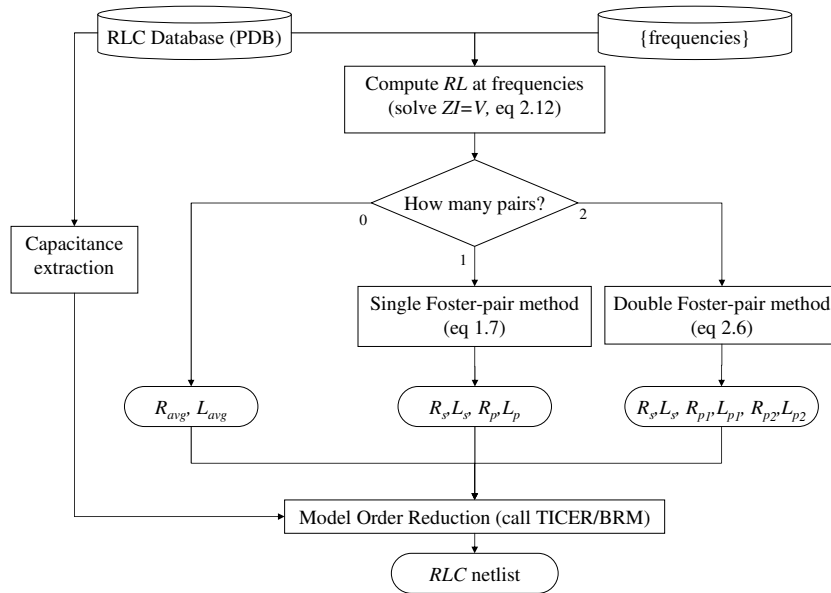


Figure 7.4: Foster pair flow diagram inserted into the Calibre xL extraction tool.

1. Input to Calibre xL is through a geometrical description of wires, that is converted at an earlier stage of the extraction flow into the Parasitics Database (PDB), containing, apart from the geometry, a placeholder for the  $R, L, C$  parameters; the only addition for doing broadband extraction is the set of frequencies.
2. For digital signal nets, in Calibre's low-frequency mode, which does not contemplate skin-effects,  $f_h$  is determined as

$$f_h = \min\left(\frac{1}{t_r}, f_{max}\right)$$

where  $t_r$  is the minimum rise time for the net, and  $f_{max}$  is the technology-dependent maximum frequency where skin effect current crowding may be safely neglected, including one piecewise-constant filament per wire.

3. Determination of the number of transitions springs from (7.17), when 2 data points are extracted; for more data points these conditions are discussed in Section 8.4.

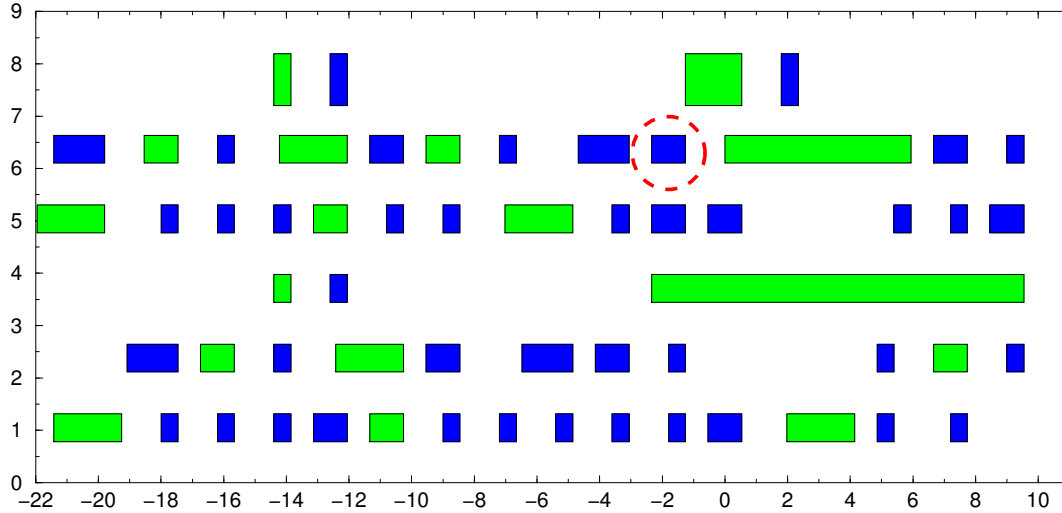


Figure 7.5: Configuration for capturing return-path selection effects; one signal (blue, circled in red) with 17 returns (in green); all lengths are  $1000\mu$  and material is copper.

## 7.5 Examples

In this section, we will analyze two numerical examples of one-pair Foster circuits, one corresponding to the each of the two types of transitions we have been discussing.

### 7.5.1 Example with return-path selection

We concentrate on the example shown in Fig. 7.5: a configuration of one signal and 17 wires identified as grounds. Therefore, the current has 17 degrees of freedom to “choose” the return paths. Original data is produced with FastHenry using one filament per conductor, in order to avoid current-crowding effects on each wire<sup>3</sup>, and computing loop resistance and inductance. These are the symbols with dashed lines in Fig. 7.6. Next, we compute the Foster pair circuit parameters as in Section 7.2 using the data at  $f_\ell = 1GHz$  and  $f_h = 10GHz$ , and plot the result of the fit for a broadband spectrum that covers one decade above and one below the fitted region.

Fig.7.7 plots the errors of these fits, compared to the original data. Worst-case 2.5% error is committed for inductance in the interpolation region, and less than 0.5% for resistance.

The importance of each component of the errors depends on the impact of that magnitude on the total impedance. In order to pinpoint the relevance of these errors, it is perhaps more instructive to decompose the impedance into its absolute value and argument (Fig.7.8, and errors in Fig. 7.7(right)). In this manner, we are able to observe that the aforementioned 2.5% error in

<sup>3</sup>These curves are indistinguishable from the one obtained with the Calibre xL *RL* extraction tool [22].

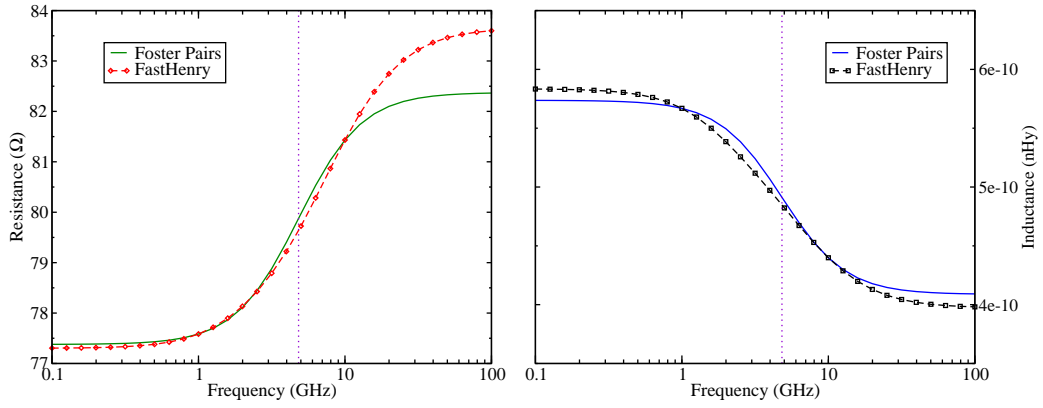


Figure 7.6: Result of fitting with one Foster pair for test case in Fig.7.5.

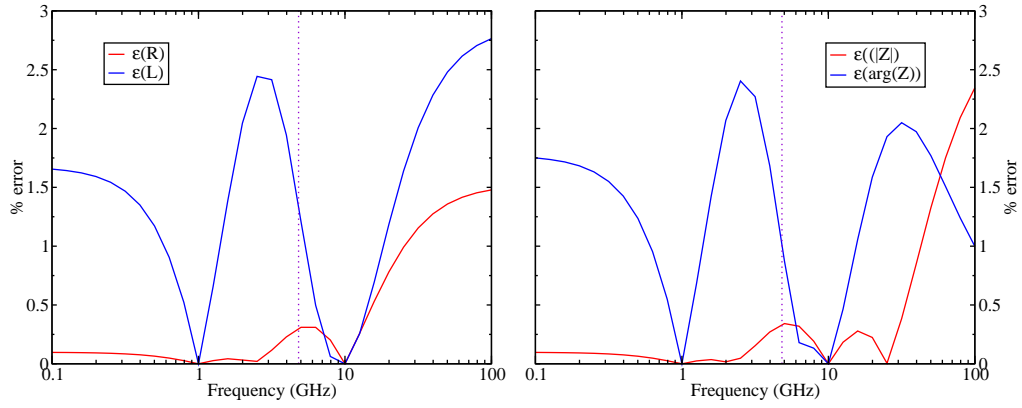


Figure 7.7: Errors for Figs.7.6 and 7.8.

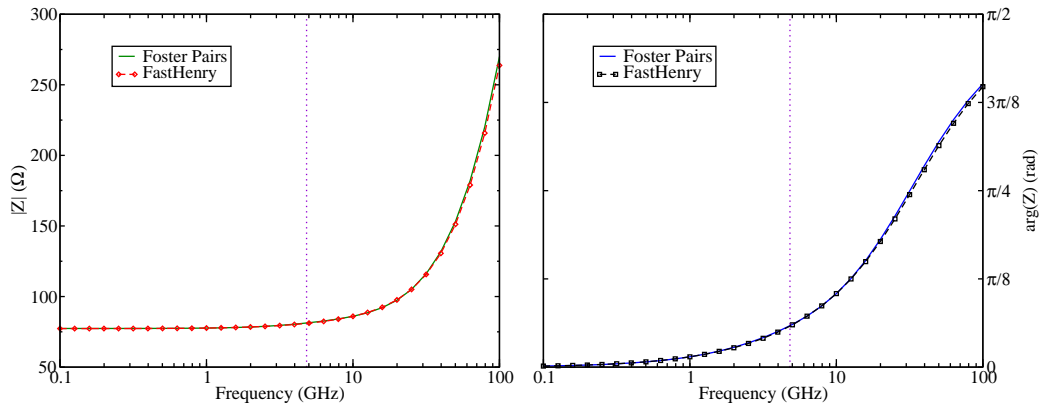


Figure 7.8: Same results as Fig. 7.6, plotting modulus and argument of impedance.

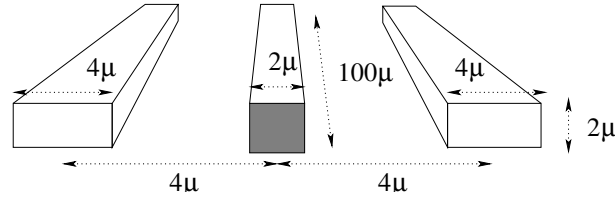


Figure 7.9: Balanced sandwich configuration for the study of skin-effect current crowding.

$L$  is not dominant in the interpolation region: the absolute value of impedance is well fitted with an error below 0.5%. The 2.5% errors in inductance are translated to errors in the argument, when this magnitude is very close to zero.

Finally, we emphasize that errors remain quite low (below 3%) well beyond the interpolated region. Thus, the Foster pair not only fits this interval, but also allows for a fair level of extrapolation. Identical figures were obtained for all the 42 signals (blue cross-sections) in Fig. 7.5.

### 7.5.2 Example with skin-effect current crowding

At very high frequencies, return paths are reduced to the nearest neighbors: the frequency is such that we are well inside the plateau observed at the right extremes of Fig.7.6. Frequency effects for this situation are given by current crowding within the conductors; i.e. the skin effects that are the subject of Part B (Chapters 4-6) of this thesis.

Consider the configuration in Fig.7.9, composed of one signal with two symmetric return paths; the material of all wires is copper. We are interested in a range of frequencies up to 100 GHz, in which the skin depth is smaller or comparable to the dimensions of the wires. By studying a perfectly symmetrical configuration with only two closest return paths, as in Fig. 7.9, we are able to isolate current-crowding effects from the return-path selection effects studied in the previous example.

In order to represent these effects with a one-pair Foster, we fit original data produced with FastHenry at a high precision level ( $9 \times 9$  filaments on the cross section), for frequencies  $f_\ell = 1GHz$  and at  $f_h = 100GHz$ . The characteristic frequency  $f_{char} = \Omega/2\pi$  for the fit is 52.9 GHz, so that condition (7.17) is comfortably satisfied.

We plot the inductance and resistance of the resulting Foster pair fit, compared to the original data, in Fig.7.10. On the right graphs of this figure, we observe that errors remain below 3%. Plotting modulus and argument for this example (Fig.7.11), we see that this time the maximum level of errors are translated to the absolute value of impedance.

Similar examples render the same error figures, with errors always bounded by 5% for representation of skin-effects by one Foster pair.

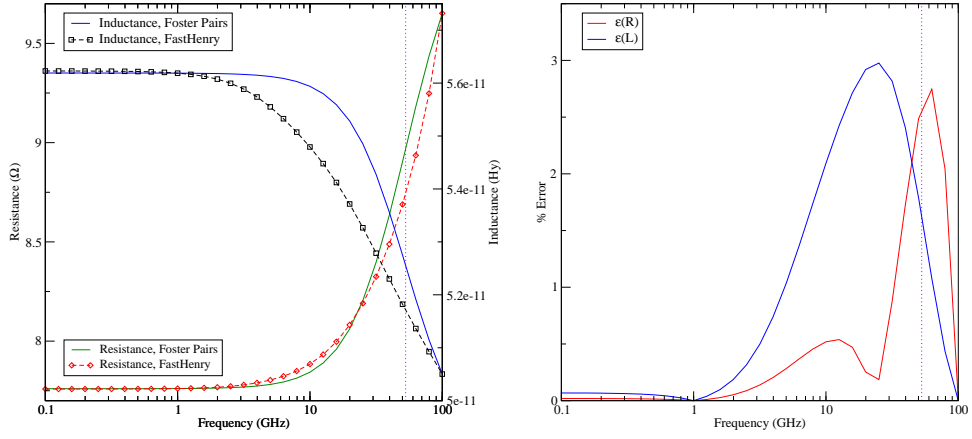


Figure 7.10: Resistance and inductance figures for the configuration on Fig.7.9, comparing Foster pair fit to original data produced with FastHenry at high precision  $9 \times 9$  discretization.

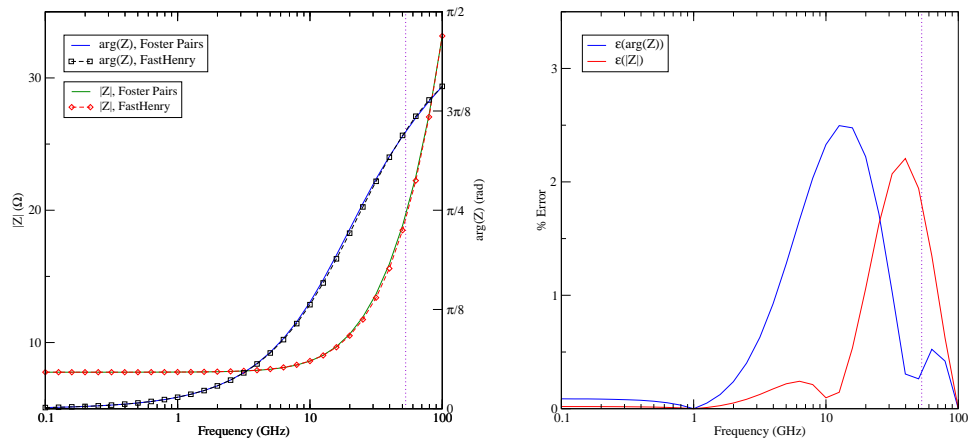


Figure 7.11: Same results as Fig. 7.10, plotting modulus and argument of total impedance.



# Pairs Foster pour des transitions multiples

## Résumé en français

*Pour certaines configurations et gammes de fréquences, les deux transitions décrites dans le chapitre précédent sont présents, et une modélisation à un pair Foster est insuffisante. Dans ce chapitre, nous considérons un cas plus général. Dans la section 8.1, nous transformerons les équations pour un circuit composé de deux pair Foster en une forme simple et maniable. Une solution graphique et simple pour ces équations est proposée dans la section 8.2. Des configurations exemplaires sont exposées et analysées dans la section 8.3. En conclusion (section 8.4.1), nous discutons les conditions de convergence de cette méthode, ainsi que des importants extensions, concernant : le problème d'un nombre arbitraire de pairs ou d'éléments d'échelle d'une part, et la représentation de la dépendance fréquentielle l'inductance mutuelle avec des Foster pairs de l'autre.*



## Chapter 8

# Multiple-transition Foster pairs

At high enough frequencies, both return-path proximity and skin effect crowding are present in the extracted data. For these cases, one Foster pair may not render an acceptable fit. If the characteristic frequencies for these two transitions are substantially different, then it is advisable to include one Foster pair for each of these. Similarly, we may wish to include several Foster pairs in order to model more detailed data.

For a system of Foster pairs, the equations for fitting the circuit parameters become more complicated, due to the non-linearity of the characteristic response  $\psi$  for a Foster pair. For the case of two Foster pairs, they are tractable if we bare in mind which are the important variables. Namely, these are the characteristic frequencies.

The contents of the present chapter are as follows:

- in Section 8.1, we will transform the equations into a simple, tractable form;
- these equations have a graphical solution, which is the subject of 8.2;
- numerical examples are exposed in 8.3;
- we conclude with a discussion on the concerns regarding implementation (Sec.8.4); this discussion is extended to three questions which are presently at the development phase: the generalization to several pairs (8.4.1);  $n$ -ladder circuits as an alternative to Foster pairs (8.4.2); a brief summary of the problem of broadband mutual inductance modeling (8.4.3).

### 8.1 Two-pair system

Consider a circuit composed of two Foster pairs, as in Fig.8.1. Being connected in series, the response of this circuit is simply the addition of two Foster pairs,

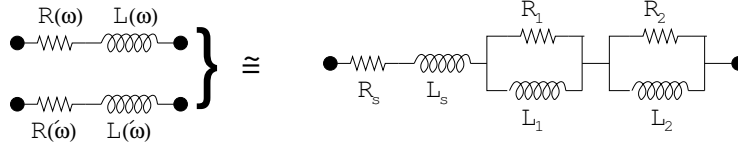


Figure 8.1: Circuit for representing frequency dependence in the presence of two transitions: a resistance and inductance in series with two Foster pair.

$$\begin{aligned}
 R(\omega) &= R_s + \frac{1}{1 + \left(\frac{\Omega_1}{\omega}\right)^2} R_{p1} + \frac{1}{1 + \left(\frac{\Omega_2}{\omega}\right)^2} R_{p2} \\
 L(\omega) &= L_s + L_{p1} + L_{p2} - \frac{1}{1 + \left(\frac{\Omega_1}{\omega}\right)^2} L_{p1} - \frac{1}{1 + \left(\frac{\Omega_2}{\omega}\right)^2} L_{p2}
 \end{aligned} \tag{8.1}$$

where  $\Omega_i \equiv R_{p_i}/L_{p_i}$ ,  $1 \leq i \leq 2$ .

There are 6 circuit parameters to be determined. Thus, we need 6 input data, i.e. 3 pairs of values  $(R, L)$ . Evaluating at 3 frequency points ( $\omega_\ell < \omega_m < \omega_h$ ) we obtain the system of six nonlinear equations,

$$\begin{aligned}
 \frac{1}{1 + x_1^2} R_{p1} + \frac{1}{1 + x_2^2} R_{p2} + R_s &= R_\ell \\
 \frac{1}{1 + x_1^2} \frac{R_{p1}}{x_1} + \frac{1}{1 + x_2^2} \frac{R_{p2}}{x_2} - \left( L_s + \frac{R_{p1}}{x_1} + \frac{R_{p2}}{x_2} \right) \omega_\ell &= -\omega_\ell L_\ell \\
 \frac{k_m^2}{k_m^2 + x_1^2} R_{p1} + \frac{k_m^2}{k_m^2 + x_2^2} R_{p2} + R_s &= R_m \\
 \frac{k_m^2}{k_m^2 + x_1^2} \frac{R_{p1}}{x_1} + \frac{k_m^2}{k_m^2 + x_2^2} \frac{R_{p2}}{x_2} - \left( L_s + \frac{R_{p1}}{x_1} + \frac{R_{p2}}{x_2} \right) \omega_\ell &= -\omega_\ell L_m \\
 \frac{k_h^2}{k_h^2 + x_1^2} R_{p1} + \frac{k_h^2}{k_h^2 + x_2^2} R_{p2} + R_s &= R_h \\
 \frac{k_h^2}{k_h^2 + x_1^2} \frac{R_{p1}}{x_1} + \frac{k_h^2}{k_h^2 + x_2^2} \frac{R_{p2}}{x_2} - \left( L_s + \frac{R_{p1}}{x_1} + \frac{R_{p2}}{x_2} \right) \omega_\ell &= -\omega_\ell L_h
 \end{aligned} \tag{8.2}$$

where we have redefined two of the unknowns as,

$$x_{1,2} \equiv \frac{\Omega_{1,2}}{\omega_\ell} \tag{8.3}$$

as well as the parameters

$$k_{m,h} \equiv \frac{\omega_{m,h}}{\omega_\ell}$$

In order to solve these equations, we first eliminate  $R_s$  and  $L_s$  by forming the relative values  $(R_m - R_\ell)$ ,  $(R_h - R_\ell)$ ,  $(L_m - L_\ell)\omega_\ell$ , and  $(L_h - L_\ell)\omega_\ell$ . Then we further eliminate  $R_{p_2}$  by combining as follows,

$$\begin{aligned} (R_m - R_\ell) + x_2\omega_\ell(L_m - L_\ell) &= \left( \frac{k_m^2}{k_m^2 + x_1^2} - \frac{1}{1 + x_1^2} \right) (x_1 - x_2)R_{p_1} \\ (R_h - R_\ell) + x_2\omega_\ell(L_h - L_\ell) &= \left( \frac{k_h^2}{k_h^2 + x_1^2} - \frac{1}{1 + x_1^2} \right) (x_1 - x_2)R_{p_1} \end{aligned} \quad (8.4)$$

Dividing left- and right-hand sides above eliminates  $R_{p_1}$ , so that we have effectively reduced the system to two unknowns, namely  $x_1$  and  $x_2$ :

$$x_2 = C - \frac{D}{x_1^2 - B} \quad (8.5)$$

where we have used the auxiliary parameters

$$\begin{aligned} D &= \frac{A(k_m^2 + k_h^2)(g_h - g_m)}{1 - A} \\ C &= \frac{g_m - Ag_h}{1 - A} \\ B &= \frac{Ak_h^2 - k_m^2}{1 - A} \\ A &= \frac{(k_m^2 - 1)(L_\ell - L_h)}{(k_h^2 - 1)(L_\ell - L_m)} \\ g_{m,h} &= \frac{1}{\omega_\ell} \frac{R_{m,h} - R_\ell}{L_\ell - L_{m,h}} \end{aligned}$$

We remark that in passing from (8.2) to (8.4), we have eliminated  $R_{p_2}$  by multiplying the “ $L$ ” equations by  $x_1$  and adding the corresponding “ $R$ ” equation; likewise, we could eliminate  $R_{p_1}$  by doing the same process with  $x_2$ . This produces exactly the same final equation (8.5) with  $x_1$  and  $x_2$  interchanged.

## 8.2 Solving the equations

In the previous section, we have reduced the two-Foster pair system of 6 nonlinear equations to one with 2:

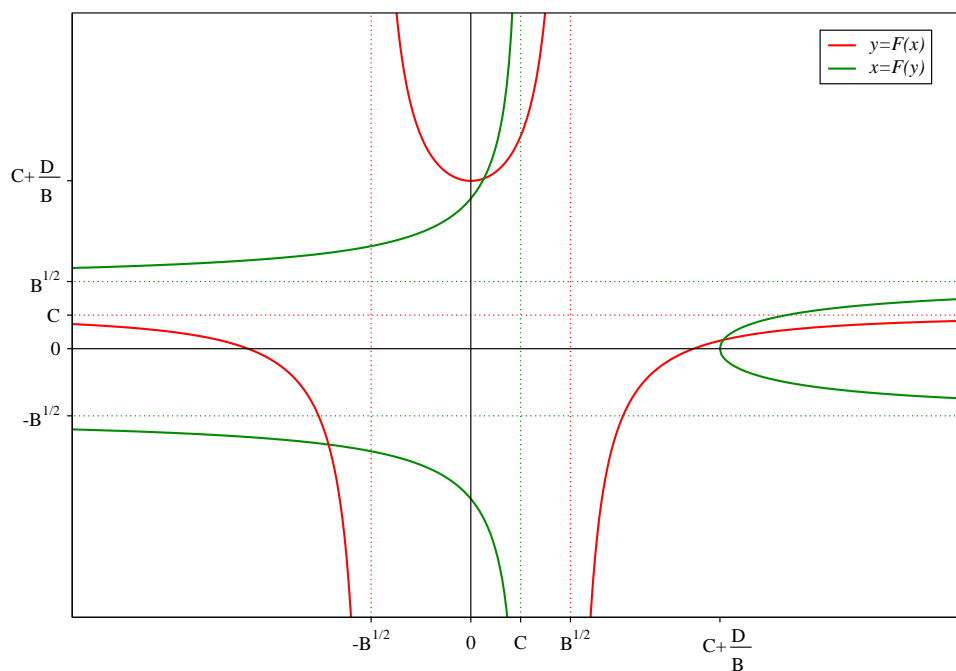


Figure 8.2: Graphical view of the solution of the 2-pair Foster system (8.6) for  $x_1, x_2$ , given by the intersection of the green and red curves (dotted lines correspond to asymptotes).

$$\begin{cases} x_1 = F(x_2) \\ x_2 = F(x_1) \end{cases} \quad \text{with } F(x) = C - \frac{D}{x^2 - B} \quad (8.6)$$

with the definitions as in (8.5).

Graphically, solving this equation is tantamount to intersecting the two curves in Fig.8.2. In the next two subsections, we will first show that a simple fixed-point iteration can be applied for solving this equation; we will later analyze the conditions for the convergence of this solution.

### 8.2.1 Fixed-point iteration

Solving (8.6) can be done very efficiently by performing the fixed-point iteration:

$$\begin{aligned} x_1^{(n+1)} &= F(x_2^{(n)}) \\ x_2^{(n+1)} &= F(x_1^{(n+1)}) \end{aligned} \quad (8.7)$$

Assuming convergence is guaranteed (see conditions (8.10) in the following section), a safe

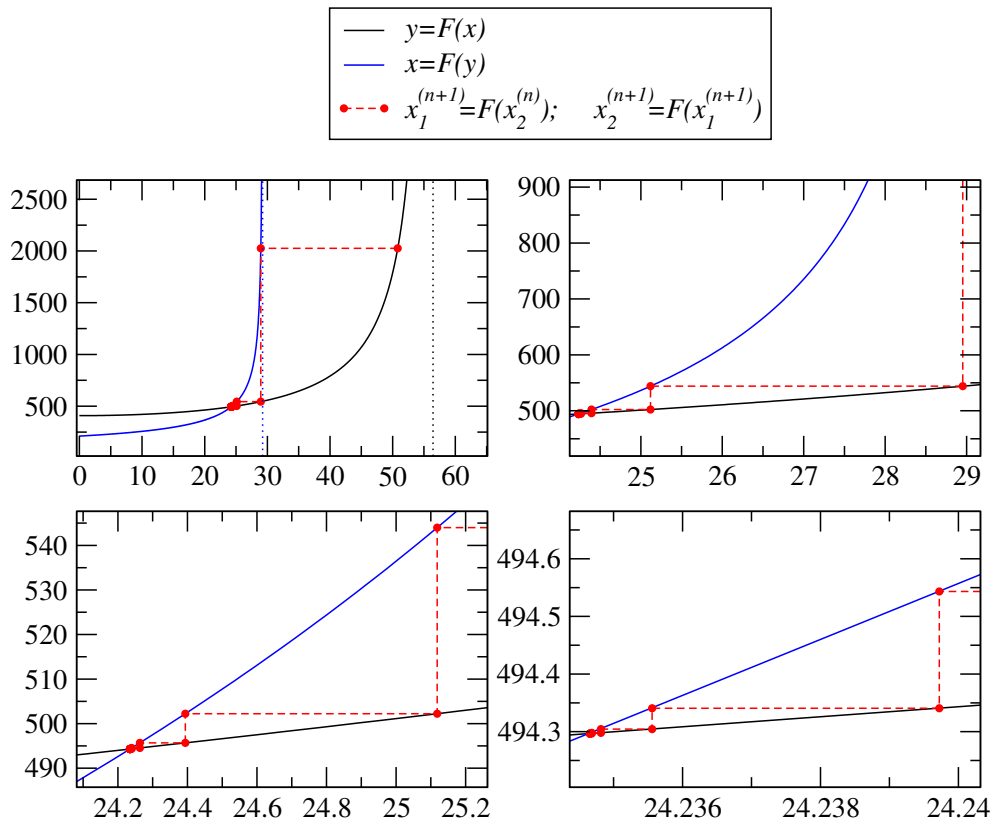


Figure 8.3: Convergence of the fixed point for a typical-case two Foster pair circuits; values are:  $C = 33.21, D = 1.25 \cdot 10^6, B = 7477$ , emanating from the test case presented in Figs.8.4 and 8.5;  $10^{-8}$  tolerance convergence is reached in 10 iterations.

and efficient starting point is  $x_2^{(1)} = \frac{1}{2}(C + \sqrt{B})$ , i.e. the mid-point between the two vertical asymptotes in Fig.8.2.

In Figs.8.3, we show an example of this convergence for a typical test case, reaching  $10^{-8}$  accuracy in the solution within 10 iterations. Similar convergence is obtained for a large variety of examples, never exceeding 15 iterations, for the same tolerance.

Once the characteristic frequencies are obtained by undoing (8.3), the circuit parameters of the circuit follow immediately:

$$\begin{aligned}
 R_{p1} &= \frac{(R_m - R_\ell) \left(1 - \frac{x_2}{g_m}\right)}{\left(1 - \frac{x_2}{x_1}\right) \left(\frac{k_m}{k_m + x_1^2} - \frac{1}{1 + x_1^2}\right)} \\
 R_{p2} &= \frac{(R_m - R_\ell) \left(1 - \frac{x_1}{g_m}\right)}{\left(1 - \frac{x_1}{x_2}\right) \left(\frac{k_m}{k_m + x_2^2} - \frac{1}{1 + x_2^2}\right)} \\
 L_{p1} &= \omega_\ell x_1 R_{p1} \\
 L_{p2} &= \omega_\ell x_2 R_{p2} \\
 R_s &= R_\ell - \frac{R_{p1}}{1 + x_1^2} - \frac{R_{p2}}{1 + x_2^2} \\
 L_s &= L_\ell - \frac{x_1^2 L_{p1}}{1 + x_1^2} - \frac{x_2^2 L_{p2}}{1 + x_2^2}
 \end{aligned} \tag{8.8}$$

Concerning the efficiency of the fixed-point iteration, we remark that (8.6) can be transformed into a single equation:

$$x = F(F(x)) \tag{8.9}$$

This is a 5-th degree equation, that can be solved with standard techniques. If we can assure that (8.7) converges, then so will (8.9). For example, we have implemented an elementary Newton-Raphson method that converges in 5 iterations, for the same example as the one shown in Fig.8.3 (which requires 10 iterations for the same accuracy).

However, the cost of calculating the order-5 polynomial coefficients, plus evaluating it and its order-4 derivative at each iteration, exceeds the total cost required for the immediate evaluations of  $F$  in (8.7). This was verified by counting the number of CPU cycles, using the same tool *quantify* [90] as in Section 5.6: for this example, the 10 fixed point iterations cost a total of 41 CPU cycles, whereas the computation of coefficients plus the 4 iterations of the Newton-Raphson require 125 cycles<sup>1</sup>.

<sup>1</sup>Given that these runtimes are negligible with respect to the ones for extraction, we do not emphasize this point, as any solution method is a valid one; we prefer the fixed-point method not only because it is slightly faster, but

### 8.2.2 Convergence conditions

Inspection of the graphs in Fig. 8.2 shows that a solution in the  $(x_1 > 0, x_2 > 0)$  quarter is guaranteed under the conditions<sup>2</sup>:

$$B, C, D > 0 \quad \wedge \quad \begin{cases} \sqrt{B} > C & \wedge \quad \Delta > 0 \\ & \vee \\ \sqrt{B} < C & \wedge \quad \Delta < 0 \end{cases} \quad (8.10)$$

where we have defined  $\Delta \equiv C + \frac{D}{B} - \sqrt{B - \frac{D}{C}}$ , the difference between the values at  $x = 0$  for  $F$  and  $F^{-1}$  (i.e., the intersections between the vertical axis and the red and green curves in Fig.8.2, respectively).

Parameters  $B, C, D$ , defined for eq. (8.5), are dimensionless ratios for the input data. As such, the conditions above depend on the quality of input data. We cannot have a mathematical proof for all possible sets of input, but we can analyze in detail the inequalities' implications. In a broad sense, these are generalizations of the condition (7.17): input data must represent a significant transition at the extracted frequencies.

In first place, let us consider an auxiliary condition, namely  $A < 1$ . Parameter  $A$  in (8.5) is the result of dividing the two steps in the input data for inductance, and multiplying this number with the division of the squares of the two steps in frequency. From all the examples we have seen, it is clear that inductance makes a shift within the same order of magnitude, even for frequencies that are separated by several decades. If the frequency values are chosen far enough apart, the ratio of squares of frequencies will be much much larger than the ration between inductance variations:

$$A < 1 \iff S_L \equiv \frac{L_\ell - L_h}{L_\ell - L_m} < \frac{k_h^2 - 1}{k_m^2 - 1} \simeq \left( \frac{\omega_h}{\omega_m} \right)^2$$

Next we consider condition  $B > 0$ . Assuming  $A < 1$ , then

$$B > 0 \iff S_L > \frac{1 - k_m^{-2}}{1 - k_h^{-2}} \simeq 1 + \left( \frac{\omega_m}{\omega_h} \right)^2 \quad (8.11)$$

Using the same argument as before, since frequencies span orders of magnitude, the right-most values of this expression is expected to be very close to 1. If data is "good", in the sense that it represents a non-trivial difference between the  $L$  values at  $\omega_\ell$  and those at  $\omega_h$ , then this condition should hold comfortably.

Next, we take into account  $g_h$  and  $g_\ell$ : they represent ratios between the characteristic fre-

---

because of its inherent graphical beauty.

<sup>2</sup>These are sufficient conditions, we make no claim concerning necessary conditions.

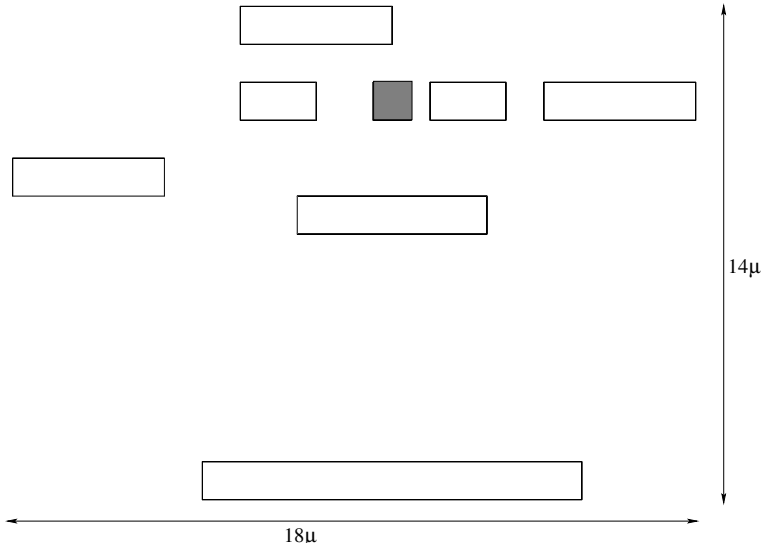


Figure 8.4: Configuration of wires for 2-pair  $RL$  extraction (signal wire shaded).

quency, implied at each extraction, and the lowest angular frequency  $\omega_\ell$ . Again, if data is well chosen, these frequencies should respect  $g_h > g_m$ , thus satisfying condition  $D > 0$ .

Considering  $C > 0$ , it translates into a similar condition as the one for  $B$ , but for resistance instead of inductance:

$$C > 0 \iff S_R \equiv \frac{R_h - R_\ell}{R_m - R_\ell} < \frac{k_h^2 - 1}{k_m^2 - 1} \simeq \left( \frac{\omega_h}{\omega_m} \right)^2 \quad (8.12)$$

We have found no strong correlation to physical conditions in order to support the inequalities inside the brackets of eq.(8.10). Nevertheless, we emphasize an empirical argument that is most convincing: no realistic test cases has violated these conditions yet. In the following section, we will present a representative example, and see that these conditions are comfortably satisfied for all types of input data.

### 8.3 Examples

In Fig. 8.5 we exemplify the fit resulting from this methodology. The configuration is shown in Fig.8.4, consisting of one signal and 7 return wires. The extractions correspond to frequencies:  $f_\ell = 0.1GHz$ ,  $f_m = 10GHz$ ,  $f_h = 54GHz$ . Original data is produced with FastHenry at a high-precision level, in order to capture skin-effect current crowding<sup>3</sup>. As in the previous chapter, we compute loop resistance and inductance.

<sup>3</sup>To be contrasted with data in Fig.7.6, in which one filament per wire is used, so that data only represents return-path selection effects; or the one in Fig.7.9, in which return-path selection effects are absent.

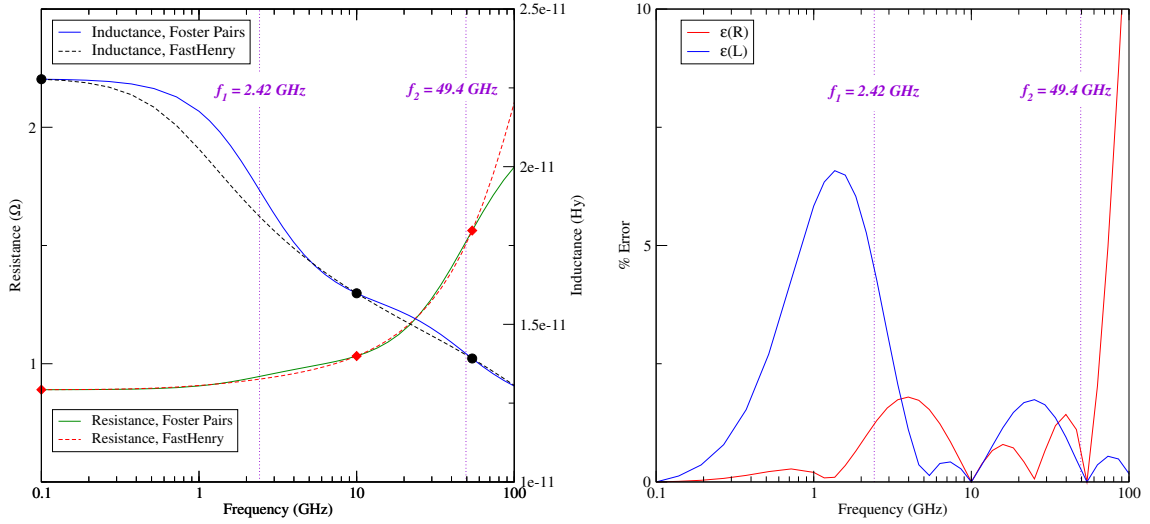


Figure 8.5: Two-pair Foster fit for the configuration of Fig. 8.4, and original data produced with FastHenry at  $9 \times 9$  discretization.

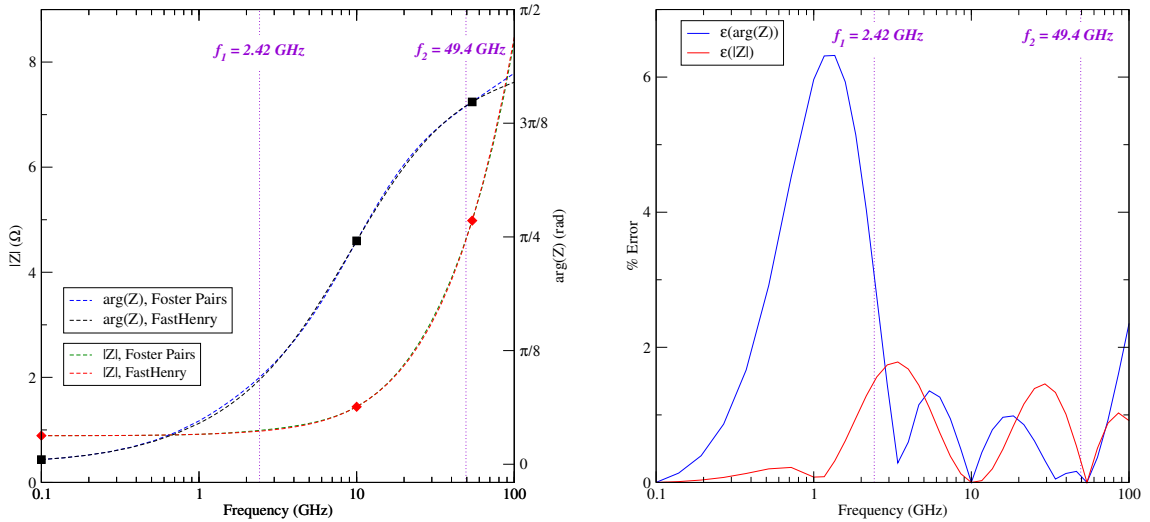


Figure 8.6: Same data as Fig. 8.5, plotting modulus and argument of impedance.

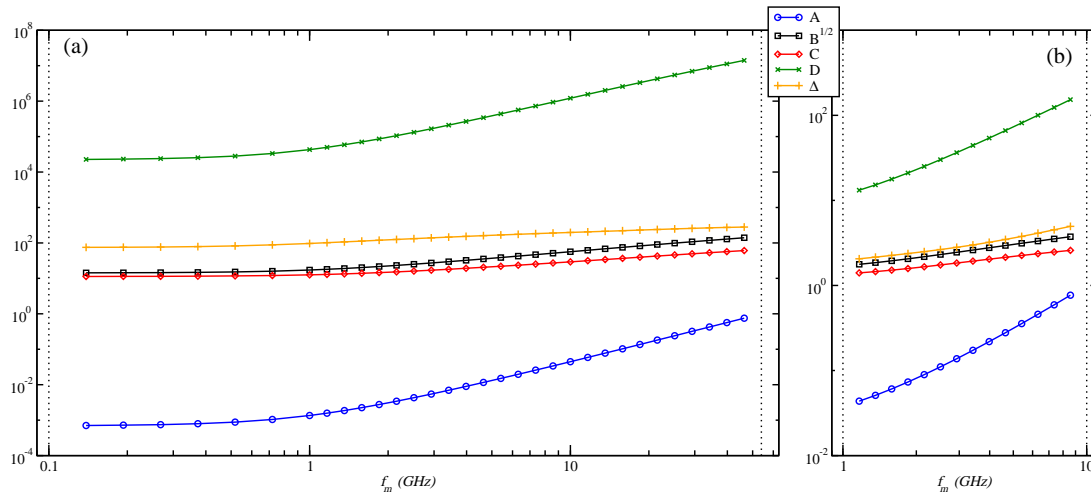


Figure 8.7: Verification of conditions in (8.10) for the 2-pair Foster solution of Fig. 8.4, varying  $f_m$  in the range  $[f_\ell, f_h]$  - indicated by the vertical dotted lines - at left: setting  $f_\ell = 0.1\text{GHz}$  and  $f_h = 54\text{GHz}$ ; at right:  $f_\ell = 1\text{GHz}$  and  $f_h = 10\text{GHz}$ .

Convergence to 8-digit precision occurs within 10 iterations of (8.7), obtaining the characteristic frequencies:  $f_1 = 2.42\text{GHz}$ ,  $f_2 = 49.4\text{GHz}$ . Inside the interpolated region, the comparison between real data and the one from the two-pair Foster circuit shows an acceptable representation of frequency effects up to frequencies of the order of  $100\text{GHz}$ .

Note that the discrepancies occur mainly for inductance at low frequencies (where its effect is negligible) and for resistance at high frequencies (idem). This is better expressed in the graphs for absolute value and argument, Fig. 8.6: the error in the magnitude of impedance is always below 2% in the interpolation region, the 6% errors in  $L$  being insignificant in the region where they occur. As in the previous chapter, the large (6%) relative errors in the argument of impedance are for values where it is close to zero.

Regarding the conditions for convergence to the solution, we now analyze this method's sensibility to the choice of data inputs. Suppose we fix, as in the example in Fig. 8.5, the maximum and minimum frequencies, at their values  $f_\ell = 0.1\text{GHz}$  and  $f_h = 54\text{GHz}$ . Then, we vary  $f_m$  in the broad range that separates these two extremes. For each of these intermediate frequencies, we calculate the four parameters  $A$ ,  $\sqrt{B}$ ,  $C$ ,  $D$  and  $\Delta$  (see eq. (8.10)). These results are plotted in Fig. 8.7a.

We observe that all the conditions are comfortably satisfied (note the logarithmic y-scale), even for values of  $f_m$  very close to  $f_\ell$  or  $f_h$ . Similar figure is obtained for values of  $f_\ell$  and  $f_h$  separated by only one decade, shown in of Fig.8.7b. The number of iterations needed for convergence at  $10^{-8}$  precision remains between 9 and 13 for all the different values of  $f_\ell$ ,  $f_m$  and

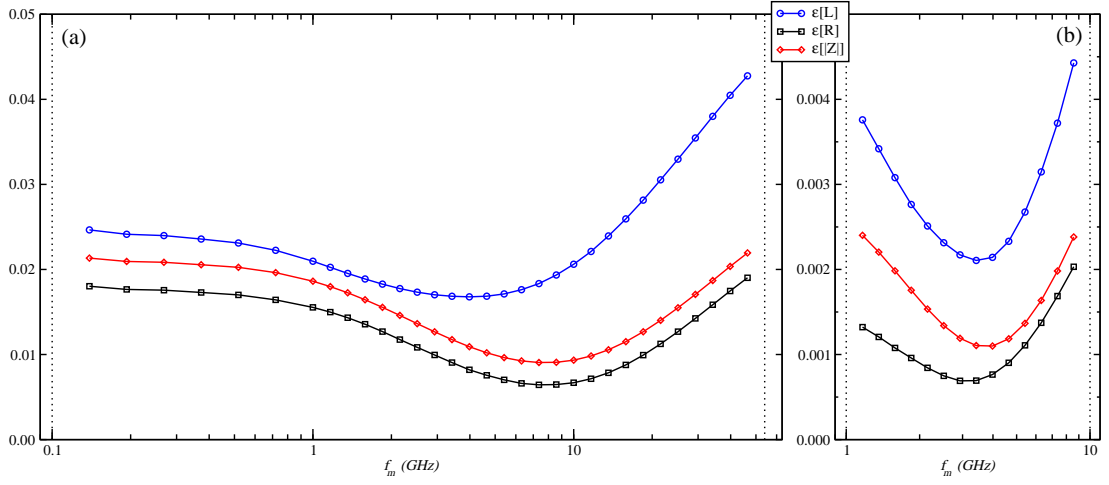


Figure 8.8: Average errors for the 2-pair Foster fits as function of the intermediate frequency  $f_m$ : at left, for range  $[0.1\text{GHz}, 54\text{GHz}]$ ; at right, for range  $[1\text{GHz}, 10\text{GHz}]$ .

$f_h$  shown in the figures.

Errors for the fits, as a function of the choice of the intermediate frequency  $f_m$ , have a minimum near the middle<sup>4</sup> of the range  $[f_\ell, f_h]$ . In Fig.8.8, we plot these average errors: for each value of  $f_m$  we compute the Foster pair parameters and the global average error of the fit as,

$$\varepsilon[X] = \frac{1}{N_f} \sum_{i=1}^{N_f} \frac{|X_i^{(fit)} - X_i^{(orig)}|}{X_i^{(orig)}} \quad (8.13)$$

for  $X = R, L, |Z|$ , the “(fit)” supra-index indicates the magnitudes produced by the 2-pair Foster circuit, and “(orig)” is the original data produced by FastHenry;  $N_f$  covers the whole interpolated region.

## 8.4 Discussion and further work

One-pair Foster circuits are implemented and tested within the Calibre xL formatter according to the specifications in Section 7.4. Concerning the 2-pair method, certain questions are of concern, mainly:

<sup>4</sup>Note: “middle” refers to the logarithmic-scale separation of frequencies; when doing broadband we assign the same weight to all frequency points chosen equally spaced according to this scale. This also applies to the estimation of average errors (i.e., we do not weigh the error with the frequency interval between points, as this would bias the figure on the side of high frequencies.)

1. When can we guarantee a solution for the input data?
2. Are the circuit parameters always real and positive?

The first point is easily implementable, since conditions (8.10) can be immediately verified, avoiding unnecessary iterations when they are not. Non-compliance to these conditions leads to the one-pair solution, by dropping one of the data input points (the  $f_m$  extraction is the natural candidate in this regard, as the user is generally interested in the range  $[f_\ell, f_h]$ ).

The second point is more delicate. We recall the discussion in Section 7.4 concerning when a significant transition is implied by the input data. Generalizing to the 2-pair situation, the analogous question is whether the data represents two significant transitions. In practice, this translates to: how much do the two characteristic frequencies differ? We will establish that the two transitions are well “resolved”<sup>5</sup> when the second one’s peak occurs at a frequency where the first one has completed 90% of the transition. Relating to Fig.7.2 this means that there are two distinct transitions at characteristic frequencies  $\Omega_1$  and  $\Omega_2$  if and only if:

$$3\Omega_1 < \frac{\Omega_2}{\sqrt{3}} \Leftrightarrow \frac{\Omega_2}{\Omega_1} > 3\sqrt{3} \approx 5.2 \quad (8.14)$$

Apart from the condition above, we must also enforce that these two characteristic frequencies comply to the single-pair condition (7.17), namely that the input data is not completely to left or to the right of the characteristic transitions of each Foster pair. When any of these conditions are not satisfied, then a 1-pair, or eventually no pair, representation is the appropriate one.

At present time, the method described in this chapter is implemented within the Calibre formatter, and is in the process of being tested for a large variety of test cases. There has been no situation in which any of the two questions above have lead to inconsistencies. In other words, if conditions (7.17) and (8.14) hold, then the method has always converged to a physically correct solution.

We finish this discussion by exposing three issues that are presently under study. The first two issues deal with the generalization of these methods to a larger number of pairs, or input data. The third issue deals with the representation of frequency dependent mutual coupling.

### 8.4.1 Generalization to $n$ -pairs

As we have mentioned over these two chapters, there are typically two types of frequency-dependent behaviors: return-path selection, for frequencies up to about 10 GHz for 90 nm technology (the frequency value scales upward with technology); and skin-depth current crowding, for higher frequencies. Within this picture, three well chosen data sets  $(R_i, L_i)$  should be enough

<sup>5</sup>We borrow this term from optics, applied to the peaks in the derivatives of the two characteristic functions.

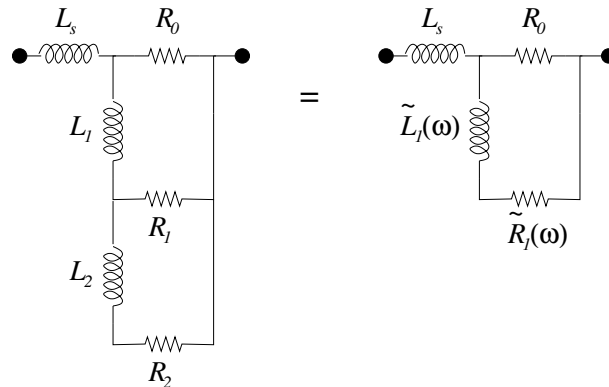


Figure 8.9: Two-ladder circuit and its reduction to a 1-ladder circuit.

to fit two Foster pairs and capture both transitions. In terms of computing cost, we emphasize that extraction is the expensive task of the whole flow, so that we are usually interested in keeping down the number of extracted data.

However, in certain cases, a user may wish to obtain more information, or assure a better fit, by extracting at more frequencies. The question is how to treat this larger data set. The first decision is whether to augment the number of Foster pairs or not:

- Extending the number of Foster pairs in order to fit more data, in a similar fashion as the one presented in this chapter, is not advisable. The functional relationship between characteristic frequencies will be a very intricate version of (8.5), and a graphical solution as the one presented in Section 8.2 is not available. Nevertheless, numerical solvers for this type of fit exist (or can be developed *ad hoc*), although the cost and capacity of avoiding unnecessary iteration is difficult to control.
- If the number of Foster pairs stays fixed at two, it is clear that the behavior can not be fitted to an exact solution, since the system is overdetermined. Instead, this becomes a problem of least-squares fit. For low-dimensional problems like this case, there are very efficient out-of-the-box implementations [109]. These kind of techniques are easily extended to more than two Foster pairs, if desired (and enough data is available, although we insist that, on physical grounds, two Foster pairs should be sufficient).

#### 8.4.2 Higher-order ladder networks

Another interesting alternative is that of considering the higher-order ladder circuits. We recall that for a single ladder element, there is no difference between a ladder and a Foster pair representation (see Section 7.3). However, for more complicated structures, this is not the case.

Consider the circuit in Fig. 8.9, with two cascaded ladder elements. Having 6 total parameters, we are able to fit the same data as with two Foster pairs (circuit 8.1). The system equations for Fig. 8.9 can be reduced to an equivalent circuit with one frequency-dependent ladder element:

$$\begin{aligned}\tilde{R}_1(\omega) &= (1 - \alpha_1\psi_1(\omega))R_1 \\ \tilde{L}_1(\omega) &= L_0 + \alpha_1^2\psi_1(\omega)L_2 = L_0 + \alpha_1\psi_1(\omega)\frac{R_1}{\Omega_1}\end{aligned}\quad (8.15)$$

with,

$$\psi_1 = \frac{1}{1 + (\omega/\Omega_1)^2}, \quad \Omega_1 = \frac{R_1 + R_2}{L_2}, \quad \alpha_1 = \frac{R_1}{R_1 + R_2}$$

as in Section 7.3. Then the total impedance of the circuit can be written as,

$$\begin{aligned}R(\omega) &= (1 - \tilde{\alpha}_0\psi_0(\omega))R_0 \\ L(\omega) &= L_s + \tilde{\alpha}_0^2\psi_0(\omega)\tilde{L}_1 = L_s + \tilde{\alpha}_0\psi_0(\omega)\frac{R_0}{\tilde{\Omega}_0}\end{aligned}\quad (8.16)$$

where we have introduced the notation:

$$\psi_0 = \frac{1}{1 + (\omega/\tilde{\Omega}_0)^2}, \quad \tilde{\Omega}_0(\omega) = \frac{\tilde{R}_1(\omega) + R_0}{L_1}, \quad \tilde{\alpha}_0(\omega) = \frac{R_0}{\tilde{R}_1(\omega) + R_0}$$

Magnitudes  $\tilde{\alpha}_0, \tilde{\Omega}_0$  for the reduced circuit, play the same role as the corresponding ones in a one-ladder network, but are frequency-dependent. Here resides the main difference between this problem and the 2-pair Foster one: characteristic frequencies are “cascaded” for ladder networks, whereas they are added for Foster pairs. Basically, this corresponds to the comparison between the arithmetic result of placing circuits in parallel or in series. Foster pairs placed in parallel do not acquire any extra degree of freedom, since they can be reduced to just one pair with the  $R_p$  and  $L_p$  corresponding to the parallel of all resistances and inductances. This is why only series Foster networks are analyzed.

Parallel ladder networks, on the other hand, respond to a more complex structure of composition, with characteristic transitions occurring within characteristic transitions. At the heart of the distinction between the two types of models, lies the main limitation for the Foster systems: each Foster transition occurs over a range of roughly one decade around  $\Omega$ ; for ladder networks, this is not the case.

Before implementing this type of model, which implies solving the intertwined equations (8.15) and (8.16) for a given set of input data, it is necessary to analyze the capacity of the output n-ladder system to be reduced. Merging parallel ladders in TICER/BMR is not as straightforward

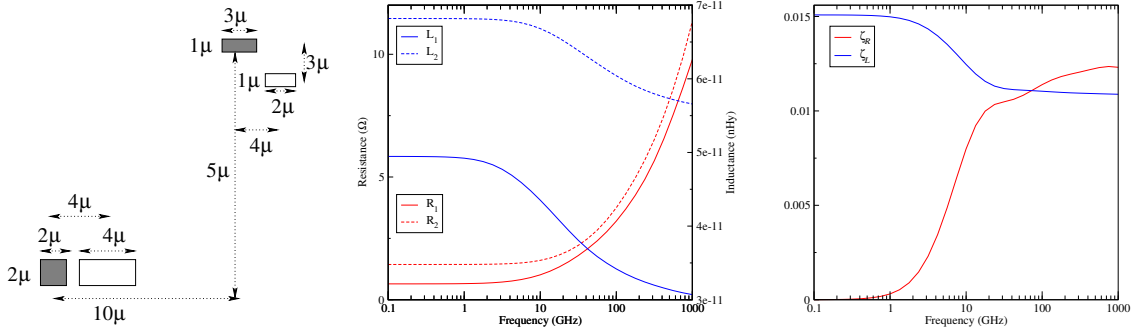


Figure 8.10: Two-bundle example configuration for study of mutual broadband  $RL$  (left), and magnitudes obtained with FastHenry: self resistance and inductance (center) and mutual coupling coefficients (right).

ward as doing so with series ladders (which are equivalent to Foster pairs) [110].

### 8.4.3 Broadband mutual impedance

Foster pairs replace the single-frequency ( $R, L$ ) values in the netlist for self inductance calculations at a fixed frequency. We now turn to the corresponding changes needed in the representation of mutual inductance.

First of all, we point out that mutual inductance calculations are generally carried out in order to obtain upper bounds for noise. In this sense, it is generally sufficient to give an estimate of the maximum coupling over a whole frequency band. This solution is currently employed for Calibre tools.

Having said this, we consider the example shown in Fig.8.10a, with two coupled bundles. We can extract the values for self and mutual impedance using, say, FastHenry. This gives a  $2 \times 2$  matrix:

$$\mathbf{Z}(\omega) = \begin{bmatrix} Z_1(\omega) & Z_{12}(\omega) \\ Z_{12}(\omega) & Z_2(\omega) \end{bmatrix} \quad (8.17)$$

For this matrix, we plot in Fig.8.10c the coupling coefficients<sup>6</sup>:

$$\zeta_L = \frac{L_{12}}{\sqrt{L_1 L_2}}; \quad \zeta_R = \frac{R_{12}}{\sqrt{R_1 R_2}} \quad (8.18)$$

Immediately, we observe that these couplings are described by a Foster-pair type of transi-

<sup>6</sup>The term "coupling resistance" is the counterpart of the more familiar coupling inductance; it acts on the real part in the same manner as the latter works on the imaginary one, and has a circuit representation as current-controlled voltage source, treated by most circuit simulators. In physical terms, it is important for loop inductance when two bundles are very close, and is specially important for configurations with shared grounds.

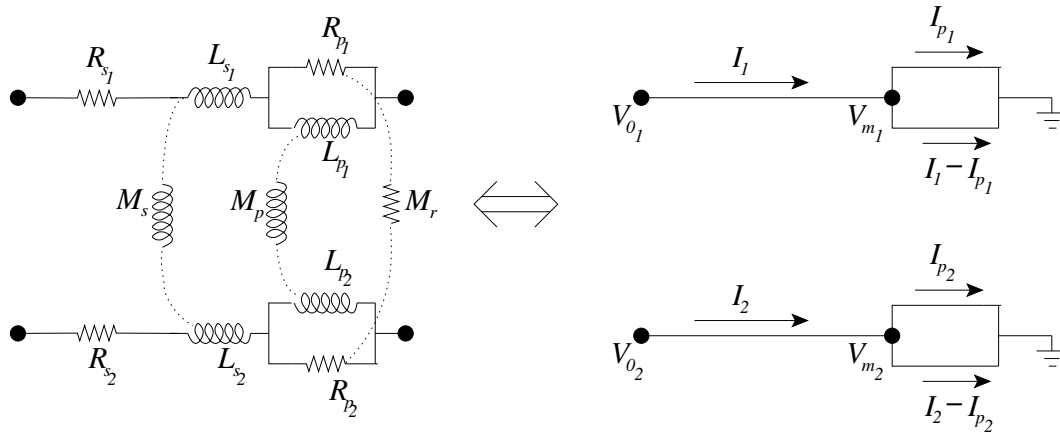


Figure 8.11: Model and circuit representation containing the notation for frequency-dependent mutual impedance.

tion:  $\zeta_L$  undergoes a monotonically decreasing step, and  $\zeta_R$  a monotonically increasing step (with zero coupling  $R$  at low frequencies). Moreover, the "characteristic frequency" corresponding to these steps is approximately the same as the ones shown for the self transitions (Fig.8.10b). Since our intention is to model the whole circuit with fixed parameters, we can picture this as two Foster circuits, with fixed coupling between the two inductive branches, and fixed coupling between the two resistive branches. In this manner, the magnitude of the total coupling is "tuned" by the current along the branches of each Foster pair. This leads us to attempt to model the this system with the circuit in Fig.8.11, adding the following elements:

- $M_s$  :inductance coupling between the two series inductances;
  - $M_p$  :inductance coupling between the two pair inductances;
  - $M_r$  :resistance coupling between the two series inductances;
- (8.19)

The equations for this circuit are given by:

$$\begin{aligned}
(R_{s_1} + j\omega L_{s_1})I_1 + j\omega M_s I_2 &= V_{o_1} - V_{m_1} \\
j\omega M_s I_1 + (R_{s_2} + j\omega L_{s_2})I_2 &= V_{o_2} - V_{m_1} \\
R_{p_1} I_{p_1} + M_r I_{p_2} &= V_{m_1} \\
M_r I_{p_1} + R_{p_1} I_{p_2} &= V_{m_2} \\
j\omega L_{p_1} (I_1 - I_{p_1}) + j\omega M_p (I_2 - I_{p_2}) &= V_{m_1} \\
j\omega M_p (I_1 - I_{p_1}) + j\omega L_{p_2} (I_2 - I_{p_2}) &= V_{m_2}
\end{aligned} \tag{8.20}$$

where all the symbols are defined in Fig. 8.11.

The system for the six unknowns  $(I_1, I_2, I_{p_1}, I_{p_2}, V_{m_1}, V_{m_2})$  can be reduced to a  $2 \times 2$  system for the two total currents, although the expressions are quite cumbersome.

Another important observation is that the self parameters (central graph of Fig.8.10) are largely unaffected by the coupling, i.e.: if we compute them individually, we obtain identical curves with at least three digits accuracy. This leads us to introduce the main assumption for estimating the parameters in our model. Namely, that the Foster-pair parameters in Fig.8.11 and eq.(8.20) are the same as the ones for the uncoupled configuration. We have encountered this situation several times throughout the present work: for example, when computing the distributions coefficients  $\alpha_i$  among return paths for a bundle in Section 2.2, we neglect the presence of other bundles. Here, we are dealing with the frequency-dependent version of the same statement.

Using this information, and the data extracted at two frequency points, we obtain a system of 3 (non-linear) equations for unknown parameters  $M_r, M_s, M_p$ . The recipe is the following:

1. extract at  $\omega_\ell$  and  $\omega_h$ ;
2. compute the two Foster pairs separately, using:

$$(Z_1(\omega_\ell), Z_1(\omega_h)) \rightarrow (R_{s_1}, L_{s_1}, R_{p_1}, L_{p_1})$$

$$(Z_2(\omega_\ell), Z_2(\omega_h)) \rightarrow (R_{s_2}, L_{s_2}, R_{p_2}, L_{p_2});$$

3. obtain the currents  $I_1$  and  $I_2$  at  $\omega_\ell$ , by inverting (8.17) for an arbitrary assignment of  $V_1$  and  $V_2$ ;
4. replace  $\omega_\ell$ , currents, voltage assignments, and Foster-pair parameters into (8.20);
5. eliminate  $I_{p_1}, I_{p_2}, V_{m_1}, V_{m_2}$ , thus obtaining two non-linear complex equations for  $M_r, M_s, M_p$ .
6. repeat steps 3,4,5 for  $f_h$ , obtaining a new set of two non-linear equations for  $M_r, M_s, M_p$ .

If the approximations are valid, then the two equations obtained in step 5 should be linearly dependent, and the same holds for the ones in step 6. Moreover, in view of the fact that the  $Z_{12}$  is purely imaginary at low frequencies, then the independent equation in step 5 should be one real equation. In this manner, the number of independent equations is 3, and we are able to solve for  $M_r, M_s, M_p$ .

The method described above is a cumbersome one, and its implementation is not straightforward. A relevant analysis of the necessity for this implementation is required, before embarking on this route. Furthermore, TICER/BMR reduction of the elements  $M_r$  and  $M_p$  is not direct, as opposed to the case of  $M_s$  [110]. Our intention is to propose a solution, for the sake of completeness of the Foster pair model, and notwithstanding the question of its utility.

## 8.5 Conclusions

In these two Chapters, we have outlined a methodology for representing  $RL$  frequency-dependent behavior using frequency-independent circuit parameters. First, we have shown the single-transition case, capturing effects due to either return-path selection, or skin-effect current crowding. Representative examples show that the interpolation errors are small. Next, we have extended the analysis to the case where data is originated from models containing both type of transitions. Analysis of errors and convergence conditions are included. Future applications are discussed in detail, along two lines of development: including more transitions or pairs (and eventually replacing Foster pairs by ladder networks); and representing, in an accurate form, frequency-dependent mutual inductance with Foster pairs.

# General Conclusions

In this Thesis, we have exhibited, analyzed and proposed solutions to three different problems related to interconnects in ICs. Apart from the fact that they have been developed within the same framework, namely Mentor Graphics's extraction tools Calibre xRC/xL, the common feature to these three problems is the search for compact models based on simple physical reasoning. We will now summarize the main contributions for each of these problems, including the implementations into Mentor's commercial tools, as well the ongoing and future work.

## Mutual inductance

Within the physically appropriate loop inductance formalism, we have developed and implemented the dipole approximation, whose main characteristic lies in capturing the leading contribution for interaction between circuit loops; more specifically, we have:

- obtained closed-form formulas for calculating mutual inductance between circuit elements in an extraction flow;
- reduced the cost of these computations, from quadratic to linear in the number of elements;
- shown that accuracy is acceptable for distances comparable to the typical dimensions of circuit loops;
- obtained simple rules that permit discarding certain types of interactions between loops;
- extended the dipole approximation for the calculation mutual inductance between intentional inductors, showing similar gains as the ones mentioned above.

The methods described above are all included within Mentor's extraction tools, and have been filed for patent awards. Concerning present and future developments, we are collaborating with researchers from UCSB along two lines: higher precision approximations at short distances; and inclusion of substrate effects via equivalent Green function methods.

## High frequency modeling of sources

For modeling non-uniform current crowding due to skin and proximity effects at high frequency, we have implemented the method of conduction modes, which consists of expanding the current distributions in terms of functions which are appropriate for this task; in particular we have:

- extended the existing  $RL$ , quasistatic ( $MQS$ ), version of conduction modes, into an  $RLC$  version;
- shown representative  $RLC$  examples with two orders of magnitudes savings in size with respect to standard references;
- developed a systematic approach for the computation of integrals for the  $RL/MQS$  method, in order to render the conduction modes method efficient in terms of computational cost;
- displayed typical  $RL/MQS$  examples with two orders of magnitudes in runtime savings with respect to similar-accuracy, methods based on piecewise constant current functions.

The  $RL/MQS$  implementation is in the process of being included in Calibre xL, replacing the current high-frequency mode. We have discussed extensively, in Chapter 6, the current and future challenges related to conduction modes methods, which are grouped into three groups: rendering  $RLC$  extraction efficient; capturing more general effects by enlarging the basis of conduction modes functions; and applications to arbitrary type of geometry. Although we do not discuss the subject explicitly, another important issue for future development is the inclusion of multi-layered media; as in the previous problem, we expect that this can be done with equivalent Green function methods. Solving these issues will lead to a fullwave Maxwell solver with a different, possibly more efficient, approach as the ones found today in the market.

## Broadband circuit representation

$RL$  effects in ICs have a characteristic increasing- $R$ /decreasing- $L$  behavior over wide frequency ranges; we have represented this behavior using constant-parameter circuits with Foster pairs, appropriate for the model order reduction (MOR) tool implemented in Mentor's tools; in this domain, we have:

- implemented a strategy allowing to capture simple transitions, while guaranteeing physically correct parameters;
- displayed examples that conserve a high accuracy level for cases arising from two physically distinct type of transitions: proximity return-path selection, and skin effect current crowding.

- presented and validated methods for a combination of these two types of transitions.

These strategies are presently included in the formatter for Calibre xRC/xL, and included in the corresponding patent requests. Future work in this area, discussed at the end of Chapter 8, include the extension of Foster pairs, or alternatively ladder circuits, to an arbitrary number of transitions/pairs; another prospect is the representation of frequency-dependent mutual inductance using Foster pairs.



# Conclusions générales

## (version française )

Dans cette thèse, nous avons exposé, analysé et proposé des solutions à trois problèmes différents liés à la modélisation des interconnexions dans les ICs. Outre le fait qu'ils sont développés dans le même cadre, à savoir les outils d'extraction Calibre xRC/xL chez Mentor Graphics, le point commun entre les trois sujets peut se situer dans la recherche des modèles compacts basés sur de simples raisonnements physiques. Nous récapitulerons dans les pages suivantes les contributions pour chacun de ces problèmes, en incluant les applications dans les outils commerciaux Mentor, ainsi qu'une mention des possibilités pour de futures recherches.

### Inductance mutuelle

Dans le formalisme physiquement approprié d'inductance de boucle, nous avons développé et mis en pratique l'approximation dipolaire, dont l'interaction entre les boucles du circuit est simplifiée en ne gardant que sa contribution principale; plus spécifiquement, nous avons:

- obtenu des formules de forme close pour l'inductance mutuelle entre les éléments de circuit, valides pour un schéma d'extraction de parasites;
- réduit le coût de ces calculs, d'une quantité qui est quadratique dans le nombre d'éléments à une qui est linéaire;
- montré que l'exactitude est acceptable pour des distances comparables aux dimensions typiques des boucles de circuit;
- obtenu des règles simples qui permettent de négliger certains types d'interactions entre les boucles;
- étendu l'approximation dipolaire au calcul de l'inductance mutuelle entre deux inducteurs intentionnels, montrant des gains semblables à ceux qui ont été mentionnés ci-dessus.

Toutes les méthodes décrites ci-dessus sont incluses dans les outils d'extraction Calibre, et ont été classées pour des récompenses de brevet. Par rapport aux développements présents et futurs, nous collaborons avec des chercheurs d'UCSB sur deux lignes : la formulation d'approximations de précision plus élevée aux courtes distances, ainsi que l'inclusion des effets de substrat en utilisant des méthodes de fonction de Green équivalentes.

## Modélisation des sources à haute fréquence

Afin de modéliser la distribution non uniforme de courant dû à l'effet de peau, nous avons appliqué la méthode des modes de conduction, dont les distributions sont développées comme une somme de fonctions appropriées à cet effet, à savoir les fonctions propres de l'équation de Helmholtz. En particulier nous avons :

- étendu la méthode des modes de conduction existante, valide pour des problèmes  $RL$  dans le régime quasistatique ( $MQS$ ), dans une version  $RLC$  applicable à un ensemble plus large de problèmes;
- montré des exemples représentatifs de l'application  $RLC$ , obtenant deux ordres de magnitude d'économie pour la taille du système, par rapport aux références standard ;
- développé un approche systématique pour le calcul des intégrales impliquées dans la méthode de  $RL/MQS$  des modes de conduction ;
- reproduit des exemples typiques dans le  $RL/MQS$  avec deux ordres de magnitudes de gains pour les temps d'exécution, pour un même niveau de précision avec des méthodes de fonctions constantes par morceaux.

L'implémentation de la méthode  $RL/MQS$  est en cours d'inclusion dans Calibre xL, remplaçant le mode actuel à haute fréquence, qui est une formulation basée sur des filaments de courant constant. Nous avons discuté en détail, au chapitre 6, les défis découverts en étendant la version actuelle des modes de conduction à une situation plus générale. Ces défis sont groupés en trois groupes : rendre efficace l'extraction  $RLC$ , capturer une gamme plus ample d'effets en agrandissant la base des fonctions de modes de conduction, et considérer un type arbitraire de géométrie. Une autre question importante pour les futurs développements est l'inclusion des médias multicouche ; comme dans le problème précédent, nous pensons que ceci peut être fait avec des méthodes de fonction de Green équivalentes. La solution de ces questions mènera à un solveur d'onde complet des équations de Maxwell, avec une approche différente, et probablement plus efficace, que ceux qui se trouvent aujourd'hui sur le marché.

## Représentation large-bande des circuit $RL$

Les effets  $RL$  dans les IC ont un comportement caractéristique avec la fréquence, consistant de l'augmentation de la résistance  $R$  plus la décroissance de l'inductance  $L$ . Nous avons représenté ce comportement à l'aide des circuits à paramètres constants en utilisant des paires de Foster. Ceux-ci conviennent pour l'outil de réduction de l'ordre du modèle (MOR) mis en application dans les outils chez Mentor. Dans ce domaine, nous avons :

- mis en marche une stratégie permettant la capture des transitions simples, tout en garantissant des paramètres physiquement corrects ;
- montré des exemples qui conservent un niveau de précision acceptable pour des transitions appartenant à deux types physiquement distinct : choix de chemin de retour (effet de proximité), et distribution des courant due à l'effet de peau.
- introduit et validé une stratégie permettant de capturer la combinaison de ces deux types de transitions.

Ces méthodes sont actuellement incluses dans le formateur pour Calibre xRC/xL, et contenues dans les demandes correspondantes de brevet. Des développements futurs dans ce secteur discuté à la fin du chapitre 8 incluent : la prolongation des paires Foster, ou autrement des circuits en échelle, vers un nombre arbitraire des transitions et/ou paires ; ainsi que la représentation des variations de l'impédance mutuelle avec des paires Foster.



# Bibliography

- [1] G. Moore, “Cramming more components onto integrated circuits,” *Electronics Magazine*, Apr. 1975.
- [2] Y. I. Ismail and E. G. Friedman, *On-Chip Inductance in High Speed Integrated Circuits*. Norwell, MA: Kluwer Academic Publisher, 2001.
- [3] T. Sakurai, “Closed-forms expressions for interconnect delay, coupling, and crosstalk in VLSI,” *IEEE Trans. Electron Devices*, vol. 40, pp. 118–124, Jan. 1993.
- [4] C. R. Paul, *Analysis of Multiconductor Transmission Lines*, 1st ed. John Wiley and sons, 1994.
- [5] R. Escovar and R. Suaya, “Optimal design of clock trees for multi-gigahertz applications,” in *IEEE Transactions on CAD*, vol. 23, March 2004, pp. 329–345.
- [6] K. S. Yee, “Numerical solution of initial boundary value problems involving Maxwell’s equations in isotropic media,” *IEEE Transactions on Antennas and Propagation*, vol. 14, no. 3, pp. 302–307, May 1966.
- [7] W. C. Chew, J.-M. Jin, E. Michielssen, and J. S. (Eds.), *Fast and efficient algorithms in computational electromagnetics*. Boston: Arter House, Inc., 2001.
- [8] J.-F. Lee, R. Lee, and A. C. Cangellaris, “Time-domain finite-element methods,” *IEEE Transactions on Antennas and Propagation*, vol. 45, no. 3, pp. 430–442, March 1997.
- [9] I. V. Lindell, “Equivalent circuit models for three-dimensional multiconductor systems,” *IEEE Transactions on Microwave Theory and Techniques*, vol. MTT-22, no. 3, pp. 216–221, August 1974.
- [10] Z. Zhu, B. Song, and J. White, “Algorithms in FastImp: a fast and wide-band impedance extraction program for complicated 3-d geometries,” *IEEE Transactions on Computer-Aided Design of Integrated Circuits and Systems*, vol. 24, pp. 981–998, July 2005.

- [11] *HFSS*, Ansoft Corporation, <http://www.ansoft.com>.
- [12] J.-S. Zhao and W. C. Chew, "Integral equation solution of Maxwell's equations from zero frequency to microwave frequencies," in *IEEE Transactions on Antennas and Propagation*, vol. 48, Oct 2000, pp. 1635–1645.
- [13] T. Moselhy, X. Hu, and L. Daniel, "pFFT in FastMaxwell: a fast impedance extraction solver for 3d conductor structures over substrate," in *Design and Automation in Europe (DATE)*, May 2007.
- [14] K. Nabors and J. White, "FastCap: a multipole accelerated 3-d capacitance extraction program," *Computer-Aided Design of Integrated Circuits and Systems, IEEE Transactions on*, vol. 10, no. 11, pp. 1441–1459, 1991.
- [15] M. Kamon, M. J. Tsuk, and J. White, "FastHenry: A multipole-accelerated 3-d inductance extraction program," *IEEE Trans. Microwave Theory Tech.*, vol. 42, no. 9, pp. 1750–1758, Sept. 1994.
- [16] L. Daniel, "Simulation and modeling techniques for signal integrity and electromagnetic interference on high frequency electronic systems," Ph.D. dissertation, University of California at Berkeley, 2003.
- [17] Y. Saad, *Iterative Methods for Sparse Linear Systems*. Boston: PWS Publishing Company, 1996.
- [18] M. Aksun, "A robust approach for the derivation of closed-form Green's functions," *IEEE Transactions on Microwave Theory and Techniques*, vol. 44, no. 5, pp. 651–657, May 1996.
- [19] V. I. Okhmatovski and A. C. Cangellaris, "A new technique for the derivation of closed-form electromagnetic Green's functions for unbounded planar layered media," *IEEE Transactions on Antennas and Propagation*, vol. 50, no. 7, pp. 1005–1015, July 2002.
- [20] A. E. Ruehli, "Inductance calculations in a complex circuit environment," *IBM J.Res.Develop.*, vol. 16, pp. 470–481, 1972.
- [21] B. Krauter and L. Pileggi, "Generating sparse partial inductance matrices with guaranteed stability," in *Computer-Aided Design IEEE/ACM International Conference on*, Nov 1995, pp. 45–52.
- [22] *Calibre<sup>TM</sup> xRC/xL extracion tool*, Mentor Graphics Corporation, <http://www.mentor.com>.

- [23] R. Escovar, "Tools for impedance extraction in ICs," Ph.D. dissertation, Université Joseph Fourier, Grenoble, France, 2006. [Online]. Available: <http://tel.archives-ouvertes.fr/tel-00127971>
- [24] K. L. Shepard and Z. Tian, "Return-limited inductances: a practical approach to on-chip inductance extraction," *Computer-Aided Design of Integrated Circuits and Systems, IEEE Transactions on*, vol. 19, pp. 425–436, April 2000.
- [25] *Assura RCX-PL*, Cadence Design Systems, [http://www.cadence.com/products/custom-ic/qrc\\_extraction/index.aspx](http://www.cadence.com/products/custom-ic/qrc_extraction/index.aspx).
- [26] H. Hu, D. Blaaw, V. Zolotov, K. Gala, M. Zhao, R. Panda, and S. Sapatnekar, "Fast on-chip inductance simulation using a precorrected-FFT method," *IEEE Transactions on Computer-Aided Design of Integrated Circuits and Systems*, vol. 22, no. 1, pp. 49–66, January 2003.
- [27] R. Escovar, S. Ortiz, and R. Suaya, "Mutual inductance extraction and the dipole approximation," in *International Symposium on Physical Design (ISPD)*, April 2004.
- [28] R. Escovar, S. Ortiz, and R. Suaya, "An improved long distance treatment for mutual inductance," *IEEE Trans. Computer-Aided Design*, vol. 24, no. 5, pp. 783–793, May 2005.
- [29] R. Suaya, R. Escovar, and S. Ortiz, "Mutual inductance extraction using dipole approximations," U.S. Patent application 20050120316, filed June 2005.
- [30] R. Escovar, S. Ortiz, and R. Suaya, "Mutual inductance between intentional inductors: Closed form expressions," in *IEEE International Symposium on Circuits and Systems (ISCAS)*, May 2006.
- [31] R. Suaya, R. Escovar, and S. Ortiz, "Determining mutual inductance between intentional inductors," U.S. Patent application 20060282492, filed Dec. 2006.
- [32] L. Daniel, A. Sangiovanni-Vincentelli, and J. White, "Using conduction modes basis functions for efficient electromagnetic analysis of on-chip and off-chip interconnect," in *Design Automation Conference (DAC), 2001. Proceedings*, 2001, pp. 563–566.
- [33] S. Ortiz and R. Suaya, "Fullwave volumetric Maxwell solver using conduction modes," in *IEEE International Conference on Computer Aided Design (ICCAD)*, November 2006.
- [34] S. Ortiz and R. Suaya, "Efficient implementation of conduction modes for modelling skin effect," in *IEEE International Symposium on Very Large Scale Integration (ISVLSI)*, May 2007.

- [35] L. Pillage, C. Wolff, and R. Rohrer, "Asymptotic Waveform Evaluation for timing analysis," *IEEE Transactions on Computer-Aided Design*, vol. 9, no. 4, pp. 352–66, 1990.
- [36] P. Feldmann and R. Freund, "Efficient linear circuit analysis by Padé approximation via the Lanczos process," *IEEE Transactions on Computer-Aided Design*, vol. 14, no. 4, pp. 639–49, 1995.
- [37] A. Odabasioglu, M. Celik, and L. Pileggi, "PRIMA: passive reduced-order interconnect modeling," *IEEE Transactions on Computer-Aided Design of Integrated Circuits and Systems*, vol. 17, no. 8, pp. 645–54, 1998.
- [38] B. N. Sheehan, "TICER: Realizable reduction of extracted RC circuits," *International Conference on Computer Aided Design*, pp. 200–203, November 1999.
- [39] B. N. Sheehan, "Branch merge reduction of RLCM networks," *International Conference on Computer Aided Design*, pp. 658–664, November 2003.
- [40] B. N. Sheehan, "Realizable reduction of passive networks," Ph.D. dissertation, University of Minnesota, 2005.
- [41] R. Suaya, R. Escovar, S. Thelapurath, S. Ortiz, and D. Petranovic, "Extracting impedance effects from a circuit design using an electronic design automation tool," U.S. Patent application 11/704,588, filed Feb. 2007.
- [42] E. Rosa, "The self and mutual inductance of linear conductors," *Bulletin of the National Bureau of Standards*, vol. 4, pp. 301–344, 1908.
- [43] Columbus, Sequence Design, Inc. [Online]. Available: <http://www.sequencedesign.com/solutions/columbus.php>
- [44] G. Golub and C. van Loan, *Matrix Computations, 3rd Ed.* Baltimore: The Johns Hopkins University Press, 1992.
- [45] Z. He, M. Celik, and L. T. Pileggi, "SPIE: Sparse partial inductance extraction," in *Design Automation Conference*, 1997, pp. 137–140.
- [46] J. Jackson, *Classical Electrodynamics*. New York: John Wiley and Sons, Inc., 1962.
- [47] A. Devgan, H. Lin, and W. Dai, "How to efficiently capture on-chip inductance effects: Introducing a new circuit element  $k$ ," in *IEEE/ACM International Conference on Computer Aided Design*, Nov 2000, pp. 150–155.

- [48] T.-H. Chen, C.Luk, and C.C.P.Chen, "Inductwise: inductance-wise interconnect simulator and extractor," in *IEEE Transactions on Computer-Aided Design of Integrated Circuits and Systems*, vol. 22, no. 7, 2003, pp. 884–894.
- [49] M. Beattie and L. Pileggi, "Inductance 101: Modeling and extraction," *Design Automation Conference*, pp. 323–328, 2001.
- [50] M. Beattie, B. Krauter, L. Alatan, and L. Pileggi, "Equipotential shells for efficient inductance extraction," *IEEE Trans. CAD of IC and Systems*, vol. 20, pp. 70–79, 2001.
- [51] H.Ji, A.Devgan, and W.Dai, "KSIM: A stable and efficient RKC simulator for capturing on-chip inductance effect," in *Proc.Asia South Pacific Design Automation Conf*, 2001, pp. 379–384.
- [52] M. Beattie and L. Pileggi, "Efficient inductance extraction via windowing," in *Proc.Design,Automation, and Test in Europe*, 2001, pp. 430–436.
- [53] *Eldo<sup>TM</sup> Analog Simulator*, Mentor Graphics Corporation, <http://www.mentor.com/eldo>.
- [54] H. Hu and S. Sapatnekar, "Efficient inductance extraction using circuit-aware techniques," *IEEE Transactions on VLSI Systems*, vol. 10, no. 6, pp. 746–761, December 2002.
- [55] M. Beattie and L. Pileggi, "Efficient inductance extraction via windowing," *Proc.Design,Automation, and Test in Europe*, pp. 430–436, 2001.
- [56] F. Grover, *Inductance Calculations Working Formula and Tables*. New York: Instrument Society of America, 1945.
- [57] R. Escovar and R. Suaya, "Transmission line design of clock trees," in *Proc. IEEE/ACM International Conference on CAD*, Nov. 2002, pp. 334–340.
- [58] T. Lin, M. Beattie, and L. Pileggi, "On the efficiency of simplified 2d on-chip inductance models," in *Design Automation Conference*, 2002, pp. 757–762.
- [59] R. Escovar, "Private communication."
- [60] N. Srivastava, K. Banerjee, and R. Suaya, "paper sent and accepted to Design and Automation in Europe (DATE) 2008."
- [61] N. Srivastava, K. Banerjee, S. Ortiz, and R. Suaya, "Paper in preparation, June 2007."
- [62] A. M. Niknejad and R. G. Meyer, *Simulation and Applications of Inductors and Transformers for Si RF ICs*. Kluwer Academic Publishers, 2000.

- [63] M. Beattie, S. Gupta, and L. Pileggi, "Hierarchical interconnect circuit models," in *Proc ICCAD*, Nov 2000.
- [64] S. Gupta and L. Pileggi, "Hierarchical modeling of electrostatic and magnetostatic couplings," in *SRC Techcon Conference*, August 2003.
- [65] S. Gupta, "Modelling inductive couplings in traditional and nanoscale interconnects," Ph.D. dissertation, Carnegie Mellon University, 2004.
- [66] *ASITIC: Analysis and Simulation of Spiral Inductors and Transformers for ICs*, <http://rfic.eecs.berkeley.edu/~niknejad/asitic.html>.
- [67] R. Beatson and L. Greengard, "A short course on fast multipole methods," *Oxford University Press*, 1997.
- [68] *Raphael<sup>TM</sup> Interconnect Analysis Tool*, Synopsys Inc., [http://www.synopsys.com/products/tcad/raphael\\_ds.html](http://www.synopsys.com/products/tcad/raphael_ds.html).
- [69] *Source code for FastHenry, FastCap, FastImp and FastMaxwell*, Massachusetts Institute of Technology, Computational Prototyping Group, [http://www.rle.mit.edu/cpg/research\\_codes.htm](http://www.rle.mit.edu/cpg/research_codes.htm).
- [70] *Source code for LargeCom*, University of Illinois at Urbana Champaign, Center for Computational Electromagnetics, <http://cceml.ece.uiuc.edu/ware.asp>.
- [71] *Sonnet*, Sonnet Software Inc., <http://www.sonnetusa.com>.
- [72] *IE3D*, Zeland Software Inc., <http://www.zeland.com/>.
- [73] P. Silvester, "Modal network theory of skin effect in flat conductors," vol. 54, no. 9, pp. 1147–1151, September 1966.
- [74] X. Hu, L. Daniel, and J. White, "Partitioned conduction modes in surface integral equation-based impedance extraction," in *Electrical Performance of Electronic Packaging*, Oct 2003, pp. 355–358.
- [75] ITRS, *International Technology Roadmap For Semiconductors - 2005 Edition*. Semiconductor Industry Association, 2005. [Online]. Available: <http://www.itrs.net/>
- [76] M. Born and E. Wolf, *Principles of optics, electromagnetic theory of propagation, interference and diffraction of light*, 7th ed. Cambridge University Press, 1999.
- [77] E. M. Purcell, *Electricity and Magnetism, Berkeley Physics Course, Vol.2*, 2nd ed. McGraw-Hill, 1985.

- [78] R. F. Harrington, *Field Computation by Moment Methods*. New York: MacMillan, 1968.
- [79] H. A. Haus and J. R. Melcher, *Electromagnetic Fields and Energy*. (out of stock), found online at [http://web.mit.edu/6.013\\_book/www/book.html](http://web.mit.edu/6.013_book/www/book.html): MIT, 1998.
- [80] J. A. Davis and J. D. Meindl, "Compact distributed RLC interconnect models," *IEEE Trans. Electron Devices*, vol. 47, no. 11, pp. 2068–2087, 2000.
- [81] W. Weeks, "Multiconductor transmission line theory in the TEM approximation," *IBM Journal of Research and Development*, pp. 604–611, November 1972.
- [82] Y. Leviatan and A. Adams, "The response of a two-wire transmission line to incident field and voltage excitation, including effects of higher order modes," *IEEE Transactions on Antennas and Propagation*, vol. AP-30, no. 5, pp. 998–1003, September 1982.
- [83] I. V. Lindell, "TE/TM decomposition of electromagnetic sources," *IEEE Transactions on Antennas and Propagation*, vol. 36, no. 10, pp. 1382–1388, October 1988.
- [84] I. V. Lindell, "On the quasi-TEM modes in inhomogeneous multiconductor transmission lines," *IEEE Transactions on Microwave Theory and Techniques*, vol. MTT-29, no. 8, pp. 812–817, August 1981.
- [85] A. dos Santos and J. Figanier, "The method of series expansion in the frequency domain applied to multielectric transmission lines," *IEEE Transactions on Microwave Theory and Techniques*, vol. MTT-23, pp. 753–756, September 1975.
- [86] W. H. Press, B. P. Flannery, S. A. Teukolsky, and W. T. Vetterling, *Numerical Recipes: The Art of Scientific Computing*, 1st ed. Cambridge (UK) and New York: Cambridge University Press, 1986.
- [87] J. Berntsen, T. Espelid, and A. Genz, "An adaptive algorithm for the approximate calculation of multiple integrals," *ACM Transactions on Mathematical Software*, vol. 17, pp. 437–451, 1991.
- [88] W. C. Chew and Z. Qian, "Private communication."
- [89] G. P. Lepage, "A new algorithm for adaptive multidimensional integration," *Journal of Computational Physics*, vol. 27, pp. 192–203, 1978.
- [90] *Quantify 2003a.06.15 FixPack 0214 060606 Linux (32-bit) (C) Copyright IBM Corporation. 1992, 2006 All Rights Reserved*, IBM, 2006.
- [91] L. Daniel, "Private communication."

- [92] W. C. Chew, *Waves and Fields in Inhomogeneous Media*. Piscataway: IEEE Press., 1995.
- [93] X. Hu, "Full-wave analysis of large conductor systems over substrate," Ph.D. dissertation, Massachusetts Institute of Technology, 2006.
- [94] H. Keller and E. Isaacson, *Analysis of Numerical Methods*. Dover publications, Inc., 1966.
- [95] L. Daniel, A. Sangiovanni-Vincentelli, and J. White, "Proximity templates for modeling of skin and proximity effects on packages and high frequency interconnect," in *Computer Aided Design, IEEE/ACM International Conference on (ICCAD)*, Nov 2002, pp. 326–333.
- [96] X. Hu, T. Moselhy, J. White, and L. Daniel, "Optimization-based wideband basis functions for efficient interconnect extraction," in *Design and Automation in Europe (DATE)*, May 2007.
- [97] R. Suaya, S. Ortiz, R. Escovar, N. Srivastava, and K. Banerjee, "Interconnect modeling and extraction in nanometer design," in *Advanced Metalisation Conference (AMC)*, October 2006.
- [98] R. Renka, "Multivariate interpolation of large sets of scattered data," *ACM Transactions on Mathematical Software*, vol. 14, no. 2, pp. 139–148, 1988.
- [99] S. Ortiz and R. Suaya, "in preparation, January 2008."
- [100] H. B. Lee, "On the differing abilities of RL structures to realize natural frequencies," *IEEE Transactions on Circuit Theory*, vol. CT-12, no. 3, pp. 365–373, September 1965.
- [101] G. T. Daryanani and J. A. Resh, "Foster-distributed-lumped network synthesis," *IEEE Transactions on Circuit Theory*, vol. CT-16, no. 4, pp. 429–434, November 1969.
- [102] K. Murthy and R. Bedford, "Transformation between Foster and Cauer equivalent networks," *IEEE Transactions on Circuits and Systems*, vol. CAS-25, no. 4, pp. 238–239, April 1978.
- [103] G. Kopcsay, B. Krauter, D. Widiger, A. Deutsch, B. Rubin, and H. Smith, "A comprehensive 2-d inductance modeling approach for VLSI frequency-dependent extraction and compact circuit model synthesis," *IEEE Transactions on VLSI*, vol. 10, no. 6, pp. 695–711, Decembet 2002.

- [104] D. Goren et al, "On-chip interconnect-aware design and modeling methodology, based on high bandwidth transmission line devices," *Design Automation Conference (DAC)*, vol. 3, pp. 724–727, June 2003.
- [105] Q. Yu and E. S. Kuh, "Accurate reduced RL model for frequency dependent transmission lines," *9th International Conference on Electronics, Circuits and Systems*, vol. 2, pp. 761–764, September 2002.
- [106] B. Krauter and S. Mehrotra, "Layout based frequency dependent inductance and resistance extraction for on-chip interconnect timing analysis," in *Proc. 35th ACM/IEEE DAC*, Jan. 1998, pp. 303–308.
- [107] S. Kim and D. Neikrik, "Compact equivalent circuit model for the skin effect," *IEEE MTT-S International Microwave Symposium Digest*, vol. 3, pp. 1815–1818, June 1996.
- [108] R. Suaya, R. Escovar, S. Thelapurath, and S. Ortiz, "Extracting impedance effects from a circuit design using broadband representations," U.S. Patent application 11/704,470, filed Feb. 2007.
- [109] G. Golub and V. Pereyra, "The differentiation of pseudo-inverses and nonlinear least squares problems whose variables separate," *SIAM J. Numer. Anal.*, vol. 10, pp. 413–432, Apr. 1973.
- [110] B. Sheehan, "Private communication."